Eigenfunctions in chaotic quantum systems

Habilitationsschrift
zur Erlangung des akademischen Grades

Dr. rer. nat. habil.

Fakultät Mathematik und Naturwissenschaften
der Technischen Universität Dresden

Institut für Theoretische Physik

Dr. Arnd Bäcker

Dresden 2007

Eingereicht am 05.06.2007

1. Gutachter: Prof. Dr. R. Ketzmerick, TU Dresden
2. Gutachter: Prof. Dr. K. Richter, Universität Regensburg
3. Gutachter: Prof. Dr. F. Haake, Universität Duisburg-Essen

Wissenschaftlicher Vortrag und Probevorlesung am 04.04.2008

Abstract:
The structure of wavefunctions of quantum systems strongly depends on the underlying classical dynamics. In this text a selection of articles on eigenfunctions in systems with fully chaotic dynamics and systems with a mixed phase space is summarized. Of particular interest are statistical properties like amplitude distribution and spatial autocorrelation function and the implication of eigenfunction structures on transport properties. For systems with a mixed phase space the separation into regular and chaotic states does not always hold away from the semiclassical limit, such that chaotic states may completely penetrate into the region of the regular island. The consequences of this flooding are discussed and universal aspects highlighted.

Contents

1 Introduction

This text contains a selection of articles on the structure of eigenfunctions in quantum systems whose classical dynamics is either fully chaotic or shows a mixed phase space. After a brief introduction on classical chaos the main results of the articles in the appendix are summarized and put into perspective.

Chaotic behaviour in dynamical systems is a phenomenon which has been studied in great detail. As quantum mechanics is the more fundamental description of nature, one would like to understand the properties of quantum systems whose corresponding classical dynamics is chaotic [1–6]. For investigating this subject billiards are a particularly suited class of systems because many rigorous mathematical results exist, see e.g. [7]. In the Euclidean case a billiard system is given by the free motion of a point particle inside a bounded domain Ω. At the boundary the particle is reflected specularly, i.e. angle of incidence and angle of reflection coincide. So it is only the boundary which determines the dynamical behaviour of the system which can range from integrable, over mixed to completely chaotic motion. Fig. 1 shows 100 successive reflections of one trajectory for different integrable and chaotic systems. For the integrable case there is an-

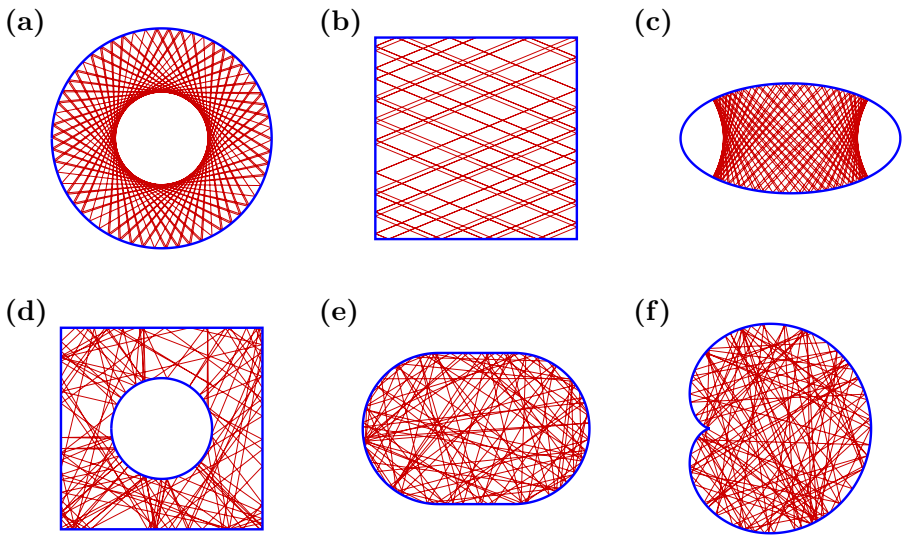

Figure 1: For different billiards 100 successive reflections of one orbit are shown. The regular dynamics for the billiard in the (a) circle, (b) square and (c) ellipse is in contrast to chaotic dynamics for the (d) Sinai billiard, (e) stadium billiard and (f) cardioid billiard.

other conserved quantity besides the energy; e.g. for the billiard in a circle this is the angular momentum such that the motion is confined to a two-dimensional manifold in phase space.

However, in general no such additional constants of motion exist and the resulting dynamics is much more complicated. For certain billiards it is possible to prove that they are fully chaotic, i.e., they are ergodic, mixing and K–systems. Ergodicity means that spatial and temporal averages agree. Considering the trajectory $(\boldsymbol{p}_{(\boldsymbol{p}_0,\boldsymbol{q}_0)}(t), \boldsymbol{q}_{(\boldsymbol{p}_0,\boldsymbol{q}_0)}(t))$ of a particle started in the point $(\boldsymbol{p}_0, \boldsymbol{q}_0)$, the probability to find it in a certain region D in position space is given by

$$\lim_{T\to\infty} \frac{1}{T} \int_0^T \chi_D(\boldsymbol{q}_{(\boldsymbol{p}_0,\boldsymbol{q}_0)}(t))\, \mathrm{d}t = \frac{\mathrm{vol}(D)}{\mathrm{vol}(\Omega)} \tag{1}$$

for almost all initial conditions $(\boldsymbol{p}_0, \boldsymbol{q}_0)$, where χ_D is the characteristic function of D. Thus in ergodic systems the probability to find the particle inside D is just the relative area of that region. Therefore a typical trajectory will asymptotically fill out the accessible space in a uniform way. This is nicely seen in Fig. 1(d–f) for the Sinai billiard [8,9], the stadium billiard [10,11], and the cardioid billiard [12–14]. The origin of ergodicity in these systems is hyperbolicity, which means that initially infinitesimally close trajectories separate exponentially in time. Usually hyperbolic billiards are also mixing, i.e. correlations decay and appear as random as a coin-toss (K–property, Bernoulli property) [15–17]. Because of these rigorous results, chaotic billiards are an important class of model systems to investigate the implications of classical chaos in the corresponding quantum systems.

2 Chaos in quantum systems

While classical mechanics describes macroscopic objects correctly, at small scales a quantum mechanical description is necessary. Due to the Heisenberg uncertainty principle it is no longer possible to specify both position and momentum of a particle at the same time. Therefore, instead of considering the time-evolution, one of the main research lines in quantum chaos concerns the statistical properties of eigenfunctions and energy levels, in particular in which way they depend on the underlying classical dynamics.

Quantum mechanically, billiards are described by the stationary Schrödinger

equation (in units $\hbar = 2m = 1$)

$$-\Delta\psi_n(\mathbf{q}) = E_n\psi_n(\mathbf{q}) \ , \quad \boldsymbol{q} \in \Omega \tag{2}$$

with e.g. Dirichlet boundary conditions $\psi_n(\mathbf{q}) = 0$ for $\boldsymbol{q} \in \partial\Omega$. Here Δ denotes the Laplace operator, which reads in two dimensions $\Delta = \left(\frac{\partial^2}{\partial q_1^2} + \frac{\partial^2}{\partial q_2^2}\right)$. The mathematical problem defined by Eq. (2) is the well–known eigenvalue problem of the Helmholtz equation, which for example also describes the eigenfrequencies of a vibrating membrane or of flat microwave cavities [4].

For some simple domains Ω it is possible to solve Eq. (2) analytically. For the billiard in a rectangle with sides a and b the (non–normalized) eigenfunctions are given by $\psi_{n_1,n_2}(\boldsymbol{q}) = \sin(\pi n_1 q_1/a)\sin(\pi n_2 q_2/b)$ with corresponding eigenvalues $E_{n_1,n_2} = \pi^2(n_1^2/a^2 + n_2^2/b^2)$ and $(n_1, n_2) \in \mathbb{N}^2$. For the billiard in a circle the eigenfunctions are given in polar coordinates by $\psi_{mn}(r,\varphi) = J_m(j_{mn}r)\exp(\mathrm{i}m\varphi)$, where j_{mn} is the n–th zero of the Bessel function $J_m(x)$ and $m \in \mathbb{Z}$, $n \in \mathbb{N}$. However, in general no analytical solutions of Eq. (2) exist, so that numerical methods have to be used to compute eigenvalues and eigenfunctions. Among the many different possibilities, the boundary-integal method is widely used, see e.g. [18–20] and [A4] for a review and further references.

2.1 Fully chaotic systems

One of the central questions in quantum chaos concerns the implications of the underlying classical dynamical properties on the statistical behaviour of eigenvalues. It has been conjectured that for fully chaotic systems these are described by the statistics of random matrices obeying appropriate symmetries [21]. For generic integrable systems one expects that the energy–level statistics can be described by a Poissonian random process [22]. These conjectures are supported by semiclassical considerations and many numerical studies. However, in both cases exceptions are known: for example, so-called arithmetic systems (see e.g. [23–27]) show Poissonian spectral statistics despite being strongly chaotic. Also quantized cat maps show non–generic spectral statistics [28, 29]. Moreover, there are also cases where a limit distribution of common spectral statistics does not exist [30]. In [31, 32] the distribution of the normalized fluctuations of the spectral staircase function around its mean has been proposed as a possible signature of quantum chaos. It has been conjectured that the limit distribution should be Gaussian for fully chaotic systems, while integrable systems should exhibit a non-Gaussian limit distribution. This conjecture was tested successfully for several regular and

chaotic billiard systems, see [32–37].

The main tool for analyzing spectral statistics are trace formulae [2] which relate quantum mechanical properties, like the density of states, with purely classical information, involving the periodic orbits and their properties. By this a semiclassial prediction for the spectral rigidity was derived using the diagonal approximation [38]. By including correlations between certain pairs of periodic orbits important progress was made recently to obtain higher order corrections for the two-point correlations [39–41]. This has been applied and extended to more general situations, leading to a semiclassical explanation of two-point spectral statistics in fully chaotic systems [42, 43].

Concerning the eigenfunctions of (2) one would expect that the classical dynamics is reflected by their structure. According to the *semiclassical eigenfunction hypothesis* the eigenstates should concentrate on those regions which a generic orbit explores in the long–time limit [44–46, 1]. For integrable systems the motion is restricted to invariant tori in phase space while for ergodic systems the whole energy surface is filled in a uniform way. In the case of ergodic systems the semiclassical eigenfunction hypothesis is proven by the quantum ergodicity theorem [47–52] (see [53] for an introduction), which states that almost all eigenfunctions become equidistributed in the semiclassical limit. Restricted to position

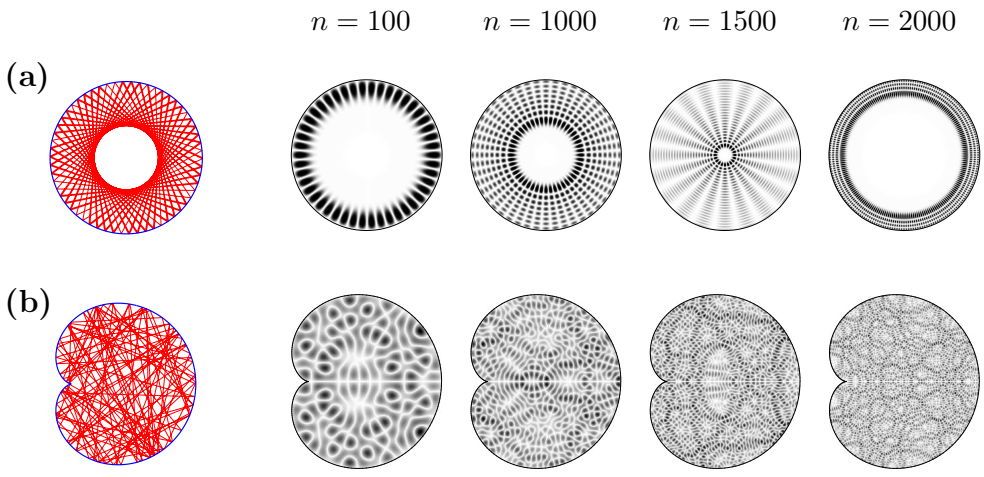

Figure 2: The eigenstates of (a) the integrable circular billiard and (b) the chaotic cardioid billiard reflect the structure of the corresponding classical dynamics. Shown is a density plot of $|\psi_n(\boldsymbol{q})|^2$ where black corresponds to high probability.

space this gives

$$\lim_{j\to\infty} \int_D |\psi_{n_j}(\boldsymbol{q})|^2 \, \mathrm{d}^2 q = \frac{\mathrm{vol}(D)}{\mathrm{vol}(\Omega)} \tag{3}$$

for a subsequence $\{\psi_{n_j}\} \subset \{\psi_n\}$ of density one. A subsequence of eigenfunctions has density one if $\lim_{E\to\infty} \#\{n_j \mid E_{n_j} \leq E\}/\#\{n \mid E_n \leq E\} = 1$. So in this sense for almost all eigenfunctions the probability of finding a particle in a certain region D of the position space Ω is in the semiclassical limit just the same as for the classical system, see Eq. (1). Fig. 2 illustrates the described behaviour qualitatively for the case of the integrable circular billiard and the chaotic cardioid billiard. In both cases the eigenfunctions show oscillations on the scale of a de Broglie wavelength. For the integrable system the probability is on average restricted to subregions of the billiard. In contrast, for the ergodic system the probability density is on average uniformly distributed over the full billiard region.

As a statistical model for the eigenfunctions of strongly chaotic systems it has been proposed that they behave like a random superposition of plane waves [45]. Heuristically, this is motivated by the underlying chaotic dynamics where a typical trajectory gets close to every point in position space with apparently random directions and random phases (corresponding to the length of trajectory segments). In the two–dimensional Euclidean case the random superposition of plane waves on a region $\Omega \subset \mathbb{R}^2$ may be written as

$$\psi_{\mathrm{RWM}}(\boldsymbol{q}) \;=\; \sqrt{\frac{2}{\mathrm{vol}(\Omega)\, N}} \sum_{n=1}^{N} a_n \cos(\boldsymbol{k}_n \boldsymbol{q} + \phi_n) \;\;, \tag{4}$$

where $a_n \in \mathbb{R}$ are assumed to be independent Gaussian random variables with mean zero and variance one; ϕ_n are equidistributed random variables on $[0, 2\pi[$. The factor in front of the sum ensures that ψ_{RWM} is normalized in the limit $N \to \infty$. The momenta $\boldsymbol{k}_n \in \mathbb{R}^2$ satisfy $|\boldsymbol{k}_n| = \sqrt{E}$ and are randomly equidistributed on the circle of radius $\sqrt{E}$.

In Fig. 3 one realization of a random wave (4) is compared with a chaotic eigenstate in the cardioid billiard. Locally, the eigenstate nicely resembles the random wave (ignoring the symmetry of the eigenstate and boundary effects). Going beyond this qualitative comparison, the random wave model can be used to obtain quantitative predictions on the statistical behaviour of wave functions in chaotic systems. One of the simplest consequence concerns the amplitude distribution. Using the central-limit-theorem one directly obtains that random

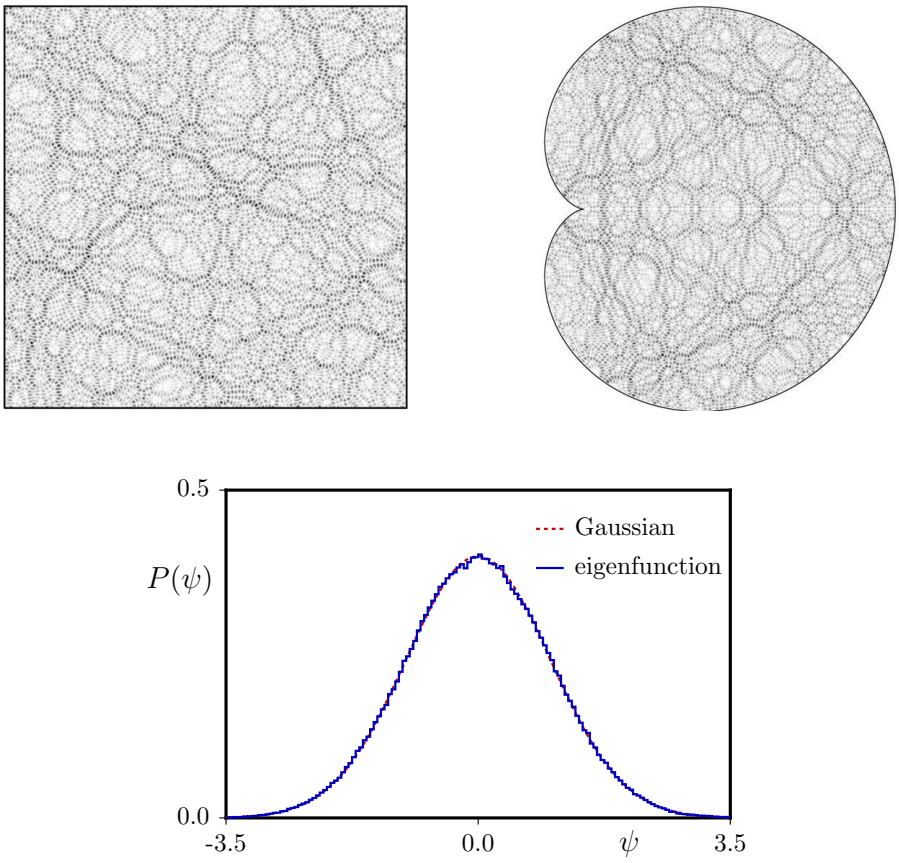

Figure 3: Example of a random wave (4) in comparison with the 6000$^{\text{th}}$ eigenfunction of the cardioid billiard (of odd symmetry). For this state one observes excellent agreement of the amplitude distribution with the expected Gaussian.

waves show a Gaussian value distribution,

$$P(\psi) = \frac{1}{\sqrt{2\pi}\sigma} \exp\left(-\frac{\psi^2}{2\sigma^2}\right) \quad , \tag{5}$$

where $\sigma^2 = 1/\operatorname{vol}(\Omega)$. This conjecture is supported by various numerical studies, see e.g. [54–57]. For the example shown in Fig. 3 the numerical histogram of the amplitude distribution is (on this scale) essentially indistinguishable from the normal distribution.

While the behaviour of expectation values for almost all eigenfunctions is proven by the quantum ergodicity theorem, a proof of the random wave model is an open problem. Still, both seem closely related, as exceptional (in the sense of

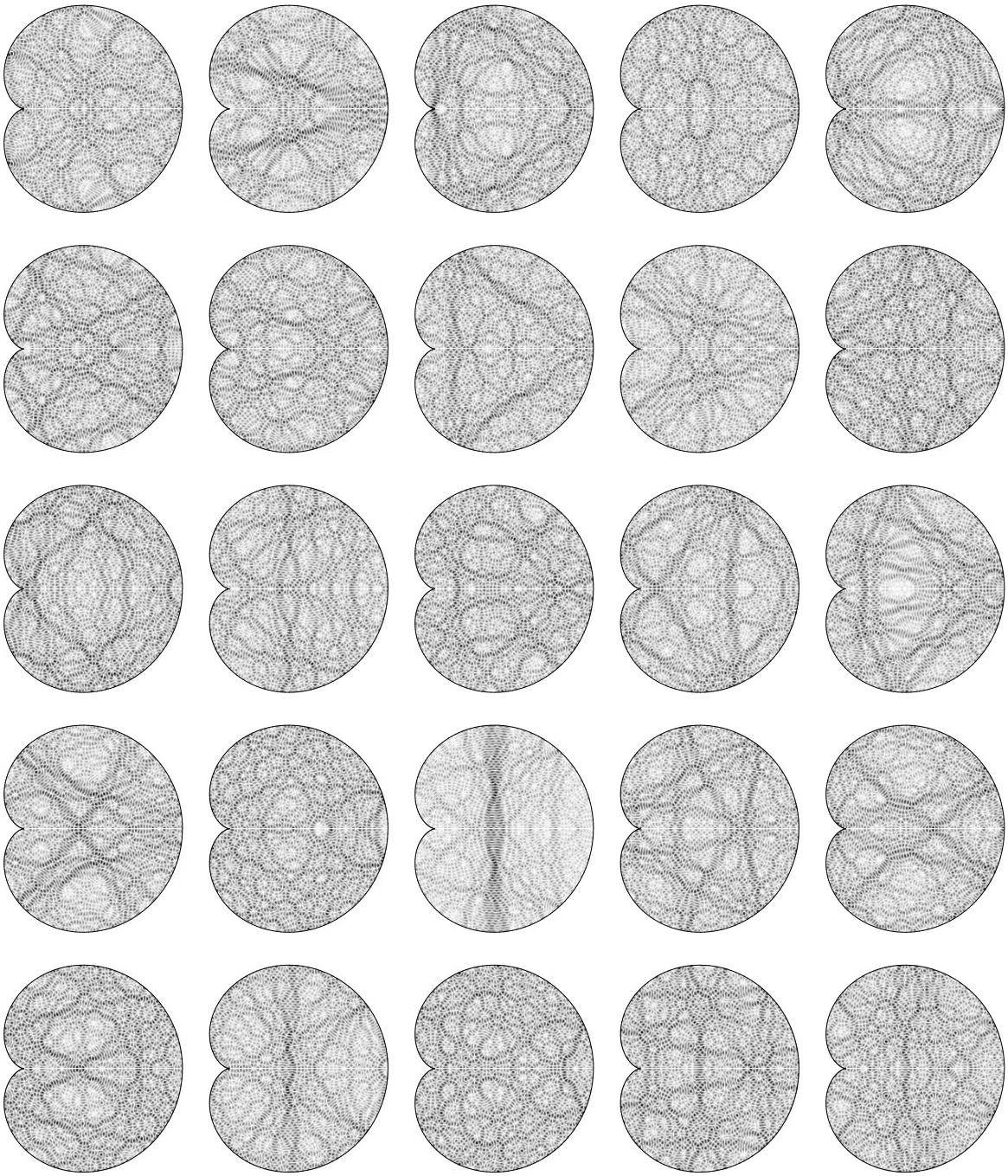

Figure 4: Sequence of eigenfunctions in the cardioid billiard, ψ_{1800} to ψ_{1824} of odd symmetry.

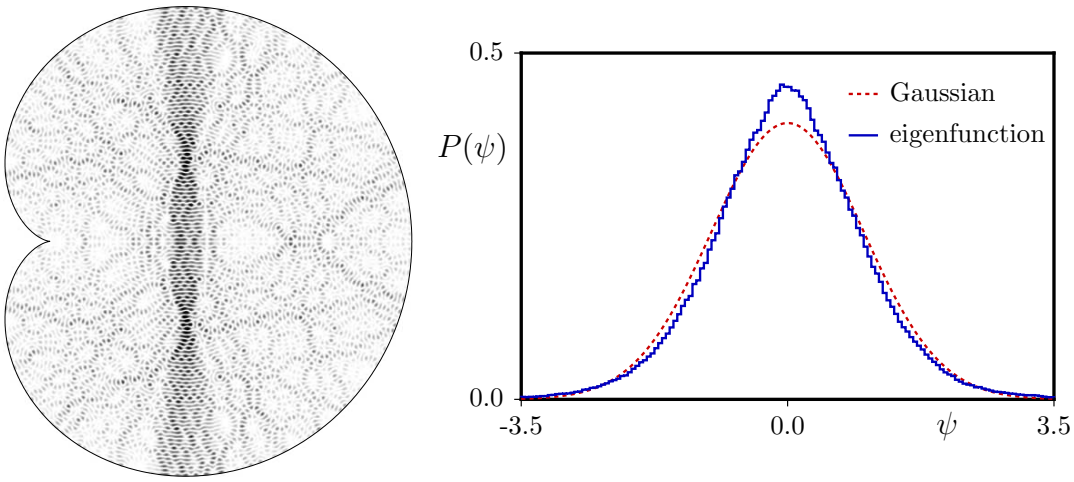

Figure 5: For the scarred state ψ_{4042} the amplitude distribution is clearly different from the Gaussian normal distribution (dashed curve).

quantum ergodicity) sequences of eigenfunctions also do not follow the prediction of the random wave model. One candidate are the so-called scars [58] which are eigenfunctions concentrating around unstable periodic orbits, see Fig. 4. For such eigenfunctions also the value distribution clearly differs from the Gaussian, see Fig. 5. By a semiclassical description for the eigenfunctions [59, 60] it should be possible to use the position-space averaged density together with the restricted random wave model [A1] (discussed in the following section) to obtain a prediction for the observed amplitude distribution.

2.2 Systems with a mixed phase space

Systems with either regular or fully chaotic dynamics are extreme cases and typically one has a so-called mixed phase space in which regular and chaotic motion coexist [61]. The transition from the integrable case to mixed dynamics under small perturbations of the system is described by KAM-theory due to Kolmogorov [62], Arnold [64], and Moser [65] which roughly speaking states that for small perturbations sufficiently irrational invariant tori will persist. At the same time small stochastic regions develop, leading to a complicated structure in phase space.

As an example let us consider the family of limaçon billiards which was introduced as a deformation of the circle billiard [66], with boundary in polar

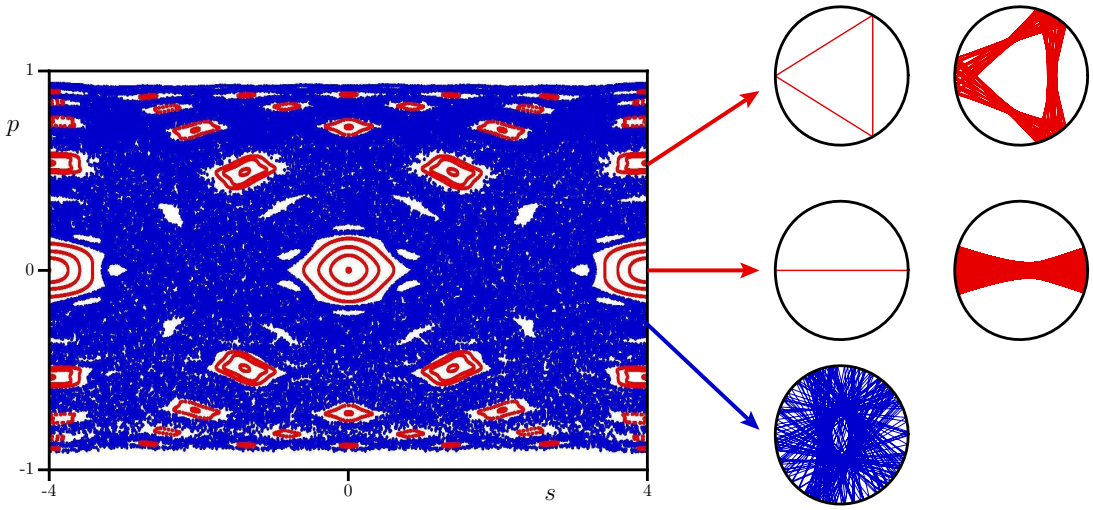

Figure 6: Example of a system with a mixed phase space. Shown are several regular orbits and one chaotic orbit in the Poincaré section of the limaçon billiard at $\varepsilon = 0.3$. To the right two regular orbits and trajectories in the surrounding are displayed in position space in comparison with a chaotic trajectory.

coordinates given by $\rho(\phi) = 1 + \varepsilon \cos(\phi)$, with $\phi \in [-\pi, \pi]$, where $\varepsilon \in [0, 1]$ is the family parameter. For $\varepsilon > 0$ one gets a mixed phase space, where (some of) the KAM curves persist until $\varepsilon = 0.5$ [67, 66, 68]. For stronger perturbations regular islands become very small. However, even arbitrarily close to the fully chaotic cardioid at $\varepsilon = 1$ one can find tiny regular islands [69].

To visualize the dynamics in phase space, it is convenient to introduce the billiard boundary as a Poincaré section. As coordinates one chooses the point of reflection, described by the arc-length s along the billiard boundary, and the projection of the unit-velocity vector after the reflection onto the tangent in s. The billiard flow therefore induces a two-dimensional area-preserving map of the Poincaré section onto itself. Fig. 6 illustrates this for the limaçon billiard at $\varepsilon = 0.3$ which shows a large irregular component ("chaotic sea") intermixed with regular islands around stable periodic orbits. An important question on the classical dynamics is, whether the irregular component has positive measure. For a constructed example [70] and the mushroom billiard [71] this has been proven rigorously, however, for general systems the problem remains open (see also [72] for a review on this coexistence problem).

2.2.1 Structure of eigenfunctions

For systems with a mixed phase space, the semiclassical eigenfunction hypothesis implies that the eigenstates can be classified in the semiclassical limit as either regular or chaotic according to the phase-space region on which they concentrate. This is supported by several studies, see e.g. [73–78] and references therein. Fig. 7 shows examples for the limaçon billiard, where in addition to a three-dimensional visualization of $|\psi_n(\boldsymbol{q})|^2$ and a density plot also a quantum Poincaré–Husimi representation is shown [A5]. For such a representation on the billiard boundary a natural starting point is to use the normal derivative (see [79] for a study of its properties) of the eigenfunction and project it onto a periodized coherent state. However, as there is no natural Hilbert space for the boundary functions, different definitions of the scalar-product are possible [80–82]. By relating the Husimi function in phase space with the one on the Poincaré–Husimi representation it is possible to show that a meaningful representation can already be obtained without further terms in the scalar product [A5]. From the relation between the Poincaré–Husimi functions and the Husimi function in phase space also a quantum ergodicity theorem for the Poincaré–Husimi functions in the case of ergodic systems follows.

The statistical properties of regular eigenstates in systems with a mixed phase space will strongly depend on the island in which they concentrate and on the characterizing quantum numbers of a semiclassical quantization rule, as can be seen for the moments of semiclassical wavefunctions [83]. However, for the irregular eigenstates which are concentrated on an irregular region D in phase space the statistical properties should be described by those of a superposition of plane waves with wave vectors of the same lengths and directions distributed uniformly on D. We thus obtain the following restricted random wave model [A1]

$$\psi_{\mathrm{RRWM},D}(\boldsymbol{q}) = \sqrt{\frac{4\pi}{\mathrm{vol}(D)N}} \sum_{n=1}^{N} \chi_D(\boldsymbol{k}_n, \boldsymbol{q}) \cos(\boldsymbol{k}_n \boldsymbol{q} + \varepsilon_n) \quad . \tag{6}$$

In contrast to the random wave model (4) for fully chaotic systems, the characteristic function $\chi_D(\cdot)$ ensures the localization on the irregular region D in phase space. Because the projection of D onto position space is in general non-uniform, we obtain locally a Gaussian distribution

$$P_{\boldsymbol{q}}(\psi) \longrightarrow \sqrt{\frac{1}{2\pi\sigma^2(\boldsymbol{q})}} \exp\left(-\frac{\psi^2}{2\sigma^2(\boldsymbol{q})}\right) \quad , \tag{7}$$

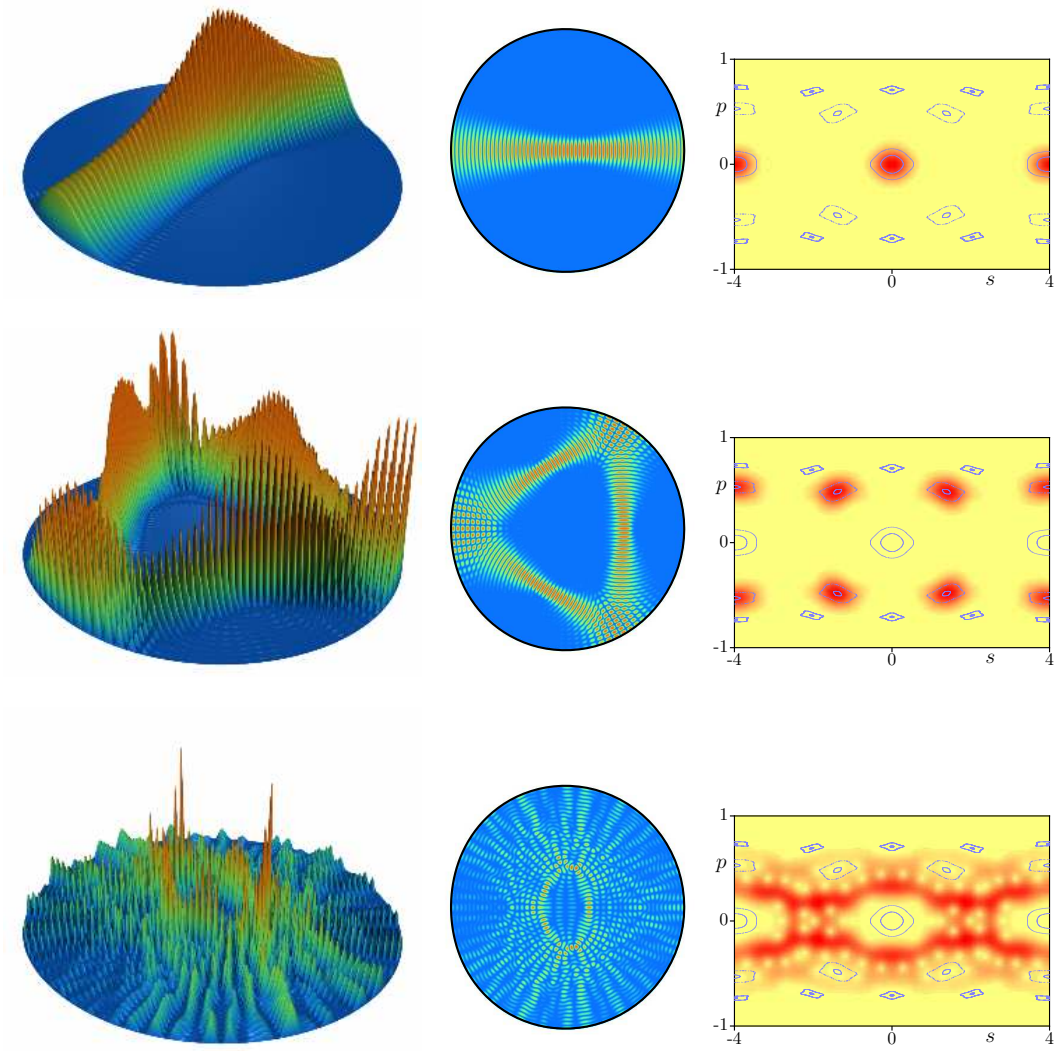

Figure 7: Eigenstates in a billiard with a mixed phase space typically either concentrate in the regular islands, or extend over the chaotic region. This is most clearly seen in the quantum Poincaré–Husimi representation displayed in the last column for each case.

but with a position dependent variance $\sigma^2(\boldsymbol{q})$. For an ergodic system $\sigma^2(\boldsymbol{q}) = 1/\operatorname{vol}(\Omega)$ and one recovers the result (5) of a Gaussian amplitude distribution. However, if $\sigma^2(\boldsymbol{q})$ depends on $\boldsymbol{q}$ then the corresponding distribution can show deviations from the Gaussian. Fig. 8 shows such an example for which $P(\psi)$ is clearly different from the normal distribution and agrees well with the prediction

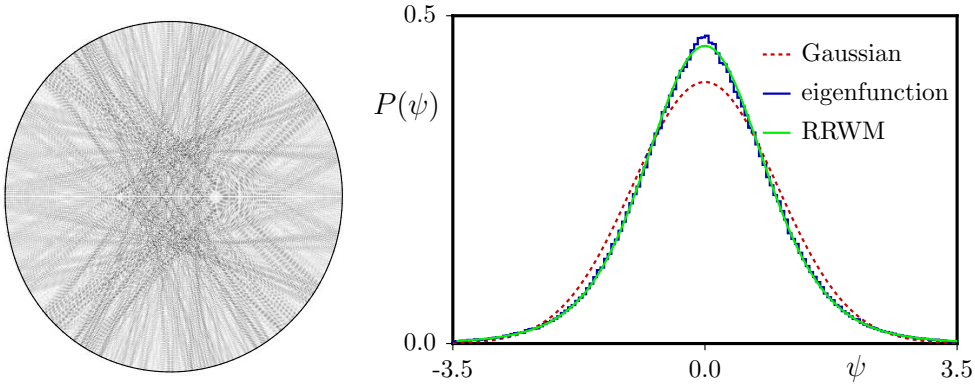

Figure 8: High lying eigenfunction ($E = 1002754.70\ldots$, approximately the 130568^{th} state) in the limaçon billiard at $\varepsilon = 0.3$. The amplitude distribution clearly differs from a normal distribution (dashed curve) expected for fully chaotic systems and is in good agreement with the prediction of the restricted random wave model (RRWM).

of the restricted random wave model [A1]. Such non-isotropic random wave models are also of importance in other situations, see e.g. [84–86].

While the amplitude distribution only provides a local measure of the statistical properties of eigenfunctions, the spatial autocorrelation function

$$C(\boldsymbol{q}, \delta\mathbf{q}) := \langle \psi(\boldsymbol{q} - \delta\mathbf{q}/2)\psi(\boldsymbol{q} + \delta\mathbf{q}/2)\rangle \tag{8}$$

measures correlations over a longer range. The average $\langle\cdot\rangle$ in Eq. (8) is performed over the random wave ensemble; when numerically computing the autocorrelation function of eigenfunctions an averaging over $\boldsymbol{q}$, sometimes with an additional spectral averaging, is used. For ergodic systems the eigenfunctions semiclassically concentrate on the energy shell. This implies that $C(\boldsymbol{q}, \delta\mathbf{q}) = \frac{1}{\mathrm{vol}(\Omega)} J_0(\sqrt{E}|\delta\mathbf{q}|)$ [45], which has been tested successfully for small correlation lengths $|\delta\mathbf{q}|$, see e.g. [54, 56, 57, 87, 88]. For larger $|\delta\mathbf{q}|$ deviations become visible, which can be shown to vanish in the semiclassical limit [A2].

For the spatial autocorrelation function of irregular eigenstates in systems with a mixed phase space, one can, similar to the case of the amplitude distribution, use information about the irregular component in phase space to obtain a semiclassical prediction which is found to be in very good agreement with numerical results [A2].

Another important aspect in systems with a mixed phase space are bifurcations of periodic orbits under parameter variation. These have a substantial

influence on spectral statistics [89–92] and also on the spatial autocorrelation function [93].

In a typical mixed phase space stable periodic orbits are not just surrounded by invariant KAM tori, but also by broken tori, the so-called cantori [94–98]. These provide partial barriers to the dynamics and may have an important influence both classically and quantum mechanically. For example, they are responsible for a sequence of hierarchical states [99] living in the chaotic component close to the regular regions. Such states can significantly influence the scattering signatures of a corresponding open system [A3]. Here the hierarchical states lead to additional isolated resonances in the conductance fluctuations. By a comparison with the eigenstates of the corresponding closed system it is possible to characterize the isolated resonances as hierarchical or regular, depending on where the corresponding eigenstates concentrate in the classical phase space.

2.2.2 Flooding of regular islands

The phase-space structure of systems with a mixed phase space is typically rather complicated because regular islands are surrounded by higher-order islands which continues to arbitrarily fine scales. The chaotic regions also contain regular islands of arbitrarily small size. This makes a treatment and understanding very difficult. One successful approach is to consider systems for which the dynamics can be tuned in such a way that for example only one large regular island exists in a mainly homogeneous chaotic sea [100]. This is possible for certain area-preserving maps on a two-torus arising from a one-dimensional kicked Hamiltonian $H(p,q,t) = T(p) + V(q)\sum_{n=-\infty}^{\infty}\delta(t-n)$. The dynamics is fully determined by the mapping of position and momentum (p_n, q_n) at times $t = n + 0^+$ just after the kicks

$$q_{n+1} = q_n + T'(p_n) \ , \tag{9}$$

$$p_{n+1} = p_n - V'(q_{n+1}) \ . \tag{10}$$

We impose periodicity for $p \in [0,1[$ and $q \in [0,M[$, where the usual case of one unit cell corresponds to $M = 1$.

For such kicked systems, the quantum evolution of a state after one period of time $|\psi(t+1)\rangle = \hat{U}|\psi(t)\rangle$ is determined by the unitary operator, see e.g. [101, 28, 102–104],

$$\hat{U} = \exp\left(-\frac{2\pi\mathrm{i}}{h_{\mathrm{eff}}}V(\hat{q})\right)\exp\left(-\frac{2\pi\mathrm{i}}{h_{\mathrm{eff}}}T(\hat{p})\right) \ . \tag{11}$$

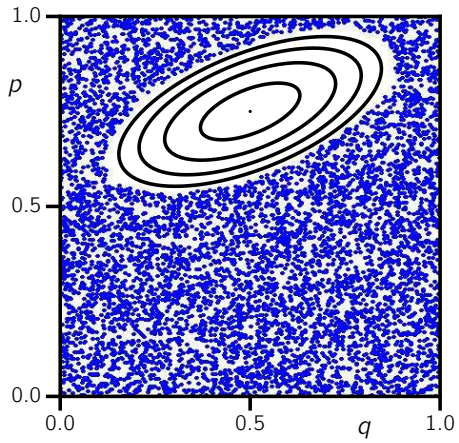

Figure 9: Phase space structure of an area-preserving map with one large regular island and a narrow transition region to a homogeneous chaotic sea.

Here the effective Planck's constant h_{eff} is Planck's constant h divided by the size of one unit cell. The eigenstates $|\psi_j\rangle$ and eigenphases φ_j of this operator are defined by

$$\hat{U}|\psi_j\rangle = \mathrm{e}^{2\pi \mathrm{i} \varphi_j}|\psi_j\rangle \quad . \tag{12}$$

To fulfill the periodicity of the classical dynamics in both p and q direction the effective Planck's constant can only be a rational number $h_{\text{eff}} = \frac{M}{N}$.

Choosing the functions $T'(p)$ and $V'(q)$ appropriately, one can obtain a system with a large regular island and a homogeneous chaotic sea, see Fig. 9. The resulting eigenstates can be classified as either irregular or regular. The irregular states mainly live outside of the regular island, see Fig. 10. The regular states concentrate on tori which fulfill the quantization condition

$$\oint p \, \mathrm{d}q = (m + 1/2) h_{\text{eff}} \qquad m = 0, 1, ... \tag{13}$$

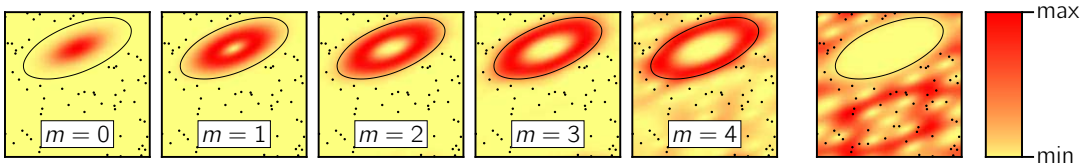

Figure 10: For $M = 1$ and $h_{\text{eff}} = 1/30$ the eigenstates are either mainly regular ($m = 0, 1, ...$) or mainly chaotic.

for the enclosed area [101].

In Ref. [A6] it was shown that Eq. (13) is not a sufficient condition for the existence of a regular eigenstate on the m-th quantized torus. In addition one has to fulfill

$$\gamma_m < \frac{1}{\tau_{\mathrm{H,ch}}} \quad , \tag{14}$$

where $\tau_{\mathrm{H,ch}} = h_{\mathrm{eff}}/\Delta_{\mathrm{ch}}$ is the Heisenberg time of the surrounding chaotic sea with mean level spacing Δ_{ch} and γ_m is the decay rate of the m-th regular state, if the chaotic sea was infinite. When condition (14) is violated one observes eigenstates which extend over the chaotic region and flood the m-th torus [A6]. For the limiting case of complete flooding of all tori, the corresponding eigenstates were called amphibious [100]. The process of flooding is most clearly seen by considering a sequence of systems with fixed h_{eff} but increasing Heisenberg time. This is possible for the kicked maps by increasing M but still keeping the ratio $h_{\mathrm{eff}} = M/N$ approximately constant. As the classical dynamics and h_{eff} are unchanged, also the tunneling rates are fixed. Because of $\tau_{\mathrm{H,ch}} \sim M$ it is possible

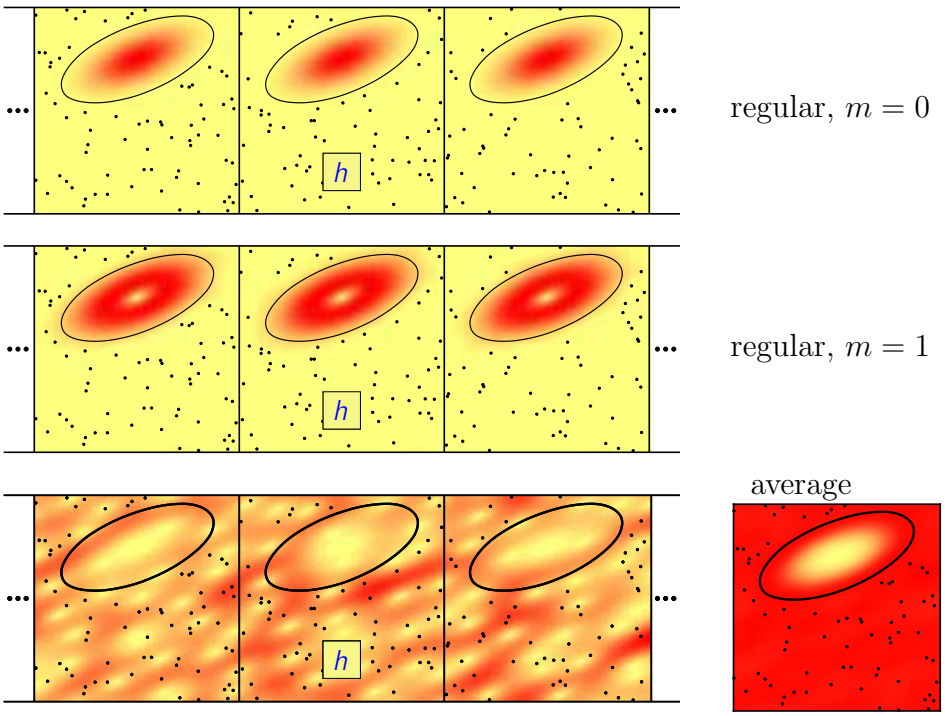

Figure 11: For $M = 1597$ and $h_{\mathrm{eff}} = 1/20$ only the regular states with $m = 0$ and $m = 1$ exist while the chaotic states flood into the phase space region previously occupied by the regular states with $m = 2$ and $m = 3$.

to violate condition (14) for sufficiently large M as illustrated in Fig. 11.

It is important to note that in the semiclassical limit, the tunneling rates γ_m become exponentially small, i.e. the effective coupling v tends to 0, such that for fixed system size condition (14) is fullfilled. Therefore the flooding of the regular island observed at finite h_{eff} is not in contradiction to the semiclassical eigenfunction hypothesis.

In Ref. [A6] the process of flooding and condition (14) was explained by scaling arguments and demonstrated for a kicked system. In order to obtain a quantitative description, in particular about the transition regime and the way how chaotic eigenstates turn into flooding eigenstates a random matrix description is used in Ref. [A8]. Random matrix models have been very successful for obtaining quantitative predictions on eigenstates in both fully chaotic systems and systems with a mixed phase space, see e.g. [73, 105–107]. For the considered situation a model is proposed which takes regular basis states and their coupling to the chaotic basis states into account. The only free parameters are the strength of the coupling and the ratio of the number of regular to the number of chaotic basis states. From this model the weight distribution for eigenstates is determined. To compare this with numerical results for the quantum system, we determine the weight in the m-th regular state by projecting the eigenstates onto semiclassical regular states [108]. By considering the fraction f_{reg} of regular states for different values of h_{eff} and system sizes M, plotted vs. the effective coupling v, a universal

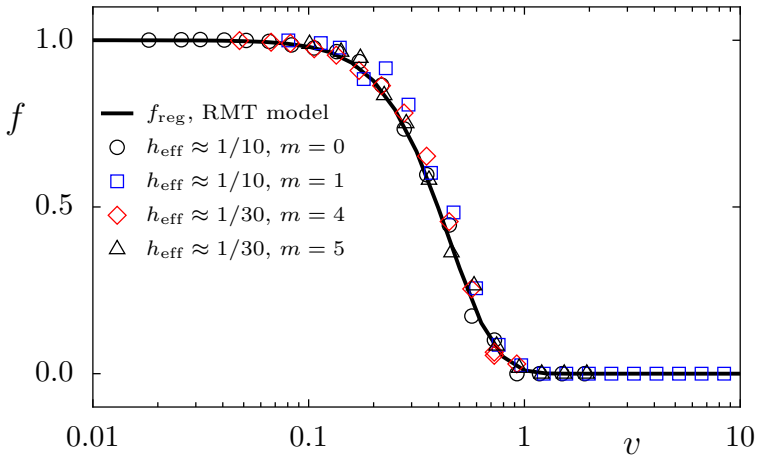

Figure 12: Fraction f_{reg} of regular states vs. coupling strength v for the random matrix model (full line) and the kicked system for various h_{eff} and m (symbols), where the system size M is rescaled to the effective coupling strength v.

behaviour is obtained (see Ref. [A6] for details), which is well described by the prediction of the random matrix model, see Fig. 12.

In [A7] it is demonstrated that the implications of flooding can also be observed in the transport properties of one-sided rough nano-wires in a magnetic field. In such a system the regular island arises from the skipping motion along the straight wall while trajectories which are reflected at the rough wall get backscattered in an irregular way. As a function of the length of the wire one observes that the total transmission decreases in a sequence of steps. Each step corresponds to the disappearance of a regular state until complete flooding occurs. At the same time this effect leads to exponentially diverging localization lengths in the semiclassical limit, which is unexpected from a random matrix description for systems with disorder and only understandable by taking the mixed phase geometry of the system into account.

3 Outlook

The results summarized in the previous section also lead to several new questions: For example, in [A6] the wave-packet dynamics in systems with flooding is briefly addressed, but a detailed understanding and quantitative description of the temporal flooding is currently under investigation [109]. For the statistical properties of both flooding states and time-evolved wave-packets it has to be investigated, whether a restricted random wave type description [A2], adapted to the case of quantum maps [110], applies. One of the future challenges is to observe flooding experimentally. For this one possible candidate are the previously mentioned mushroom billiards, realized as a microwave cavity. For these the Heisenberg time may be increased by enlarging the chaotic part of phase space, such that the dissappearance of regular states might be observable in the structure of resonances. Another important issue is the determination of tunneling rates, which is crucial for the existence criterion (14) for regular states. For a certain class of quantized maps important progress was made recently [111–113], while its extension to more general systems, in particular to billiards, is an open question.

Acknowledgements

First, I would like to thank all co-workers of the joint publications. Moreover, I would like to thank Prof. Dr. J. P. Keating and the Applied Mathematics Department in Bristol for the kind hospitality during my stay in Bristol. Moreover I am grateful to Prof. Dr. F. Steiner and Prof. Dr. R. Ketzmerick for their support.

References

[1] M. V. Berry: *Semiclassical mechanics of regular and irregular motion*, in: *Comportement Chaotique des Systèmes Déterministes — Chaotic Behaviour of Deterministic Systems* (Eds. G. Iooss, R. H. G. Hellemann and R. Stora), 171–271, North-Holland, Amsterdam, (1983).

[2] M. C. Gutzwiller: *Chaos in Classical and Quantum Mechanics*, Springer-Verlag, New York, (1990).

[3] M. V. Berry: *Some quantum-to-classical asymptotics*, in: *Proceedings of the 1989 Les Houches School on Chaos and Quantum Physics* (Eds. M.-J. Giannoni, A. Voros and J. Zinn Justin), 251–303, North–Holland, Amsterdam, (1991).

[4] H.-J. Stöckmann: *Quantum chaos*, Cambridge University Press, Cambridge, (1999).

[5] K. Richter: *Semiclassical Theory of Mesoscopic Quantum Systems*, vol. 161 of *Springer Tracts in Modern Physics*, Springer, Berlin, (2000).

[6] F. Haake: *Quantum Signatures of Chaos*, Springer-Verlag, Berlin, 2nd edn., (2001).

[7] S. Tabachnikov: *Billiards*, Panoramas et Synthèses 1, Société Mathematique de France, Paris, (1995).

[8] Ya. G. Sinai: *On the foundations of the ergodic hypothesis for a dynamical system of statistical mechanics*, Sov. Math. Dokl. **4** (1963) 1818–1822.

[9] Ya. G. Sinai: *Dynamical systems with elastic reflections*, Russ. Math. Surveys **25** (1970) 137–189.

[10] L. A. Bunimovich: *On ergodic properties of certain billiards*, Funct. Anal. Appl. **8** (1974) 254–255.

[11] L. A. Bunimovich: *On the ergodic properties of nowhere dispersing billiards*, Commun. Math. Phys. **65** (1979) 295–312.

[12] M. Wojtkowski: *Principles for the design of billiards with nonvanishing Lyapunov exponents*, Commun. Math. Phys. **105** (1986) 391–414.

[13] D. Szász: *On the K-property of some planar hyperbolic billiards*, Commun. Math. Phys. **145** (1992) 595–604.

[14] R. Markarian: *New ergodic billiards: exact results*, Nonlinearity **6** (1993) 819–841.

[15] G. Gallavotti and D. S. Ornstein: *Billiards and Bernoulli schemes*, Commun. Math. Phys. **38** (1974) 83–101.

[16] D. S. Ornstein and B. Weiss: *Statistical properties of chaotic systems*, Bull. Am. Math. Soc. **24** (1991) 11–116.

[17] N. I. Chernov and C. Haskell: *Nonuniformly hyperbolic K-systems are Bernoulli*, Ergodic Theory Dynam. Systems **16** (1996) 19–44.

[18] A. J. Burton and G. F. Miller: *The application of integral equation methods to the numerical solution of some exterior boundary-value problems*, Proc. R. Soc. London Ser. A **323** (1971) 201–210.

[19] M. V. Berry and M. Wilkinson: *Diabolical points in the spectra of triangles*, Proc. R. Soc. London Ser. A **392** (1984) 15–43.

[20] M. Sieber and F. Steiner: *Quantum chaos in the hyperbola billiard*, Phys. Lett. A **148** (1990) 415–419.

[21] O. Bohigas, M.-J. Giannoni and C. Schmit: *Characterization of chaotic quantum spectra and universality of level fluctuation laws*, Phys. Rev. Lett. **52** (1984) 1–4.

[22] M. V. Berry and M. Tabor: *Level clustering in the regular spectrum*, Proc. R. Soc. London Ser. A **356** (1977) 375–394.

[23] R. Aurich and F. Steiner: *On the periodic orbits of a strongly chaotic system*, Physica D **32** (1988) 451–460.

[24] E. B. Bogomolny, B. Georgeot, M.-J. Giannoni and C. Schmit: *Chaotic billiards generated by arithmetic groups*, Phys. Rev. Lett. **69** (1992) 1477–1480.

[25] J. Bolte, G. Steil and F. Steiner: *Arithmetical chaos and violation of universality in energy level statistics*, Phys. Rev. Lett. **69** (1992) 2188–2191.

[26] J. Bolte: *Some studies on arithmetical chaos in classical and quantum mechanics*, Int. J. Mod. Phys B **7** (1993) 4451–4553.

[27] P. Sarnak: *Arithmetic quantum chaos*, Israel Math. Conf. Proc. **8** (1995) 183–236.

[28] J. H. Hannay and M. V. Berry: *Quantization of linear maps on a torus — Fresnel diffraction by periodic grating*, Physica D **1** (1980) 267–290.

[29] J. P. Keating: *The cat maps: Quantum mechanics and classical motion*, Nonlinearity **4** (1991) 309–341.

[30] A. Bäcker and G. Haag: *Spectral statistics for quantized skew translations on the torus,*, J. Phys. A **32** (1999) L393–L398.

[31] F. Steiner: *Quantum chaos*, in *Schlaglichter der Forschung. Zum 75. Jahrestag der Universität Hamburg 1994*, (ed. R. Ansorge) Festschrift published on the occasion of the 75th anniversary of the University of Hamburg, pp. 543–564, Dietrich Reimer Verlag, Berlin und Hamburg (1994).

[32] R. Aurich, J. Bolte and F. Steiner: *Universal signatures of quantum chaos*, Phys. Rev. Lett. **73** (1994) 1356–1359.

[33] R. Aurich, F. Scheffler and F. Steiner: *On the subtleties of arithmetical quantum chaos*, Phys. Rev. E **51** (1995) 4173–4189.

[34] A. Bäcker, F. Steiner and P. Stifter: *Spectral statistics in the quantized cardioid billiard*, Phys. Rev. E **52** (1995) 2463–2472.

[35] R. Aurich, A. Bäcker and F. Steiner: *Mode fluctuations as fingerprints of chaotic and non-chaotic systems*, Int. J. Mod. Phys. B **11** (1997) 805–849.

[36] H. Alt, A. Bäcker, C. Dembowski, H.-D. Gräf, R. Hofferbert, H. Rehfeld and A. Richter: *Mode fluctuation distribution for spectra of superconducting microwave billiards*, Phys. Rev. E **58** (1998) 1737–1742.

[37] M. Tomiya and N. Yoshinaga: *Mode fluctuation distribution of coupled quartic oscillators*, Phys. Rev. E **58** (1998) 8017–8020.

[38] M. V. Berry: *Semiclassical theory of spectral rigidity*, Proc. R. Soc. London Ser. A **400** (1985) 229–251.

[39] M. Sieber and K. Richter: *Correlations between periodic orbits and their rôle in spectral sta tistics*, Physica Scripta **2001** (2001) T90 128–133.

[40] M. Sieber: *Leading off-diagonal approximation for the spectral form factor for uniformly hyperbolic systems*, J. Phys. A **35** (2002) 42 L613–L619.

[41] K. Richter and M. Sieber: *Semiclassical Theory of Chaotic Quantum Transport*, Phys. Rev. Lett. **89** (Oct 2002) 20 206801.

[42] P. A. Braun, F. Haake and S. Heusler: *Action correlation of orbits through non-conventional time reversal*, J. Phys. A **35** (2002) 6 1381–1388.

[43] S. Heusler, S. Müller, A. Altland, P. Braun and F. Haake: *Periodic-Orbit Theory of Level Correlations*, Phys. Rev. Lett. **98** (2007) 4 044103.

[44] I. C. Percival: *Regular and irregular spectra*, J. Phys. B **6** (1973) L229–L232.

[45] M. V. Berry: *Regular and irregular semiclassical wavefunctions*, J. Phys. A **10** (1977) 2083–2091.

[46] A. Voros: *Semi-classical ergodicity of quantum eigenstates in the Wigner representation*, in: *Stochastic Behavior in Classical and Quantum Hamiltonian Systems* [63], 326–333.

[47] A. I. Shnirelman: *Ergodic properties of eigenfunctions* (in Russian), Usp. Math. Nauk **29** (1974) 181–182.

[48] S. Zelditch: *Uniform distribution of eigenfunctions on compact hyperbolic surfaces*, Duke. Math. J. **55** (1987) 919–941.

[49] Y. Colin de Verdière: *Ergodicité et fonctions propres du laplacien* (in French), Commun. Math. Phys. **102** (1985) 497–502.

[50] B. Helffer, A. Martinez and D. Robert: *Ergodicité et limite semi-classique* (in French), Commun. Math. Phys. **109** (1987) 313–326.

[51] P. Gérard and E. Leichtnam: *Ergodic properties of eigenfunctions for the Dirichlet problem*, Duke Math. J. **71** (1993) 559–607.

[52] S. Zelditch and M. Zworski: *Ergodicity of eigenfunctions for ergodic billiards*, Commun. Math. Phys. **175** (1996) 673–682.

[53] A. Bäcker, R. Schubert and P. Stifter: *Rate of quantum ergodicity in Euclidean billiards*, Phys. Rev. E **57** (1998) 5425–5447, erratum ibid. **58** (1998) 5192.

[54] S. W. McDonald and A. N. Kaufmann: *Wave chaos in the stadium: Statistical properties of short-wave solutions of the Helmholtz equation*, Phys. Rev. A **37** (1988) 3067–3086.

[55] P. W. O'Connor and E. J. Heller: *Quantum localization for a strongly classically chaotic system*, Phys. Rev. Lett. **61** (1988) 2288–2291.

[56] R. Aurich and F. Steiner: *Statistical properties of highly excited quantum eigenstates of a strongly chaotic system*, Physica D **64** (1993) 185–214.

[57] B. Li and M. Robnik: *Statistical properties of high-lying chaotic eigenstates*, J. Phys. A **27** (1994) 5509–5523.

[58] E. J. Heller: *Bound-state eigenfunctions of classically chaotic Hamiltonian systems: Scars of periodic orbits*, Phys. Rev. Lett. **53** (1984) 1515–1518.

[59] E. B. Bogomolny: *Smoothed wave functions of chaotic quantum systems*, Physica D **31** (1988) 169–189.

[60] M. V. Berry: *Quantum scars of classical closed orbits in phase space*, Proc. R. Soc. London Ser. A **423** (1989) 219–231.

[61] L. Markus and K. Meyer: *Generic Hamiltonian Dynamical Systems are neither Integrable nor Chaotic*, no. 114 in Mem. Amer. Math. Soc., American Mathematical Society, Providence, Rhode Island, (1974).

[62] A. N. Kolmogorov: *Preservation of conditionally periodic movements with small change in the Hamilton function* (in Russian), Dokl. Akad. Nauk. SSSR **98** (1954) 527–530, English translation in [63], 51–56.

[63] G. Casati and J. Ford (eds.): *Stochastic Behavior in Classical and Quantum Hamiltonian Systems*, no. 93 in Lecture Notes in Physics, Springer-Verlag, Berlin, (1979).

[64] V. I. Arnold: *Proof of a theorem of A. N. Kolmogorov on the invariance of quasi-periodic motions under small perturbations of the Hamiltonian*, Russ. Math. Surv. **18** (1963) 9–36.

[65] J. Moser: *On invariant curves of area-preserving mappings of an annulus*, Nachr. Akad. Wiss. Göttingen **1** (1962) 1–20.

[66] M. Robnik: *Classical dynamics of a family of billiards with analytic boundaries*, J. Phys. A **16** (1983) 3971–3986.

[67] V. F. Lazutkin: *The existence of caustics for a billiard problem in a convex domain*, Math. USSR Izv. **7** (1973) 185–215.

[68] A. Hayli, T. Dumont, J. Moulin-Ollagnier and J.-M. Strelcyn: *Quelques résultats nouveaux sur les billiards de Robnik*, J. Phys. A **20** (1987) 3237–3249.

[69] H. R. Dullin and A. Bäcker: *About ergodicity in the family of limaçon billiards*, Nonlinearity **14** (2001) 1673–1687.

[70] M. Wojtkowski: *A model problem with the coexistence of stochastic and integrable behaviour*, Commun. Math. Phys. **80** (1981) 453–464.

[71] L. A. Bunimovich: *Mushrooms and other billiards with divided phase space*, Chaos **11** (2001) 802–808.

[72] J.-M. Strelcyn: *The "coexistence problem" for conservative dynamical systems: a review*, Colloquium mathematicum **62** (1991) 331–345.

[73] O. Bohigas, S. Tomsovic and D. Ullmo: *Manifestations of classical phase space structures in quantum mechanics*, Phys. Rep. **223** (1993) 43–133.

[74] T. Prosen and M. Robnik: *Survey of the eigenfunctions of a billiard system between integrability and chaos*, J. Phys. A **26** (1993) 5365–5373.

[75] B. Li and M. Robnik: *Separating the regular and irregular energy levels and their statistics in a Hamiltonian system with mixed classical dynamics*, J. Phys. A **28** (1995) 4843–4857.

[76] G. Carlo, E. Vergini and A. Fendrik: *Numerical verification of Percival's conjecture in a quantum billiard*, Phys. Rev. E **57** (1998) 5397–5403.

[77] G. Veble, M. Robnik and J. Liu: *Study of regular and irregular states in generic systems*, J. Phys. A **32** (1999) 6423–6444.

[78] J. Marklof and S. O'Keefe: *Weyl's law and quantum ergodicity for maps with divided phase space*, Nonlinearity **18** (2005) 277–304.

[79] A. Bäcker, S. Fürstberger, R. Schubert and F. Steiner: *Behaviour of boundary functions for quantum billiards*, J. Phys. A **35** (2002) 10293–10310.

[80] B. Crespi, G. Perez and S.-J. Chang: *Quantum Poincaré sections for two-dimensional billiards*, Phys. Rev. E **47** (1993) 986–991.

[81] J. M. Tualle and A. Voros: *Normal modes of billiards portrayed in the stellar (or nodal) representation*, Chaos, Solitons and Fractals **5** (1995) 1085–1102.

[82] F. P. Simonotti, E. Vergini and M. Saraceno: *Quantitative study of scars in the boundary section of the stadium billiard*, Phys. Rev. E **56** (1997) 3859–3867.

[83] M. V. Berry, J. H. Hannay and A. M. Ozorio de Almeida: *Intensity moments of semiclassical wavefunctions*, Physica D **8** (1983) 229–242.

[84] M. V. Berry and H. Ishio: *Nodal densities of Gaussian random waves satisfying mixed boundary conditions*, J. Phys. A **35** (2002) 5961–5972.

[85] W. E. Bies, N. Lepore and E. J. Heller: *Quantum billiards and constrained random wave correlations*, J. Phys. A **36** (2003) 6 1605–1613.

[86] J. D. Urbina and K. Richter: *Supporting random wave models: a quantum mechanical approach*, J. Phys. A **36** (2003) 38 L495–L502.

[87] S. Hortikar and M. Srednicki: *Correlations in chaotic eigenfunctions at large separation*, Phys. Rev. Lett. **80** (1998) 1646–1649.

[88] B. Eckhardt, U. Dörr, U. Kuhl and H.-J. Stöckmann: *Correlations of electromagnetic fields in chaotic cavities*, Europhys. Lett. **46** (1999) 134–140.

[89] M. V. Berry, J. P. Keating and S. D. Prado: *Orbit bifurcations and spectral statistics*, J. Phys. A **31** (1998) L245–L254.

[90] M. V. Berry, *Spectral twinkling*, in Proc. Int School of Physics "Enrico Fermi", course CXLIII (eds: G. Casati, I. Guarneri and U. Smilansky), IOS Press, Amsterdam (2000) 45–63.

[91] M. V. Berry, J. P. Keating and H. Schomerus: *Universal twinkling exponents for spectral fluctuations associated with mixed chaology*, Proc. Roy. Soc. Lond. A **456** (2000) 1659–1668.

[92] J. P. Keating and S. D. Prado: *Orbit bifurcations and the scarring of wavefunctions*, Proc. R. Soc. Lond. A **457** (2001) 1855–1872.

[93] A. Bäcker, J. Keating and S. Prado: *Orbit bifurcations and wavefunction autocorrelations*, Nonlinearity **15** (2002) 1417–1433.

[94] R. S. MacKay, J. D. Meiss and I. C. Percival: *Transport in Hamiltonian systems*, Physica D **13** (1984) 55–81.

[95] J. D. Hanson, J. R. Cary and J. D. Meiss: *Algebraic decay in self-similar Markov chains*, J. Statist. Phys. **39** (1985) 327–345.

[96] J. D. Meiss and E. Ott: *Markov tree model of transport in area-preserving maps*, Physica D **20** (1986) 387–402.

[97] T. Geisel, G. Radons and J. Rubner: *Kolmogorov-Arnol'd-Moser barriers in the quantum dynamics of chaotic systems*, Phys. Rev. Lett. **57** (1986) 2883–2886.

[98] J. Meiss: *Symplectic maps, variational principles, and transport*, Rev. Mod. Phys. **64** (1992) 795–848.

[99] R. Ketzmerick, L. Hufnagel, F. Steinbach and M. Weiss: *New class of eigenstates in generic Hamiltonian systems*, Phys. Rev. Lett. **85** (2000) 1214–1217.

[100] L. Hufnagel, R. Ketzmerick, M.-F. Otto and H. Schanz: *Eigenstates ignoring regular and chaotic phase-space structures*, Phys. Rev. Lett. **89** (2002) 154101 (4 pages).

[101] M. V. Berry, N. L. Balazs, M. Tabor and A. Voros: *Quantum maps*, Ann. Phys. **122** (1979) 26–63.

[102] S.-J. Chang and K.-J. Shi: *Evolution and exact eigenstates of a resonant quantum system*, Phys. Rev. A **34** (1986) 7–22.

[103] M. Degli Esposti: *Quantization of the orientation preserving automorphisms of the torus*, Ann. Inst. H. Poincaré Phys. Théor. **58** (1993) 3 323–341.

[104] M. Degli Esposti and S. Graffi: *Mathematical aspects of quantum maps*, in: *The Mathematical Aspects of Quantum Maps*, M. Degli Esposti and S. Graffi (Eds.), Springer Lecture Notes in Physics **618** (2003) 49–90.

[105] F. Haake and K. Życzkowski: *Random-matrix theory and eigenmodes of dynamical systems*, Phys. Rev. A **42** (1990) 1013–1016.

[106] S. Tomsovic and D. Ullmo: *Chaos-assisted tunneling*, Phys. Rev. E **50** (1994) 145–162.

[107] F. Leyvraz and D. Ullmo: *The level splitting distribution in chaos-assisted tunnelling*, J. Phys. A **29** (1996) 2529–2551.

[108] A. Bäcker, R. Ketzmerick, A. G. Monastra and L. Schilling: *Regular states in systems with a mixed phase space*, in preparation.

[109] L. Bittrich: *Zeitliches Fluten in Systemen mit gemischtem Phasenraum*, Diploma Thesis, Technische Universität Dresden (2006).

[110] A. Bäcker and S. Nonnenmacher: *Restricted random vector models and eigenvector statistics in systems with mixed phase space*, in preparation .

[111] L. Schilling: *Direct dynamical tunneling in systems with a mixed phase space*, PhD Thesis, Technische Universität Dresden (2006).

[112] S. Löck: *Dynamisches Tunneln im gemischten Phasenraum*, Diploma Thesis, Technische Universität Dresden (2006).

[113] A. Bäcker, R. Ketzmerick, S. Löck and L. Schilling: *Regular-to-chaotic tunneling rates using a fictitious integrable system*, in preparation.

Selected publications

[A1] Amplitude distribution of eigenfunctions in mixed systems

A. Bäcker and R. Schubert
J. Phys. A **35** (2002) 527–538.

We study the amplitude distribution of irregular eigenfunctions in systems with mixed classical phase space. For an appropriately restricted random wave model a theoretical prediction for the amplitude distribution is derived and good agreement with numerical computations for the family of limaçon billiards is found. The natural extension of our result to more general systems, e.g. with a potential, is also discussed.

INSTITUTE OF PHYSICS PUBLISHING JOURNAL OF PHYSICS A: MATHEMATICAL AND GENERAL

J. Phys. A: Math. Gen. **35** (2002) 527–538 PII: S0305-4470(02)24384-X

Amplitude distribution of eigenfunctions in mixed systems

Arnd Bäcker[1,2] **and Roman Schubert**[3]

[1] School of Mathematics, University of Bristol, University Walk, Bristol BS8 1TW, UK
[2] BRIMS, Hewlett-Packard Laboratories, Filton Road, Bristol BS12 6QZ, UK
[3] Abteilung Theoretische Physik, Universität Ulm, Albert-Einstein-Allee 11, D–89069 Ulm, Germany

E-mail: a.backer@bristol.ac.uk and roman.schubert@physik.uni-ulm.de

Received 20 April 2001, in final form 14 September 2001
Published 11 January 2002
Online at stacks.iop.org/JPhysA/35/527

Abstract
We study the amplitude distribution of irregular eigenfunctions in systems with mixed classical phase space. For an appropriately restricted random wave model, a theoretical prediction for the amplitude distribution is derived and a good agreement with numerical computations for the family of limaçon billiards is found. The natural extension of our result to more general systems, e.g. with a potential, is also discussed.

PACS numbers: 03.65.Sq, 02.50.Ey, 05.45.Mt

1. Introduction

The semiclassical behaviour of the eigenfunctions of a quantum mechanical system strongly depends on the ergodic properties of the underlying classical system. The semiclassical eigenfunction hypotheses [1, 2] state that the Wigner function of a semiclassical eigenstate is concentrated on a region in phase space explored by a typical trajectory of the classical system. In integrable systems the phase space is foliated into invariant tori, and the Wigner functions of the quantum mechanical eigenfunctions tend to delta functions on these tori in the semiclassical limit [3]. On the other hand, in an ergodic system almost all trajectories cover the energy shell uniformly, and hence the Wigner functions of the eigenstates are expected to become a delta function on the energy shell. That this actually happens for an ergodic system for almost all eigenstates follows from the quantum ergodicity theorem, see [4–6] and [7, 8] for billiards (the relation of the quantum ergodicity theorem with the semiclassical behaviour of Wigner functions is explicitly derived for Hamiltonian systems in [9]). However, a generic system is neither integrable nor ergodic [10], but has a mixed phase space in which regular regions (e.g. islands around stable periodic orbits) and stochastic regions coexist. Whether these numerically observed stochastic regions are ergodic and of positive measure is an open

0305-4470/02/030527+12$30.00

question, see [11] for a review on the coexistence problem. The eigenfunctions in mixed systems are expected to be separated into regular and irregular eigenfunctions according to an early conjecture by Percival [12] which has been numerically confirmed for several systems (see e.g. [13–16]). In addition, at finite energies there is a small (semiclassically vanishing) fraction of 'hierarchical states' which are of intermediate nature, and localize in regions bounded by cantori [17].

Besides the localization properties of the Wigner function, the local amplitude fluctuations of the eigenfunctions also strongly depend on the classical system, as has been pointed out in [1, 18]. The basic idea is that an eigenfunction can be represented locally as a superposition of de Broglie waves with wavelength determined by the energy and momenta distributed according to the semiclassical limit of the Wigner function. In a chaotic system one therefore expects an isotropic distribution of the momenta. If one additionally assumes that the phases are randomly distributed, one obtains locally a Gaussian amplitude distribution of a typical eigenfunction in a quantum mechanical system with chaotic classical limit. For instance, in a chaotic billiard a Gaussian amplitude distribution is expected, and this has been confirmed by several numerical studies (see e.g. [19–24]). Predictions of the random wave model on the behaviour of the maxima of eigenfunctions have been derived and successfully tested in [22, 25]. In mixed systems the situation is more complicated; for some studies on matrix elements and eigenfunctions in this case, see, for example [26–28]. In contrast, in an integrable system the localization of the Wigner function on the invariant tori enforces a more coherent superposition of the de Broglie waves, leading to a regular structure of the eigenfunction [1].

Our aim is to determine the amplitude distribution for irregular states in systems with mixed classical dynamics. We assume that the motion on a stochastic region D in phase space is ergodic and that the statistical properties of eigenfunctions can be described by a random wave model restricted to D (see the following section for a precise definition). The derivation shows that locally the fluctuations are Gaussian with a position-dependent variance which is given by the classical probability density on position space defined by the ergodic density on D. Thus the resulting amplitude distribution may be significantly different from a Gaussian. In section 3 we compare the theoretical prediction of the restricted random wave model with numerical computations.

2. Amplitude distribution for the restricted random wave model

In this section we consider a restricted random wave model for the two-dimensional Euclidean quantum billiards in order to describe the statistical properties of irregular eigenfunctions in systems with a mixed classical phase space. The quantum mechanical system is defined by the Euclidean Laplacian on a compact domain $\Omega \subset \mathbb{R}^2$ with suitable boundary conditions on the boundary $\partial\Omega$. (Usually one chooses the Dirichlet conditions.) The quantum mechanical eigenvalue problem is given by

$$\Delta\psi_n(\boldsymbol{q}) = E_n\psi_n(\boldsymbol{q}) \qquad \text{with} \quad \psi_n(\boldsymbol{q}) = 0 \quad \text{for} \quad \boldsymbol{q} \in \partial\Omega \tag{1}$$

and we are interested in the behaviour of the eigenfunctions ψ_n in the semiclassical limit $E_n \to \infty$.

The corresponding classical system is given by a free particle moving along straight lines inside the billiard, making elastic reflections on the billiard boundary $\partial\Omega$. The phase space is $T^*\Omega = \mathbb{R}^2 \times \Omega$, and the Hamiltonian is $H(\boldsymbol{p}, \boldsymbol{q}) = |\boldsymbol{p}|^2$. Since the Hamiltonian is scaled we can restrict our attention to the equi-energyshell with energy $E = 1$,

$$S^*\Omega := \{(\boldsymbol{p}, \boldsymbol{q}) \in \mathbb{R}^2 \times \Omega\,;\, |\boldsymbol{p}| = 1\}. \tag{2}$$

Introducing polar coordinates $(r,\ \phi)$ for the momentum $\boldsymbol{p}$, we can parametrize $S^*\Omega$ by $(\phi, \boldsymbol{q}) \in [0, 2\pi) \times \Omega$ where ϕ is the direction of the momentum. In these coordinates the Liouville measure on $S^*\Omega$ is given by

$$\mathrm{d}\mu = \mathrm{d}\phi\ \mathrm{d}^2q \tag{3}$$

which is invariant under the Hamiltonian flow on $S^*\Omega$.

Now let $D \subset S^*\Omega$ be an open domain which is invariant under the classical flow, and on which the flow is chaotic. The existence of such a domain where the flow is, for instance, ergodic, is an open problem. But numerically one observes invariant domains on which the flow is at least irregular in the sense that most orbits are unstable, and regular islands inside this domain are very small. The uncertainty principle implies a finite quantum mechanical resolution of phase space quantities at finite energies. Therefore at finite energies the small islands of such an irregular domain are not resolved by the quantum system.

So we expect, in the spirit of [1], that the statistical properties of irregular eigenfunctions associated with D can be described by those of a superposition of plane waves with wave vectors of the same lengths and directions distributed uniformly on D. Furthermore if we assume random phases, we arrive at the following restricted random wave model for real valued functions, which is a superposition of plane waves of the form

$$\psi_{\mathrm{RRWM},D}(\boldsymbol{q}) = \sqrt{\frac{4\pi}{\mathrm{vol}(D)N}} \sum_{n=1}^{N} \chi_D(\widehat{\boldsymbol{k}}_n, \boldsymbol{q}) \cos(\boldsymbol{k}_n \cdot \boldsymbol{q} + \varepsilon_n). \tag{4}$$

Here $\chi_D(\cdot)$ is the characteristic function of D, the phases ε_n are independent random variables equidistributed on $[0, 2\pi]$, and the momenta $\boldsymbol{k}_n \in \mathbb{R}^2$ are independent random variables which are equidistributed on the circle of radius $\sqrt{E}$. So the characteristic function $\chi_D(\cdot)$ ensures the localization on D. Furthermore, it is natural to take $N \sim \sqrt{E}$, the scaling of the number of line segments of a typical Heisenberg-length orbit. The volume of D measured with the Liouville measure (3) is denoted by $\mathrm{vol}(D)$. With this choice of normalization the expectation value of the norm $\|\psi_{\mathrm{RRWM},D}\|$ is 1.

Let us first consider the value distribution $P_q(\psi)$ of $\psi_{\mathrm{RRWM},D}(\boldsymbol{q})$ at a given point $\boldsymbol{q} \in \Omega$. Our restricted random wave model (4) is a sum of identical independent random variables which have zero mean and whose variance is given by

$$\sigma^2(\boldsymbol{q}) = \mathbb{E}\left(\frac{4\pi}{\mathrm{vol}(D)}(\chi_D(\hat{\boldsymbol{k}}_n, \boldsymbol{q}) \cos(\boldsymbol{k}_n \cdot \boldsymbol{q} + \varepsilon_n))^2\right) = \frac{1}{\mathrm{vol}(D)} \int_0^{2\pi} \chi_D(\boldsymbol{e}(\phi), \boldsymbol{q})\, \mathrm{d}\phi \tag{5}$$

where $\boldsymbol{e}(\phi) := (\cos(\phi), \sin(\phi))$ denotes the unit vector in the ϕ-direction. So by the central limit theorem we obtain for $E \to \infty$, i.e. $N \to \infty$, a Gaussian distribution of $\psi_{\mathrm{RRWM},D}(\boldsymbol{q})$ at $\boldsymbol{q}$,

$$P_q(\psi) \longrightarrow \sqrt{\frac{1}{2\pi\sigma^2(\boldsymbol{q})}} \exp\left(-\frac{\psi^2}{2\sigma^2(\boldsymbol{q})}\right) \tag{6}$$

with variance given by (5). If the classical dynamics on D is ergodic, then the variance $\sigma^2(\boldsymbol{q})$ is exactly the probability density of finding the particle at the point $\boldsymbol{q} \in \Omega$ if it moves on a generic trajectory in D. So $\sigma^2(\boldsymbol{q})$ is the classical probability density in position space.

By integrating equation (6) over Ω we obtain the complete amplitude distribution as a mean over a family of Gaussians with variances given by (5),

$$P_{\mathrm{RRWM},D}(\psi) = \frac{1}{\mathrm{vol}(\Omega)} \int_\Omega P_q(\psi)\, \mathrm{d}^2q \tag{7}$$

$$= \frac{1}{\mathrm{vol}(\Omega)} \int_\Omega \sqrt{\frac{1}{2\pi\sigma^2(\boldsymbol{q})}} \exp\left(-\frac{1}{2\sigma^2(\boldsymbol{q})}\psi^2\right) \mathrm{d}^2q. \tag{8}$$

So the amplitude distribution is completely determined by the classical probabality density (5), and it will be typically non-Gaussian if $\sigma^2(\boldsymbol{q})$ is not constant.

The moments of the distribution (8) can be computed directly and turn out to be proportional to the moments of the classical probability density $\sigma^2(\boldsymbol{q})$,

$$\int \psi^{2k} P_{\mathrm{RRWM},D}(\psi)\,\mathrm{d}\psi = \rho_{2k}\frac{1}{\mathrm{vol}(\Omega)}\int_\Omega [\sigma^2(\boldsymbol{q})]^k\,\mathrm{d}q \tag{9}$$

where the factor $\rho_{2k} = \frac{(2k)!}{k!2^k}$ denotes the $2k$th moment of a Gaussian. The odd moments are of course zero. Note that the second moment is always $1/\mathrm{vol}(\Omega)$, due to the normalization of ψ.

If the system is ergodic one has $\sigma^2(\boldsymbol{q}) = \frac{1}{\mathrm{vol}(\Omega)}$ and we get the classical result that $P_{\mathrm{RRWM},D}(\psi)$ is Gaussian with variance $\sigma^2 = \frac{1}{\mathrm{vol}(\Omega)}$. However, if $\sigma^2(\boldsymbol{q})$ depends on $\boldsymbol{q}$ then the corresponding distribution can show deviations from the Gaussian distribution. In particular, if $\sigma^2(\boldsymbol{q}) = 0$ for some region $\Omega' \subset \Omega$, we get a contribution $\frac{\mathrm{vol}(\Omega')}{\mathrm{vol}(\Omega)}\delta(\psi)$ to the corresponding distribution of $P_{\mathrm{RRWM},D}(\psi)$ as the integrand in (7) tends to a δ distribution as $\sigma^2(\boldsymbol{q}) \to 0$.

Finally, we would like to point out that the main ingredient in formula (7) is the assumption that the local amplitude distribution of an irregular eigenfunction around a point $\boldsymbol{q}$ in position space is Gaussian, with a variance given by the classical probability density in position space $\sigma^2(\boldsymbol{q})$, defined by the projection of the invariant measure on D in the position space. Clearly this assumption is not restricted to billiards, but is expected to be true for arbitrary quantum mechanical systems for which the underlying classical system contains chaotic components in phase space. So formula (7) is expected to be valid in far more general situations, with $\sigma^2(\boldsymbol{q})$ denoting the classical probability density defined by the ergodic measure on the chaotic component.

3. Comparison with irregular eigenfunctions

We now compare the predictions of the restricted random wave model with the results for some numerically computed eigenfunctions. As systems to study the amplitude distribution of irregular states in mixed systems, we have chosen the family of limaçon billiards introduced by Robnik [29, 30] with boundary given in polar coordinates by $\rho(\varphi) = 1 + \varepsilon\cos(\varphi), \varphi \in [-\pi, \pi]$, with $\varepsilon \in [0, 1]$ being the system parameter. We consider the case $\varepsilon = 0.3$, for which the billiard has a phase space of mixed type [29], see figure 1. In [31] examples of eigenstates far into the semiclassical regime have been studied in this system and, in particular, the amplitude distribution has been studied numerically, but no analytical predictions have been made.

First we have to determine the classical position space probability density $\sigma^2(\boldsymbol{q})$ of the ergodic measure on the invariant domain D. The normalized ergodic measure on D is given by

$$\mathrm{d}\mu_D(\phi, \boldsymbol{q}) = \frac{1}{\mathrm{vol}(D)}\chi_D(\boldsymbol{e}(\phi), \boldsymbol{q})\,\mathrm{d}\phi\,\mathrm{d}^2q$$

so we can express the variance $\sigma^2(\boldsymbol{q})$ as a mean value

$$\sigma^2(\boldsymbol{q}) = \int_{S^*\Omega} \delta(\boldsymbol{q} - \boldsymbol{q}')\,\mathrm{d}\mu_D(\phi', \boldsymbol{q}'). \tag{10}$$

As the motion on D is assumed to be ergodic, in order to determine $\sigma^2(\boldsymbol{q})$ we could replace the integral over $S^*\Omega$ by a time average over a typical trajectory of D and the δ function by a smoothed δ function, e.g. a narrow Gaussian. However, as we will see below, the eigenfunctions turn out not to be concentrated on the whole chaotic component, but rather on a subset which is almost invariant in the sense that it is bounded by partial barriers in phase

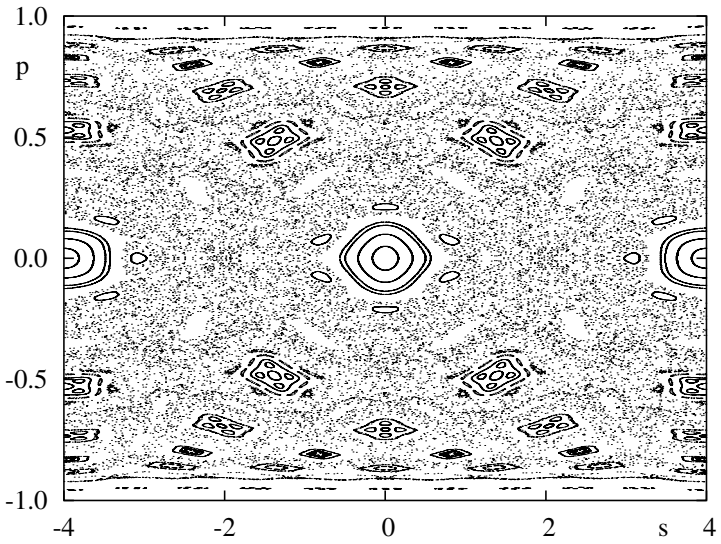

Figure 1. Plot of several stable and irregular orbits in the Poincaré section $\mathcal{P}$ of the limaçon billiard for $\varepsilon = 0.3$. Here $\mathcal{P}$ is parametrized by the (rescaled) arclength coordinate $s \in [-4, 4]$ along the billiard boundary and $p \in [-1, 1]$ which is the projection of the unit velocity vector on the tangent at the point s after the reflection.

space. Since at finite energies quantum mechanics has only a finite resolution in phase space, these partial barriers appear like real barriers. But since any classical trajectory will pass such a barrier after a certain time, the time average is not suitable for the determination of $\sigma^2(\boldsymbol{q})$ in such a situation.

For a more direct approach to determine $\sigma^2(\boldsymbol{q})$ we use the Poincaré section $\mathcal{P} = \{(s, p); s \in [-4, 4], p \in [-1, 1]\}$, which is parametrized by the (rescaled) arclength coordinate s (corresponding to $\varphi \in [-\pi, \pi]$) along the boundary $\partial\Omega$ and the projection p of the unit velocity vector on the tangent at the point s after the reflection. Let $\mathcal{D} \subset \mathcal{P}$ be the projection of the region D in the energy shell $S^*\Omega := \{(\boldsymbol{p}, \boldsymbol{q}) \in \mathbb{R}^2 \times \Omega; \|\boldsymbol{p}\| = 1\}$ on the Poincaré section. This projection is defined as follows: for a point $(\boldsymbol{e}(\phi), \boldsymbol{q}) \in D$ we can associate the trajectory which passes through $\boldsymbol{q}$ in direction $\boldsymbol{e}(\phi)$, then $s(\phi, \boldsymbol{q})$ is defined as the first intersection with the boundary $\partial\Omega$ when traversing the trajectory backwards from $\boldsymbol{q}$ and $p(\phi, \boldsymbol{q}) := \boldsymbol{e}(\phi)\boldsymbol{T}(s(\phi, \boldsymbol{q}))$ which is the projection of the unit velocity vector $\boldsymbol{e}(\phi)$ on the unit tangent vector $\boldsymbol{T}(s(\phi, \boldsymbol{q}))$ to $\partial\Omega$ at $s(\phi, \boldsymbol{q})$.

For a given point $\boldsymbol{q}$ we therefore get a curve parametrized by ϕ

$$(p(\phi, \boldsymbol{q}), s(\phi, \boldsymbol{q})) \in \mathcal{P}. \tag{11}$$

Since $\chi_D(\boldsymbol{e}(\phi), \boldsymbol{q}) = \chi_{\mathcal{D}}(p(\phi, \boldsymbol{q}), s(\phi, \boldsymbol{q}))$, we get

$$\sigma^2(\boldsymbol{q}) = \frac{1}{\mathrm{vol}(D)} \int_0^{2\pi} \chi_{\mathcal{D}}(p(\phi, \boldsymbol{q}), s(\phi, \boldsymbol{q}))\, \mathrm{d}\phi \tag{12}$$

and therefore we have to determine the fraction of the angular interval(s) for which the curve (11) is in $\mathcal{D}$. That is, one has to determine the angles $\phi_i^{\mathrm{entry}}(\boldsymbol{q})$ and $\phi_i^{\mathrm{exit}}(\boldsymbol{q})$ where the

curve (11) enters or leaves the region $\mathcal{D}$, i.e. the intersection points of (11) with the boundary of $\mathcal{D}$. In terms of these angles we obtain

$$\sigma^2(\boldsymbol{q}) = \frac{1}{\mathrm{vol}(D)} \sum_i \phi_i^{\mathrm{exit}}(\boldsymbol{q}) - \phi_i^{\mathrm{entry}}(\boldsymbol{q}) \tag{13}$$

which is proportional to the fraction of directions in the ergodic component visible from the point $\boldsymbol{q}$.

With this classical probability density $\sigma^2(\boldsymbol{q})$, one can compute the corresponding amplitude distribution via equation (8). If $\sigma^2(\boldsymbol{q}) = 0$ for some region, then the local amplitude distribution (6) becomes a delta function, and it is necessary to consider for a concrete comparison a binned distribution,

$$P_{\mathrm{binned}}(\psi, \Delta\psi) := \frac{1}{\Delta\psi} \int_{\psi-\Delta\psi/2}^{\psi+\Delta\psi/2} P(\psi')\,\mathrm{d}\psi' \tag{14}$$

$$= \frac{1}{2|\Omega|} \int_\Omega \left[\mathrm{erf}\left(\frac{\psi + \Delta\psi/2}{\sqrt{2\sigma^2(\boldsymbol{q})}} \right) - \mathrm{erf}\left(\frac{\psi - \Delta\psi/2}{\sqrt{2\sigma^2(\boldsymbol{q})}} \right) \right] \mathrm{d}^2 q. \tag{15}$$

We now use a Husimi Poincaré section representation of the eigenstate (see e.g. [32, 33]) to determine the boundary of the relevant component $\mathcal{D}$ by a spline approximation. The Poincaré Husimi representation of an eigenfunction ψ_n in a billiard is defined by projecting the normal derivative $u_n(s)$ of an eigenfunction $\psi_n(\boldsymbol{q})$ at the boundary onto a coherent state on the boundary. The coherent states, semiclassically centred in $(s, p) \in \mathcal{P}$, are defined as

$$c_{(s,p),k}(s') := \left(\frac{k}{\sigma\pi}\right)^{1/4} \sum_{m=-\infty}^{\infty} \exp(\mathrm{i}pk(s' - mL - s)) \exp\left(-\frac{k}{2\sigma}(s' - mL - s)^2 \right) \tag{16}$$

where $s' \in [-4, 4]$, $\sigma > 0$ and $L = 8$ is the total (rescaled) length of the boundary. This definition is just a periodized version of the standard coherent states. The Poincaré Husimi function of a state ψ_n with normal derivative $u_n(s)$ is then defined as

$$H_n(s, p) = \frac{k_n}{2\pi} \frac{1}{\int_{-4}^{4} |u_n(s)|^2\,\mathrm{d}s} \left| \int_{-4}^{4} c^*_{(s,p),k_n}(s')\, u_n(s')\,\mathrm{d}s' \right|^2 \tag{17}$$

with $k_n = \sqrt{E_n}$; the prefactor ensures the normalization $\iint H_n(s, p)\mathrm{d}p\,\mathrm{d}s = 1$.

An example is shown in figure 2. In (*a*) a high-lying eigenfunction ($E = 1002\,754.70\ldots$, approximately the 130 568th state of odd symmetry) in the limaçon billiard with $\varepsilon = 0.3$ is shown as density plot (black corresponding to high intensity of $|\psi|^2$). In (*b*) the corresponding Husimi representation on the Poincaré section is shown. The boundary of the irregular region $\mathcal{D}$ is described by a cubic spline which is shown as a full curve. With these boundary curves we can use (13) to compute $\sigma^2(\boldsymbol{q})$, which is shown in figure 2(*c*). Finally, in figure 2(*d*) the comparison of the amplitude distribution of ψ with the prediction of the restricted random wave model is given. Clearly, $P(\psi)$ is non-Gaussian, and the agreement is very good. Table 1 lists the first moments and also a very good agreement of the results using (9) and the moments of ψ is found. Both the resulting amplitude distribution $P_{\mathrm{RRWM},D}$ and the moments turn out to be quite robust with respect to small changes of the selection of $\mathcal{D}$. Note that we have rescaled $\sigma^2(\boldsymbol{q})$ such that the variance of the distributions is 1.

Another example is shown in figure 3. The eigenfunction ($E = 1003\,030.75\ldots$, approximately the 130 607th state of odd symmetry) plotted in (*a*) has a quite large region in the centre where it is almost vanishing. So from this alone the amplitude distribution is expected to show a very clear deviation from the normal distribution. Using the same procedure as in the previous case, we determine $\mathcal{D}$, compute $\sigma^2(\boldsymbol{q})$ and then $P_{\mathrm{RRWM}}(\psi)$. The comparison

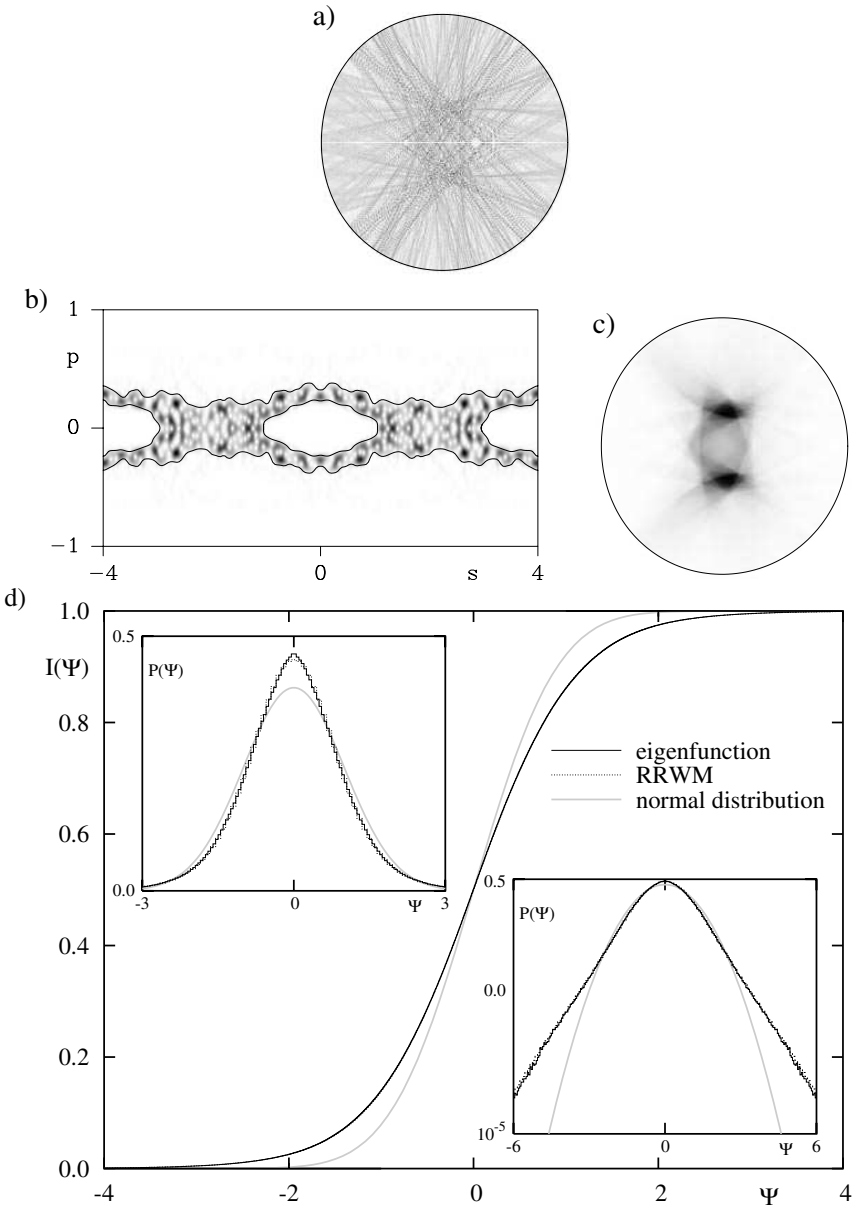

Figure 2. In (*a*) a high-lying eigenfunction ($E = 1002\,754.70\ldots$, approximately the 130 568th state) in the limaçon is shown as a grey scale plot (black corresponding to high intensity). In (*b*) the corresponding Husimi function on the Poincaré section is shown together with the boundary (full curves) of the region on which the eigenfunction is concentrated. In (*c*) a density plot of $\sigma^2(\boldsymbol{q})$, computed via equation (13), is shown. In (*d*) the cumulative amplitude distribution of the eigenfunction is compared with the prediction of the RRWM; on this scale no differences are visible. The left inset shows $P(\psi)$, and for the right inset a logarithmic vertical scale is used to emphasize the tails of the distribution. For comparison the normal distribution is shown as grey curve.

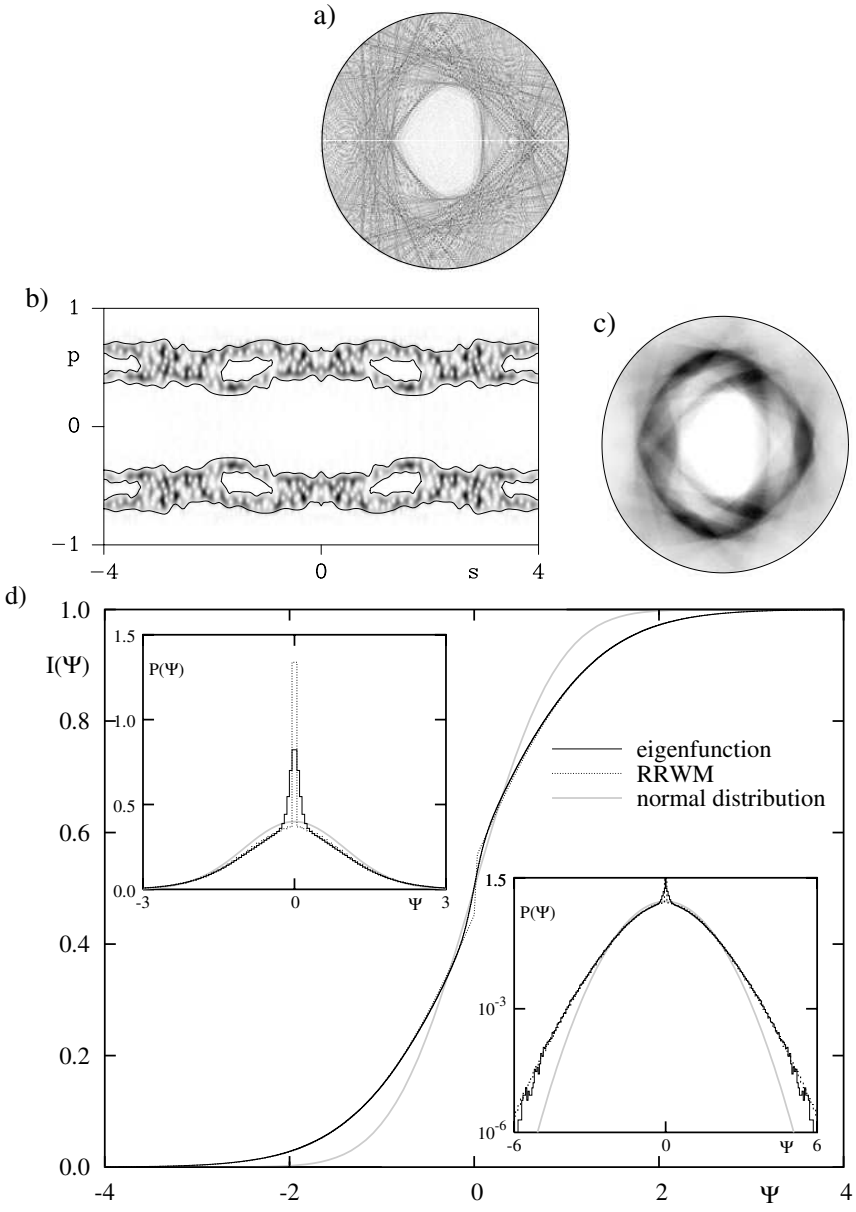

Figure 3. The same plots as in the previous figure are shown for another high-lying eigenfunction ($E = 1003\,030.75\ldots$, approximately the 130 607th state). In this case there is a deviation of the amplitude distribution of the eigenfunction from the prediction of the restricted random wave model around $\psi = 0$. This is because $\sigma^2(q) = 0$ in the central region, whereas the eigenfunction does not vanish there (see the text for further discussion). For the tails of the distribution, the agreement of the two distributions is again very good.

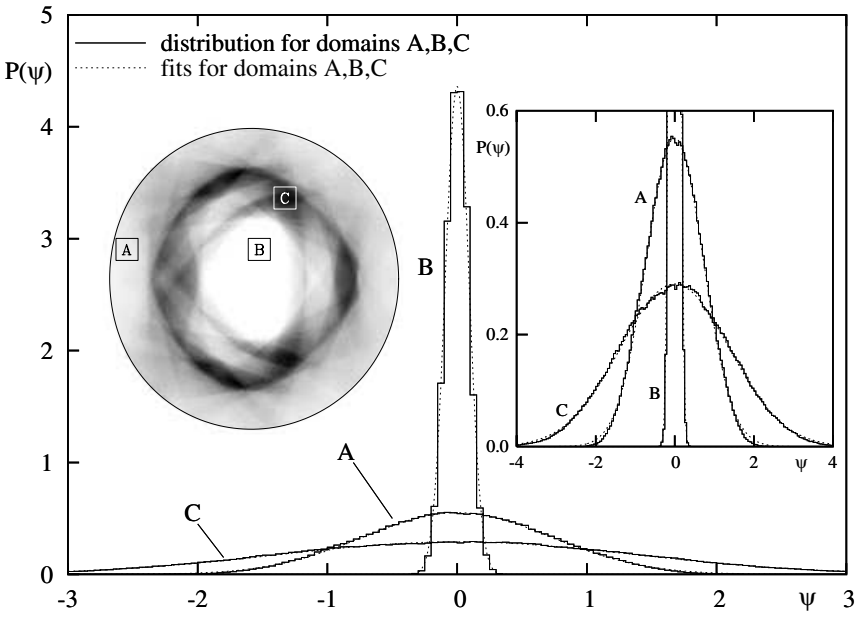

Figure 4. For the three domains indicated in the inset, the local amplitude distribution is shown (for the same state as in figure 3). The dotted curves are Gaussian fits and the agreement of the position-dependent variance for regions A and C is very good with the theoretical prediction (equation (5)). The non-zero width of the distribution for the region B corresponds to the widening of the δ-contribution (see figure 3).

Table 1. Comparison of the even moments for the distributions of the eigenfunction and the RRWM (equation (9)). The last column lists, for comparison, the moments of the normal distribution.

	Example 1, figure 2		Example 2, figure 3		
Moment	Eigenfunction	RRWM	Eigenfunction	RRWM	Normal distribution
4	4.39	4.46	3.85	3.75	3
6	45.1	47.6	26.9	25.8	15
8	819	899	269	269	105
10	2199	2501	3774	3841	945

of the prediction with $P(\psi)$ is shown in figure 3(d). The strongest deviation occurs for $\psi \approx 0$. The peak of $P_{\mathrm{RRWM}}(\psi)$ at $\psi = 0$ is due to the fact that $\sigma^2(\boldsymbol{q}) = 0$ for the region in the centre of the billiard. The eigenfunction, however, is not exactly zero, but shows a decay in that region and thus still fluctuates there. This causes a broadening of the δ-contribution, which is clearly visible in the plot of $P(\psi)$ in figure 3(d). For $|\psi| > 0.25$ this region is not relevant anymore, and the agreement of $P(\psi)$ and $P_{\mathrm{RRWM}}(\psi)$ is very good. In the right inset to figure 3(d) the distribution is shown with a logarithmic vertical scale to illustrate the agreement of the distributions even in the tails.

The moments, computed via equation (9), are listed in table 1. The agreement of the moments of the eigenfunction with the prediction of the restricted random wave model is quite

good. All moments of the two examples are larger than those of a Gaussian, corresponding to the larger tails. Compared to the moments of the restricted random wave model, those of the eigenfunctions tend to be smaller, in particular, for the larger moments. This is reasonable, as an actual eigenfunction is always bounded, which reduces higher moments compared to the result of equation (9).

Furthermore, we have tested our basic assumption (6), that the local value distribution of a sufficiently high-lying eigenfunction is Gaussian with a variance given by the local classical probability density associated with D, more directly. To this end we have computed the value distribution of the eigenfunction in figure 3 for three small regions on which $\sigma^2(\boldsymbol{q})$ is almost invariant, and we therefore expect a Gaussian. The results are shown in figure 4, and a good agreement with the prediction (6) is found. Since many fewer wavelengths are contained in these small domains than those in Ω, the statistics is of course not as good as that for the full system, but the results give strong support for a local Gaussian behaviour. The variances for the two domains A and C coincide with the expected classical one $\sigma^2(\boldsymbol{q})$. But for domain B the observed variance is larger than $\sigma^2(\boldsymbol{q}) = 0$. This corresponds to the widening of the delta peak in figure 3, and is due to the fact that the eigenfunction cannot become exactly zero on some open set at finite energies, but instead fluctuates around zero.

4. Summary

In this paper we have extended the random wave model for eigenfunctions from the case of chaotic systems to the case of irregular eigenfunctions in systems with mixed phase space. Our main result is one particular prediction of this model, namely, the amplitude distribution (7) of irregular eigenfunctions. Numerical tests have been performed for two high-lying eigenfunctions of the limaçon billiard with $\varepsilon = 0.3$, and impressive agreement, even in the tails of the distribution, with the theoretical prediction was found.

The physical picture underlying our analysis is that the local hyperbolicity in the irregular part of the phase space forces the eigenfunctions localizing on this part of phase space to behave locally like a Gaussian random function with a variance given by the classical probability density in position space defined by the uniform measure on the irregular component. By taking the mean over all these local Gaussians with varying variance, it gives our result for the global amplitude distribution. We have tested this intuitive picture by computing local amplitude distributions. The agreement of these with the Gaussian prediction is very good, giving further strong support to the picture of local Gaussian fluctuations with variance determined by the underlying classical system. A further natural question relates to the correlations of such eigenfunctions between different points in position space; this topic is addressed in [34].

We should point out that in view of the complicated structure of the phase space of a mixed system, it is quite surprising that our simple model fits so well. The only additional ingredient which appeared in the numerical tests was that the relevant irregular domains in phase space are only slighthy invariant, even for very high-lying eigenfunctions. A detailed understanding of these findings poses an important challenge for future research.

Although we have restricted our study to the Euclidean billiards, the general picture of local Gaussian fluctuations is of course not limited to these special types of systems. We therefore expect our results to be valid for irregular eigenfunctions in arbitrary systems (e.g. systems with potential), with $\sigma^2(\boldsymbol{q})$ defined as the projection of the ergodic measure on the irregular component to the position space.

Acknowledgments

We would like to thank Francesco Mezzadri for pointing out a shortening of the original derivation and Professor Jonathan Keating for useful comments on the manuscript. AB acknowledges support by the Deutsche Forschungsgemeinschaft under contract no DFG-Ba 1973/1-1. RS acknowledges support by the Deutsche Forschungsgemeinschaft under contract no DFG-Ste 241/7-3.

References

[1] Berry M V 1977 Regular and irregular semiclassical wavefunctions *J. Phys. A: Math Gen.* **10** 2083
[2] Voros A 1979 Semi-classical ergodicity of quantum eigenstates in the Wigner representation *Stochastic Behavior in Classical and Quantum Hamiltonian Systems (Lecture Notes in Physics no 93)* (Berlin: Springer) pp 326–33
[3] Berry M V 1977 Semi-classical mechanics in phase space: a study of Wigner's function *Phil. Trans. R. Soc.* A **287** 237
[4] Shnirelman A I 1974 Ergodic properties of eigenfunctions *Usp. Math. Nauk* **29** 181 (in Russian)
[5] Zelditch S 1987 Uniform distribution of eigenfunctions on compact hyperbolic surfaces *Duke. Math. J.* **55** 919
[6] Colin de Verdière Y 1985 Ergodicité et fonctions propres du laplacien *Commun. Math. Phys.* **102** 497 (in French)
[7] Gérard P and Leichtnam E 1993 Ergodic properties of eigenfunctions for the Dirichlet problem *Duke Math. J.* **71** 559
[8] Zelditch S and Zworski M 1996 Ergodicity of eigenfunctions for ergodic billiards *Commun. Math. Phys.* **175** 673
[9] Bäcker A, Schubert R and Stifter P 1998 Rate of quantum ergodicity in Euclidean billiards *Phys. Rev.* E **57** 5425
Bäcker A, Schubert R and Stifter P 1998 *Phys. Rev.* E **58** 5192 (erratum)
[10] Markus L and Meyer K 1974 *Generic Hamiltonian Dynamical Systems are Neither Integrable nor Chaotic (Mem. Am. Math. Soc. no 114)* (Providence, RI: American Mathematical Society)
[11] Strelcyn J-M 1991 The 'coexistence problem' for conservative dynamical systems: a review *Coll. Math.* **62** 331
[12] Percival I C 1973 Regular and irregular spectra *J. Phys. B: At. Mol. Phys.* **6** L229
[13] Bohigas O, Tomsovic S and Ullmo D 1990 Dynamical quasidegeneracies and separation of regular and irregular quantum levels *Phys. Rev. Lett.* **64** 1479
[14] Prosen T and Robnik M 1993 Survey of the eigenfunctions of a billiard system between integrability and chaos *J. Phys. A: Math. Gen.* **26** 5365
[15] Li B and Robnik M 1995 Separating the regular and irregular energy levels and their statistics in a Hamiltonian system with mixed classical dynamics *J. Phys. A: Math. Gen.* **28** 4843
[16] Carlo G, Vergini E and Fendrik A 1998 Numerical verification of Percival's conjecture in a quantum billiard *Phys. Rev.* E **57** 5397
[17] Ketzmerick R, Hufnagel L, Steinbach F and Weiss M 2000 New class of eigenstates in generic Hamiltonian systems *Phys. Rev. Lett.* **85** 1214
[18] Berry M V 1983 Semiclassical mechanics of regular and irregular motion *Comportement Chaotique des Systèmes Déterministes—Chaotic Behaviour of Deterministic Systems* ed G Iooss, R H G Hellemann and R Stora (Amsterdam: North-Holland) pp 171–271
[19] Shapiro M and Goelman G 1984 Onset of chaos in an isolated energy eigenstate *Phys. Rev. Lett.* **53** 1714
[20] McDonald S W and Kaufmann A N 1988 Wave chaos in the stadium: statistical properties of short-wave solutions of the Helmholtz equation *Phys. Rev.* A **37** 3067
[21] Aurich R and Steiner F 1991 Exact theory for the quantum eigenstates of a strongly chaotic system *Physica* D **48** 445
[22] Hejhal D A and Rackner B N 1992 On the topography of Maass waveforms for PSL(2, $\mathbb{Z}$) *Exp. Math.* **1** 275
[23] Aurich R and Steiner F 1993 Statistical properties of highly excited quantum eigenstates of a strongly chaotic system *Physica* D **64** 185
[24] Li B and Robnik M 1994 Statistical properties of high-lying chaotic eigenstates *J. Phys. A: Math. Gen.* **27** 5509
[25] Aurich R, Bäcker A, Schubert R and Taglieber M 1999 Maximum norms of chaotic quantum eigenstates and random waves *Physica* D **129** 1
[26] Bohigas O, Tomsovic S and Ullmo D 1993 Manifestations of classical phase space structures in quantum mechanics *Phys. Rep.* **223** 43
[27] Müller K, Mehlig B, Milde F and Schreiber M 1995 Statistics of wave functions in disordered and in classically chaotic systems *Phys. Rev. Lett.* **78** 215

[28] Mehlig B, Müller K and Eckhardt B 1999 Phase space localization and matrix element distributions in systems with mixed classical phase space *Phys. Rev.* E **59** 5272
[29] Robnik M 1983 Classical dynamics of a family of billiards with analytic boundaries *J. Phys. A: Math. Gen.* **16** 3971
[30] Robnik M 1984 Quantising a generic family of billiards with analytic boundaries *J. Phys. A: Math. Gen.* **17** 1049
[31] Li B and Robnik M 1995 Geometry of high-lying eigenfunctions in a plane billiard system having mixed-type classical dynamics *J. Phys. A: Math. Gen.* **28** 2799
[32] Tualle J M and Voros A 1995 Normal modes of billiards portrayed in the stellar (or nodal) representation *Chaos, Solitons Fractals* **5** 1085
[33] Simonotti F P, Vergini E and Saraceno M 1997 Quantitative study of scars in the boundary section of the stadium billiard *Phys. Rev.* E **56** 3859
[34] Bäcker A and Schubert R 2002 Autocorrelation function of eigenstates in chaotic and mixed systems *J. Phys. A: Math. Gen.* **35** 539 (following paper) (nlin.cd/0106018)

[A2] Autocorrelation function of eigenstates in chaotic and mixed systems

A. Bäcker and R. Schubert
J. Phys. A **35** (2002) 539–564.

We study the autocorrelation function of different types of eigenfunctions in quantum mechanical systems with either chaotic or mixed classical limits. We obtain an expansion of the autocorrelation function in terms of the correlation length. For localized states, like bouncing ball modes or states living on tori, a simple model using only classical input gives good agreement with the exact result. In particular, a prediction for irregular eigenfunctions in mixed systems is derived and tested. For chaotic systems, the expansion of the autocorrelation function can be used to test quantum ergodicity on different length scales.

INSTITUTE OF PHYSICS PUBLISHING JOURNAL OF PHYSICS A: MATHEMATICAL AND GENERAL

J. Phys. A: Math. Gen. **35** (2002) 539–564 PII: S0305-4470(02)24383-8

Autocorrelation function of eigenstates in chaotic and mixed systems

Arnd Bäcker[1,2] **and Roman Schubert**[3]

[1] School of Mathematics, University of Bristol, University Walk, Bristol BS8 1TW, UK
[2] BRIMS, Hewlett-Packard Laboratories, Filton Road, Bristol BS12 6QZ, UK
[3] Abteilung Theoretische Physik, Universität Ulm, Albert-Einstein-Allee 11, D–89069 Ulm, Germany

E-mail: a.backer@bristol.ac.uk and roman.schubert@physik.uni-ulm.de

Received 20 April 2001, in final form 14 September 2001
Published 11 January 2002
Online at stacks.iop.org/JPhysA/35/539

Abstract
We study the autocorrelation function of different types of eigenfunctions in quantum mechanical systems with either chaotic or mixed classical limits. We obtain an expansion of the autocorrelation function in terms of the correlation distance. For localized states in billiards, like bouncing ball modes or states living on tori, a simple model using only classical input gives good agreement with the exact result. In particular, a prediction for irregular eigenfunctions in mixed systems is derived and tested. For chaotic systems, the expansion of the autocorrelation function can be used to test quantum ergodicity on different length scales.

PACS numbers: 05.45.Mt, 02.50.Ey, 03.65.SQ, 05.45.−a

1. Introduction

The behaviour of a quantum mechanical system in the semiclassical limit strongly depends on the ergodic properties of the corresponding classical system. In particular, the eigenfunctions semiclassically reflect the phase space structure of the classical system and therefore they depend strongly on whether the classical system is chaotic or regular. In this study we are interested in the fluctuations of the wavefunctions, and in the correlations between the fluctuations in different regions which are induced by the classical phase space structures. In particular, we will consider the case of quantum billiards in a domain $\Omega \subset \mathbb{R}^2$, which are described by the time-independent Schrödinger equation (in units $\hbar = 2m = 1$)

$$(\Delta + E)\psi(\boldsymbol{q}) = 0 \qquad \text{for} \quad \boldsymbol{q} \in \Omega \backslash \partial\Omega \tag{1}$$

with Dirichlet boundary conditions, $\psi(\boldsymbol{q}) = 0$ for $\boldsymbol{q} \in \partial\Omega$. For compact Ω one obtains a discrete spectrum $\{E_n\}$ of eigenvalues, $0 < E_1 \leqslant E_2 \leqslant \ldots$, with associated eigenfunctions

0305-4470/02/030539+26$30.00

$\psi_n \in L^2(\Omega)$, which we assume to be normalized, i.e. $\|\psi_n\| := \int_\Omega |\psi_n(\boldsymbol{q})|^2 \, \mathrm{d}q = 1$. The corresponding classical billiard is given by the free motion of a point particle inside Ω with elastic reflections at the boundary $\partial\Omega$.

The amplitude distribution of an eigenfunction of a quantum mechanical system whose classical limit is chaotic is conjectured to become Gaussian in the semiclassical limit [1], and numerical studies support this conjecture, see e.g. [2–4]. A more sensitive quantity is the *local* autocorrelation function [1] which measures correlations between different points of an eigenfunction ψ

$$C^{\mathrm{loc}}(\boldsymbol{x}, \delta\boldsymbol{x}) := \psi^*(\boldsymbol{x} - \delta\boldsymbol{x}/2)\psi(\boldsymbol{x} + \delta\boldsymbol{x}/2). \tag{2}$$

The crucial fact for the theoretical analysis of $C^{\mathrm{loc}}(\boldsymbol{x}, \delta\boldsymbol{x})$, observed by Berry [1], is that the autocorrelation function can be expressed as the Fourier transformation of the Wigner function (see equation (7) below) of ψ

$$C^{\mathrm{loc}}(\boldsymbol{x}, \delta\boldsymbol{x}) = \int W(\boldsymbol{p}, \boldsymbol{x}) \mathrm{e}^{-\mathrm{i}\boldsymbol{p}\delta\boldsymbol{x}} \, \mathrm{d}p. \tag{3}$$

Hence information on the behaviour of the Wigner function can be used to predict the behaviour of the autocorrelation function, and since semiclassical limits of Wigner functions are concentrated on invariant sets in phase space, see e.g. [5], it follows that in the semiclassical limit autocorrelation functions are determined by the classical phase space structure. For example, if the classical system is ergodic, the quantum ergodicity theorem [6–11] (roughly speaking) states that almost all quantum expectation values tend to the corresponding classical limit. One can show [12] that for ergodic systems this is equivalent to the semiclassical eigenfunction hypothesis [1, 13–15], when restricted to a subsequence of density one. Using this result in (3) one gets Berry's result [1] that for chaotic billiards in two dimensions

$$C^{\mathrm{loc}}(\boldsymbol{x}, \delta\boldsymbol{x}) \sim \frac{1}{\mathrm{vol}(\Omega)} J_0(\sqrt{E}|\delta\boldsymbol{x}|) \tag{4}$$

weakly as a function of $\boldsymbol{x}$ (for fixed $\delta\boldsymbol{x}$) as $E \to \infty$, where E denotes the energy of the eigenstate ψ in (2). Equivalently we have

$$\lim_{E\to\infty} C^{\mathrm{loc}}(\boldsymbol{x}, \delta\boldsymbol{x}/\sqrt{E}) = \frac{1}{\mathrm{vol}(\Omega)} J_0(|\delta\boldsymbol{x}|). \tag{5}$$

Numerical tests of this relation have been performed for several chaotic systems [2–4] and at finite energies show notable fluctuations of the autocorrelation function around the high energy limit (4), especially for correlation distances larger than a few de Broglie wavelengths.These fluctuations have been studied further in [16–19], where for a small correlation distance $|\delta\boldsymbol{x}|$ a random model for the eigenfunctions of a chaotic system was used to predict the variance of these fluctuations, and for larger $|\delta\boldsymbol{x}|$ a formula involving closed orbits of the system has been derived. In [23, 24] the path correlation function, which is an average of the local correlations along a given trajectory, has been introduced. A further study of autocorrelations of eigenfunctions in the framework of the nonlinear σ-model has been recently conducted in [20], and spectral averages of autocorelation functions are studied in [21, 22]. The path correlation function is closely related to the autocorrelation function and for ergodic systems also tends asymptotically to a Bessel function (4). This path correlation function has been studied in [3] for a hyperbolic octagon, and an expansion in terms of Legendre functions has been derived, which can be used to determine corrections to the leading Bessel part (4).

The autocorrelation function in nonchaotic systems has attracted very less attention. The integrable case has already been discussed by Berry [1], and the corresponding formula has been successfully tested for the circle billiard in [2]. For a system with mixed classical

phase space the autocorrelation function has been studied in [25], in particular for irregular eigenfunctions an expansion of the Wigner function in polar coordinates has been used.

In this paper we are interested in the question how the universal limit (4) is reached, and how, in the case of mixed systems, further constraints on the classical motion are reflected in the autocorrelation function. For instance, if an eigenfunction is concentrated on an ergodic component, then by a generalization of the quantum ergodicity theorem [26], the Wigner function becomes equidistributed on that component, and this will determine the autocorrelation function.

The paper is organized as follows. In section 2 we discuss some examples of the autocorrelation function for different eigenfunctions in systems with chaotic and mixed classical dynamics. In section 3 a general expansion of the autocorrelation function for eigenfunctions in billiards is derived, which allows a systematic study of their properties. It is an expansion in the correlation distance $|\delta \boldsymbol{x}|$ which reflects the fact that the determination of correlations at larger distances needs classical information on finer length scales than for short range correlations. In section 4 it is shown that the correlation distance expansion provides an efficient way to explain the fine structure of the autocorrelation functions of the systems studied in the first section. Of particular interest is that for chaotic systems deviations of the autocorrelation function from the quantum ergodic limit (4) can be related to the rate of quantum ergodicity. In turn the autocorrelation function can be used to study the rate of quantum ergodicity on different classical length scales.

2. Examples of autocorrelation functions

For numerical computations as well as for theoretical considerations it is much more convenient to consider a smoothed version of the local autocorrelation function (2). Furthermore, as the eigenfunctions oscillate on a scale proportional to $1/\sqrt{E}$, we rescale the autocorrelation function by this factor. Hence we will study the autocorrelation function in the form

$$C_\rho(\boldsymbol{x}, \delta\boldsymbol{x}) := \int_\Omega \rho(\boldsymbol{x}-\boldsymbol{q})\psi^*\left(\boldsymbol{q}-\frac{\delta\boldsymbol{x}}{2\sqrt{E}}\right)\psi\left(\boldsymbol{q}+\frac{\delta\boldsymbol{x}}{2\sqrt{E}}\right)\mathrm{d}q \tag{6}$$

where ρ is a positive function which determines the smoothing of the local autocorrelation function. In the literature (see the papers mentioned in the introduction) the mean is usually taken over a small disc, which corresponds to taking the characteristic function of a disc for ρ in (6). However, nothing prevents one considering the case $\rho \equiv 1$, i.e. taking the mean value of the local autocorrelation function (2) over the whole position space. In terms of the Wigner function

$$W(\boldsymbol{p}, \boldsymbol{q}) := \frac{1}{(2\pi)^2}\int \mathrm{e}^{\mathrm{i}pq'}\psi^*(\boldsymbol{q}-\boldsymbol{q}'/2)\psi(\boldsymbol{q}+\boldsymbol{q}'/2)\,\mathrm{d}q' \tag{7}$$

one obtains in this case

$$C(\delta\boldsymbol{x}) := \int \psi^*\left(\boldsymbol{q}-\frac{\delta\boldsymbol{x}}{2\sqrt{E}}\right)\psi\left(\boldsymbol{q}+\frac{\delta\boldsymbol{x}}{2\sqrt{E}}\right)\mathrm{d}q \tag{8}$$

$$= \iint W(\boldsymbol{p}, \boldsymbol{q})\mathrm{e}^{-\mathrm{i}\boldsymbol{p}\delta\boldsymbol{x}/\sqrt{E}}\,\mathrm{d}q\,\mathrm{d}p = \int |\hat{\psi}(\boldsymbol{p})|^2\mathrm{e}^{-\mathrm{i}\boldsymbol{p}\delta\boldsymbol{x}/\sqrt{E}}\,\mathrm{d}p. \tag{9}$$

This is a particularly good choice for the numerical computation of the autocorrelation function in billiards because it can be reduced to boundary integrals (see the appendix). The resulting formula reads

$$C(\delta\boldsymbol{x}) = \frac{1}{8\sqrt{E}}\iint_{\partial\Omega\times\partial\Omega} |\boldsymbol{q}(s)-\boldsymbol{q}(s')+\delta\boldsymbol{x}|\,Y_1(\sqrt{E}|\boldsymbol{q}(s)-\boldsymbol{q}(s')+\delta\boldsymbol{x}|)u^*(s)u(s')\,\mathrm{d}s\,\mathrm{d}s' \tag{10}$$

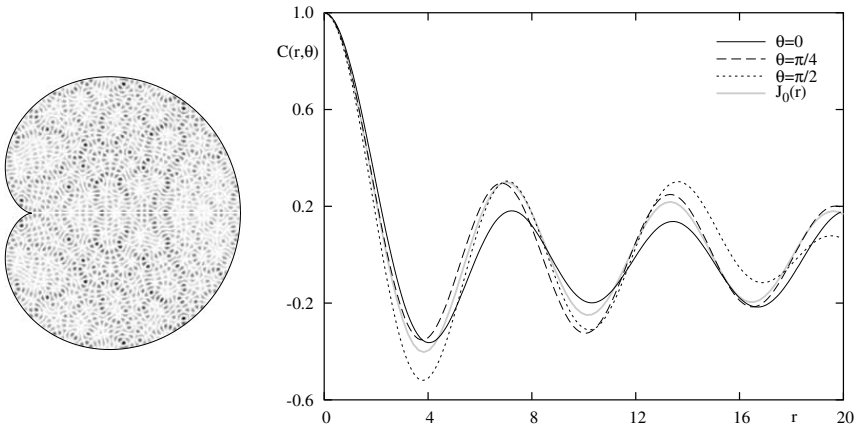

Figure 1. Grey scale plot of $|\psi_{1277}(q)|^2$ in the cardioid billiard with odd symmetry, where black corresponds to high intensity. To the right the autocorrelation function $C(r,\theta)$, computed using (10), is shown for three different directions $\theta = 0, \pi/4$ and $\pi/2$. For comparison the asymptotic result $C(r,\theta) = J_0(r)$ is shown as the grey line.

where $u(s)$ is the normal derivative of the normalized eigenfunction ψ on the billiard boundary. This relation provides a very efficient method for the numerical computation of the autocorrelation function.

The systems for which we study the autocorrelation functions are the stadium billiard and two members of the family of limaçon billiards, namely the cardioid billiard, and a billiard with mixed classical phase space. The stadium billiard is proved to be strongly chaotic, i.e. it is ergodic, mixing and a K-system [27, 28].The height of the desymmetrized billiard is chosen to be 1, and a denotes the length of the upper horizontal line, for which we have $a = 1.8$ in the following. The family of limaçon billiards is given by the simplest nontrivial conformal mapping of the unit circle [29, 30] and can be parametrized in polar coordinates by $\rho(\varphi) = 1 + \varepsilon\cos(\varphi)$ with $\varphi \in [-\pi, \pi]$, and $\varepsilon \in [0, 1]$ denotes the family parameter. We consider the case $\varepsilon = 0.3$ which leads to a mixed dynamics in phase space. For $\varepsilon = 1$ one obtains the cardioid billiard,which is also proved to be strongly chaotic [31–33]. The eigenvalues of the cardioid billiard have been provided by Prosen and Robnik [34] and were calculated by means of the conformal mapping technique, see e.g. [30, 35]. For the stadium billiard the eigenvalues and eigenfunctions have been computed using the boundary element method, see e.g. [36, 37], and for the limaçon billiard the eigenvalues have been computed using the conformal mapping technique and then the boundary element method has been used to compute the eigenfunctions (see [38] for details). For the high-lying states in the limaçon billiard the scaling method has been used [39].

First we consider a 'typical' eigenfunction in the cardioid billiard (figure 1). In the plots we show

$$C(r,\theta) = C(r\hat{\boldsymbol{e}}(\theta)) \tag{11}$$

where $\hat{\boldsymbol{e}}(\theta) = (\cos\theta, \sin\theta)$, as a function of r for three different values of θ .The quantum ergodicity theorem implies that there is a subsequence $\{n_j\} \subset \mathbb{N}$ of density one such that $C_{n_j}(r,\theta) \to J_0(r)$ as $n_j \to \infty$ with r fixed. This convergence is, however, not uniform in r.

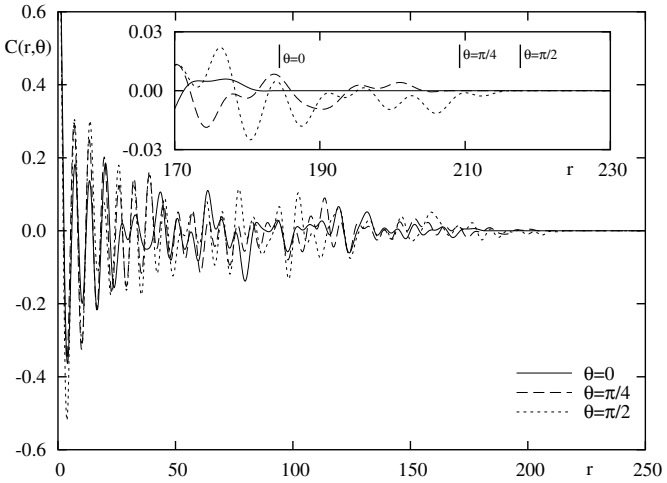

Figure 2. Autocorrelation function for the same state as figure 1, but for a larger r-interval showing the non-universal behaviour at larger r. The inset shows a magnification and the vertical bars indicate the places $r = \sqrt{E_n}\mathrm{diam}(\Omega, \theta)$ from where on $C(r, \theta) = 0$, due to the compactness of the billiard.

For the example shown in figure 1 $C(r, \theta)$ fluctuates, as expected for a 'quantum ergodic' state, around the asymptotic result

$$C(r, \theta) \sim J_0(r). \tag{12}$$

Actually, for an eigenstate with energy E_n we have $C(r, \theta) = 0$ for $r > \sqrt{E_n}\mathrm{diam}(\Omega, \theta)$, where $\mathrm{diam}(\Omega, \theta)$ is the diameter of Ω in the direction θ, as follows directly from the definition (6). This is illustrated in figure 2 which clearly shows the non-universal behaviour for larger r.

In contrast to the case of quite uniformly distributed eigenfunctions one expects a stronger directional dependence of the autocorrelation function for localized eigenfunctions, such as scars [40]. One example is shown in figure 3, where the eigenfunctions shows localization along the shortest unstable periodic orbit in the cardioid. The corresponding autocorrelation function shows clear deviations from (12).

A class of eigenfunctions which show even stronger localization are the bouncing ball modes in billiards with two parallel walls (see, e.g. [2, 41–44]). Figure 4 shows for the stadium billiard an example of a bouncing ball mode, which localizes on the so-called bouncing ball orbits having perpendicular reflections at the parallel walls and thus forming a one-parameter family. The simplest approximation is to consider them as a product of two sines, one in the x direction and the other in the y direction. In this case the autocorrelation function can be computed explicitly. For the odd–odd eigenfunctions

$$\psi_{n_x,n_y}(x, y) = \frac{1}{\sqrt{l_x l_y}} \sin(\pi n_x x/l_x) \sin(\pi n_y y/l_y) \tag{13}$$

in a box $B := [-l_x, l_x] \times [-l_y, l_y]$ one gets

$$C^{\mathrm{box}}_{n_x,n_y}(r, \theta) = F(r\cos(\theta)/\sqrt{E}, n_x, l_x)\, F(r\sin(\theta)/\sqrt{E}, n_y, l_y) \tag{14}$$

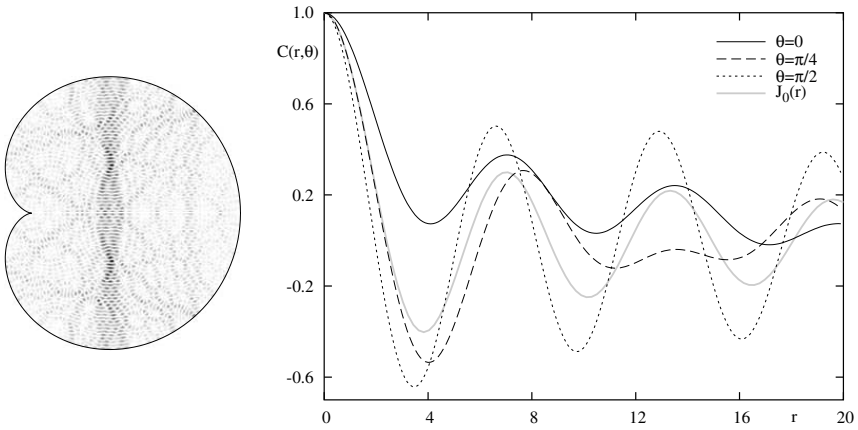

Figure 3. Grey scale plot of $|\psi_n(\boldsymbol{q})|^2$ with $n = 1277$ in the cardioid billiard with odd symmetry. For the autocorrelation function $C(r, \theta)$ one observes clear deviations from $C(r, \theta) = J_0(r)$.

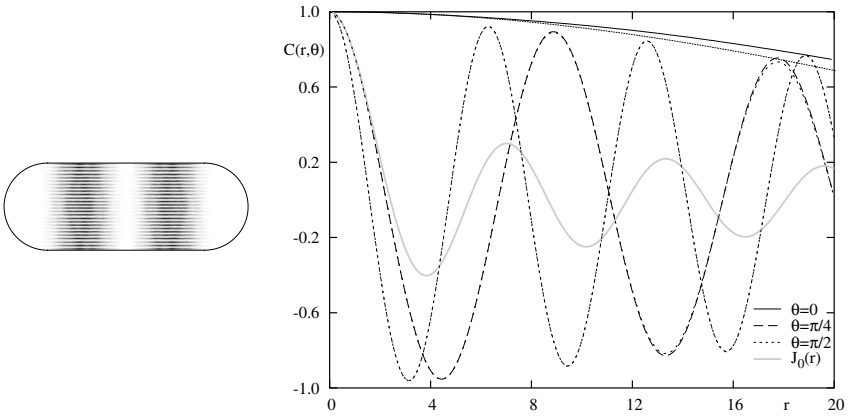

Figure 4. For the stadium billiard with odd–odd symmetry, $a = 1.8$, $\psi_{320}(\boldsymbol{q})$ is a bouncing ball mode. The corresponding autocorrelation function is compared with the result $C^{\mathrm{box}}_{1,13}(r, \theta)$, equation (14), obtained for a box, shown as dotted curves, which follow $C(r, \theta)$. Only for $\theta = 0$ (full line) and $\theta = \pi/4$ at $r \approx 17$ are small deviations visible.

where

$$F(z, n, l) := \chi_{[-l,l]}(z/2)\frac{1}{l}\int_{-l+z/2}^{l-z/2} \sin(\pi n(x - z/2)/l)\ \sin(\pi n(x + z/2)/l)\ \mathrm{d}x \tag{15}$$

$$= \chi_{[-l,l]}(z/2)\left[\left(1 - \frac{z}{2l}\right)\cos(\pi n z/l) + \frac{1}{2\pi n}\ \sin(\pi n z/l)\right] \tag{16}$$

and $\chi_{[-l,l]}(z)$ denotes the characteristic function of the interval $[-l, l]$.

In figure 4 we compare the autocorrelation $C(r, \theta)$function for a bouncing ball mode in the stadium billiard with $C^{\mathrm{box}}_{1,13}(r, \theta)$, equation (14), and observe very good agreement. Mainly

for $\theta = 0$ some deviations are visible; these are understandable from the fact that in this case only correlations in the x-direction are measured, where the bouncing ball mode 'leaks' outside the rectangular region. To take this into account one can determine an effective $l_x^{\mathrm{eff}} > 2a$, by fitting $\sin^2\left(\pi x / l_x^{\mathrm{eff}}\right)$ to

$$\psi_n^{\mathrm{proj}}(x) := \int_0^1 |\psi(x, y)|^2 \, \mathrm{d}y. \tag{17}$$

For the case shown in figure 4 this procedure leads to $l_x^{\mathrm{eff}} \approx 4$ (whereas $2a = 3.6$) and the corresponding autocorrelation function gives excellent agreement with the one for ψ_{320}.

3. Expansion of the autocorrelation function

In this section we derive an expansion of the autocorrelation function which will lead to an understanding of the directional dependence of the autocorrelation function observed in the last section. We start from the representation of the local autocorrelation function in terms of the Wigner function

$$C_\rho(\boldsymbol{x}, \delta\boldsymbol{x}) = \iint \rho(\boldsymbol{x} - \boldsymbol{q}) W(\boldsymbol{p}, \boldsymbol{q}) \mathrm{e}^{-\mathrm{i}\boldsymbol{p}\delta\boldsymbol{x}/\sqrt{E}} \, \mathrm{d}p \, \mathrm{d}q. \tag{18}$$

Since the Wigner function is concentrated around the energy shell $|\boldsymbol{p}| = \sqrt{E}$, and is furthermore even in $\boldsymbol{p}$ by time reversal symmetry, we get

$$\begin{aligned} C_\rho(\boldsymbol{x}, \delta\boldsymbol{x}) &= \int_0^\infty \int_0^{2\pi} \int_\Omega \rho(\boldsymbol{x} - \boldsymbol{q}) W(\boldsymbol{p}, \boldsymbol{q}) \, \mathrm{d}q' \, \mathrm{e}^{-\mathrm{i}|\delta\boldsymbol{x}| \cos(\varphi - \theta)} \, r \, \mathrm{d}\varphi \, \mathrm{d}r + O(|\delta\boldsymbol{x}| E^{-1/2}) \\ &= \int_0^\infty \int_0^{2\pi} \int_\Omega \rho(\boldsymbol{x} - \boldsymbol{q}) W(\boldsymbol{p}, \boldsymbol{q}) \, \mathrm{d}q \, \cos(|\delta\boldsymbol{x}| \cos(\varphi - \theta)) \, r \, \mathrm{d}\varphi \, \mathrm{d}r + O(|\delta\boldsymbol{x}| E^{-1/2}) \end{aligned} \tag{19}$$

where we have used polar coordinates $\boldsymbol{p} = (|\boldsymbol{p}| \cos\varphi, |\boldsymbol{p}| \sin\varphi)$, $\delta\boldsymbol{x} = (|\delta\boldsymbol{x}| \cos\theta, |\delta\boldsymbol{x}| \sin\theta)$. Because of the rescaling by $\sqrt{E}$ the factor $\mathrm{e}^{-\mathrm{i}\boldsymbol{p}\delta\boldsymbol{x}/\sqrt{E}}$ is only slowly oscillating for $\boldsymbol{p}$ close to the energy shell, on which the Wigner function is concentrated. Therefore we get that the error is of order $|\delta\boldsymbol{x}|/\sqrt{E}$ (see appendix B for a sketch of the derivation of this remainder estimate). If we now use that $\cos(r \cos\varphi)$ is a generating function for Bessel functions [45]

$$\cos(|\delta\boldsymbol{x}| \cos\varphi) = J_0(|\delta\boldsymbol{x}|) + 2 \sum_{l=1}^{\infty} (-1)^l \cos(2l\varphi) J_{2l}(|\delta\boldsymbol{x}|) \tag{20}$$

we obtain

$$C_\rho(\boldsymbol{x}, \delta\boldsymbol{x}) = \xi_0(\boldsymbol{x}) \, J_0(|\delta\boldsymbol{x}|) + 2 \sum_{l=1}^{\infty} (-1)^l \xi_{2l}(\boldsymbol{x}, \theta) \, J_{2l}(|\delta\boldsymbol{x}|) + O(E^{-1/2}) \tag{21}$$

with (setting $r = |\boldsymbol{p}|$)

$$\xi_{2l}(\boldsymbol{x}, \theta) := \int_0^\infty \int_0^{2\pi} \int_\Omega \rho(\boldsymbol{x} - \boldsymbol{q}) W(\boldsymbol{p}, \boldsymbol{q}) \, \mathrm{d}q \cos(2l(\varphi - \theta)) \, r \, \mathrm{d}\varphi \, \mathrm{d}r. \tag{22}$$

The coefficients $\xi_{2l}(\boldsymbol{x}, \theta)$ can be further decomposed

$$\begin{aligned} \xi_{2l}(\boldsymbol{x}, \theta) = \cos(2l\theta) &\int_0^\infty \int_0^{2\pi} \int_\Omega \rho(\boldsymbol{x} - \boldsymbol{q}) W(\boldsymbol{p}, \boldsymbol{q}) \, \mathrm{d}q \cos(2l\varphi) \, r \, \mathrm{d}\varphi \, \mathrm{d}r \\ + \sin(2l\theta) &\int_0^\infty \int_0^{2\pi} \int_\Omega \rho(\boldsymbol{x} - \boldsymbol{q}) W(\boldsymbol{p}, \boldsymbol{q}) \, \mathrm{d}q \sin(2l\varphi) \, r \, \mathrm{d}\varphi \, \mathrm{d}r. \end{aligned} \tag{23}$$

Recall that for an operator $\hat{A}$ with Weyl symbol $A(\boldsymbol{p}, \boldsymbol{q})$ the expectation value $\langle\psi, \hat{A}\psi\rangle$ can be written as an integral over the phase space of the symbol multiplied by the Wigner function of ψ, see e.g. [46],

$$\langle\psi, \hat{A}\psi\rangle = \iint W(\boldsymbol{p}, \boldsymbol{q}) A(\boldsymbol{p}, \boldsymbol{q}) \, \mathrm{d}p \, \mathrm{d}q. \tag{24}$$

Therefore the coefficients in (23) can be interpreted as expectation values of certain operators $\hat{A}_{2l}(\boldsymbol{x})$, $\hat{B}_{2l}(\boldsymbol{x})$ given as the Weyl quantizations of the functions

$$A_{2l}(\boldsymbol{p}, \boldsymbol{q}) := \rho(\boldsymbol{x} - \boldsymbol{q}) \cos(2l\varphi) \qquad B_{2l}(\boldsymbol{p}, \boldsymbol{q}) = \rho(\boldsymbol{x} - \boldsymbol{q}) \sin(2l\varphi) \tag{25}$$

respectively,

$$\int_\Omega \int_0^{2\pi} \int_0^\infty W(\boldsymbol{p}, \boldsymbol{q}) \, \rho(\boldsymbol{x} - \boldsymbol{q}) \cos(2l\varphi) \, r \, \mathrm{d}r \, \mathrm{d}\varphi \, \mathrm{d}q = \langle\psi, \hat{A}_{2l}(\boldsymbol{x})\psi\rangle \tag{26}$$

$$\int_\Omega \int_0^{2\pi} \int_0^\infty W(\boldsymbol{p}, \boldsymbol{q}) \, \rho(\boldsymbol{x} - \boldsymbol{q}) \sin(2l\varphi) \, r \, \mathrm{d}r \, \mathrm{d}\varphi \, \mathrm{d}q = \langle\psi, \hat{B}_{2l}(\boldsymbol{x})\psi\rangle. \tag{27}$$

Note that the operators $\hat{A}_{2l}(\boldsymbol{x})$ and $\hat{B}_{2l}(\boldsymbol{x})$ depend on the parameter $\boldsymbol{x}$. Since their symbols are smooth and homogeneous of degree zero in $\boldsymbol{p}$ they are classical pseudodifferential operators of order zero, see e.g. [46] for the definition of pseudodifferential operators. So we finally obtain the following general expansion of the autocorrelation function

$$\begin{aligned} C_\rho(\boldsymbol{x}, \delta\boldsymbol{x}) = \langle\psi, \hat{A}_0(\boldsymbol{x})\psi\rangle \, J_0(|\delta\boldsymbol{x}|) + 2 \sum_{l=1}^{\infty} (-1)^l [\langle\psi, \hat{A}_{2l}(\boldsymbol{x})\psi\rangle \cos(2l\theta) \\ + \langle\psi, \hat{B}_{2l}(\boldsymbol{x})\psi\rangle \, \sin(2l\theta)] \, J_{2l}(|\delta\boldsymbol{x}|) + O(|\delta\boldsymbol{x}|E^{-1/2}) \end{aligned} \tag{28}$$

in terms of the expectation values of a sequence of bounded operators given as Weyl quantizations of the symbols (25). Recall that the only approximation we have made was to insert for $|\boldsymbol{p}|$ in the exponent in equation (19) the value at the energy shell $\sqrt{E}$.

Since the Bessel functions have the property that $J_{2l}(|\delta\boldsymbol{x}|) \approx 0$ for $|\delta\boldsymbol{x}| \ll 2l$, this representation is an efficient expansion for small $|\delta\boldsymbol{x}|$, then only a few terms in the sum contribute. But the larger $|\delta\boldsymbol{x}|$ becomes, the more terms of the sum have to be taken into account. Therefore it is desirable to have an estimate of the number of terms which have to be taken into account for large $|\delta\boldsymbol{x}|$. The first, and largest, maximum of $J_{2l}(r)$ lies around $r \sim 2l$, and close to it one has the expansion [45]

$$J_{2l}(2l - zl^{1/3}) = \frac{1}{l^{1/3}} \mathrm{Ai}(z) + O(1/l). \tag{29}$$

So the first peak becomes broader with a rate $\sim l^{1/3}$ and therefore we have to take for large r approximately

$$m \sim \frac{r}{2} + \frac{z}{2} \left(\frac{r}{2}\right)^{1/3} \tag{30}$$

terms in the sum over l into account; here z determines the error term. We refer to appendix C for a more detailed discussion.

We would like to mention two papers in which related results have been obtained. For the case of a free particle on a surface of constant negative curvature an expansion of the path correlation function in terms of the Legendre function was derived in [3]. In the special case of averaging over the whole billiard (i.e. $\rho = 1$) the path correlation function for ergodic systems should be the same as the autocorrelation function. In [25] an expansion similar to (28) was derived for the case when the eigenfunction is concentrated on an ergodic component of the phase space of a classically mixed system, however, without extracting the Bessel function

from the expectation values. To make this possible is the main reason why we have restricted our attention here to billiards. For more general systems one could derive similar expansions which approximate the autocorrelation function for small correlation distances using only a few terms, but their structure becomes more complicated.

The correlation distance expansion (28) has various possible applications; some of them will be discussed and illustrated in the next section. In particular, the expansion leads to a prediction for the asymptotic limit of the autocorrelation function in different situations. More precisely, consider a subsequence of eigenfunctions $\{\psi_{n_j}\}_{j\in\mathbb{N}}$ for which the corresponding sequence of Wigner functions converges weakly to a measure ν on phase space. Such a measure ν is called a quantum limit, and it is an invariant measure of the classical flow [5].

If a sequence of eigenfunctions $\{\psi_{n_j}\}_{j\in\mathbb{N}}$ converges to a quantum limit, the correlation distance expansion for the autocorrelation function (28) shows that the corresponding sequence of autocorrelation functions converges as well and their limit is obtained by substituting in (28) the expectation values of $\hat{A}_{2l}(\boldsymbol{x})$ and $\hat{B}_{2l}(\boldsymbol{x})$ by their corresponding classical limit. Explicitly, this gives

$$C_\rho^{\text{limit}}(\boldsymbol{x},\delta\boldsymbol{x}) = \bar{A}_0 J_0(|\delta\boldsymbol{x}|) + 2\sum_{l=1}^{\infty}(-1)^l[\bar{A}_{2l}(\boldsymbol{x})\,\cos(2l\theta) + \bar{B}_{2l}(\boldsymbol{x})\,\sin(2l\theta)]\,J_{2l}(|\delta\boldsymbol{x}|) \quad (31)$$

where

$$\bar{A} := \int_{T^*\Omega} A\,\mathrm{d}\nu. \quad (32)$$

As we will discuss in section 4.4, for ergodic systems almost all eigenfunctions have the Liouville measure as the quantum limit, then the terms $\bar{A}_{2l}$ and $\bar{B}_{2l}$ vanish, and with $\bar{A}_0 = 1$ we recover (12).

4. Applications of the correlation distance expansion

4.1. Direct comparison

In the numerical examples we have studied the autocorrelation function in the case $\rho = 1$, which allows for an exact computation of the autocorrelation function using the representation (10), which is much more efficient than a direct computation of the autocorrelation function by its definition, equation (8). In this case the general expansion (28) gives the representation

$$C(r,\theta) = J_0(r) + 2\pi\sum_{l=1}^{\infty}(-1)^l[a_{2l}\cos(2l\theta) + b_{2l}\sin(2l\theta)]\,J_{2l}(r) + O(rE^{-1/2}) \quad (33)$$

where the coefficients a_{2l} and b_{2l} are the Fourier coefficients

$$a_{2l} = \frac{1}{\pi}\int_0^{2\pi} I(\varphi)\cos(2l\varphi)\,\mathrm{d}\varphi \qquad b_{2l} = \frac{1}{\pi}\int_0^{2\pi} I(\varphi)\sin(2l\varphi)\,\mathrm{d}\varphi \quad (34)$$

of the radially integrated momentum density [47, 48]

$$I(\varphi) := \int_0^{\infty} |\hat{\psi}(r\boldsymbol{e}(\varphi))|^2 r\,\mathrm{d}r \quad (35)$$

where $\boldsymbol{e}(\varphi) = (\cos\varphi, \sin\varphi)$. Also for $I(\varphi)$ a representation in terms of a double integral of the normal derivative function is available [48]. Taking the symmetries into account, one can show that for the odd eigenfunctions in the limaçon billiards and the odd–odd eigenfunctions in the stadium billiard all b_{2l} vanish, so only the cosine terms remain in (28) and (33).

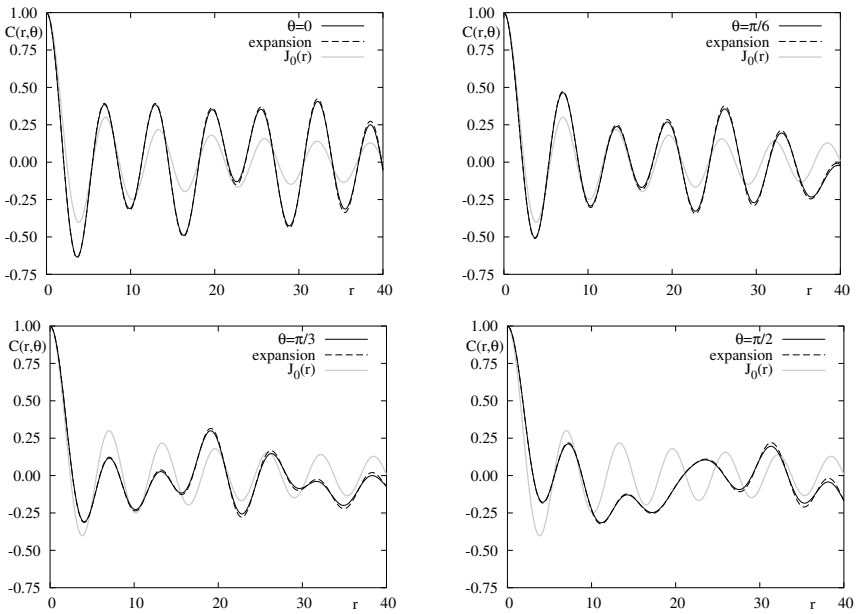

Figure 5. Comparison of the autocorrelation function $C(r, \theta)$ for ψ_{1907} in the stadium billiard (full curve) with the expansion (33). In particular, for small r the agreement is excellent, whereas for larger r small differences become visible.

First we will test the influence of the error term $O(E^{-1/2})$ in equation (33) for computations at finite energies. To that end we use the exact quantum $I(\varphi)$ in equation (34). In figure 5 the autocorrelation function $C(r, \theta)$ for four different angles θ is compared to (33). In particular, for r not too big the agreement is excellent. Only for larger r do small deviations become visible, which go to zero for higher energies and r fixed. One should remark that for any $r > 0$ the effective integration region in equation (8) is reduced by the factor

$$c(r, \theta) := \frac{\mathrm{vol}(\Omega \cap \Omega(r/\sqrt{E}, \theta))}{\mathrm{vol}(\Omega)} \tag{36}$$

where $\Omega(r/\sqrt{E}, \theta)$ is the set Ω shifted by the vector $r/\sqrt{E}$ $(\cos\theta, \sin\theta)$. Incorporating this factor leads to an improvement in the agreement of the expansion with the exact autocorrelation function at larger r.

Instead of looking at the dependence of the autocorrelation function $C(r, \theta)$ for fixed θ and varying r, it is also interesting to keep r fixed and consider the angular dependence. For a 'chaotic' eigenfunction in the cardioid billiard some examples are shown in figure 6. The result of the expansion (33) is in good agreement with the exact result. For larger r the autocorrelation function $C(r, \theta)$ oscillates more strongly around $J_0(r)$. For even larger r we observe clear deviations of the expansion from the exact result (not shown). For comparison

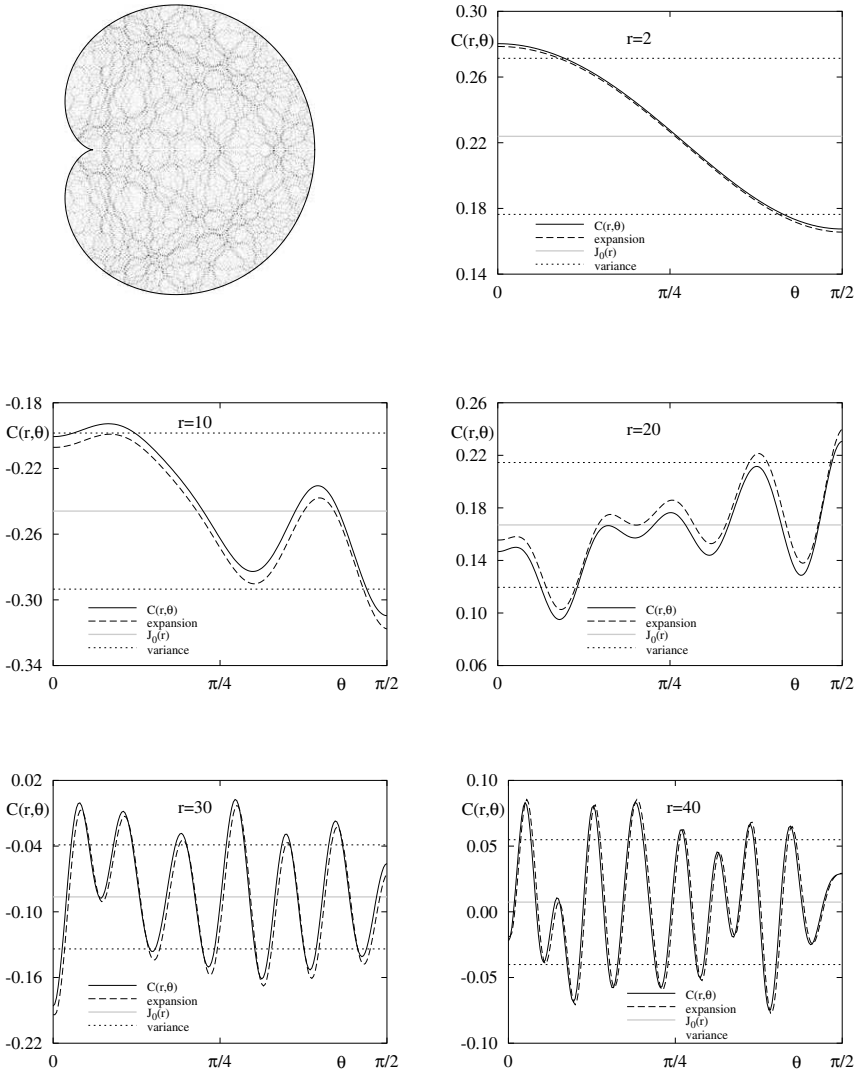

Figure 6. Angular dependence of the autocorrelation function $C(r, \theta)$ for different r. Shown are the results for ψ_{6000} in the cardioid billiard with odd symmetry. The full line is the result for $C(r, \theta)$ using (10), the dashed line shows the result of the expansion (33), the full grey line is the value of $J_0(r)$ and the dotted horizontal lines show the variance $J_0(r) \pm \Delta^{1/2}$ (see equation (37)).

the variance of the autocorrelation function around the prediction $J_0(r)$ for a random wave model [16] in leading order

$$\Delta^{1/2} = \left(\frac{16}{3\pi^{3/2}A}\right)^{1/2} \frac{1}{E^{1/4}} \tag{37}$$

is shown and good agreement is found. Note that for bounded r this error is much larger than the additional error term $O(rE^{-1/2})$ from (33).

4.2. Localized eigenfunctions

For a state strongly localized on an periodic orbit of length l_γ we have (either in the semiclassical limit, or as a crude model at finite energies)

$$I(\varphi) \sim \frac{1}{l_\gamma} \sum l_{\gamma_i} \delta(\varphi - \varphi_i) \tag{38}$$

where l_{γ_i} are the lengths of the segments of the orbit with direction φ_i. Thus we get

$$a_{2l} = \frac{1}{\pi l_\gamma} \sum l_{\gamma_i} \cos(2l\varphi_i) \qquad b_{2l} = \frac{1}{\pi l_\gamma} \sum l_{\gamma_i} \sin(2l\varphi_i) \tag{39}$$

which therefore using (33) gives a prediction for $C(\delta\boldsymbol{x})$ for such states, namely

$$C(\delta\boldsymbol{x}) \sim \frac{1}{l_\gamma} \sum_i l_{\gamma_i} \cos(|\delta\boldsymbol{x}| \cos(\theta - \varphi_i)). \tag{40}$$

Note that in the presence of symmetries all symmetry-related directions have to be taken into account in equation (38). For this simple model one can determine the autocorrelation function more directly by using (3)

$$\begin{aligned} C(\delta\boldsymbol{x}) &= \iint W(\boldsymbol{p}, \boldsymbol{q}) \mathrm{e}^{\mathrm{i}\boldsymbol{p}\delta\boldsymbol{x}} \, \mathrm{d}p \, \mathrm{d}q = \int |\hat{\psi}(\boldsymbol{p})|^2 \mathrm{e}^{\mathrm{i}\boldsymbol{p}\delta\boldsymbol{x}} \, \mathrm{d}p \\ &= \int_0^{2\pi} I(\varphi) \cos(|\delta\boldsymbol{x}| \cos(\theta - \varphi)) \, \mathrm{d}\varphi + O(|\delta\boldsymbol{x}| E^{-1/2}) \end{aligned} \tag{41}$$

inserting (38) directly gives (40).

In figure 7 we compare the limiting behaviour (40) with the autocorrelation function of a high-lying eigenstate in the limaçon billiard. The state localizes on the (stable) orbit of triangular shape. Up to $r \approx 10$ the agreement is very good; for larger r the autocorrelation function of the eigenstate shows deviations from the asymptotic behaviour. Note that the state has a much higher energy than the other examples. At lower energies the agreement is not as good, because the region in phase space on which the state localizes is broader. This in turn implies that its corresponding radially integrated momentum distribution $I(\varphi)$ also has broad peaks, which are not accounted for properly by the ansatz (38). However, when considering states of this type with increasing energies, a clear trend to the asymptotic result (40) is observed.

This simple model has also been tested for a scarred state in the cardioid. However, the agreement is limited to a qualitative description for up to $r \approx 2$. This is understandable in view of the observation (see [48, figure 8(a)]) that for a scarred state the radially integrated momentum distribution $I(\varphi)$ shows quite large fluctuations, and also in the considered case the direction $\varphi = \pi/2$ is not clearly pronounced. As these fluctuations essentially correspond to the random 'background' fluctuations of the state, a simple ansatz to model this behaviour is

$$C(r, \theta) = (1 - \alpha) J_0(r) + \alpha \frac{1}{l_\gamma} \sum_i l_{\gamma_i} \cos(|\delta\boldsymbol{x}| \cos(\theta - \varphi_i)). \tag{42}$$

It turns out that one can vary α such that quite good agreement of this model with the exact autocorrelation function is obtained (see figure 8 where $\alpha = 0.22$ (for all directions)). Depending on the direction θ the 'optimal' value for α does vary, which already indicates the limitations of this simple model. To get a better agreement a more precise description of

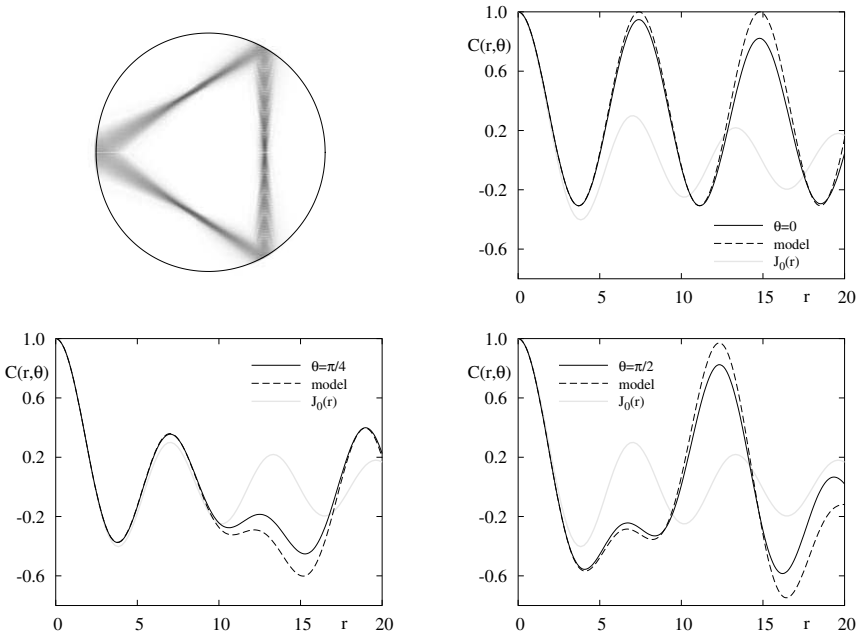

Figure 7. High-lying eigenfunction ($E = 367\,984.82\ldots$, approx. 47 788th eigenfunction of odd symmetry) in the limaçon billiard ($\varepsilon = 0.3$), which localizes on the stable orbit of triangular shape. The autocorrelation function for three different directions is compared with the δ-model, equation (40), shown as the dashed line using the directions of the stable orbit.

$I(\varphi)$ for scarred states is necessary. In particular, this should also lead to an understanding of the energy dependence of α which is expected to go to zero in the semiclassical limit. Note that the structure of the autocorrelation function is quite similar to the one for ψ_{1817} shown in figure 3.

Another case, for which we obtain much better agreement, is for an eigenfunction localized on an invariant torus. In such a case the expectation values, equations (26), (27), tend to the mean of the classical observable over the torus (see equations (31), (32)). Figure 9(*a*) shows for the limaçon billiard the eigenfunction and the corresponding Husimi Poincaré representation [49, 50]; see [51] for a more detailed discussion and the formula which has been used. Also shown in the Husimi plot are the points of some orbits. Using an initial condition on the torus we can determine the classical angular distribution $I^{\text{classical}}(\varphi)$. As this has a singularity due to the caustic of the torus we show in figure 9(*c*) a binned distribution together with the corresponding quantum radially integrated momentum distribution $I_{3056}(\varphi)$. There is qualitative agreement between these two curves in the sense that smoothing $I^{\text{classical}}(\varphi)$ describes the mean behaviour of the quantum $I_{3056}(\varphi)$. Of course, the classical distribution cannot describe the (quantum) oscillations visible for $I_{3056}(\varphi)$. It turns out, see figures 9(*d*)–(*f*), that already this simple model leads to surprisingly good agreement between the exact autocorrelation function and the expansion (33) computed using $I^{\text{classical}}(\varphi)$.

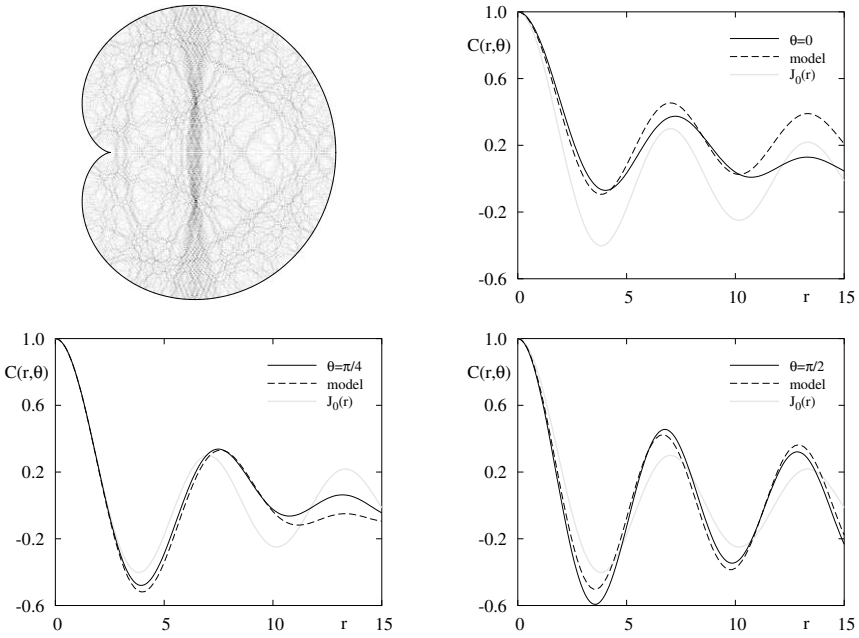

Figure 8. For a scarred state (ψ_{7147} of odd symmetry) in the cardioid billiard the autocorrelation function is compared with the simple model (42) for $\alpha = 0.22$.

4.3. Autocorrelation function of irregular states in mixed systems

In classical systems with mixed phase space regions with regular and regions with stochastic behaviour coexist. It is conjectured [52] that correspondingly the quantum mechanical eigenfunctions split into regular and irregular ones, respectively, living semiclassically on the corresponding parts of phase space. This has been confirmed numerically for several systems (see e.g. [53–57]). Consider now a sequence of eigenfunctions ψ_{n_j} which localize on some open ergodic domain D in a system with mixed phase space, then almost all the expectation values $\langle \psi_{n_j} \hat{A} \psi_{n_j} \rangle$ tend to the mean $\bar{A}^D$ of the corresponding classical observable A over this domain D [26]. Therefore using (33) we get in the limit $E \to \infty$ for the autocorrelation function of such a sequence

$$C_\rho^{\text{limit}}(\boldsymbol{x}, \delta\boldsymbol{x}) = \bar{A}_0^D J_0(|\delta\boldsymbol{x}|) + 2\sum_{l=1}^{\infty}(-1)^l\left[\bar{A}_{2l}^D(\boldsymbol{x})\cos(2l\theta) + \bar{B}_{2l}^D(\boldsymbol{x})\sin(2l\theta)\right] J_{2l}(|\delta\boldsymbol{x}|). \tag{43}$$

Instead of computing $\bar{A}_{2l}^D$ and $\bar{B}_{2l}^D$ directly, we can also use a typical trajectory of the ergodic component to determine the corresponding classical $I^{\text{classical}}(\varphi)$ via

$$I^{\text{classical}}(\varphi) = \lim_{l\to\infty}\frac{1}{l}\sum l_i \delta(\varphi - \varphi_i) \tag{44}$$

where l is the total length of the trajectory and φ_i is the direction of the ith segment having length l_i. Then we use (33) to get a prediction for the autocorrelation function.

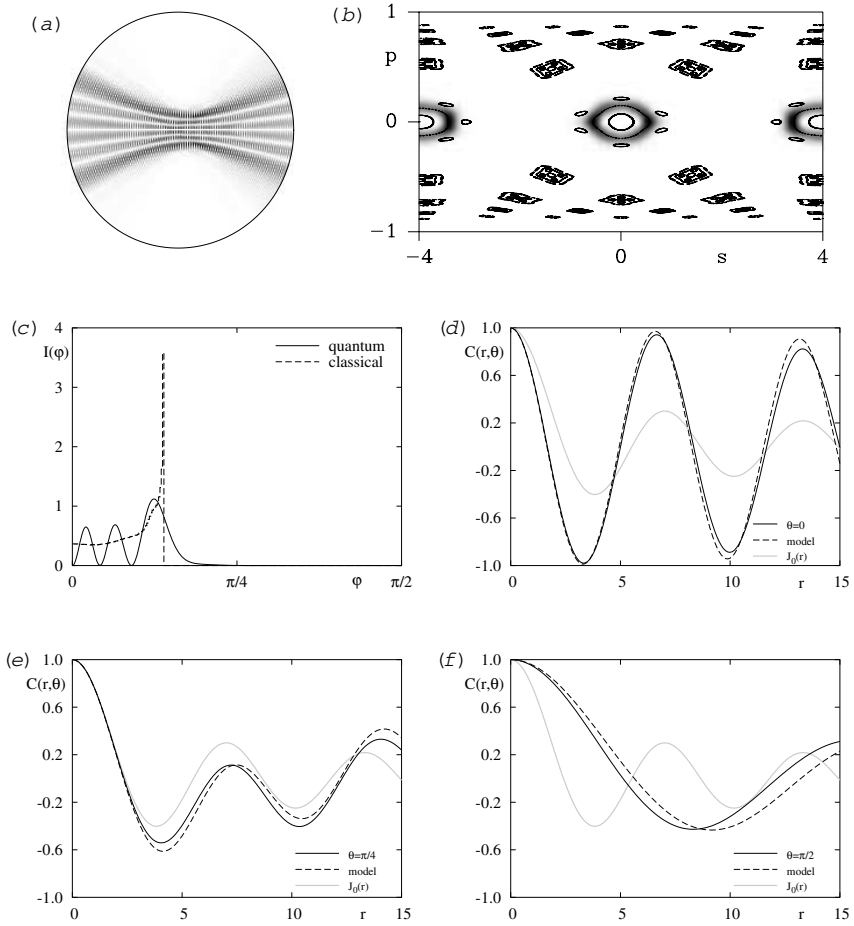

Figure 9. Grey scale plot of ψ_{3056} for the limaçon billiard with $\varepsilon = 0.3$ together with the corresponding Husimi plot, for which in addition some orbits are shown. In (c) the radially integrated momentum distribution $I_{3056}(\varphi)$ and the corresponding classical distribution $I^{\text{classical}}(\varphi)$ for the torus are shown. In (d)–(f) the exact autocorrelation function is compared with the expansion of the autocorrelation function, equation (33), using $I^{\text{classical}}(\varphi)$ for different angles θ.

However, we observe that even quite high-lying states do not yet localize on the whole chaotic component. Instead they are confined to smaller subregions due to partial barriers in phase space. Figure 10(a) shows an example of a high-lying state in the limaçon billiard ($\varepsilon = 0.3$) In figure 10(b) the corresponding Husimi function is plotted, which clearly shows the localization on a chaotic subdomain (the whole irregular region is much larger). If D is an open region in phase space, then the corresponding classical distribution of the momentum directions is given by

$$I^{\text{classical}}(\varphi) = \frac{1}{\text{vol}(D)} \int \chi_D(\boldsymbol{p}(\varphi), \boldsymbol{q})\, \mathrm{d}q \tag{45}$$

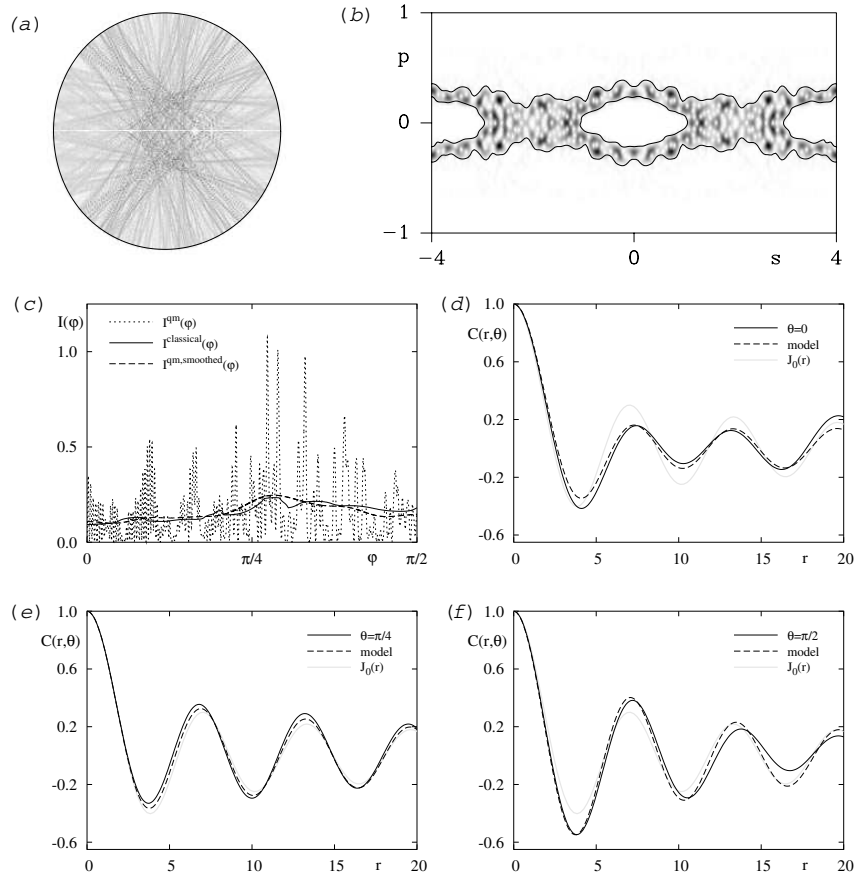

Figure 10. Autocorrelation function for a high-lying irregular state ($E = 1002\,754.70\ldots$, approx. 130 516th eigenfunction of odd symmetry) in the limaçon billiard with $\varepsilon = 0.3$. In (*b*) the Husimi representation on the boundary is shown together with an approximate boundary (full curve) of the region $\mathcal{D}$ on which the state localizes. The resulting classical momentum distribution $I^{\text{classical}}(\varphi)$ is shown in (*c*) as a full curve and compared with the radially integrated momentum distribution $I^{\text{qm}}(\varphi)$ of the state in (*a*) and a smoothing of this, $I^{\text{qm,smoothed}}(\varphi)$, shown as a dashed curve. In (*d*)–(*f*) the autocorrelation function $C(r, \theta)$ of the eigenfunction is compared for three different directions with result of the expansion (43) using $I^{\text{classical}}(\varphi)$.

where $\boldsymbol{p}(\varphi) = (\cos\varphi, \sin\varphi)$. One can show that in terms of the projection $\mathcal{D}$ of D on the Poincaré section this equation can be reduced to

$$I^{\text{classical}}(\varphi) = \frac{\int_{\mathcal{D}} l(s,p)\delta(\varphi - \phi(s,p))\,\mathrm{d}s\,\mathrm{d}p}{\int_{\mathcal{D}} l(s,p)\,\mathrm{d}s\,\mathrm{d}p} \tag{46}$$

$$= \frac{\int_{\partial\Omega'(\varphi)} l(s,p(s,\varphi))\sqrt{1-p^2(s,\varphi)}\chi_{\mathcal{D}}(s,p(s,\varphi))\,\mathrm{d}s}{\int_{\mathcal{D}} l(s,p)\,\mathrm{d}s\,\mathrm{d}p} \tag{47}$$

where $l(s, p)$ is the length of the orbit segment starting in the point $(s, p) \in \mathcal{P}$ with direction $\phi(s, p)$ and in the second equation $p(s, \varphi) = \boldsymbol{p}(\varphi)\boldsymbol{t}(s)$, with $\boldsymbol{t}(s)$ denoting the unit tangent vector to ∂D at the point s. Furthermore, $\partial\Omega'(\varphi) := \{s \in \partial\Omega \mid \boldsymbol{p}(\varphi)\boldsymbol{n}(s) \leqslant 0\}$, where $\boldsymbol{n}(s)$ denotes the outer normal vector to ∂D in the point s, is the subset of $\partial\Omega$ where the vector $\boldsymbol{p}(\varphi)$ points inwards. For the numerical computation we have used (47) because we just have to deal with a one-dimensional integral to compute the φ dependence, and also compared to (46) no binning of $I^{\text{classical}}(\varphi)$ is necessary.

After these general remarks on the computation of $I^{\text{classical}}(\varphi)$ let us describe how we compute the relevant quantities to determine the autocorrelation function for the state shown in figure 10(*a*). To describe the projection $\mathcal{D}$ of the domain D in phase space, we use an approximation of the boundary of $\mathcal{D}$ by a splines, which are shown in the figure 10(*b*) as full curves. Then we use equation (47) to determine the corresponding $I^{\text{classical}}(\varphi)$, shown in (*c*) as a full curve. Of course the radially integrated momentum distribution $I^{\text{qm}}(\varphi)$ of the eigenstate shows strong fluctuations, but the smoothing $I^{\text{qm,smoothed}}(\varphi)$ is well described by $I^{\text{classical}}(\varphi)$, although the agreement is not perfect. Using $I^{\text{classical}}(\varphi)$ we employ the expansion (43) to get a prediction for the autocorrelation function for states localizing on $\mathcal{D}$, which is compared in figures 10(*d*)–(*f*) with the exact autocorrelation function. Up to $r \approx 10$ we get quite good agreement, whereas for larger r deviations become more visible. This shows that the eigenfunction has more structure than accounted for by $I^{\text{classical}}(\varphi)$, i.e. it is not yet far enough in the semiclassical limit.

For higher energies the states tend to localize on the full ergodic region, and then $I^{\text{classical}}(\varphi)$ can simply be computed using (44) by averaging a typical trajectory in D. One should emphasize that the agreement has to be compared with the agreement of the autocorrelation function for ergodic systems with (12) as the prediction equation (43) only takes into account the classical limit. This has been studied in [25] (in the case of averaging the local autocorrelation function over a small disc), where in particular for [25, figure 13(*b*)] very good agreement has been found.

4.4. Ergodic systems and the rate of quantum ergodicity

If the classical billiard is ergodic, then by the quantum ergodicity theorem [6–11] almost all eigenfunctions become equidistributed in the semiclassical limit. More precisely, there exists a subsequence $\{\psi_{n_j}\}_{j\in\mathbb{N}}$ of density one, i.e. $\lim_{E\to\infty} \frac{\#\{E_{n_j} \leqslant E\}}{\#\{E_n \leqslant E\}} = 1$, such that

$$\lim_{j\to\infty} \langle \psi_{n_j}, \hat{A}\psi_{n_j} \rangle = \bar{A} \tag{48}$$

for all pseudodifferential operators $\hat{A}$, and $\bar{A}$ denotes the mean with respect to the Liouville measure of the corresponding classical observable. The rate by which this equidistribution is reached is called the rate of quantum ergodicity. It is an important quantity, as it determines the practical applicability of the quantum ergodicity theorem at finite energies.

If the billiard is ergodic and ψ_{n_j} is a quantum ergodic sequence of eigenfunctions, then for $j \to \infty$

$$\langle \psi_{n_j}, \hat{A}_{2l}(\boldsymbol{x})\psi_{n_j} \rangle \sim \bar{A}_{2l} = \delta_{l0} \tag{49}$$

$$\langle \psi_{n_j}, \hat{B}_{2l}(\boldsymbol{x})\psi_{n_j} \rangle \sim \bar{B}_{2l} = 0. \tag{50}$$

Thus using the expansion (28) we again get (12) for $E \to \infty$. Deviations from this universal behaviour are then determined by the rate at which the limit in (49) and (50) is reached, i.e. the

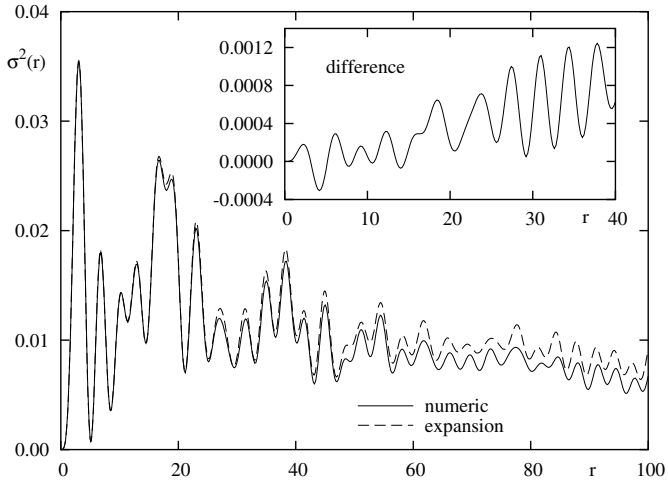

Figure 11. Comparison of the second moment $\sigma^2{}_{1907}(r)$ of the autocorrelation function, equation (52), with the expansion (53) for the stadium billiard. The inset shows the difference for $r \in [0, 20]$.

rate of quantum ergodicity. In order to exploit this it will be convenient to remove the angular dependence by taking the mean over all angular directions in $C(\delta\boldsymbol{x})$. Since by equation (33)

$$\frac{1}{2\pi}\int_0^{2\pi} C_n(r,\theta)\,\mathrm{d}\theta = J_0(r) + O(rE^{-1/2}) \tag{51}$$

we consider the second moment

$$\sigma_n^2(r) := \frac{1}{2\pi}\int_0^{2\pi} [C_n(r,\theta) - J_0(r)]^2\,\mathrm{d}\theta \tag{52}$$

where $C_n(r,\theta)$ denotes the autocorrelation function of ψ_n. Inserting the expansion (33) of $C_n(\delta\boldsymbol{x})$ leads to

$$\sigma_n^2(r) = 2\pi^2 \sum_{l=1}^{\infty} \left(a_{2l,n}^2 + b_{2l,n}^2\right) [J_{2l}(r)]^2\,(1 + O(rE^{-1/2})). \tag{53}$$

In figure 11 we compare $\sigma^2(r)$ for an eigenfunction in the stadium billiard with the expansion (53). For small r we get excellent agreement and some deviations become visible in the plot for $r > 20$. The inset shows a plot of the difference up to $r = 20$. It is surprising that even though for large r the amplitudes do not match anymore, still the expansion gives the right oscillatory structure.

If we take the mean of (53) over all eigenfunctions up to energy E, we get

$$\bar{\sigma}^2(E,r) := \frac{1}{N(E)} \sum_{E_n \leqslant E} \sigma_n^2(r) \tag{54}$$

$$= 2\pi^2 \sum_{l=1}^{\infty} \frac{1}{N(E)} \sum_{E_n \leqslant E} \left(a_{2l,n}^2 + b_{2l,n}^2\right)\ [J_{2l}(r)]^2\,(1 + O(rE^{-1/2})). \tag{55}$$

Remarkably, together with equations (28) and (53) this shows that the rate of quantum ergodicity can be studied in terms of the autocorrelation function. Particularly interesting is

that the observables in the expansion (28) become more and more oscillatory with increasing l, so by varying $|\delta \boldsymbol{x}|$ one can determine the rate of quantum ergodicity on different length scales.

A prediction for the behaviour of $\bar{\sigma}^2(E, r)$ follows from [58], where it is argued that (under suitable conditions on the system) in the mean

$$\frac{1}{N(E)} \sum_{E_n \leqslant E} \left[\langle \psi_{n_j}, \hat{A} \psi_{n_j} \rangle - \bar{A} \right]^2 \sim \frac{4\sigma_{\mathrm{cl}}^2(A)}{\mathrm{vol}\,\Omega} \frac{1}{\sqrt{E}} \tag{56}$$

for any pseudodifferential operator $\hat{A}$ of order zero with symbol A. Here $\bar{A}$ denotes the mean value of A, and $\sigma_{\mathrm{cl}}^2(A)/\sqrt{T}$ is the variance of the fluctuations of

$$\frac{1}{T} \int_0^T A(\boldsymbol{p}(t), \boldsymbol{q}(t))\, \mathrm{d}t \tag{57}$$

around $\bar{A}$. So if we insert (56) into (55) we obtain

$$\bar{\sigma}^2(E, r) \sim \frac{8\pi^2}{\mathrm{vol}\,\Omega} \sum_{l=1}^{\infty} \left[\sigma_{\mathrm{cl}}^2(A_{2l}) + \sigma_{\mathrm{cl}}^2(B_{2l}) \right] [J_{2l}(r)]^2 \frac{1}{\sqrt{E}}. \tag{58}$$

A detailed study of the rate of quantum ergodicity in terms of the autocorrelation function, i.e. via equation (54), and a comparison with the semiclassical expectation (58) will be given in a separate paper.

5. Summary

We have discussed the autocorrelation function for eigenstates of quantum mechanical systems, and its relation to the behaviour of the classical system. For billiards we have derived a formula for the autocorrelation function of an eigenfunction in terms of the normal derivative on the boundary (10), which enables an efficient numerical computation.

Our main result is the correlation distance expansion of the autocorrelation function (28) for billiards, which provides an efficient expansion for small correlation distances, where only a small number of terms enters the sum. Moreover, it provides a tool for understanding the behaviour of the autocorrelation function for different types of eigenfunctions in terms of their semiclassical limit.

The coefficients in the correlation distance expansion (28) can be computed in terms of the radially integrated momentum density. Even though it is based on an approximation, our numerical study shows very good agreement with the corresponding exact results; only for large correlation distances do deviations become visible. As the expansion coefficients have to be determined just once for a given eigenfunction, this is also a numerically efficient method to compute the autocorrelation function. Similar, but more complicated, expansions can be derived in higher dimension and for more general systems (e.g. systems with potential and magnetic field), but then the Bessel functions have to be modified in order to reflect the structure of the energy shell of the classical system.

We applied the expansion of the autocorrelation function to different types of eigenfunctions, and showed that it provides a good tool for the understanding of their autocorrelation functions. In systems with mixed phase space regular states concentrated on tori and irregular states have been successfully treated. For chaotic system the fluctuations of the autocorrelation functions around the leading term are shown to be connected with the rate of quantum ergodicity. Moreover, by varying the correlation distance the autocorrelation function is shown to be an interesting new tool to measure the rate of quantum ergodicity on different length scales.

Acknowledgments

We would like to thank Professor Jonathan Keating for useful comments on the manuscript. AB acknowledges support by the Deutsche Forschungsgemeinschaft under contract no DFG-Ba 1973/1-1. RS acknowledges support by the Deutsche Forschungsgemeinschaft under contract no DFG-Ste 241/7-3.

Appendix A. Autocorrelation function in terms of normal derivatives on the boundary

We will give a derivation of the formula (10) which provides an expression of the autocorrelation function $C(\delta\boldsymbol{x})$ in terms of the normal derivative. Let $\psi(\boldsymbol{q})$ be a solution of the Helmholtz equation with Dirichlet boundary condition on $\partial\Omega$,

$$(\Delta + k^2)\psi(\boldsymbol{q}) = 0 \qquad \psi(\boldsymbol{q}) = 0 \qquad \text{for} \quad \boldsymbol{q} \in \partial\Omega \tag{59}$$

where we have defined $k = \sqrt{E}$, and let

$$u(s) := \boldsymbol{n}(s)\nabla\psi(\boldsymbol{q}(s)) \tag{60}$$

be the outer normal derivative of ψ on $\partial\Omega$, where s parametrizes $\partial\Omega$ in arclength. It is well known that

$$-\frac{1}{4}\int_{\partial\Omega} Y_0(k|\boldsymbol{q}-\boldsymbol{q}(s)|)u(s)\,\mathrm{d}s = \begin{cases}\psi(\boldsymbol{q}) & \text{for} \quad \boldsymbol{q} \in \Omega^\circ \\ 0 & \text{for} \quad \boldsymbol{q} \notin \Omega\end{cases} \tag{61}$$

and furthermore

$$\int_{\partial\Omega} J_0(k|\boldsymbol{q}-\boldsymbol{q}(s)|)u(s)\,\mathrm{d}s = 0. \tag{62}$$

Let $\rho(t)$ be a smooth cut-off function with

$$\rho(t) = \begin{cases}1 & \text{for} \quad t \leqslant 2\,\mathrm{diam}(\Omega) \\ 0 & \text{for} \quad t \geqslant 3\,\mathrm{diam}(\Omega)\end{cases} \tag{63}$$

where $\mathrm{diam}(\Omega)$ denotes the diameter of Ω. Then we have for $\boldsymbol{q}$ in some neighbourhood of Ω

$$\psi(\boldsymbol{q}) = -\frac{1}{4}\int_{\partial\Omega} \rho(k|\boldsymbol{q}-\boldsymbol{q}(s)|)Y_0(k|\boldsymbol{q}-\boldsymbol{q}(s)|)u(s)\,\mathrm{d}s \tag{64}$$

and obtain

$$C(\delta\boldsymbol{x}) = \int_{\mathbb{R}^2} \psi^*(\boldsymbol{q})\psi(\boldsymbol{q}+\delta\boldsymbol{x})\,\mathrm{d}q = \iint_{\partial\Omega\times\partial\Omega} K_\rho(\delta\boldsymbol{x}, s, s')u^*(s)u(s')\,\mathrm{d}s\,\mathrm{d}s' \tag{65}$$

with

$$\begin{aligned} K_\rho(\delta\boldsymbol{x}, s, s') &= \frac{1}{16}\int_{\mathbb{R}^2} \rho(k|\boldsymbol{q}-\boldsymbol{q}(s)|)Y_0(k|\boldsymbol{q}-\boldsymbol{q}(s)|)Y_0(k|\boldsymbol{q}-\boldsymbol{q}(s')+\delta\boldsymbol{x}|)\,\mathrm{d}q \\ &= \frac{1}{16}\int_{\mathbb{R}^2} \rho(k|\boldsymbol{q}|)Y_0(k|\boldsymbol{q}|)Y_0(k|\boldsymbol{q}+\boldsymbol{q}(s)-\boldsymbol{q}(s')+\delta\boldsymbol{x}|)\,\mathrm{d}q. \end{aligned} \tag{66}$$

Due to the factor $\rho(k|\boldsymbol{q}-\boldsymbol{q}(s)|)$ this integral is absolutely convergent. We now use Grafs addition theorem [45]

$$Y_0(k|\boldsymbol{q}+\Delta\boldsymbol{q}|) = \begin{cases}\sum_{l\in\mathbb{Z}} Y_l(k|\Delta\boldsymbol{q}|)J_l(k|\boldsymbol{q}|)\cos(l\varphi) & \text{for} \quad |\boldsymbol{q}| < |\Delta\boldsymbol{q}| \\ \sum_{l\in\mathbb{Z}} Y_l(k|\boldsymbol{q}|)J_l(k|\Delta\boldsymbol{q}|)\cos(l\varphi) & \text{for} \quad |\boldsymbol{q}| > |\Delta\boldsymbol{q}|\end{cases} \tag{67}$$

where $\Delta\boldsymbol{q} = \boldsymbol{q}(s) - \boldsymbol{q}(s') + \delta\boldsymbol{x}$ and φ is the angle between $\Delta\boldsymbol{q}$ and $\boldsymbol{q}$. Introducing polar coordinates in the integral in (66) and using (67) gives

$$K_\rho(\delta\boldsymbol{x}, s, s') = \frac{\pi}{8}\int_0^{|\Delta\boldsymbol{q}|} Y_0(kr)J_0(kr)r\,\mathrm{d}r\; Y_0(k|\Delta\boldsymbol{q}|) + \frac{\pi}{8}\int_{|\Delta\boldsymbol{q}|}^{\infty} \rho(kr)Y_0(kr)Y_0(kr)r\;\mathrm{d}r\; J_0(k|\Delta\boldsymbol{q}|) \tag{68}$$

where we have furthermore used that $\rho(r) = 1$ for $r \leqslant |\Delta\boldsymbol{q}|$ by (63). The first integral is

$$\int_0^{|\Delta\boldsymbol{q}|} Y_0(kr)J_0(kr)r\;\mathrm{d}r = \frac{|\Delta\boldsymbol{q}|^2}{2}[Y_0(k|\Delta\boldsymbol{q}|)J_0(k|\Delta\boldsymbol{q}|) + Y_1(k|\Delta\boldsymbol{q}|)J_1(k|\Delta\boldsymbol{q}|)] \tag{69}$$

see, e.g. [45], and for the second one partial integration gives

$$\int_{|\Delta\boldsymbol{q}|}^{\infty} \rho(kr)Y_0(kr)Y_0(kr)r\;\mathrm{d}r = -\frac{|\Delta\boldsymbol{q}|^2}{2}[Y_0(k|\Delta\boldsymbol{q}|)Y_0(k|\Delta\boldsymbol{q}|) + Y_1(k|\Delta\boldsymbol{q}|)Y_1(k|\Delta\boldsymbol{q}|)] - \frac{k}{2}\int_{|\Delta\boldsymbol{q}|}^{\infty} \rho'(kr)[Y_0(kr)Y_0(kr) + Y_1(kr)Y_1(kr)]r^2\;\mathrm{d}r. \tag{70}$$

Note that since ρ' has compact support the second integral is over a finite interval, and for $s, s' \in \partial\Omega$, $\delta\boldsymbol{x} \in \Omega$ the lower limit of the integral, $|\Delta\boldsymbol{q}|$, is outside the support of ρ', hence the second term on the right-hand side of equation (70) is constant. So we get

$$K_\rho(\delta\boldsymbol{x}, s, s') = K(\delta\boldsymbol{x}, s, s') + R_\rho(\delta\boldsymbol{x}, s, s') \tag{71}$$

with

$$K(\delta\boldsymbol{x}, s, s') = \frac{\pi|\Delta\boldsymbol{q}|^2}{16}[Y_1(k|\Delta\boldsymbol{q}|)J_1(k|\Delta\boldsymbol{q}|)Y_0(k|\Delta\boldsymbol{q}|) - Y_1(k|\Delta\boldsymbol{q}|)Y_1(k|\Delta\boldsymbol{q}|)J_0(k|\Delta\boldsymbol{q}|)] \tag{72}$$

and

$$R_\rho(\delta\boldsymbol{x}, s, s') = C\,J_0(k|\Delta\boldsymbol{q}|) \tag{73}$$

with C constant and by (62) this term gives no contribution to $C(\delta\boldsymbol{x})$. Using a Wronsky determinant of Bessel functions [45] we can simplify $K(\delta\boldsymbol{x}, s, s')$ further

$$K(\delta\boldsymbol{x}, s, s') = \frac{\pi|\Delta\boldsymbol{q}|^2}{16}Y_1(k|\Delta\boldsymbol{q}|)[J_1(k|\Delta\boldsymbol{q}|)Y_0(k|\Delta\boldsymbol{q}|) - Y_1(k|\Delta\boldsymbol{q}|)J_0(k|\Delta\boldsymbol{q}|)] = \frac{\pi|\Delta\boldsymbol{q}|^2}{16}Y_1(k|\Delta\boldsymbol{q}|)\frac{2}{\pi k|\Delta\boldsymbol{q}|} = \frac{|\Delta\boldsymbol{q}|}{8k}Y_1(k|\Delta\boldsymbol{q}|) \tag{74}$$

which gives the final result.

Appendix B. Remainder estimate

In this appendix we sketch the derivation of the remainder estimate in equation (19). We start by representing the integral as an expectation value, see (24)

$$\int_0^\infty\int_0^{2\pi}\int_\Omega \rho(\boldsymbol{x}-\boldsymbol{q})W(\boldsymbol{p},\boldsymbol{q})\;\mathrm{d}q'\,\mathrm{e}^{\mathrm{i}r|\delta\boldsymbol{x}|\cos(\varphi-\theta)/\sqrt{E}}\,r\;\mathrm{d}\varphi\,\mathrm{d}r = \langle\psi, A\psi\rangle \tag{75}$$

where A is the Weyl quantization of the symbol

$$a(\boldsymbol{p},\boldsymbol{q}) := \rho(\boldsymbol{x}-\boldsymbol{q})\,\mathrm{e}^{\mathrm{i}\frac{|\boldsymbol{p}|}{\sqrt{E}}|\delta\boldsymbol{x}|\cos(\varphi-\theta)}. \tag{76}$$

The basic idea is to find a decomposition of the operator A

$$A = A_0 + (\sqrt{-\Delta} - \sqrt{E})A_1 + R \tag{77}$$

where A_0 has the Weyl symbol

$$a_0(\boldsymbol{p},\boldsymbol{q}) = \rho(\boldsymbol{x}-\boldsymbol{q})\,\mathrm{e}^{\mathrm{i}|\delta\boldsymbol{x}|\cos(\varphi-\theta)} \tag{78}$$

and the remainder R satisfies

$$\|R\| \leqslant C\,E^{-1/2}. \tag{79}$$

If we assume the decomposition (77) and take the expectation value of both sides, one gets

$$\langle\psi, A\psi\rangle = \langle\psi, A_0\psi\rangle + \langle\psi, R\psi\rangle \tag{80}$$

where $(\sqrt{-\Delta}-\sqrt{E})\psi = 0$ has been used. In terms of the symbols equation (80) is the desired result, see (19)

$$\int_0^\infty\int_0^{2\pi}\int_\Omega W(\boldsymbol{p},\boldsymbol{q})\rho(\boldsymbol{x}-\boldsymbol{q})\,\mathrm{d}q'\,\mathrm{e}^{\mathrm{i}r|\delta\boldsymbol{x}|\cos(\varphi-\theta)/\sqrt{E}}\,r\,\mathrm{d}\varphi\,\mathrm{d}r$$
$$= \int_0^\infty\int_0^{2\pi}\int_\Omega W(\boldsymbol{p},\boldsymbol{q})\rho(\boldsymbol{x}-\boldsymbol{q})\,\mathrm{d}q'\,\mathrm{e}^{\mathrm{i}|\delta\boldsymbol{x}|\cos(\varphi-\theta)/}\,r\,\mathrm{d}\varphi\,\mathrm{d}r + O(rE^{-1/2}). \tag{81}$$

Let us now show that the decomposition (77) is basically a quantization of the Taylor expansion of the symbol $a(\boldsymbol{p},\boldsymbol{q})$ around $|\boldsymbol{p}| = \sqrt{E}$,

$$a(\boldsymbol{p},\boldsymbol{q}) = a_0(\boldsymbol{p},\boldsymbol{q}) + (|\boldsymbol{p}|-\sqrt{E})a_1(\boldsymbol{p},\boldsymbol{q}). \tag{82}$$

Quantizing this classical decomposition yields (77) with R given as the Weyl quantization of

$$r(\boldsymbol{p},\boldsymbol{q}) = (|\boldsymbol{p}|-\sqrt{E})a_1(\boldsymbol{p},\boldsymbol{q}) - (|\boldsymbol{p}|-\sqrt{E})\#a_1(\boldsymbol{p},\boldsymbol{q}) \tag{83}$$

since the Weyl symbol of $(\sqrt{-\Delta}-\sqrt{E})A_1$ is $(|\boldsymbol{p}|-\sqrt{E})\#a_1(\boldsymbol{p},\boldsymbol{q})$ with # denoting the symbol product (see e.g. [46]). Since E is a constant we have

$$r(\boldsymbol{p},\boldsymbol{q}) = |\boldsymbol{p}|a_1(\boldsymbol{p},\boldsymbol{q}) - |\boldsymbol{p}|\#a_1(\boldsymbol{p},\boldsymbol{q}) \tag{84}$$

and this is a function which is bounded and of order $O(|\delta\boldsymbol{x}|E^{-1/2})$, and all its derivatives are bounded and of order $O(|\delta\boldsymbol{x}|E^{-1/2})$, too. So by the Calderon Vallaincourt theorem [46] the estimate (79) follows.

Appendix C. Estimating the Bessel sum

In this appendix we determine how many terms in the sum (28) have to be taken into account such that the remainder is smaller than some given error δ. From (26) and (27) it follows that for fixed ψ

$$|\langle\psi, \hat{A}_{2l}(\boldsymbol{x})\psi\rangle\cos(2l\theta) + \langle\psi, \hat{B}_{2l}(\boldsymbol{x})\psi\rangle\sin(2l\theta)| \leqslant C. \tag{85}$$

Thus if we split the sum

$$\sum_{l=1}^{\infty}(-1)^l[\langle\psi, \hat{A}_{2l}(\boldsymbol{x})\psi\rangle\cos(2l\theta) + \langle\psi, \hat{B}_{2l}(\boldsymbol{x})\psi\rangle\sin(2l\theta)]\,J_{2l}(|\delta\boldsymbol{x}|)$$
$$= \sum_{l=1}^{m-1}(-1)^l[\langle\psi, \hat{A}_{2l}(\boldsymbol{x})\psi\rangle\cos(2l\theta) + \langle\psi, \hat{B}_{2l}(\boldsymbol{x})\psi\rangle\sin(2l\theta)]\,J_{2l}(|\delta\boldsymbol{x}|) + R_m(|\delta\boldsymbol{x}|) \tag{86}$$

we get for the remainder

$$|R_m(r)| \leqslant C\sum_{l=m}^{\infty}|J_{2l}(r)|. \tag{87}$$

Therefore we have to estimate the sum over Bessel functions

$$\sum_{l=m}^{\infty} |J_{2l}(r)| \tag{88}$$

and determine its dependence on m and r. The asymptotics in the transition region

$$J_{2l}(2l - z(2l)^{1/3}) \sim \frac{1}{l^{1/3}} \operatorname{Ai}(2^{1/3}z) \tag{89}$$

gives that $J_{2l}(r)$ is monotonically increasing for $r < 2l$, such that for $r < 2m$

$$\sum_{l=m}^{\infty} |J_{2l}(r)| = \sum_{l=m}^{\infty} \frac{1}{l^{1/3}} \operatorname{Ai}\left(\frac{2l - r}{l^{1/3}}\right) + O(m^{-1}). \tag{90}$$

Defining z by

$$r = 2m - zm^{1/3} \tag{91}$$

we obtain

$$\begin{aligned}\sum_{l=m}^{\infty} \frac{1}{l^{1/3}} \operatorname{Ai}\left(\frac{2l - r}{l^{1/3}}\right) &= \sum_{l=m}^{\infty} \frac{1}{l^{1/3}} \operatorname{Ai}\left(\frac{2(l-m)}{l^{1/3}} + z\left(\frac{m}{l}\right)^{1/3}\right) \\ &= \sum_{l=0}^{\infty} \frac{1}{(l+m)^{1/3}} \operatorname{Ai}\left(\frac{2l}{(l+m)^{1/3}} + z\left(\frac{m}{l+m}\right)^{1/3}\right) \\ &= \sum_{l=0}^{\infty} \frac{1}{m^{1/3}} \operatorname{Ai}\left(\frac{2l}{m^{1/3}} + z\right) + O(m^{-1/3})\end{aligned} \tag{92}$$

where we have furthermore used that for large m only the terms with $l \ll m$ contribute, because the Airy function is exponentially decreasing for positive arguments. The Euler McLaurin formula then gives

$$\begin{aligned}\sum_{l=0}^{\infty} \frac{1}{m^{1/3}} \operatorname{Ai}\left(\frac{2l}{m^{1/3}} + z\right) &= \int_0^{\infty} \frac{1}{m^{1/3}} \operatorname{Ai}\left(\frac{2l}{m^{1/3}} + z\right) \mathrm{d}l + O(m^{-1/3}) \\ &= \frac{1}{2} \int_z^{\infty} \operatorname{Ai}(x)\, \mathrm{d}x + O(m^{-1/3}).\end{aligned} \tag{93}$$

And so finally we arrive at

$$\sum_{l=m}^{\infty} |J_{2l}(r)| = \frac{1}{2} \int_z^{\infty} \operatorname{Ai}(x)\, \mathrm{d}x + O(m^{-1/3}). \tag{94}$$

The function $\int_z^{\infty} \operatorname{Ai}(x)\, \mathrm{d}x$ is monotonically decreasing, so for a given $\delta > 0$ we can define a $z(\delta)$ by

$$\frac{1}{2} \int_{z(\delta)}^{\infty} \operatorname{Ai}(x)\, \mathrm{d}x = \delta \tag{95}$$

and then (91) defines together with (95) a function $m(r, \delta)$ such that

$$\sum_{l=[m(r,\delta)+1]}^{\infty} |J_{2l}(r)| = \delta + O(r^{-1/3}). \tag{96}$$

By solving (91) for large r, we see that we have to take approximately

$$m(r, \delta) \sim \frac{r}{2} + \frac{z}{2}\left(\frac{r}{2}\right)^{1/3} \tag{97}$$

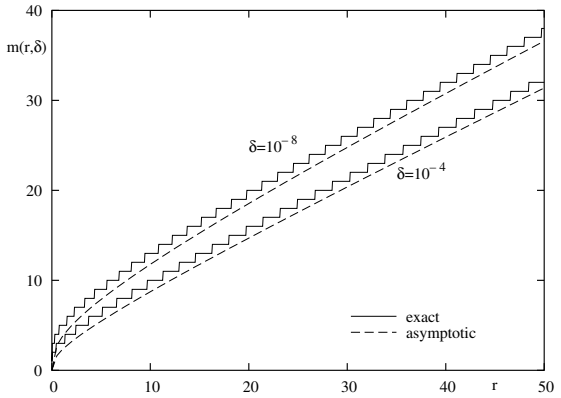

Figure 12. For the bounds $\delta = 10^{-4}$ and $\delta = 10^{-8}$ of the sum over Bessel functions (88) the result of the exact computation of $m(r, \delta)$ (full curves) and the asymptotic result (97) are compared. The asymptotic result approaches the exact one slowly from below with a rate $O(r^{-1/3})$.

terms in the sum (28) over l into account such that the error is $\delta + O(r^{-1/3})$.

For instance, if we require $\delta = 10^{-4}$, then (95) gives $z(\delta) = 4.359\ldots$; for $\delta = 10^{-8}$ one gets $z(\delta) = 7.925\ldots$. In figure 12 we show for these choices of z the asymptotic result (97) compared to the exact computation, corresponding to (88). The asymptotic result approaches the exact one slowly from below; in the plotted region a constant offset by two compared to (97) gives a good bound for $m(r, \delta)$.

References

[1] Berry M V 1977 Regular and irregular semiclassical wavefunctions *J. Phys. A: Math. Gen.* **10** 2083
[2] McDonald S W and Kaufmann A N 1988 Wave chaos in the stadium: statistical properties of short-wave solutions of the Helmholtz equation *Phys. Rev.* A **37** 3067
[3] Aurich R and Steiner F 1993 Statistical properties of highly excited quantum eigenstates of a strongly chaotic system *Physica* D **64** 185
[4] Li B and Robnik M 1994 Statistical properties of high-lying chaotic eigenstates *J. Phys. A: Math. Gen.* **27** 5509
[5] Robert D 1998 Semi-classical approximation in quantum mechanics. A survey of old and recent mathematical results *Helv. Phys. Acta* **71** 44
[6] Shnirelman A I 1974 Ergodic properties of eigenfunctions *Usp. Math. Nauk* **29** 181 (in Russian)
[7] Zelditch S 1987 Uniform distribution of eigenfunctions on compact hyperbolic surfaces *Duke. Math. J.* **55** 919
[8] Colin de Verdiére Y 1985 Ergodicité et fonctions propres du laplacien *Commun. Math. Phys.* **102** 497 (in French)
[9] Helffer B, Martinez A and Robert D 1987 Ergodicité et limite semi-classique *Commun. Math. Phys.* **109** 313 (in French)
[10] Gérard P and Leichtnam E 1993 Ergodic properties of eigenfunctions for the Dirichlet problem *Duke Math. J.* **71** 559
[11] Zelditch S and Zworski M 1996 Ergodicity of eigenfunctions for ergodic billiards *Commun. Math. Phys.* **175** 673
[12] Bäcker A, Schubert R and Stifter P 1998 Rate of quantum ergodicity in Euclidean billiards *Phys. Rev.* E **57** 5425
Bäcker A, Schubert R and Stifter P 1998 *Phys. Rev.* E **58** 5192 (erratum)
[13] Voros A 1976 Semi–classical approximations *Ann. Inst. H Poincaré* A **24** 31
[14] Voros A 1977 Asymptotic $\hbar$–expansions of stationary quantum states *Ann. Inst. H Poincaré* A **26** 343
[15] Berry M V 1983 Semiclassical mechanics of regular and irregular motion *Comportement Chaotique des Systémes Déterministes—Chaotic Behaviour of Deterministic Systems* ed G Iooss, R H G Hellemann and R Stora (Amsterdam: North-Holland) pp 171–271
[16] Srednicki M and Stiernelof F 1996 Gaussian fluctuations in chaotic eigenstates *J. Phys. A: Math. Gen.* **29** 5817

[17] Srednicki M 1996 Gaussian random eigenfunctions and spatial correlations in quantum dots *Phys. Rev.* E **54** 954
[18] Hortikar S and Srednicki M 1998 Correlations in chaotic eigenfunctions at large separation *Phys. Rev. Lett.* **80** 1646
[19] Hortikar S and Srednicki M 1998 Random matrix elements and eigenfunctions in chaotic systems *Phys. Rev.* E **57** 7313
[20] Gornyi I V and Mirlin A D 2001 Wave function correlations on the ballistic scale: Exploring quantum chaos by quantum disorder *Preprint* cond-mat/0105103
[21] Li B and Rouben D C 2001 Correlations of chaotic eigenfunctions: a semiclassical analysis *J. Phys. A: Math. Gen.* **34** 7381
[22] Toscano F and Lewenkopf C H 2001 Semiclassical spatial correlations in chaotic wave functions *Preprint* nlin.CD/0108032
[23] Shapiro M and Goelman G 1984 Onset of chaos in an isolated energy eigenstate *Phys. Rev. Lett.* **53** 1714
[24] Shapiro M, Ronkin J and Brumer P 1988 Scaling laws and correlation length of quantum and classical ergodic states *Chem. Phys. Lett.* **148** 177
[25] Veble G, Robnik M and Liu J 1999 Study of regular and irregular states in generic systems *J. Phys. A: Math. Gen.* **32** 6423
[26] Schubert R 2001 Semiclassical localization in phase space *PhD Thesis* Abteilung Theoretische Physik, Universität Ulm
[27] Bunimovich L A 1974 On ergodic properties of certain billiards *Funct. Anal. Appl.* **8** 254
[28] Bunimovich L A 1979 On the ergodic properties of nowhere dispersing billiards *Commun. Math. Phys.* **65** 295
[29] Robnik M 1983 Classical dynamics of a family of billiards with analytic boundaries *J. Phys. A: Math. Gen.* **16** 3971
[30] Robnik M 1984 Quantising a generic family of billiards with analytic boundaries *J. Phys. A: Math. Gen.* **17** 1049
[31] Wojtkowski M 1986 Principles for the design of billiards with nonvanishing Lyapunov exponents *Commun. Math. Phys.* **105** 391
[32] Szász D 1992 On the K-property of some planar hyperbolic billiards *Commun. Math. Phys.* **145** 595
[33] Markarian R 1993 New ergodic billiards: exact results *Nonlinearity* **6** 819
[34] Prosen T and Robnik M Private communication
[35] Prosen T and Robnik M 1993 Energy level statistics in the transition region between integrability and chaos *J. Phys. A: Math. Gen.* **26** 2371
[36] Riddel R J Jr 1979 Boundary-distribution solution of the Helmholtz equation for a region with corners *J. Comput. Phys.* **31** 21
[37] Berry M V and Wilkinson M 1984 Diabolical points in the spectra of triangles *Proc. R. Soc.* A **392** 15
[38] Bäcker A 1998 Classical and quantum chaos in billiards *PhD Thesis* Abteilung Theoretische Physik, Universität Ulm
[39] Vergini E and Saraceno M 1995 Calculation of highly excited states of billiards *Phys. Rev.* E **52** 2204
[40] Heller E J 1984 Bound-state eigenfunctions of classically chaotic Hamiltonian systems: scars of periodic orbits *Phys. Rev. Lett.* **53** 1515
[41] Bai Y Y, Hose G, Stefański K and Taylor H S 1985 Born–Oppenheimer adiabatic mechanism for regularity of states in the quantum stadium billiard *Phys. Rev.* A **31** 2821
[42] O'Connor P W and Heller E J 1988 Quantum localization for a strongly classically chaotic system *Phys. Rev. Lett.* **61** 2288
[43] Tanner G 1997 How chaotic is the stadium billiard? A semiclassical analysis *J. Phys. A: Math. Gen.* **30** 2863
[44] Bäcker A, Schubert R and Stifter P 1997 On the number of bouncing-ball modes in billiards *J. Phys. A: Math. Gen.* **30** 6783
[45] Abramowitz M and Stegun I A (eds) 1984 *Pocketbook of Mathematical Functions* (Thun–Frankfurt/Main: Deutsch) abridged edition
[46] Folland G B 1989 *Harmonic Analysis in Phase Space (Annals of Mathematics Studies vol 122)* (Princeton: Princeton University Press)
[47] Zyczkowski K 1992 Classical and quantum billiards, integrable, nonintegrable, and pseudo-integrable *Acta Phys. Pol.* B **23** 245
[48] Bäcker A and Schubert R 1999 Chaotic eigenfunctions in momentum space *J. Phys. A: Math. Gen.* **32** 4795
[49] Tualle J M and Voros A 1995 Normal modes of billiards portrayed in the stellar (or nodal) representation, *Chaos, Solitons Fractals* **5** 1085
[50] Simonotti F P, Vergini E and Saraceno M 1997 Quantitative study of scars in the boundary section of the stadium billiard *Phys. Rev.* E **56** 3859

[51] Bäcker A and Schubert R 2002 Amplitude distribution of eigenfunctions in mixed systems *J. Phys. A: Math. Gen.* **35** 527 (preceding paper) (nlin.CD/0106017)
[52] Percival I C 1973 Regular and irregular spectra *J. Phys. B: At. Mol. Phys.* **6** L229
[53] Bohigas O, Tomsovic S and Ullmo D 1990 Dynamical quasidegeneracies and separation of regular and irregular quantum levels *Phys. Rev. Lett.* **64** 1479
[54] Prosen T and Robnik M 1993 Survey of the eigenfunctions of a billiard system between integrability and chaos *J. Phys. A: Math. Gen.* **26** 5365
[55] Li B and Robnik M 1995 Separating the regular and irregular energy levels and their statistics in a Hamiltonian system with mixed classical dynamics *J. Phys. A: Math. Gen.* **28** 4843
[56] Li B and Robnik M 1995 Geometry of high-lying eigenfunctions in a plane billiard system having mixed-type classical dynamics *J. Phys. A: Math. Gen.* **28** 2799
[57] Carlo G, Vergini E and Fendrik A 1998 Numerical verification of Percival's conjecture in a quantum billiard *Phys. Rev.* E **57** 5397 (chao-dyn/9804016)
[58] Eckhardt B, Fishman S, Keating J, Agam O, Main J and Müller K 1995 Approach to ergodicity in quantum wave functions *Phys. Rev.* E **52** 5893

[A3] Isolated resonances in conductance fluctuations and hierarchical states

A. Bäcker, A. Manze, B. Huckestein, and R. Ketzmerick

Phys. Rev. E **66** (2002) 016211 (8 pages).

We study the isolated resonances occurring in conductance fluctuations of quantum systems with a classically mixed phase space. We demonstrate that the isolated resonances and the resonant scattering states can be associated to eigenstates of the closed system. They can all be categorized as hierarchical or regular, depending on where the corresponding eigenstates live in the classical phase space.

PHYSICAL REVIEW E **66**, 016211 (2002)

Isolated resonances in conductance fluctuations and hierarchical states

Arnd Bäcker,[1,2] Achim Manze,[3] Bodo Huckestein,[3] and Roland Ketzmerick[4]
[1]*School of Mathematics, University of Bristol, University Walk, Bristol BS8 1TW, United Kingdom and BRIMS, Hewlett-Packard Laboratories, Filton Road, Bristol BS12 6QZ, United Kingdom*
[2]*Abteilung Theoretische Physik, Universität Ulm, Albert-Einstein-Allee 11, D-89081 Ulm, Germany*
[3]*Institut für Theoretische Physik III, Ruhr-Universität Bochum, D-44780 Bochum, Germany*
[4]*Max-Planck-Institut für Strömungsforschung and Institut für Nichtlineare Dynamik der Universität Göttingen, Bunsenstraße 10, D-37073 Göttingen, Germany*
(Received 29 January 2002; published 22 July 2002)

We study the isolated resonances occurring in conductance fluctuations of quantum systems with a classically mixed phase space. We demonstrate that the isolated resonances and their scattering states can be associated with eigenstates of the closed system. They can all be categorized as hierarchical or regular, depending on where the corresponding eigenstates are concentrated in the classical phase space.

DOI: 10.1103/PhysRevE.66.016211 PACS number(s): 05.45.Mt, 03.65.Sq, 72.20.Dp

I. INTRODUCTION

The classical dynamics of a scattering system is reflected in the transport properties of its quantum mechanical analog. A prominent example in quantum chaos is the universal conductance fluctuations exhibited by a scattering system with classically completely chaotic dynamics [1]. Generic systems, however, are neither completely chaotic nor integrable, but show chaotic as well as regular motion [2]. The chaotic dynamics is strongly influenced by the presence of islands of regular motion; in particular, one finds a trapping of chaotic trajectories close to regular regions with trapping times distributed according to power laws [3]. A semiclassical analysis revealed that conductance fluctuations of generic scattering systems have corresponding power-law correlations [4,5] and most interestingly that the graph of conductance vs control parameter is a fractal [5]. Fractal conductance fluctuations have indeed been observed experimentally in semiconductor nanostructures [6,7], as well as numerically [8].

Surprisingly, for the cosine billiard [9,10], a system with a mixed phase space and power-law distributed classical trapping times, a recent numerical study did not show fractal conductance fluctuations [11]. Instead, sharp isolated resonances were found with a width distribution covering several orders of magnitude. Only about one-third of them can be related to quantum tunneling into the islands of regular motion [12], while the rest remained unexplained. It was later shown that conductance fluctuations for mixed systems should in general show fractal fluctuations on large scales and isolated resonances on smaller scales [13]. The isolated resonances in the scattering system were conjectured to be related to a subset of eigenstates of the closed system, namely, hierarchical states [14] concentrating in the chaotic component close to the regular regions and regular states concentrating within the islands of regular motion [12]. This type of behavior was obtained for a quantum graph that modeled relevant features of a mixed phase space [13].

The purpose of the present paper is to establish the origin of all isolated resonances for a system with a mixed phase space. To this end, we study the cosine billiard for suitable parameters in a threefold way: (i) as a quantum scattering system, (ii) as a closed quantum system, and (iii) its classical phase-space structures. We find that the resonances have scattering states and corresponding eigenstates of the closed system that are concentrated in the hierarchical and regular parts of phase space. The number of resonances of each type is directly related to the corresponding volumes in the classical phase space. Each resonance width is quite well described by the strength of the corresponding eigenfunction at the billiard boundary. Exceptions are shown to arise from the presence of avoided crossings in the closed system. It is demonstrated that the simultaneous appearance of fractal conductance fluctuations and isolated resonances, as observed in a quantum graph model [13], would for our system with a mixed phase space require much higher energies. These are currently computationally inaccessible.

In the following section, we define the model we use to study the relation between the scattering resonances and the eigenstates of the corresponding closed system. Our main results for the classification of resonant scattering states and corresponding eigenstates of the closed system into hierarchical and regular are presented in Secs. III and IV. The role of partial transport barriers is analyzed in Sec. V. In Sec. VI we discuss the effect of avoided crossings on the assignment of resonances of the open billiard to eigenstates of the closed system and Sec. VII gives a summary of the results. Finally, the Appendix contains some details of the numerical methods employed in the present work.

II. THE MODEL

We study the cosine billiard [9,10], either closed or with semi-infinite leads attached. The boundaries of the billiard are hard walls (i.e., Dirichlet boundary conditions) at $y=0$ and

$$y(x)=W+\frac{M}{2}\left[1-\cos\left(\frac{2\pi x}{L}\right)\right] \tag{1}$$

for $0\leqslant x\leqslant L$ [see Fig. 1(a)]. In the open billiard two semi-infinite leads of width W are attached at the openings at $x=0$ and $x=L$, while in the closed billiard the openings are

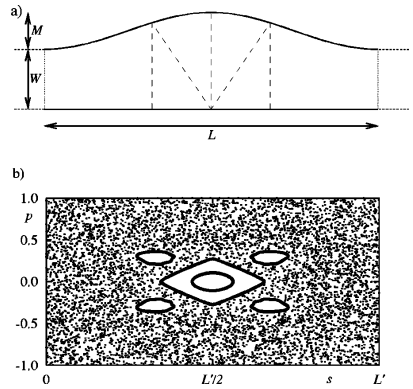

FIG. 1. (a) The cosine billiard with semi-infinite leads (short dashed lines) and hard walls for closing the system (dotted lines) for $W/L=0.18$ and $M/L=0.11$. Also shown are the two most prominent stable periodic orbits for these parameters (long dashed lines). (b) Poincaré section of some regular and one chaotic orbit for the above parameters in Poincaré-Birkhoff coordinates p vs arclength s along the upper boundary of the billiard. A major island at $(s,p)=(L'/2,0)$ around the elliptic I-shaped orbit and four smaller islands surrounding the M-shaped orbit can be seen.

closed by hard walls. The classical phase-space structure can be changed by varying the ratios W/L and M/L. For $M/L=0$ the dynamics is integrable and, for example, for $M/L=1/2$ and $W/L=1$ the dynamics appears to be ergodic (at least the islands of regular motion, if any, are very small) [9].

In the present work, we use the same parameters as in Ref. [11], namely, $W/L=0.18$ and $M/L=0.11$, for which the I- and M-shaped orbits depicted in Fig. 1(a) are stable. The corresponding Poincaré section is shown in Fig. 1(b). We use Poincaré-Birkhoff coordinates (s,p), where s is the arclength along the upper boundary of the billiard with length $L'\approx 1.029\,L$ and p is the projection of the unit momentum vector after reflection on the tangent at the point s.

Quantum mechanically, for a given wave number k_F the number N of transmitting modes in a lead of width W is the largest integer with $N\leqslant k_F W/\pi$. We measure energies in units of the energy $E_0=\hbar^2\pi^2/(2mW^2)$ of the lowest mode in such a lead, i.e., $E=\hbar^2k_F^2/(2mE_0)=(k_FW/\pi)^2\geqslant N^2$. The larger the number N of modes is, the more details of the classical phase space can be resolved by quantum mechanics. At the same time the computational effort increases as N^4 and we compromise, as in Ref. [11], on the case of $N=45$ transmitting modes in the energy range $E\in[2026,2100]$.

III. RESONANCES AND SCATTERING STATES

Resonances in the scattering system, which have been observed as isolated features in conductance fluctuations [11], were identified by isolated peaks in the Wigner-Smith time delay τ of the system. The time delay is given by

$$\tau=\frac{-i\hbar}{2N}\mathrm{Tr}(S^{\dagger}dS/dE), \tag{2}$$

where $2N$ is the dimension of the S matrix. The calculation of S and τ was already outlined in Ref. [11] and is presented in greater detail in the Appendix.

In Fig. 2 we show the Wigner-Smith time delay τ [in units of $\hbar/E_0=2mW^2/(\hbar\pi^2)$] for $E\in[2026,2100]$. The isolated resonances found in Ref. [11] are clearly seen. Each isolated resonance $E_{\mathrm{res},i}$ has a Breit-Wigner shape

$$\tau_i(E)=\tau_i\frac{\Gamma_i^2/4}{(E-E_{\mathrm{res},i})^2+\Gamma_i^2/4}, \tag{3}$$

with $\tau_i\Gamma_i=2/N$. Note that the heights τ_i and the corresponding widths Γ_i of the individual resonances cover several orders of magnitude.

In order to elucidate the nature of the resonances, we calculated the scattering states inside the open billiard. For a given configuration of waves incoming in both leads, knowledge of the S matrix allows the determination of the outgoing waves and hence the wave function amplitudes at the openings of the billiard. Since the S matrix is defined between asymptotic, propagating modes, this procedure neglects the contribution of evanescent modes in the leads in the vicinity of the billiard. The wave function amplitudes at the openings can then be used as boundary conditions for the solution of the Schrödinger equation inside the billiard. For the examples of scattering states presented below, we occupied the

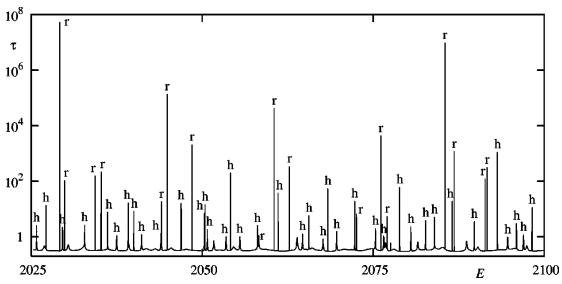

FIG. 2. Wigner-Smith delay time τ vs energy E. For each resonance a corresponding eigenstate of the closed system was found and the labels indicate whether it is concentrated in the regular (r) or hierarchical (h) region of phase space.

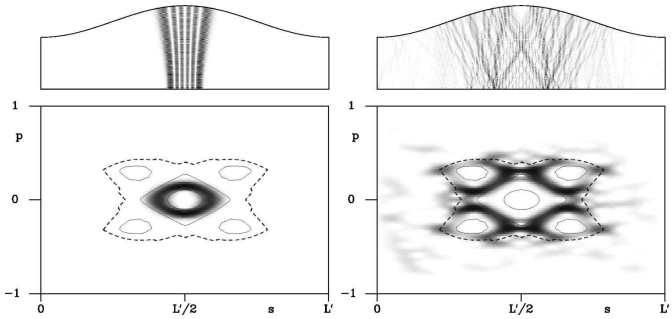

FIG. 3. Resonant scattering states (top row) and Husimi projections (bottom row) onto the classical Poincaré section with KAM tori (solid lines) and a partial transport barrier (dashed line). Two examples at resonance energies 2029.172 (left) and 2041.109 (right) are shown. They are concentrated in the regular and the hierarchical region of phase space, respectively. For the representation of the scattering states a superposition with equal weight's of the ten topmost modes incoming from the left is shown.

ten topmost modes incoming from the left with equal amplitudes. Similar pictures were obtained for other boundary conditions.

For the comparison of the scattering states with the classical phase-space structures we have calculated Husimi projections $H^{\mathrm{sc}}(s,p)$. Similar to the case of closed billiards (see Sec. IV), we define these by the projection of the scattering state onto a coherent state on the upper boundary of the billiard,

$$H^{\mathrm{sc}}(s,p)=\left|\langle \partial_{\mathbf{n}}\psi|\phi_{\gamma}^{\mathrm{coherent}}(s,p)\rangle\right|^2 \tag{4}$$

$$=\left|\int_0^{L'} ds'\,\partial_{\mathbf{n}}\psi^*(s')e^{ikp(s'-s)-(1/2)k(s'-s)^2}\right|^2, \tag{5}$$

with $k=\sqrt{E}\pi/W$. Here $\partial_{\mathbf{n}}\psi(s)=\mathbf{n}(s)\cdot\nabla\psi(\mathbf{q}(s))$ is the normal derivative of the scattering state on the upper boundary. $\mathbf{n}(s)$ is the normal vector and $\mathbf{q}(s)$ is the position of the boundary as a function of arclength s. Note that these Husimi projections are not normalized and are influenced by the openings over a range of a few Fermi wavelengths. Also, they do not include the full billiard boundary and therefore no periodization of the coherent state has been used.

As a first example, we present in Fig. 3 on the left the scattering state at an energy of approximately 2029.172, the center energy of the sharpest observed resonance. Obviously, the scattering state is associated with the I-shaped periodic orbit. The wave function amplitude is concentrated near the orbit and the Husimi projection concentrates predominantly inside the central stable island of the classical phase space. For comparison, we present in Fig. 3 on the right the scattering state at energy 2041.109. The width of the resonance at this energy is about 6×10^7 times larger than the width of the sharpest resonance. Evidently, this resonance is not related to the stable islands in phase space. In contrast, by comparing with the superimposed Kolmogorov-Arnold-Moser (KAM) tori of the Poincaré section and a partial transport barrier surrounding the island hierarchy (see Sec. V), we see that the Husimi projection is concentrated in the hierarchical region between the islands and a partial transport barrier.

As scattering states allow a great variability in the boundary conditions, e.g., the incoming modes, we do not use them for a detailed analysis of the isolated resonances. Instead we

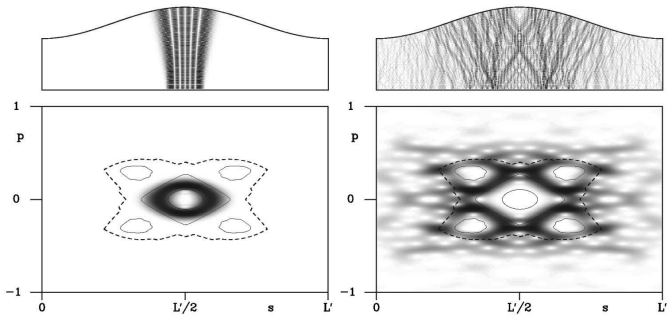

FIG. 4. Eigenfunctions (top row) and Husimi representations (bottom row) of a regular state (5686^-, left) and a hierarchical state (5720^-, right) corresponding to the scattering states of Fig. 3.

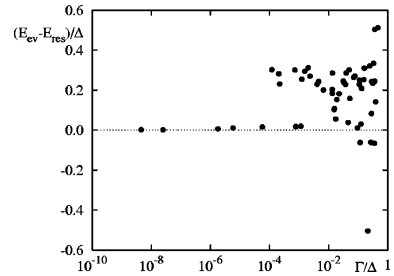

FIG. 5. Difference of eigenstate energy E_{ev} and resonance energy E_{res} in units of the mean level spacing Δ vs Γ/Δ. The deviations increase with Γ.

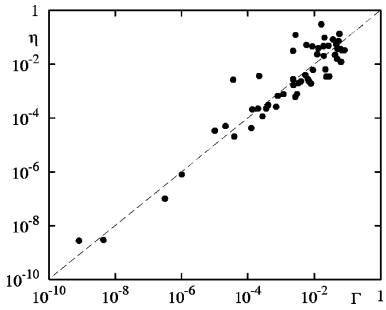

FIG. 6. The strength η of an eigenstate at the left boundary vs the resonance width Γ of the corresponding resonance. An approximate proportionality can be seen.

consider the corresponding eigenstates of the closed system in the next section.

IV. RESONANCES AND CORRESPONDING EIGENSTATES

In this section we want to demonstrate that the isolated resonances of the conductance fluctuations and their scattering states have corresponding eigenstates of the closed billiard. In particular, we will show that *all* these eigenstates are concentrated in the hierarchical and regular part of phase space, as was conjectured in Ref. [13]. This allows a labeling of all isolated resonances appearing in Fig. 2.

For the closed system the eigenvalues and eigenfunctions are computed using the boundary element method; see, e.g., [15] and references therein. Since the cosine billiard is symmetric with respect to the axis $x=L/2$, the eigenstates have definite parity $P=+,-$. The actual calculations are performed for the desymmetrized billiard with either Dirichlet or Neumann boundary conditions on the symmetry axis yielding the antisymmetric ($P=-$) and symmetric ($P=+$) states, respectively. We label the nth eigenstate of parity P by n^P. The mean level spacing Δ is determined by the area $A=L(W+M/2)$ of the billiard using Weyl's formula $\Delta/E_0=(4\pi\hbar^2/2mA)/E_0=0.176$.

We present in Fig. 4 the two eigenstates corresponding to the scattering states shown in Fig. 3. For each state, we show the eigenfunction density $|\psi_n(\mathbf{q})|^2$ and the corresponding Husimi representation $H_n(s,p)$ (see, e.g., [16,17]). The state 5686^-, displayed on the left of Fig. 4, differs in energy by about 0.01Δ from the sharpest observed resonance with energy 2029.172. Note that this energy difference is of the order of the accuracy to which our resonance energies and eigenvalues are calculated. On the right hand side of Fig. 4, a hierarchical state is displayed. Its energy differs from the resonance at energy 2041.109 by about 0.1Δ. This shift of the resonance energy from the eigenenergy of the closed system is due to the opening of the system by attaching the leads. As for the scattering states, we have superimposed some KAM tori onto the Husimi representations of Fig. 4. In addition, a partial transport barrier surrounding the island hierarchy is shown (see next section).

Now we want to associate all resonances of the scattering system with width Γ at energy E_{res} with an eigenstate of the closed billiard with energy E_{ev}. We use a Husimi representation $H_n(s,p)$ on the Poincaré section to determine the region in which an eigenstate localizes. We introduce the quantity

$$\eta_n=\int_{-W}^{0}ds\int_{-1}^{1}dpH_n(s,p), \tag{6}$$

which integrates the Husimi distribution over the left boundary of the billiard (not shown in Fig. 4) with the normalization of the Husimi distribution chosen such that $\int_{-W}^{L'/2}ds\int_{-1}^{1}dpH_n(s,p)=1$. This quantity gives an estimate of how strongly a state of the closed system will couple to the leads in the scattering system and should be roughly proportional to Γ. This allowed us to find, for each of the 54 resonances with $\Gamma\leqslant\Delta/2$, a state with $E_{ev}\approx E_{res}$ and with $\eta\approx\Gamma$. Figures 5 and 6 show the difference $E_{ev}-E_{res}$ in units of the mean level spacing Δ and the approximate proportionality of η and Γ, respectively. Clearly, larger differences appear for bigger Γ, but still a clear identification is possible (see Sec. VI). This assignment also works the other way around, as of the 46 eigenstates with the smallest values of η, we can identify 40 with isolated resonances, missing only the six regular eigenstates quantized most deeply in the central island of phase space, as discussed below.

For the 54 resonances with width Γ less than half a mean level spacing, we analyze the structure of the corresponding eigenstates. We find that 17 states can be categorized as regular states, as their Husimi representations are concentrated inside the five major stable islands in phase space. Of these states, seven are associated with the I-shaped orbit and ten with the M-shaped orbit. While we observe all states in the energy interval associated with the M-shaped orbit, six further eigenstates are concentrated near the center of the central stability island are not resolved as resonances. As these are the innermost states in the island, we expect them to couple more weakly to the leads and their resonance widths to be much smaller than the sharpest observed resonance.

Apparently, these resonances are so narrow that we were not able to find them, given our current numerical accuracy, even knowing their approximate energy from the eigenvalues.

The remaining 37 resonances are not related to regular states, but the Husimi representations of their corresponding eigenstates have large intensity in the region between the regular islands and the partial transport barrier and a much weaker intensity in the rest of the chaotic region. It should be noted that in the studied energy range accessible to our methods the wavelength is of the order of the distance between regular islands and the partial transport barrier. Therefore the eigenstates look either like regular states concentrated outside the island [18] or similar to scarred states on a hyperbolic orbit close to the island [19]. For higher energies they would show the true properties of hierarchical states, i.e., similar to a chaotic state, but restricted to the hierarchical region [14]. We therefore classify these states as hierarchical states.

In Fig. 2 we have labeled the resonances by r and h according to our classification of the corresponding eigenstates as regular and hierarchical, respectively. This demonstrates that the origin of *all* isolated resonances is hierarchical or regular eigenstates of the closed system.

V. PARTIAL TRANSPORT BARRIERS

Classical transport in the chaotic part of phase space is dominated by partial barriers [20–24]. They are formed by cantori as well as by stable and unstable manifolds. Such a partial transport barrier coincides with its iterate, with the exception of so-called turnstiles where phase-space volume is exchanged between both sides of the partial barrier. We have constructed partial barriers using the methods described in Ref. [20]. The fluxes Φ are determined from the length l of the maximizing and minimax orbits, according to

$$\Phi = \hbar k_F |l_{\mathrm{maximizing}} - l_{\mathrm{minimax}}| \tag{7}$$

$$= \hbar \pi \sqrt{E} |l_{\mathrm{maximizing}} - l_{\mathrm{minimax}}| / W. \tag{8}$$

Quantum mechanically, partial transport barriers with fluxes up to the order of $\hbar$ divide the chaotic part of phase space into distinct regions with chaotic and hierarchical eigenfunctions are concentrated mainly on one or the other side [14]. We found that the partial barrier with smallest flux that surrounds the main island and the four neighboring islands can be constructed from the stable and unstable manifolds of the period-4 hyperbolic fixed points. Each of its two turnstiles has for our largest energy $E=2100$ a flux $1.06\hbar$. Further outside are many other partial barriers with only slightly bigger fluxes. As an example, we show in Figs. 3 and 4 the partial barrier constructed from an unstable periodic orbit with winding number 5/23, which is an approximant of the most noble irrational between winding numbers 1/4 and 1/5. It has a flux $1.65\hbar$.

A check on the validity of our identification of regular and hierarchical states is provided by a comparison of their numbers to the corresponding relative volumes in phase space. To this end, we calculate the volume of the tori associated with stable periodic orbits, V_r, and the chaotic phase-space volume inside the partial transport barrier, V_h. We find V_r and V_h to cover 5.9% and 8.5% of the energy shell, respectively. From the total number of eigenstates in the energy interval, $N=426$, we get for 23 $(17+6)$ regular and 37 hierarchical states relative fractions of 5.4% and 8.7%, respectively, in good agreement with the volumes of the associated regions in phase space.

The absence of fractal conductance fluctuations in this system now has a clear explanation. According to Ref. [13] for fractal fluctuations to occur a hierarchy of partial transport barriers with fluxes larger than $\hbar$ must exist. For the energies studied we find that even the outermost partial barriers surrounding the hierarchical phase-space structure have fluxes of the order of $\hbar$. This causes a quantum dynamical decoupling of the chaotic part connected to the leads from the entire hierarchical part. As the hierarchical region is the semiclassical origin of fractal fluctuations, they are not observed. For much higher energies only, the hierarchy of partial transport barriers would have an outer region with fluxes larger than $\hbar$, leading to fractal conductance fluctuations. The inner region of this hierarchy with fluxes smaller than $\hbar$ has now a smaller phase-space volume. Still, together with the regular regions it will cause isolated resonances on smaller scales than the fractal fluctuations. Unfortunately, this energy regime is currently computationally inaccessible for the studied system.

Power laws in the distribution of resonance widths and in the variance of conductance increments had been observed in Ref. [11], apparently reflecting the classical dwell time exponent. They were related to the resonances below the mean level spacing. For these resonances we have now demonstrated that they arise due to hierarchical and regular states. This allows us to apply the arguments of Ref. [13] about the resonance width distribution of hierarchical states. They lead to the conclusion that these apparent power laws come from broad transition regions to asymptotic distributions that are unrelated to the classical dwell time exponent.

VI. AVOIDED CROSSINGS

While for most resonances and corresponding eigenstates the parameters η and Γ are of the same order of magnitude, for some states η exceeds Γ by up to two orders of magnitude. This phenomenon can be understood as an effect of avoided level crossings in the closed system. In Fig. 7(a) we show as an example the dependence of the energy of states 5736^- and 5737^- as a function of the parameter M/L for the narrow range $0.109\,99 \leqslant M/L \leqslant 0.110\,01$, displaying the typical features of an avoided crossing. A comparison of the associated Husimi representations shows that the states 5736^- and 5737^- do indeed exchange their character from chaotic to regular and from regular to chaotic, respectively, showing a superposition at $M/L=0.11$. Upon opening the system, the chaotic state couples much more strongly to the leads as compared to the regular one. Consequently, in the complex energy plane of the scattering system there is no longer an avoided crossing. The regular state leads to an isolated resonance with an almost linear energy dependence on M/L and the phase-space signature of the regular state

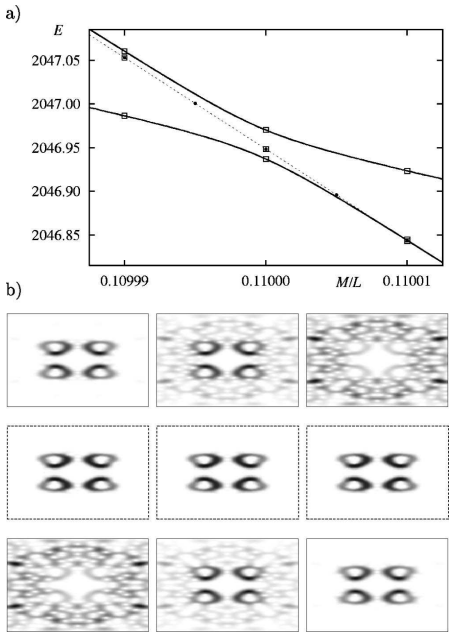

FIG. 7. (a) Energies of states 5736^- and 5737^- (solid lines) showing an avoided crossing under variation of M/L. The energy of the only isolated resonance in this energy range (dots connected by a dashed line) follows the regular state of the closed system. The slight offset in the resonance energy is within the systematic numerical error of the numerical method. (b) The Husimi representations for state 5737^- (top row), the scattering state (middle row), and eigenstate 5736^- (bottom row) are shown for $M/L = 0.10999, 0.11, 0.11001$ (left to right). For the eigenstates one clearly sees the typical exchange of the structure while passing the avoided crossing, whereas the scattering state is not affected.

[middle row in Fig. 7(b)]. It closely follows the expected energy dependence of the regular state in the closed system if it had not made an avoided crossing with the chaotic state [Fig. 7(a)].

Another example of an avoided crossing is given by state 5801^- with an eigenvalue about 0.5Δ less than the resonance position (see the lower right corner of Fig. 5) and the state 5802^-, with an eigenenergy about 1.4Δ above the resonance energy. Both states show similar Husimi representations and have η values exceeding Γ by about a factor of 10.

In all the cases when η drastically exceeds Γ a closer look at these eigenstates reveals that they are superpositions of regular or hierarchical states with chaotic states. They are due to avoided crossings and the chaotic part leads to a comparatively large value of η. In contrast, in the open system no avoided crossing occurs in the complex energy plane and the resonance width Γ is unaffected.

VII. CONCLUSION AND OUTLOOK

We demonstrate a clear correspondence of the isolated resonances observed in the transport properties of the open cosine billiard to hierarchical and regular eigenstates of the closed billiard. We can identify all resonances with widths less than half of the mean level spacing. The classification of resonances into a hierarchical or regular origin yields numbers in agreement with the relative phase-space volumes. On a quantitative level, we find a roughly linear relation between the widths of the isolated resonances and the weights of the associated eigenstates at the part of the boundary where the leads are attached. States with unusually large weights can be attributed to avoided crossings with chaotic eigenstates.

We find that the island hierarchy is separated from the chaotic part of phase space by partial transport barriers with fluxes of the order of $\hbar$. This supports the notion that the absence of fractal conductance fluctuations in the currently accessible energy range is due to the quantum dynamical decoupling of the hierarchical part of phase space from the chaotic part connected to the external leads.

The simultaneous appearance of isolated resonances and fractal fluctuations, beyond the quantum graph model studied in Ref. [13], remains to be demonstrated numerically or experimentally for a system with a mixed phase space. Numerically, the challenge is the observation of fractal fluctuations of the conductance, which go beyond one order of magnitude [25]. This requires calculations with a drastically increased number of modes, the use of improved techniques like the modular recursive Green's function method [26], and the search for suitable billiard systems where the turnstile fluxes across partial barriers are particularly large. Isolated resonances will easily appear as soon as the parameter is varied on a sufficiently small scale. We note that fluctuations of the quantum staying probability, which can be fractal [8], cannot show isolated resonances. Similarly, we expect no appearance of isolated resonances within the fractal fluctuations observed in recent studies [27], as they are unrelated to a classical mixed phase space.

On the experimental side, fractal conductance fluctuations have been observed [6,7] and also isolated resonances coming from regular regions have recently been reported [28]. The simultaneous appearance of both types including isolated resonances from hierarchical regions requires one to go far enough into the semiclassical regime, i.e., to quantum dots with dimensions bigger than 1 μm, as in Ref. [6]. At the same time the phase coherence time must be large enough to resolve isolated resonances of a given width and, of course, the parameter, typically a magnetic field, must be varied on a sufficiently fine scale. Given the experimental limitations it would be helpful if an optimal form for such a quantum dot could be provided by theoretical considerations. This seems to be quite difficult at present, since the difference in the lithographic shape and the actual potential experienced by electrons has dramatic consequences on the electron dynamics and thus on the scales over which fractal fluctuations and isolated resonances appear.

ACKNOWLEDGMENTS

R.K. acknowledges helpful discussions with L. Hufnagel and M. Weiss. A.B. acknowledges support by the Deutsche

Forschungsgemeinschaft under contract No. DFG-Ba 1973/1-1.

APPENDIX: HYBRID REPRESENTATION AND RECURSIVE GREEN'S FUNCTION METHOD

In this appendix we discuss the numerical method to determine the scattering matrix S and the time delay τ. The S matrix of a symmetric scattering system can be expressed in terms of the Green's function G:

$$S=\begin{pmatrix} r & t' \\ t & r' \end{pmatrix}, \tag{A1}$$

$$t'=t^T, \tag{A2}$$

$$r'=r, \tag{A3}$$

$$t_{\alpha\beta}=-i\hbar\sqrt{v_\alpha v_\beta}G_{\alpha\beta}(0,L), \tag{A4}$$

$$r_{\alpha\beta}=\delta_{\alpha\beta}-i\sqrt{v_\alpha v_\beta}G_{\alpha\beta}(0,0), \tag{A5}$$

where

$$v_\alpha=\left[\frac{2}{m}\left(E-\frac{\hbar^2}{2mW^2}\alpha^2\pi^2\right)\right]^{1/2} \tag{A6}$$

is the velocity of mode α and

$$G_{\alpha\beta}(x,x')=\int_x dy\int_{x'}dy'\,\phi^*_\alpha(y;x)\,\phi_\beta(y';x') \times G^+(\mathbf{r},\mathbf{r}';E) \tag{A7}$$

is the projection of the retarded Green's function $G^+(\mathbf{r},\mathbf{r}';E)$ onto the local transverse modes

$$\phi_\alpha(y;x)=\sqrt{\frac{2}{W(x)}}\sin\left(\frac{\alpha\pi y}{W(x)}\right). \tag{A8}$$

The Green's function can be calculated recursively. Expanding the Hamiltonian

$$H=\frac{\hbar^2}{2m}\left(\frac{\partial^2}{\partial x^2}+\frac{\partial^2}{\partial y^2}\right) \tag{A9}$$

in terms of the local transverse modes (A8) and discretizing in the x direction with a lattice constant a, $x=ma$, we obtain the Hamiltonian in hybrid representation [29]

$$H_h=\sum_{\alpha,m}|\alpha,m\rangle(\epsilon^\alpha_m+2E_t)\langle\alpha,m|-\sum_{\alpha,\beta,m}(t^{\alpha\beta}_{m,m+1}|\alpha,m\rangle \times\langle\beta,m+1|+t^{\alpha\beta}_{m+1,m}|\alpha,m+1\rangle\langle\beta,m|), \tag{A10}$$

with

$$\epsilon^\alpha_m=\left(\alpha\frac{a}{W(ma)}\right)^2,$$

$$t^{\alpha\beta}_{m,m+1}=E_t\int\phi^*_\alpha(y;ma)\,\phi_\beta(y;(m+1)a)dy, \tag{A11}$$

and $E_t=\hbar^2/(2ma^2)$. In order to recursively calculate the Green's function associated with H_h, we split the Hamiltonian H_h^{M+1} of a system with $m=1,\ldots,M+1$ into two parts,

$$H_h^{M+1}=H_0+U, \tag{A12}$$

$$H_0=H_h^M+\sum_\alpha|\alpha,M+1\rangle(\epsilon^\alpha_{M+1}+2E_t)\langle\alpha,M+1|, \tag{A13}$$

$$U=-\sum_{\alpha,\beta}(t^{\alpha\beta}_{M,M+1}|\alpha,M\rangle\langle\beta,M+1| +t^{\alpha\beta}_{M+1,M}|\alpha,M+1\rangle\langle\beta,M|). \tag{A14}$$

Dyson's equation,

$$G^{M+1}=G_0+G_0UG^{M+1}, \tag{A15}$$

then allows us to calculate the Green's function G^{M+1} of H_h^{M+1} from G^M and

$$G_0=(E-H_0)^{-1}=G^M+\sum_\alpha|\alpha,M+1\rangle g_0^{M+1}\langle\alpha,M+1|, \tag{A16}$$

$$g_0^{M+1}=(E-\epsilon^\alpha_{M+1}-2E_t)^{-1}.$$

We start the recursion with $M=1$ at the left edge of the closed billiard and iterate to the right edge at $M=N_L=L/a$. In order to attach the leads, we again split the Hamiltonian according to Eq. (A12), but this time H_0 contains the Hamiltonian of the closed billiard and the semi-infinite leads. In the leads, $\epsilon^\alpha_m=(\alpha a/W)^2$ and $t^{\alpha\beta}_{m,m+1}=\delta_{\alpha\beta}E_t$. U is the coupling between the billiard and the semi-infinite leads. The Green's function for the leads is known analytically [30].

The recursion scheme is exact for an infinite number N_L of slices and an infinite number N_C of transverse modes. For numerical calculations, both numbers have to be kept finite. We find that the deviations from the asymptotic values for, e.g., the width Γ of a resonance scale as

$$\Gamma(N_C,N_L)=\Gamma+bN_C^{-4}+cN_L^{-2}, \tag{A17}$$

with positive numerical coefficients b and c. For our choice of parameters, $N=45$ transmitting modes in the leads, the values $N_C=108$ and $N_L=12\,000$ give an accuracy of about 1% for the resonance width. The corrections to the position of the resonance have the same functional form as in Eq. (A17); however, they can be either positive or negative, depending on the values of N_C and N_L. This explains the slight offset of the resonance energies with respect to the eigenenergies of the closed system seen in Fig. 7(a).

[1] R. A. Jalabert, in *New Directions in Quantum Chaos*, Proceedings of the International School of Physics "Enrico Fermi," Course CXLIII, edited by G. Casati, I. Guarneri, and U. Smilansky (IOS Press, Amsterdam, 2000).
[2] A. J. Lichtenberg and M. A. Liebermann, *Regular and Chaotic Dynamics*, 2nd ed. (Springer-Verlag, New York, 1992).
[3] B. V. Chirikov and D. L. Shepelyansky, in *Proceedings of the IXth International Conference on Nonlinear Oscillations, Kiev, 1981* [Naukova Dumka **2**, 420 (1984)] [English translation: Princeton University Report No. PPPL-TRANS-133, 1983 (unpublished)]; C.F.F. Karney, Physica D **8**, 360 (1983); B.V. Chirikov and D.L. Shepelyansky, *ibid.* **13**, 395 (1984); P. Grassberger and H. Kantz, Phys. Lett. **113A**, 167 (1985); Y.C. Lai, M. Ding, C. Grebogi, and R. Blümel, Phys. Rev. A **46**, 4661 (1992).
[4] Y.-C. Lai, R. Blümel, E. Ott, and C. Grebogi, Phys. Rev. Lett. **68**, 3491 (1992).
[5] R. Ketzmerick, Phys. Rev. B **54**, 10 841 (1996).
[6] A.S. Sachrajda *et al.*, Phys. Rev. Lett. **80**, 1948 (1998).
[7] A.P. Micolich *et al.*, Phys. Rev. Lett. **87**, 036802 (2001).
[8] G. Casati, I. Guarneri, and G. Maspero, Phys. Rev. Lett. **84**, 63 (2000).
[9] P. Stifter, Diploma thesis, Universität Ulm, 1993; Ph.D. thesis, Universität Ulm, 1996.
[10] G.A. Luna-Acosta *et al.*, Phys. Rev. B **54**, 11 410 (1996); A. Bäcker, R. Schubert, and P. Stifter, J. Phys. A **30**, 6783 (1997).
[11] B. Huckestein, R. Ketzmerick, and C.H. Lewenkopf, Phys. Rev. Lett. **84**, 5504 (2000); **87**, 119901(E) (2001).
[12] P. Šeba, Phys. Rev. E **47**, 3870 (1993).
[13] L. Hufnagel, M. Weiss, and R. Ketzmerick, Europhys. Lett. **54**, 703 (2001).
[14] R. Ketzmerick, L. Hufnagel, F. Steinbach, and M. Weiss, Phys. Rev. Lett. **85**, 1214 (2000).
[15] A. Bäcker, in The Mathematical Aspects of Quantum Chaos I, Proceedings of the Summer School, Bologna, 2001 (in press) http://arXiv.org/abs/nlin/0204061.
[16] J.M. Tualle and A. Voros, Chaos, Solitons Fractals **5**, 1085 (1995).
[17] F.P. Simonotti, E. Vergini, and M. Saraceno, Phys. Rev. E **56**, 3859 (1997).
[18] O. Bohigas, S. Tomsovic, and D. Ullmo, Phys. Rep. **223**, 43 (1993).
[19] G. Radons and R.E. Prange, Phys. Rev. Lett. **61**, 1691 (1988); G. Radons and R. E. Prange, in *Quantum Chaos (Trieste, 1990)*, edited by H.A. Cerdeiva, R. Ramaswamy, and M.C. Gutzwiller (World Scientific, Berlin, 1991), p. 333.
[20] R.S. MacKay, J.D. Meiss, and I.C. Percival, Physica D **13**, 55 (1984).
[21] J.D. Hanson, J.R. Cary, and J.D. Meiss, J. Stat. Phys. **39**, 327 (1985).
[22] J.D. Meiss and E. Ott, Physica D **20**, 387 (1986).
[23] T. Geisel, A. Zacherl, and G. Radons, Phys. Rev. Lett. **59**, 2503 (1987).
[24] J. Meiss, Rev. Mod. Phys. **64**, 795 (1992).
[25] Y. Takagaki and K.H. Ploog, Phys. Rev. B **61**, 4457 (2000).
[26] S. Rotter *et al.*, Phys. Rev. B **62**, 1950 (2000).
[27] E. Louis and J.A. Verges, Phys. Rev. B **61**, 13 014 (2000); G. Benenti, G. Casati, I. Guarneri, and M. Terraneo, Phys. Rev. Lett. **87**, 014101 (2001); I. Guarneri and M. Terraneo, Phys. Rev. E **65**, 015203(R) (2001).
[28] A. P. S. de Moura *et al.*, Phys. Rev. Lett. **88**, 236804 (2002).
[29] F.A. Maaø, I.V. Zozulenko, and E.H. Hauge, Phys. Rev. B **50**, 17 320 (1994).
[30] E. N. Economou, *Green's Functions in Quantum Physics*, 2nd ed., Vol. 7 in Solid-State Sciences (Springer-Verlag, Berlin, 1990).

[A4] Numerical aspects of eigenvalues and eigenfunctions of chaotic quantum systems

A. Bäcker

in: *The Mathematical Aspects of Quantum Chaos I*, M. Degli Esposti and S. Graffi (Eds.), Springer Lecture Notes in Physics **618**, 99–144 (2003).

We give an introduction to some of the numerical aspects in quantum chaos. The classical dynamics of two–dimensional area–preserving maps on the torus is illustrated using the standard map and a perturbed cat map. The quantization of area–preserving maps given by their generating function is discussed and for the computation of the eigenvalues a computer program in Python is presented. We illustrate the eigenvalue distribution for two types of perturbed cat maps, one leading to COE and the other to CUE statistics. For the eigenfunctions of quantum maps we study the distribution of the eigenvectors and compare them with the corresponding random matrix distributions. The Husimi representation allows for a direct comparison of the localization of the eigenstates in phase space with the corresponding classical structures. Examples for a perturbed cat map and the standard map with different parameters are shown. Billiard systems and the corresponding quantum billiards are another important class of systems (which are also relevant to applications, for example in mesoscopic physics). We provide a detailed exposition of the boundary integral method, which is one important method to determine the eigenvalues and eigenfunctions of the Helmholtz equation. We discuss several methods to determine the eigenvalues from the Fredholm equation and illustrate them for the stadium billiard. The occurrence of spurious solutions is discussed in detail and illustrated for the circular billiard, the stadium billiard, and the annular sector billiard. We emphasize the role of the normal derivative function to compute the normalization of eigenfunctions, momentum representations or autocorrelation functions in a very efficient and direct way. Some examples for these quantities are given and discussed.

Numerical Aspects of Eigenvalue and Eigenfunction Computations for Chaotic Quantum Systems

Arnd Bäcker

Abteilung Theoretische Physik Universität Ulm, Albert-Einstein-Allee 11, D-89081 Ulm, Germany, *arnd.baecker@physik.uni-ulm.de*

Summary. We give an introduction to some of the numerical aspects in quantum chaos. The classical dynamics of two–dimensional area–preserving maps on the torus is illustrated using the standard map and a perturbed cat map. The quantization of area–preserving maps given by their generating function is discussed and for the computation of the eigenvalues a computer program in Python is presented. We illustrate the eigenvalue distribution for two types of perturbed cat maps, one leading to COE and the other to CUE statistics. For the eigenfunctions of quantum maps we study the distribution of the eigenvectors and compare them with the corresponding random matrix distributions. The Husimi representation allows for a direct comparison of the localization of the eigenstates in phase space with the corresponding classical structures. Examples for a perturbed cat map and the standard map with different parameters are shown.

Billiard systems and the corresponding quantum billiards are another important class of systems (which are also relevant to applications, for example in mesoscopic physics). We provide a detailed exposition of the boundary integral method, which is one important method to determine the eigenvalues and eigenfunctions of the Helmholtz equation. We discuss several methods to determine the eigenvalues from the Fredholm equation and illustrate them for the stadium billiard. The occurrence of spurious solutions is discussed in detail and illustrated for the circular billiard, the stadium billiard, and the annular sector billiard.

We emphasize the role of the normal derivative function to compute the normalization of eigenfunctions, momentum representations or autocorrelation functions in a very efficient and direct way. Some examples for these quantities are given and discussed.

1 Introduction

In this text, which is an expanded version of lectures held at a summer school in Bologna in 2001, we give an introduction to some of the numerical aspects in quantum chaos; some of the sections on the boundary integral method contain more advanced material. In quantum chaos one studies quantum systems whose classical limit is (in some sense) chaotic. In this subject computer experiments play an important role. For integrable systems the eigenvalues and eigenfunctions can be determined either explicitly or as solutions of simple equations. In contrast, for chaotic systems there are no explicit formulae

Mirko Degli Esposti, Sandro Graffi (Eds.): LNP 618, pp. 91–144, 2003.

for eigenvalues and eigenfunctions such that numerical methods have to be used. In many cases numerical observations have lead to the formulation of important conjectures. Such numerical computations also allow us to test analytical results which have been derived under certain assumptions or by using approximations.

An important class of systems for the study of classical chaos are area–preserving maps as several types of different dynamical behaviour like integrable motion, mixed dynamics, ergodicity, mixing or Anosov systems can be found. We discuss the numerics for the corresponding quantum maps and illustrate some of the methods and results using the standard map and the perturbed cat map as prominent examples.

Another important class of systems are classical billiards and the corresponding quantum billiards. In Sect. 3 we discuss in detail the boundary integral method, which is one of the main methods for the solution of the Helmholtz equation, which is the time–independent Schrödinger equation for these systems.

2 Area Preserving Maps

2.1 Some Examples

We will restrict ourselves to area-preserving maps on the two-torus

$$P : \mathbb{T}^2 \to \mathbb{T}^2 \tag{1}$$

$$(q,p) \mapsto (q',p') \ , \tag{2}$$

where $\mathbb{T}^2 \simeq \mathbb{R}^2/\mathbb{Z}^2$, i.e. the map is defined on a square with opposite sides identified. The requirement that the map P is area–preserving is equivalent to the condition that $\det DP = 1$, where DP is the linearization of the map P. The natural invariant measure on $\mathbb{T}^2$ is the Lebesgue measure $\mathrm{d}\mu = \mathrm{d}q\mathrm{d}p$.

As a first example let us consider the so-called *standard map*, defined by

$$\begin{pmatrix} q' \\ p' \end{pmatrix} = \begin{pmatrix} q + p - \frac{\kappa}{2\pi}\sin(2\pi q) \\ p - \frac{\kappa}{2\pi}\sin(2\pi q) \end{pmatrix} \bmod 1 \ . \tag{3}$$

One easily checks that this map is area-preserving. Figure 1 shows some orbits (i.e. for different initial points (q,p) the points $(q_n,p_n) = P^n(q,p)$ are plotted for $n \leq 1000$) of the standard map for different parameters κ. For $\kappa = 0$ an initial point (q,p) stays on the horizontal line and in q it rotates with frequency p. So for irrational p the corresponding line is filled densely. For $\kappa > 0$, the lines with rational p break up into an island-chain structure composed of (initially) stable orbits and their corresponding unstable (hyperbolic) partner. For small enough perturbation there are invariant (Kolmogorov–Arnold–Moser or short KAM) curves which are absolute barriers to the motion (for a more detailed discussion of these aspects the review [1]

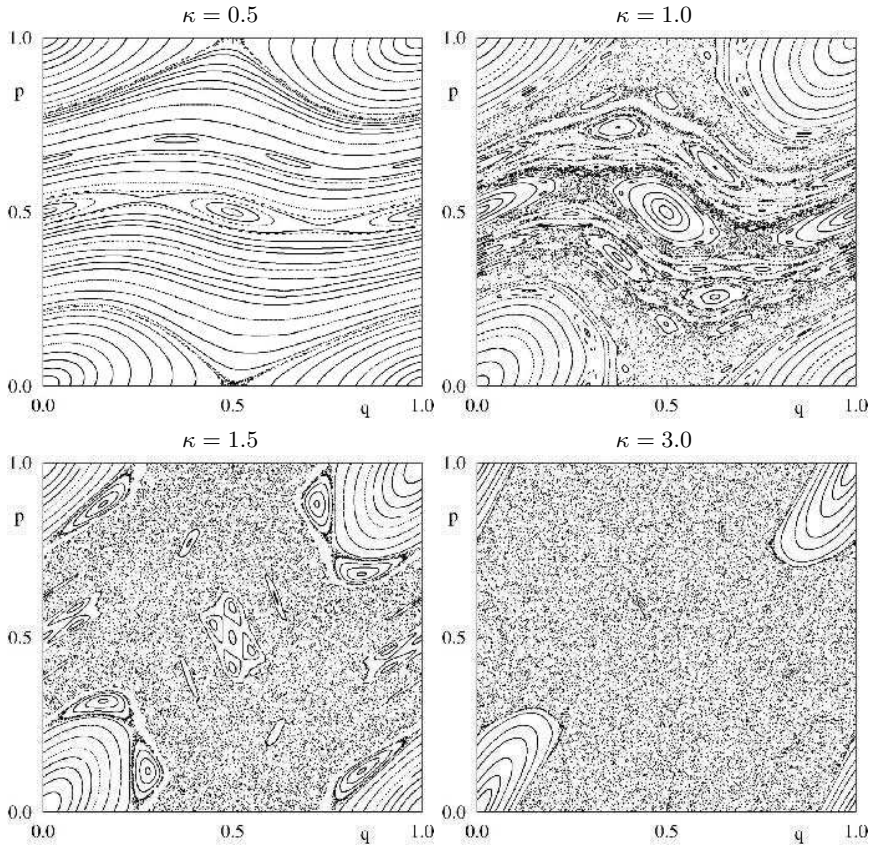

Fig. 1. Examples of orbits in the standard map for different parameters κ.

is a good starting point). For stronger perturbations, e.g. $\kappa = 1$ or $\kappa = 1.5$, the stochastic bands become larger and for even stronger perturbation (see the picture for $\kappa = 3.0$) there appears to be just one quite big stochastic region together with the elliptic island. The elliptic islands coexist with regions of irregular motion, therefore the standard map is an example of a so-called system with mixed phase space or, more briefly, a *mixed system*. Whether the motion in those stochastic regions is ergodic is one of the big unsolved problems, see [2] for a review on the coexistence problem. For some recent results on the classical dynamics of the standard map, in particular at large parameters, see [3, 4, 5].

An alternative way to specify a map $P : \mathbb{T}^2 \to \mathbb{T}^2$ is to use a generating function $S(q', q)$, from which the map is obtained by

$$p = -\frac{\partial S(q', q)}{\partial q} \qquad p' = \frac{\partial S(q', q)}{\partial q'} \quad . \tag{4}$$

One easily checks that

$$S(q',q) = \frac{1}{2}(q-q')^2 + \frac{\kappa}{4\pi^2}\cos(2\pi q) \ , \tag{5}$$

is a generating function for the standard map (3).

Another important class are perturbed cat maps [6,7], like

$$\begin{pmatrix} q' \\ p' \end{pmatrix} = A \begin{pmatrix} q \\ p \end{pmatrix} + \kappa G(q) \begin{pmatrix} A_{12} \\ A_{22} \end{pmatrix} \qquad \mod 1 \ , \tag{6}$$

where

$$A = \begin{pmatrix} A_{11} & A_{12} \\ A_{21} & A_{22} \end{pmatrix} \tag{7}$$

is a matrix with integer entries (ensuring the continuity of the map), $\det A = 1$ (area preservation) and $\mathrm{Tr}\, A > 2$ (hyperbolicity). The perturbation $G(q)$ is a smooth periodic function on $[0,1[$. For $\kappa = 0$ the mapping is Anosov (see e.g. [8]), in particular it is ergodic and mixing. Moreover, following from the the Anosov theorem the map (6) is structurally stable, i.e. it stays Anosov as long

$$\kappa \leq \kappa_{\max} := \frac{\sqrt{(\mathrm{Tr}\, A)^2 - 4} - \mathrm{Tr}\, A + 2}{2\max_q |G'(q)| \sqrt{1 + A_{22}^2}} \ ; \tag{8}$$

in particular the orbits are topologically conjugate to those of the unperturbed cat map. For larger parameters there are typically elliptic islands, so it becomes a mixed system.

A common choice for A and the perturbation is

$$\begin{pmatrix} q' \\ p' \end{pmatrix} = \begin{pmatrix} 2 & 1 \\ 3 & 2 \end{pmatrix} \begin{pmatrix} q \\ p \end{pmatrix} + \frac{\kappa}{2\pi}\cos(2\pi q) \begin{pmatrix} 1 \\ 2 \end{pmatrix} \qquad \mod 1 \ . \tag{9}$$

For $\kappa \leq \kappa_{\max} = (\sqrt{3}-1)/\sqrt{5} = 0.33\ldots$ the map is Anosov. The corresponding generating function is given by

$$S(q',q) = {q'}^2 - qq' + q^2 + \frac{\kappa}{4\pi^2}\sin(2\pi q) \ . \tag{10}$$

In Fig. 2a) one orbit for 20 000 iterations for the perturbed cat map (9) with $\kappa = 0.3$ is shown. The orbit appears to fill the torus in a uniform way, as it has to be asymptotically for almost all initial conditions because of the ergodicity of the map. For $\kappa = 6.5$ Fig. 2b) shows one orbit (20 000 iterates) in the irregular component and some orbits (1000 iterations) in the elliptic islands.

2.2 Quantization of Area-Preserving Maps

For the quantization of area–preserving maps exist several approaches, see for example [9,10,11,12,13,6,14,15,16]; a detailed account can be found in [17],

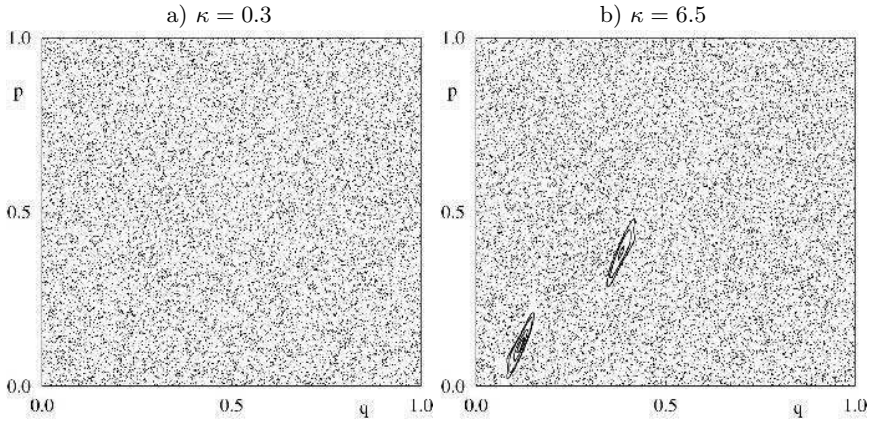

Fig. 2. Examples of orbits in the perturbed cat map (9) for $\kappa = 0.3$ and $\kappa = 6.5$.

and [18] provides a pedagogical introduction to the subject. First one has to find a suitable Hilbert space which incorporates the topology of the torus $\mathbb{T}^2$, i.e. the eigenfunctions in position and momentum have to fulfil

$$\psi(q+j) = \mathrm{e}^{\frac{\mathrm{i}}{\hbar} j\theta_2}\psi(q) \qquad ; \quad j \in \mathbb{N} \tag{11}$$

$$\widehat{\psi}(p+k) = \mathrm{e}^{-\frac{\mathrm{i}}{\hbar} k\theta_1}\widehat{\psi}(p) \qquad ; \quad k \in \mathbb{N} \ . \tag{12}$$

These conditions imply that Planck's constant $\hbar$ can only take the values $\hbar = \frac{1}{2\pi N}$ with $N \in \mathbb{N}$. Thus the semiclassical limit $\hbar \to 0$ corresponds to $N \to \infty$. The phases $(\theta_1, \theta_2) \in [0,1[^2$ are at first arbitrary; for $\theta_1 = \theta_2 = 0$ one obtains periodic boundary conditions. For each N one has a Hilbert space $\mathcal{H}_N$ of finite dimension N. Observables $f \in C^\infty(\mathbb{T}^2)$ can be quantized analogous to the Weyl quantization to give an operator $\mathrm{Op}(f)$ on $\mathcal{H}_N$. Finally, a quantum map is a sequence of unitary operators U_N, $N \in \mathbb{N}$ on a Hilbert space $\mathcal{H}_N$. The quantum map is a quantization of a classical map P on $\mathbb{T}^2$, if the so–called Egorov property is fulfilled, i.e.

$$\lim_{N\to\infty} ||U_N^{-1}\mathrm{Op}(f)U_N - \mathrm{Op}(f \circ P)|| = 0 \qquad \forall f \in C^\infty(\mathbb{T}^2) \ . \tag{13}$$

This means that semiclassically quantum time evolution and classical time evolution commute.

So the aim is to find for a given classical map a corresponding sequence of unitary operators. Unfortunately, this is not as straight forward as the quantization of Hamiltonian systems and a lot of information on this can be found in the above cited literature and references therein. One of the simplest approaches to determine U_N corresponding to a given area–preserving map uses its generating function to define

$$(U_N)_{j',j} := \langle q_{j'}|U_N|q_j\rangle$$
$$= \frac{1}{\sqrt{N}}\left|\frac{\partial^2 S(\tilde{q}',\tilde{q})}{\partial\tilde{q}'\partial\tilde{q}}\right|^{1/2}_{\tilde{q}'=q_{j'},\tilde{q}=q_j} \exp\left(2\pi \mathrm{i} N S\left(q_{j'},q_j\right)\right) \tag{14}$$

with $q_j = j/N$, $q_{j'} = j'/N$, where $j, j' = 0, 1, \ldots, N-1$. In the same way one may (and for certain maps which cannot represented in terms of $S(q',q)$ one has to) use other generating functions such as $S(p',p)$ or $S(q,p)$; usually these will lead to different eigenvalues and eigenfunctions. The question is to determine conditions on the generating function $S(q',q)$ such that U_N is unitary and fulfils the Egorov property (13). To my knowledge this question has not yet been fully explored, even though the quantum maps studied in the literature provide both examples and counterexamples. We will leave this as an interesting open question.

For the examples introduced before the quantization via (14) can be used. For the standard map we get

$$(U_N)_{j',j} = \frac{1}{\sqrt{N}} \exp\left[\frac{\mathrm{i}\pi}{N}(j'-j)^2 + \frac{\mathrm{i}\kappa N}{2\pi}\cos\left(\frac{2\pi}{N}j\right)\right] \tag{15}$$

with $j, j' = 0, \ldots, N-1$. A quantization of the standard map which takes the symmetries into account can be found in [19]. For the perturbed cat map (9) one gets using its generating function (10)

$$(U_N)_{j',j} = \frac{1}{\sqrt{N}} \exp\left(\frac{2\pi\mathrm{i}}{N}(j'^2 - j'j + j^2) + \mathrm{i}N\frac{\kappa}{2\pi}\sin(2\pi j/N)\right) \quad . \tag{16}$$

For the unitary operator one has to solve the eigenvalue problem

$$U_N\psi_n = \lambda_n\psi_n \qquad \text{with } n = 0, \ldots, N-1, \;\; \psi_n \in \mathbb{C}^N \quad . \tag{17}$$

Here λ_n is the n–th eigenvalue and the corresponding eigenvector ψ_n consists of N complex components, where N is the size of the unitary matrix U_N. Because of the unitarity of U_N the eigenvalues lie on the unit circle, i.e. $|\lambda_n| = 1$.

Let us discuss some of the numerical aspects relevant for finding the solutions of (17) without going into implementation specific details (see the appendix and [20] for an implementation using `Python`).

Computing the eigenvalues of (17) consists of two main steps

– Setting up the matrix U_N:
  The computational effort increases proportional to N^2 (unless each matrix element requires further loops) as we have to fill the N^2 matrix elements. The memory requirement to store U_N is $16\,N^2$ Bytes (for a IEEE-compliant machine a double precision floating point number requires 8 Bytes; as we have both real and imaginary part we end up with 16 Bytes per matrix element).

– Computing the eigenvalues:
The computational effort for the matrix diagonalization (typically) scales like N^3.
Usually one will use a black-box routine such as one from the NAG-library [21] or from LAPACK [22]. To my knowledge there are no routines which make use of the fact that the matrix U_N is unitary so we may for example use the NAG routine `F02GBF` or the LAPACK routine `ZGEES` (or the more recent routine `ZGEEV` which is faster for larger matrices, e.g. $N \geq 500$) which compute all eigenvalues of a complex matrix.
For certain maps specific optimizations are possible, see e.g. [19] for the standard map. For this type of mapping a different approach employing a combination of fast Fourier transform and Lanczos method reduces the computational effort to $N^2 \ln N$ [23].

After successful compilation and running of the program it is useful to see whether the eigenvalues really lie on the unit circle. In Fig. 3 this is illustrated for $N = 200$ and the standard map with $\kappa = 1.5$. For small N the running times of the program for setting up the matrix U_N and its diagonalization is just a matter of minutes. For example on an Intel Pentium III processor with 666 MHz one needs just 6 minutes to compute the eigenvalues of (17) when $N = 1000$. However, for $N = 3000$ already 140 MB of RAM are required to store U_N and the computing time increases to 6 hours. Depending on

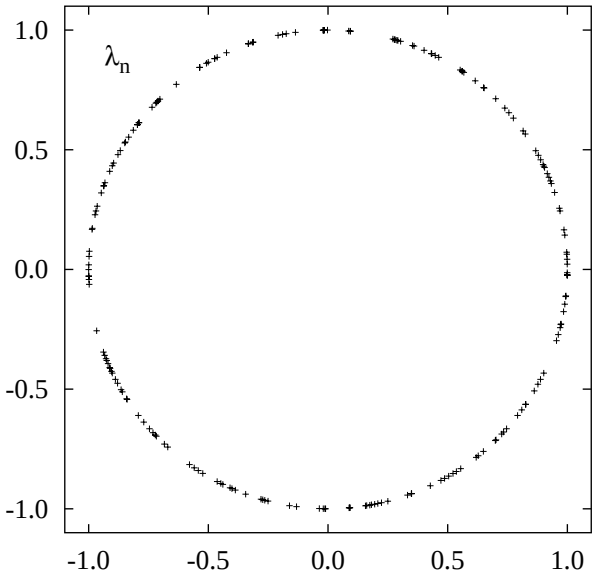

Fig. 3. Plotting the eigenvalues of U_N allows to check the numerical implementation and the unitarity of U_N; the picture shows for $N = 200$ and $\kappa = 1.5$ the eigenvalues λ_n for the quantized standard map (15).

available memory, computing power, patience and motivation one may use larger values of N.

Let us conclude this part with a more technical remark: In addition to the choice of computer language, compiler, optimizations and algorithm there is one very important component for achieving good performance when doing numerical linear algebra computations: the BLAS (Basic Linear Algebra Subprograms). Libraries such as LAPACK defer all the basics tasks like adding vectors, vector–matrix or matrix–matrix multiplication to the BLAS such that highly optimized (machine-specific) BLAS routines should be used. Most hardware vendors provide these (of differing quality). Recently the software system ATLAS (Automatically Tuned Linear Algebra Software) [24] has been introduced which generates a machine dependent optimized BLAS library. For some computers ATLAS-based BLAS can be even faster than the vendor supplied ones!

2.3 Eigenvalue Statistics

One central research line in quantum chaos is the investigation of spectral statistics. It has been conjectured [25] that for generic chaotic systems the eigenvalue statistics can be described by random matrix theory, whereas generic integrable systems should follow Poissonian statistics [26]. To study the eigenvalue statistics for quantum maps one considers the eigenphases $\varphi_n \in [0, 2\pi[$, defined by $\lambda_n = \mathrm{e}^{\mathrm{i}\varphi_n}$ (in the following we will also call φ_n levels in analogy to the energy levels for the Schrödinger equation). The simplest statistics is the nearest neighbour level spacing distribution $P(s)$ which is the distribution of the spacings

$$s_n := \frac{N}{2\pi}(\varphi_{n+1} - \varphi_n) \qquad \text{with } n = 0, \ldots, N-1 \quad \text{and } \varphi_N := \varphi_0 \ .$$

The factor $\frac{N}{2\pi}$ ensures that the average of all spacings s_n is 1. To compute the distribution practically one chooses a division of the interval $[0, 10]$ (usually this interval is sufficient, but more precisely the upper limit is determined by the largest s_n) into b bins and determines the fraction of spacings s_n falling into the corresponding bins. If N is too small it is better to consider instead of $P(s)$ the corresponding cumulative distribution

$$I(s) := \frac{\#\{n \mid s_n \le s\}}{N} \tag{18}$$

which avoids the binning and results in a smoother curve.

Fig. 4 shows for the perturbed cat map (9) with $\kappa = 0.3$ the level spacing distribution $P(s)$ and the cumulative level spacing distribution $I(s)$ for $N = 3001$. For this parameter value κ the map is still Anosov so one expects that the correlations of the eigenphases follow random matrix theory; in particular because the perturbation should break up the number theoretical degeneracies which lead to non-generic spectral statistics for the cat maps

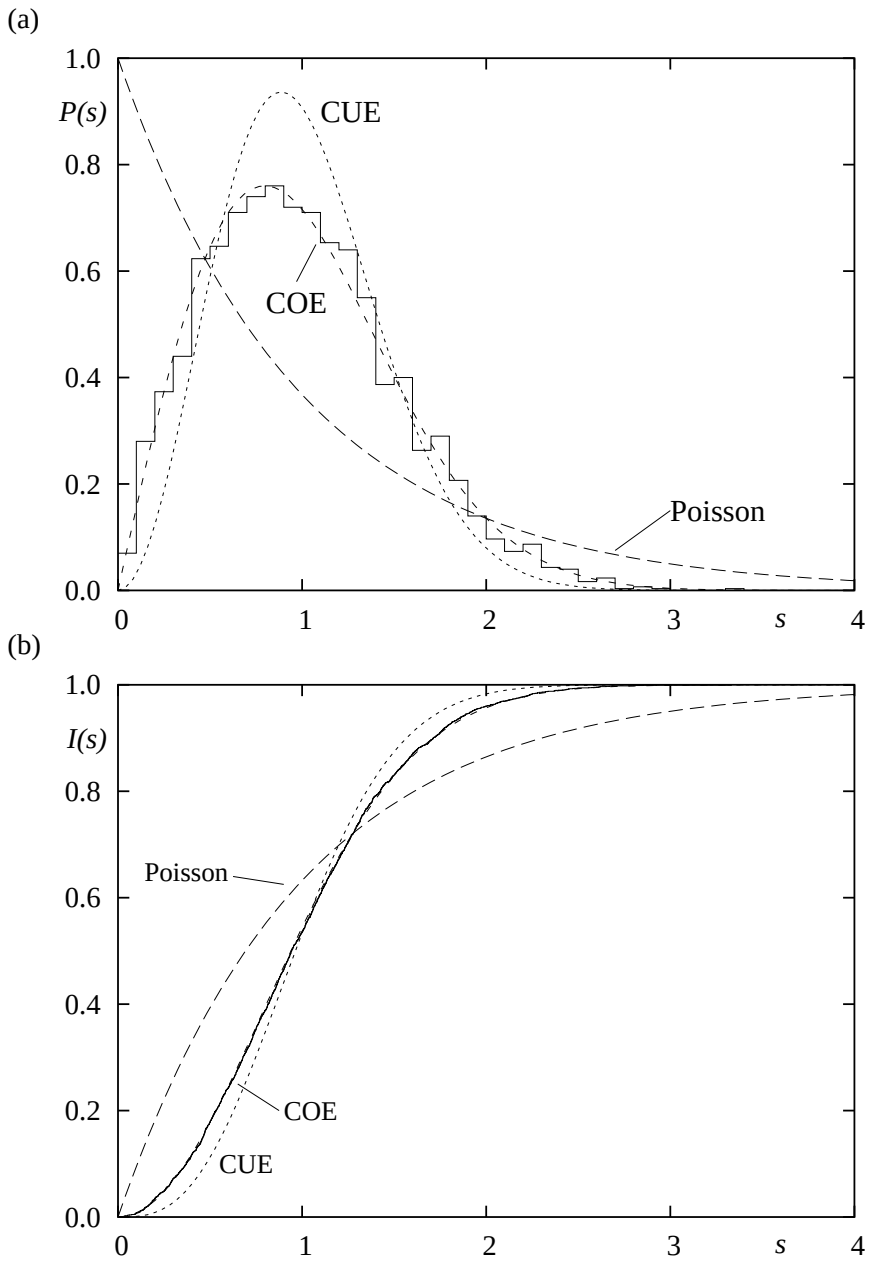

Fig. 4. (a) Level spacing distribution $P(s)$ and (b) cumulative level spacing distribution $I(s)$ for the perturbed cat map (9) with $\kappa = 0.3$ and $N = 3001$.

at $\kappa = 0$ [27, 28]. In [29, 30] it is shown that for all perturbations which are just a shear in position one of the symmetries of the cat map survives, so that the statistics are expected to be described by the circular orthogonal ensemble (COE). In the limit $N \to \infty$ this is the same as the Gaussian orthogonal ensemble (GOE). In Fig. 4 we show the Wigner distribution $P_{\mathrm{Wigner}}(s)$ which is very close to the COE distribution,

$$P_{\mathrm{COE}}(s) \approx P_{\mathrm{Wigner}}(s) = \frac{\pi}{2} s \exp\left(-\frac{\pi}{4} s^2\right) \quad . \tag{19}$$

and for comparison the CUE distribution

$$P_{\mathrm{CUE}}(s) \approx \frac{32}{\pi^2} s^2 \exp\left(-\frac{4}{\pi} s^2\right) \tag{20}$$

and the Poisson distribution (expected for generic integrable systems)

$$P_{\mathrm{Poisson}}(s) = \mathrm{e}^{-s} \quad . \tag{21}$$

The agreement with the expected COE distribution is very good.

A specific example, which breaks the above mentioned unitary symmetry and thus leads to CUE statistics, uses two shears, one in position and one in momentum [29],

$$\begin{pmatrix} q' \\ p' \end{pmatrix} = (A \circ P_q \circ P_p) \begin{pmatrix} q \\ p \end{pmatrix} \quad , \tag{22}$$

where

$$A = \begin{pmatrix} 12 & 7 \\ 41 & 24 \end{pmatrix} \tag{23}$$

and $P_q(q,p) = (q + \kappa_q G(p), p)$, $P_p(q,p) = (q, p + \kappa_p F(q))$ with $F(q) = \frac{1}{2\pi}(\sin(2\pi q) - \sin(4\pi q))$ and $G(p) = \frac{1}{2\pi}(\sin(4\pi q) - \sin(2\pi q))$. For the corresponding quantum map with $\kappa_p = \kappa_q = 0.012$ and $N = 3001$ the level spacing distribution is shown in Fig. 5. One observes very good agreement with the CUE distribution.

2.4 Eigenfunctions

Another interesting question concerns the statistical behaviour of eigenfunctions, and more specifically for quantum maps the eigenvector statistics and the properties of phase space representations like the Husimi function.

Eigenvector Distributions

Consider an eigenvector ψ of a quantum map given by the N numbers $c_j \in \mathbb{C}$, $j = 0, ..., N-1$. The distribution $P(\psi)$ is given (similarly to the level spacing distribution) by

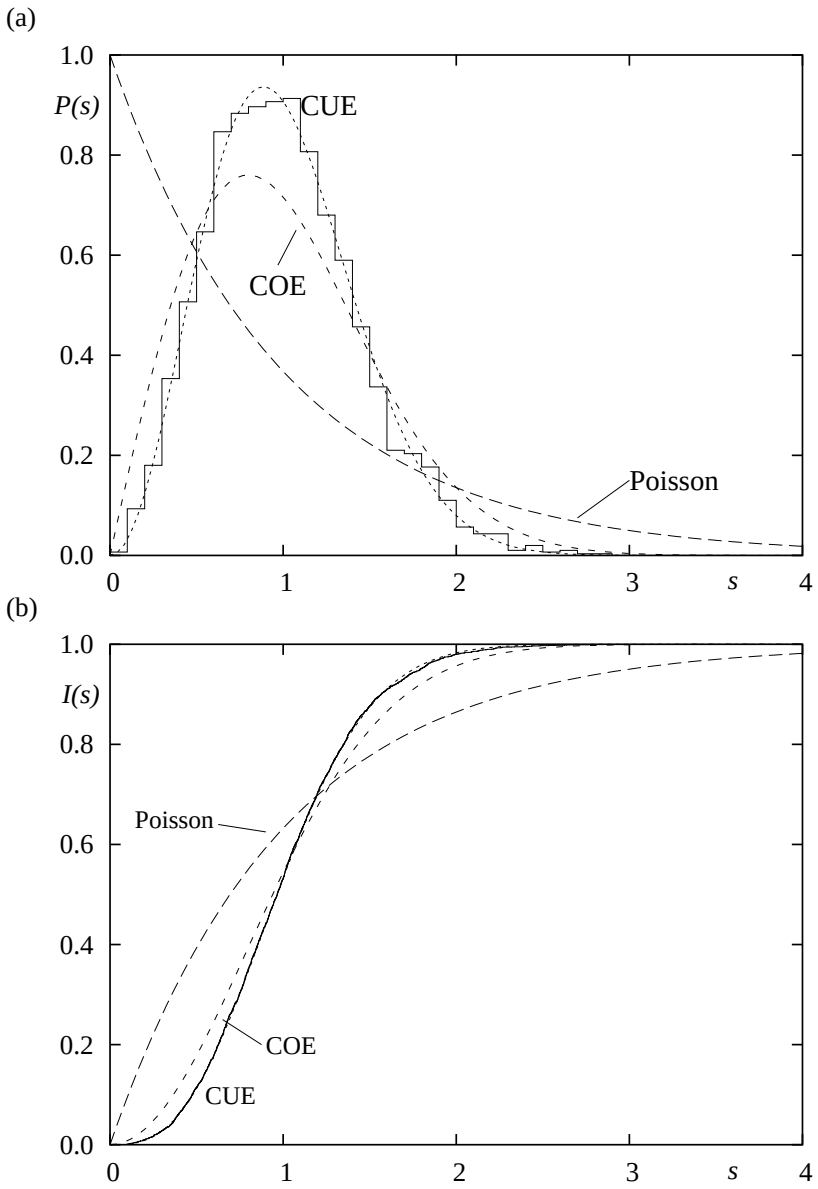

Fig. 5. (a) Level spacing distribution $P(s)$ and (b) cumulative level spacing distribution $I(s)$ for the perturbed cat map (22) with $\kappa_p = \kappa_q = 0.012$ and $N = 3001$.

$$\frac{1}{N}\#\{a \le |c_j|^2 \le b\} = \int_a^b P(\psi)\mathrm{d}\psi \quad . \tag{24}$$

Let us first discuss the corresponding random matrix results (see e.g. [31,32]). For the COE the eigenvectors can be chosen to be real and the coefficients c_j, $j = 0, \ldots, N-1$, only have to obey the normalization condition

$$\sum_{j=0}^{N-1} c_j^2 = 1 \qquad \text{with } c_j \in \mathbb{R} \quad . \tag{25}$$

Thus the joint probability for an eigenvector $\boldsymbol{c} = (c_0, \ldots, c_{N-1}) \in \mathbb{R}^N$ is

$$P_N^{\mathrm{COE}}(\boldsymbol{c}) = \frac{\Gamma(N/2)}{\pi^{N/2}} \delta\left(1 - \sum_{j=0}^{N-1} c_j^2\right) \quad , \tag{26}$$

where the prefactor ensures normalization. So the probability of one component to have a specific value y is given by integrating $P_N^{\mathrm{COE}}(\boldsymbol{c})$ over all other components,

$$\begin{aligned} P_N^{\mathrm{COE}}(y) &= \int \delta(y - c_0^2) P_N^{\mathrm{COE}}(\boldsymbol{c}) \, \mathrm{d}c_0 \cdots \mathrm{d}c_{N-1} \\ &= \frac{1}{\sqrt{\pi y}} \frac{\Gamma(N/2)}{\Gamma((N-1)/2)} (1-y)^{(N-3)/2} \quad . \end{aligned} \tag{27}$$

The mean of $P_N^{\mathrm{COE}}(y)$ is $\int_0^1 y P_N^{\mathrm{COE}}(y) \, \mathrm{d}y = 1/N$. So using the rescaling $\eta = yN$ gives

$$P_N^{\mathrm{COE}}(\eta) = \frac{1}{\sqrt{\pi N \eta}} \frac{\Gamma(N/2)}{\Gamma((N-1)/2)} (1-\eta/N)^{(N-3)/2} \quad . \tag{28}$$

In the limit of large N one gets the so-called Porter-Thomas distribution [33]

$$P_N^{\mathrm{COE}}(\eta) = \frac{1}{\sqrt{2\pi\eta}} \exp(-\eta/2) \quad , \tag{29}$$

and the corresponding cumulative distribution $I(y) = \int_0^y P(y') \, \mathrm{d}y'$ reads

$$I(\eta) = \mathrm{erf}\left(\sqrt{\eta/2}\right) \quad . \tag{30}$$

Figure 6 shows an example for the eigenvector distribution of an eigenstate of the perturbed cat map (9) with $\kappa = 0.3$ and $N = 1597$. There is good agreement with the expected COE distribution, (29), shown as dashed line.

Finally, let us consider again the map (22) which shows CUE level statistics. From this one would expect that also the eigenvector statistics follows

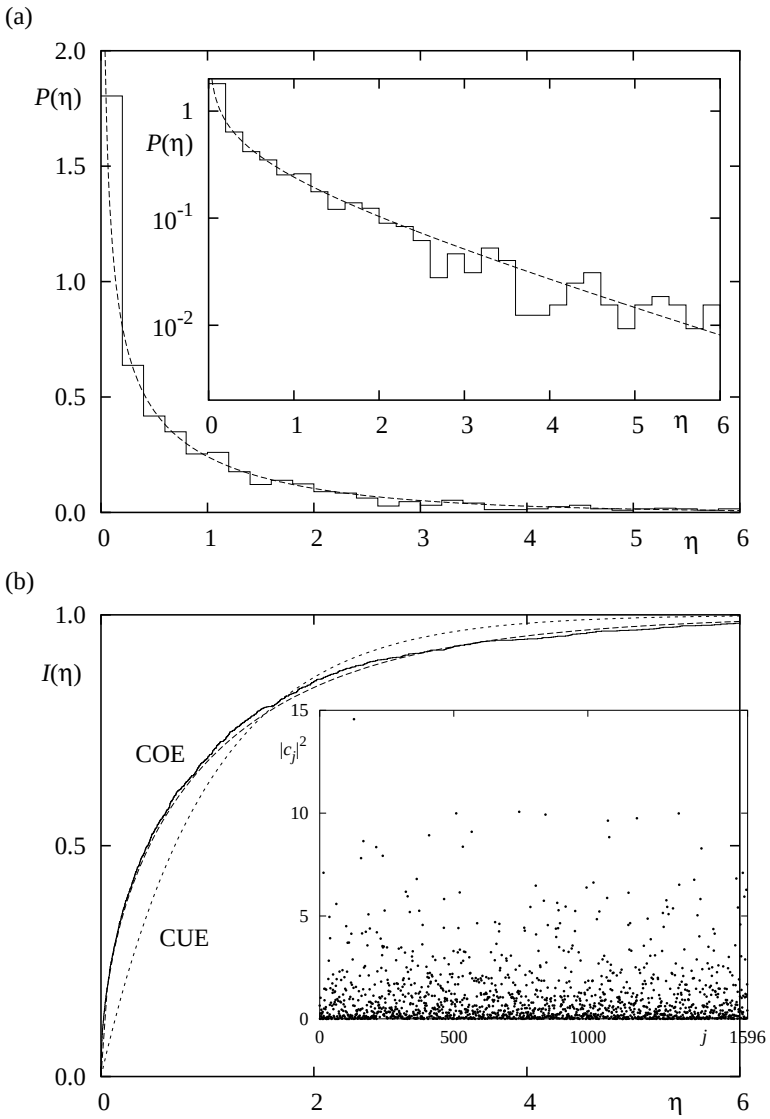

Fig. 6. (a) Eigenvector distribution for the perturbed cat map (9) with $N = 1597$ and $\kappa = 0.3$. In comparison with the asymptotic COE distribution, (28), dashed line. The inset shows the same curves in a log-normal plot. In (b) the cumulative distribution is shown and in the inset a plot of the absolute value of the components $c_j^{(n)}$, $j = 0, \ldots, N-1$ of the corresponding eigenvector $\psi_{n=20}$ is displayed.

the CUE. Similar to the case of the COE one has the normalization condition

$$\sum_{j=0}^{N-1} |c_j|^2 = 1 \qquad \text{with } c_j \in \mathbb{C} \quad . \tag{31}$$

Thus the joint probability for an eigenvector $\boldsymbol{c} = (c_0, \ldots, c_{N-1}) \in \mathbb{C}^N$ reads

$$P_N^{\mathrm{CUE}}(\boldsymbol{c}) = \frac{\Gamma(N)}{\pi^N} \delta \left(1 - \sum_{j=0}^{N-1} |c_j|^2 \right) \quad . \tag{32}$$

The probability of one component to have a specific value y is given by integrating $P_N^{\mathrm{CUE}}(\boldsymbol{c})$ over all other (complex) components,

$$\begin{aligned} P_N^{\mathrm{CUE}}(y) &= \int \delta(y - |c_0|^2) P_N^{\mathrm{COE}}(\boldsymbol{c}) \, \mathrm{d}^2 c_0 \cdots \mathrm{d}^2 c_{N-1} \\ &= (N-1)(1-y)^{N-2} \quad . \end{aligned} \tag{33}$$

Again as for the COE, the mean of $P_N^{\mathrm{CUE}}(y)$ is $1/N$ and the rescaling $\eta := yN$ leads to

$$P_N^{\mathrm{CUE}}(\eta) = \frac{N-1}{N} \left(1 - \frac{\eta}{N} \right)^{N-2} \tag{34}$$

which has mean 1. In the large N limit we have

$$P^{\mathrm{CUE}}(\eta) = \exp(-\eta) \quad . \tag{35}$$

and the cumulative distribution simply is

$$I^{\mathrm{CUE}}(\eta) = 1 - \exp(-\eta) \quad . \tag{36}$$

Figure 7 shows $P(\eta)$ for one eigenvector of the perturbed cat map (22). There is good agreement with $P^{\mathrm{CUE}}(\eta)$.

A different distribution is obtained for unperturbed cat maps: for certain subsequences of prime numbers (which depend on the map) the distribution of $\eta = \frac{1}{2} \mathrm{Re}\, \psi$ tends to the semicircle law,

$$P(\psi) = \begin{cases} \frac{2}{\pi} \sqrt{1 - \eta^2} & \text{for } \eta \le 1 \\ 0 & \text{for } \eta > 1 \quad , \end{cases} \tag{37}$$

see [34] for details (see also [35]). In Fig. 8 we show an example of an eigenstate with $N = 1597$ for the quantum map corresponding to the map (9) with $\kappa = 0$. For this N the map fulfils the conditions of [34] and one observes a nice semicircle distribution of the eigenvector. However, it seems that the approach to the asymptotic distribution is slower than for the case of the random matrix situations.

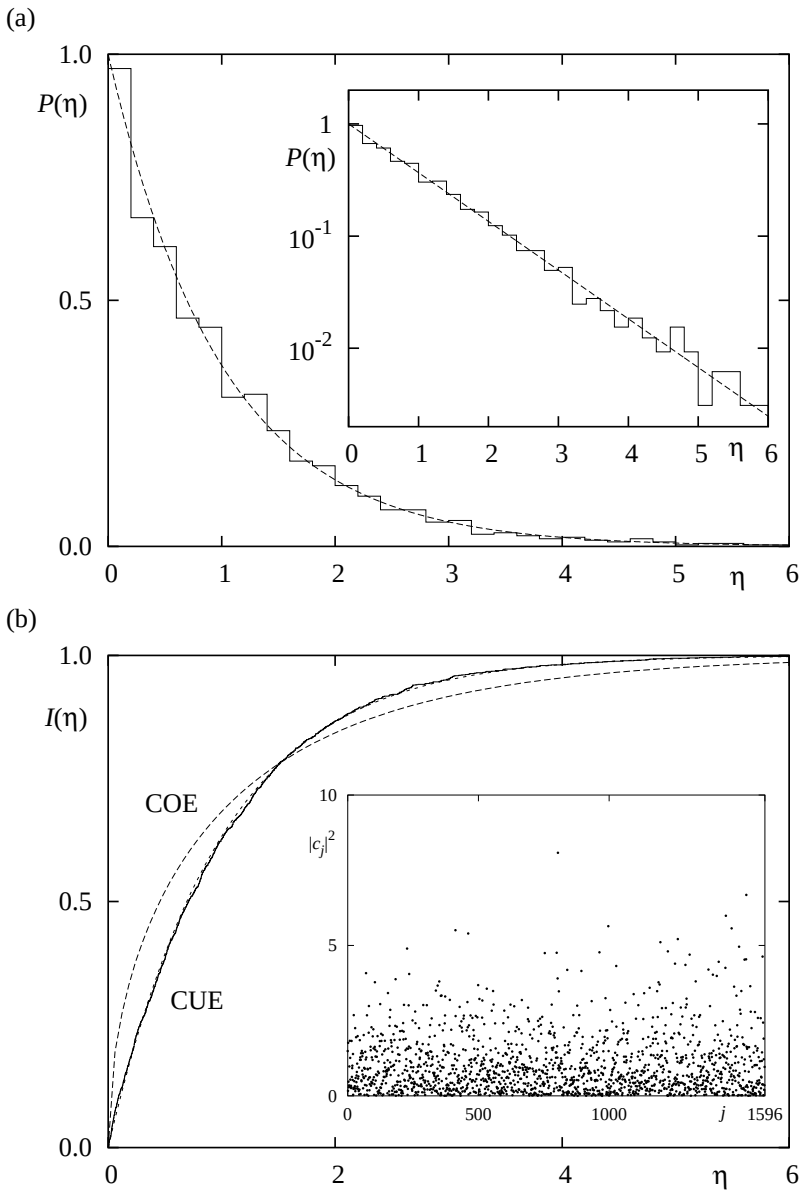

Fig. 7. (a) Eigenvector distribution of an eigenvector for the perturbed cat map (22) with $N = 1597$ and $\kappa_p = \kappa_q = 0.012$ is shown in comparison with the asymptotic CUE distribution, (35), dashed line. The inset shows the same curves in a log-normal plot. In (b) the corresponding cumulative distributions are shown and in the inset a plot of the absolute value of the components $c_j^{(n)}$, $j = 0, \ldots, N-1$ of the corresponding eigenvector $\psi_{n=2}$ is displayed.

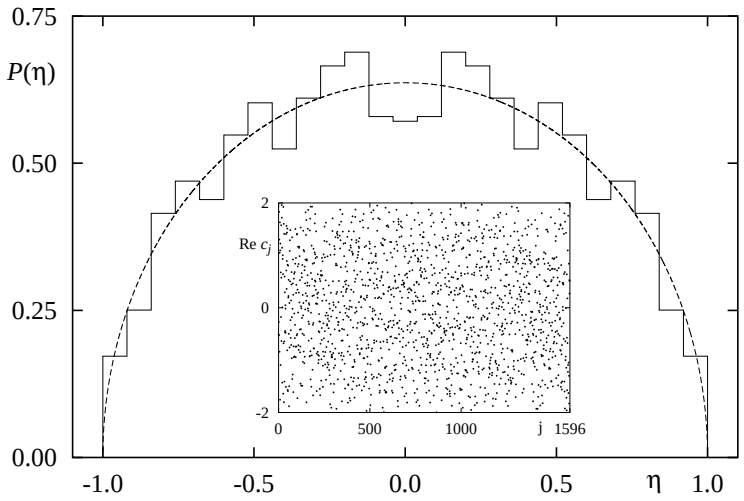

Fig. 8. Eigenvector distribution of an eigenvector for the unperturbed (i.e. $\kappa = 0$) cat map (9) with $N = 1597$. This is compared with the asymptotic semicircle law, (37). The inset shows the corresponding eigenvector (compare with the eigenvectors shown in the previous two figures).

Husimi Functions

A different representation of eigenstates is to consider a phase space representation, like for example the Husimi function, which allows for a more direct comparison with the structures for the classical map. Without going into the mathematical details, the Husimi representation is obtained by projecting the eigenstate onto a coherent state centered in a point $(q,p) \in \mathbb{T}^2$,

$$H_n(q,p) = |\langle C_{q,p}|\psi_n\rangle|^2 = \left|\sum_{j=0}^{N-1} \langle C_{q,p}|q_j\rangle\langle q_j|\psi\rangle\right|^2 = \left|\sum_{j=0}^{N-1} \langle C_{q,p}|q_j\rangle c_j\right|^2$$
$$= \left|\sum_{j=0}^{N-1} (2N)^{1/4} \exp\left(-\pi N(q^2 - \mathrm{i}pq)\right)\right. \tag{38}$$
$$\left.\exp(\pi N(-q_j^2 + 2(q-\mathrm{i}p)q_j))\vartheta_3\left(\mathrm{i}\pi N\left(q_j - \frac{\mathrm{i}\theta_1}{N} - q + \mathrm{i}p\right)\middle|\,\mathrm{i}N\right) c_j\right|^2 .$$

Here $q_j = \frac{1}{N}(\theta_2 + j)$, $j = 0,\ldots,N-1$ and $\vartheta_3(Z|\tau)$ is the Jacobi-Theta function,

$$\vartheta_3(Z|\tau) = \sum_{n\in\mathbb{Z}} \mathrm{e}^{\mathrm{i}\pi\tau n^2 + 2\mathrm{i}nZ} \quad , \qquad \text{with } Z,\tau \in \mathbb{C},\ \ \mathrm{Im}(\tau) > 0 \ . \tag{39}$$

The coefficients c_j are the components of the eigenvector ψ_n in the position representation as obtained from the diagonalization of U_N (for other generating functions than the one used in (14) one has to adapt (38)).

If one wants to compute a Husimi function on a grid of $N \times N$ points on $\mathbb{T}^2$ the computational effort grows with N^3. So for computing all Husimi function of a quantum map for a given N the computational effort grows with N^4. Already for moderate N this can be quite time-consuming, but even more importantly, usually one also wants to store all these Husimi functions on the hard-disk which limits the accessible range of N. Sometimes a smaller grid, e.g. of size $10\sqrt{N} \times 10\sqrt{N}$ can be sufficient which reduces the growth of the computational effort to N^2 for a single Husimi function and to N^3 for all Husimi functions at a given N. Even then one still needs $800\,N^2$ Bytes to store these on the hard-disk. For example for $N = 1600$ this roughly leads to 2 GB of data and for $N = 3000$ one needs approximately 7 GB. However, there are also cases where a finer grid, e.g. $2N \times 2N$ is necessary.

Theoretically one expects that for $N \to \infty$ the Husimi functions concentrate on those regions in phase space which are invariant under the map (this follows from the Egorov property). So for ergodic systems the expectation is that (in the weak sense)

$$H_n(q,p) \to 1 \quad \text{with } n = 0, ..., N-1 \text{ as the matrix size } N \to \infty \ . \qquad (40)$$

The precise formulation of this statement is the contents of the quantum ergodicity theorem for maps [36] (see [37] for the case of discontinuous maps). The quantum ergodicity theorem only makes a statement about a subsequence of density one (i.e. almost all states) which for example leaves space for scars, i.e. eigenstates localized on unstable periodic orbits. For systems with mixed phase space one (asymptotically) expects localization in the stochastic region(s) and on the tori in the elliptic regions.

In Fig. 9a) we show for the perturbed cat map with $\kappa = 0.3$ the Husimi function for the same eigenstate as in Fig. 6. As expected it shows a quite uniform distribution (of course with the usual fluctuations). In contrast for $\kappa = 6.5$ there are eigenstates such as the one shown in Fig. 9b) which localizes on the elliptic island (compare with Fig. 2).

In some sense more interesting are the Husimi functions for mixed systems as the classical dynamics shows more structure. In Fig. 10 we show some examples for the standard map with $\kappa = 3.0$. Figure 10a) shows a Husimi function which is spread out in the irregular component. In contrast in b) the Husimi function localizes on a torus around the elliptic fixpoint. The Husimi function in c) shows quite strong localization around the small elliptic island of a periodic orbit with period 4. This island is so small that it is not visible in Fig. 1. Therefore, the Husimi function displayed in Fig. 10d) indicates that the region of 'influence' of this island is much larger than the area of the island. This region is also visible in the Husimi function in Fig. 10a), as the irregular state has a very small probability in the regions around these

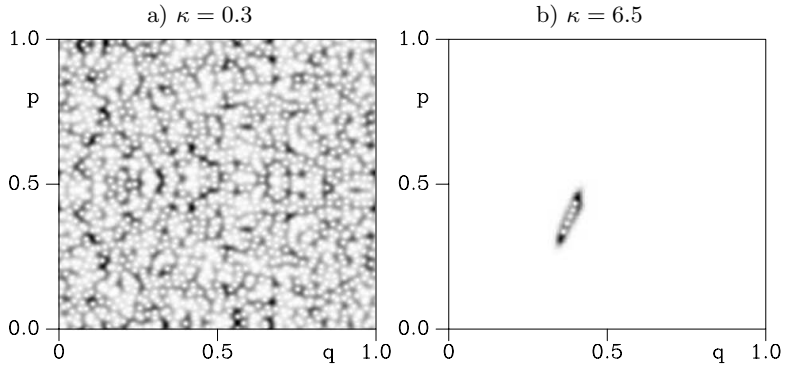

Fig. 9. In a) a Husimi function $H_n(q,p)$ of the perturbed cat map (9) with $\kappa = 0.3$ is plotted which shows the expected 'uniform' distribution. Here black corresponds to large values of $H_n(q,p)$. In b) for $\kappa = 6.5$ a state localizing on one of the elliptic islands is shown (compare with Fig. 2).

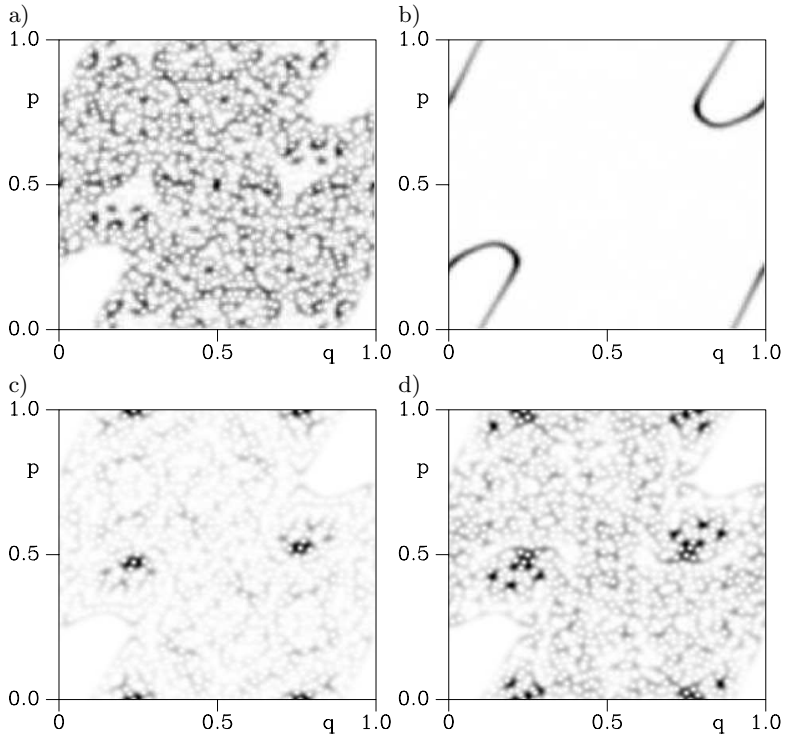

Fig. 10. Examples of Husimi functions for the standard map with $\kappa = 3.0$ and $N = 1600$.

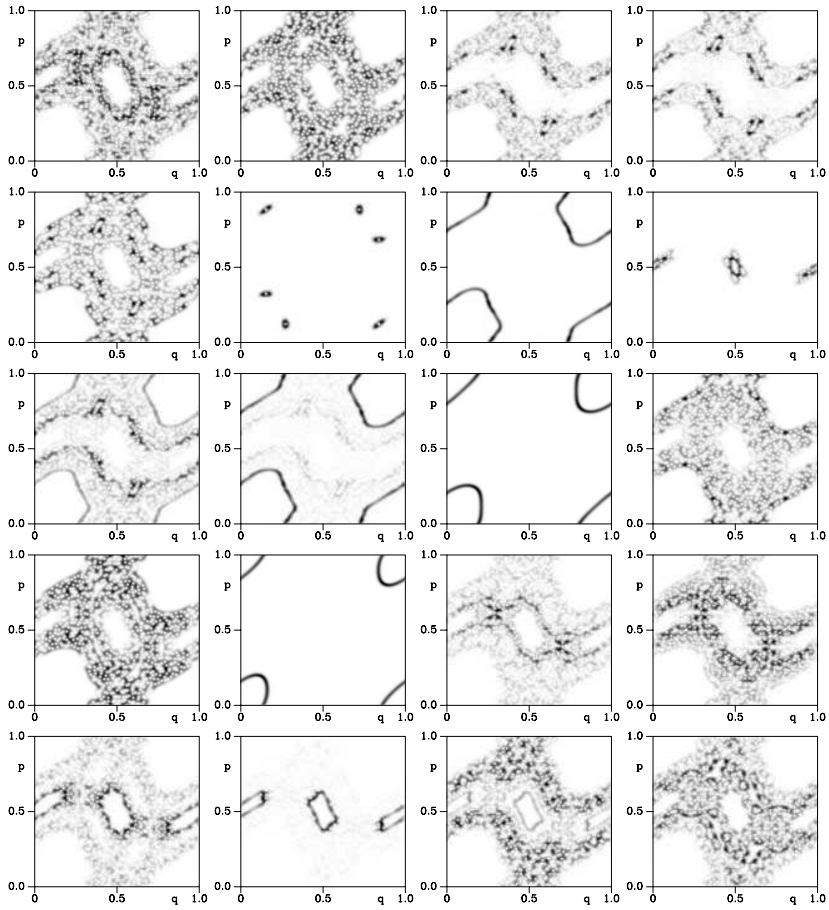

Fig. 11. Examples of Husimi functions $H_n(q,p)$ for the standard map with $\kappa = 1.5$ and $N = 1600$ for $n = 0, \ldots, 19$. (Compare with Fig. 1.)

islands. A longer sequence of Husimi functions for the standard map with $\kappa = 1.5$ shown in Fig. 11 illustrates the different types of localized states (compare with Fig. 1).

3 Billiards

3.1 Classical Billiards

A two-dimensional Euclidean billiard is given by the free motion of a point particle in some domain $\Omega \subset \mathbb{R}^2$ with elastic reflections at the boundary $\partial\Omega$. Depending on the boundary one obtains completely different dynamical

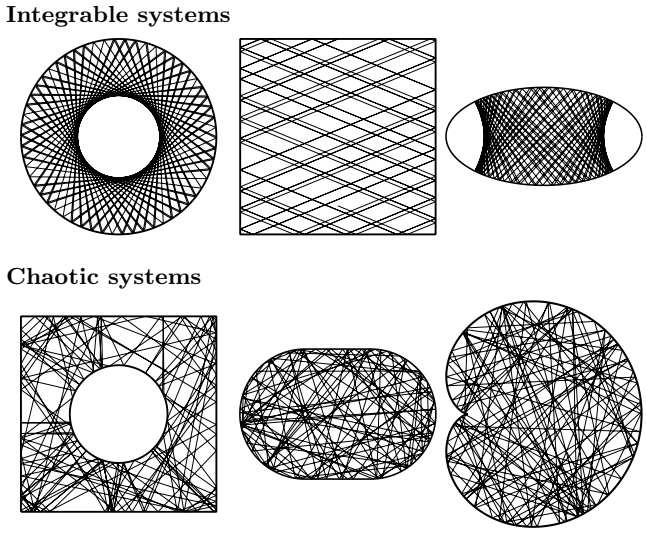

Fig. 12. Billiard dynamics in integrable and chaotic systems.

behaviour, see Fig. 12 where this is illustrated by showing orbits of billiards in a circle, a square and an ellipse, which are all integrable giving rise to regular motion. In contrast the Sinai billiard (motion in a square with a circular scatterer), the stadium billiard (two semicircles joined by parallel straight lines) and the cardioid billiard show strongly chaotic motion (they are all proven to be hyperbolic, ergodic, mixing and K-systems).

As the motion inside the billiard is on straight lines it is convenient to use the boundary to define a Poincaré section,

$$\mathcal{P} := \{(s,p) \mid s \in [0, |\partial\Omega|],\ p \in [-1,1]\} \quad . \tag{1}$$

Here s is the arclength along $\partial\Omega$ and $p = \langle \boldsymbol{v}, \boldsymbol{T}(s)\rangle$ is the projection of the unit velocity vector $\boldsymbol{v}$ after the reflection on the unit tangent vector $\boldsymbol{T}(s)$ in the point $s \in \partial\Omega$. The Poincaré map is then given by

$$\begin{aligned} P : \mathcal{P} &\to \mathcal{P} \\ \xi = (s,p) &\mapsto \xi' = (s',p') \ , \end{aligned}$$

i.e. for a given point $\xi = (s,p)$ one considers the ray starting at the point $\boldsymbol{r}(s) \in \partial\Omega$ in the direction specified by p and determines the first intersection with the boundary, leading to the new point $\xi' = (s',p')$. Explicitly, the Cartesian components of the unit velocity $\boldsymbol{v}$ of a point particle starting on $\partial\Omega$ at $\boldsymbol{r}(s)$ are determined by the angle $\beta \in [-\pi/2, \pi/2]$ measured with respect to the inward pointing normal $\boldsymbol{N} = (-T_y, T_x)$. The velocity in the $\boldsymbol{T}, \boldsymbol{N}$ coordinate system is denoted by $(p,n) = (\sin\beta, \cos\beta)$, so that in Cartesian coordinates

$$\begin{aligned} \boldsymbol{v} = (v_x, v_y) &= \begin{pmatrix} T_x & N_x \\ T_y & N_y \end{pmatrix} (p, n) \\ &= \left(T_x p + N_x \sqrt{1-p^2}, T_y p + N_y \sqrt{1-p^2} \right) \quad . \end{aligned} \tag{2}$$

Starting in the point $\boldsymbol{r}(s) \in \partial\Omega$ in the direction $\boldsymbol{v}$, the ray $\boldsymbol{r} + t\boldsymbol{v}$ intersects $\partial\Omega$ at some point $\boldsymbol{r}' = (x', y')$. If the boundary is determined by the implicit equation

$$F(x, y) = 0 \quad , \tag{3}$$

the new point $\boldsymbol{r}'$ can be determined by solving

$$F(x + tv_x, y + tv_y) = 0 \quad . \tag{4}$$

For non-convex billiards there are points $\xi = (s, p) \in \mathcal{P}$ for which there is more than one solution (apart from $t = 0$); obviously the one with the smallest $t > 0$ has to be chosen. The condition (3) can be used to remove the $t = 0$ solution analytically from (4). If F is a polynomial in x and y this allows to reduce the order of (4) by one. This approach has for example been used for the cardioid billiard leading to a cubic equation for t, see [38] for details. From the solution t one gets the coordinates $(x', y') = (x, y) + t\boldsymbol{v}$ which have to be converted (in a system dependent way) to the arclength coordinate s' (in many practical applications there is a more suitable internal variable, for example the polar angle etc.). The corresponding new projection of the momentum is given by $p' = -\langle \boldsymbol{v}, \boldsymbol{T}(s') \rangle$.

3.2 Quantum Billiards

For a classical billiard system the associated quantum billiard is given by the stationary Schrödinger equation (in units $\hbar = 2m = 1$)

$$-\Delta\psi_n(\boldsymbol{q}) = E_n \psi_n(\boldsymbol{q}) \quad , \quad \boldsymbol{q} \in \Omega \tag{5}$$

with (for example) Dirichlet boundary conditions, i.e. $\psi_n(\boldsymbol{q}) = 0$ for $\boldsymbol{q} \in \partial\Omega$. Here Δ denotes the Laplace operator, which reads in two dimensions

$$\Delta = \left(\frac{\partial^2}{\partial q_1^2} + \frac{\partial^2}{\partial q_2^2} \right) \quad . \tag{6}$$

In the Schrödinger representation the state of a particle is described in configuration space by a wave function $\psi \in L^2(\Omega)$, where $L^2(\Omega)$ is the Hilbert space of square integrable functions on Ω. The interpretation of ψ is that $\int_D |\psi(\boldsymbol{q})|^2 \ \mathrm{d}^2 q$ is the probability of finding the particle inside the domain $D \subset \Omega$.

Due to the compactness of Ω, the quantal energy spectrum $\{E_n\}$ is purely discrete and can be ordered as $0 < E_1 \leq E_2 \leq E_3 \leq \ldots$. The eigenfunctions can be chosen to be real and to form an orthonormal basis of $L^2(\Omega)$,

$$\langle \psi_n | \psi_m \rangle := \int\limits_{\Omega} \psi_n(\boldsymbol{q}) \psi_m(\boldsymbol{q}) \, \mathrm{d}^2 q = \delta_{mn} \ .$$

The mathematical problem defined by (5) is the well-known eigenvalue problem of the Helmholtz equation, which for example also describes a vibrating membrane or flat microwave cavities. For some simple domains Ω it is possible to solve (5) analytically. For example for the billiard in a rectangle with sides a and b the (non-normalized) eigenfunctions are given by $\psi_{n_1,n_2}(\boldsymbol{q}) = \sin(\pi n_1 q_1/a) \sin(\pi n_2 q_2/b)$ with corresponding eigenvalues $E_{n_1,n_2} = \pi^2(n_1^2/a^2 + n_2^2/b^2)$ and $(n_1, n_2) \in \mathbb{N}^2$. For the billiard in a circle the eigenfunctions are given in polar-coordinates by $\psi_{mn}(r, \varphi) = J_m(j_{mn} r) \exp(\mathrm{i} m \varphi)$, where j_{mn} is the n-th zero of the Bessel function $J_m(x)$ and $m \in \mathbb{Z}$, $n \in \mathbb{N}$. However, in general no analytical solutions of (5) exist so that numerical methods have to be used to compute eigenvalues and eigenfunctions.

The spectral staircase function $N(E)$ (integrated level density)

$$N(E) := \#\{n \mid E_n \leq E\} \tag{7}$$

counts the number of energy levels E_n below a given energy E. $N(E)$ can be separated into a mean smooth part $\overline{N}(E)$ and a fluctuating part

$$N(E) = \overline{N}(E) + N_{\mathrm{fluc}}(E) \ . \tag{8}$$

For two-dimensional billiards, $\overline{N}(E)$ is given by the generalized Weyl formula [39]

$$\overline{N}(E) = \frac{\mathcal{A}}{4\pi} E - \frac{\mathcal{L}}{4\pi} \sqrt{E} + \mathcal{C} + \ldots \ , \tag{9}$$

where $\mathcal{A}$ denotes the area of the billiard, and $\mathcal{L} := \mathcal{L}^- - \mathcal{L}^+$, where $\mathcal{L}^-$ and $\mathcal{L}^+$ are the lengths of the pieces of the boundary $\partial\Omega$ with Dirichlet and Neumann boundary conditions, respectively. The constant $\mathcal{C}$ takes curvature and corner corrections into account.

The simplest quantity is the δ_n-statistics, which is obtained from the fluctuating part of the spectral staircase evaluated at the unfolded energy eigenvalues $x_n := \overline{N}(E_n)$

$$\delta_n := N_0(E_n) - \overline{N}(E_n) = n - \frac{1}{2} - x_n \ , \tag{10}$$

where

$$N_0(E) := \lim_{\epsilon \to 0} \frac{N(E+\epsilon) + N(E-\epsilon)}{2} \ . \tag{11}$$

The quantity δ_n is a good measure for the completeness of a given energy spectrum. For a complete spectrum δ_n, or equivalently $N_{\mathrm{fluc}}(x)$, should fluctuate around zero. Figure 13a) shows $N_{\mathrm{fluc}}(x)$ for the stadium billiard, which indeed fluctuates around zero. In addition there is an overall modulation of

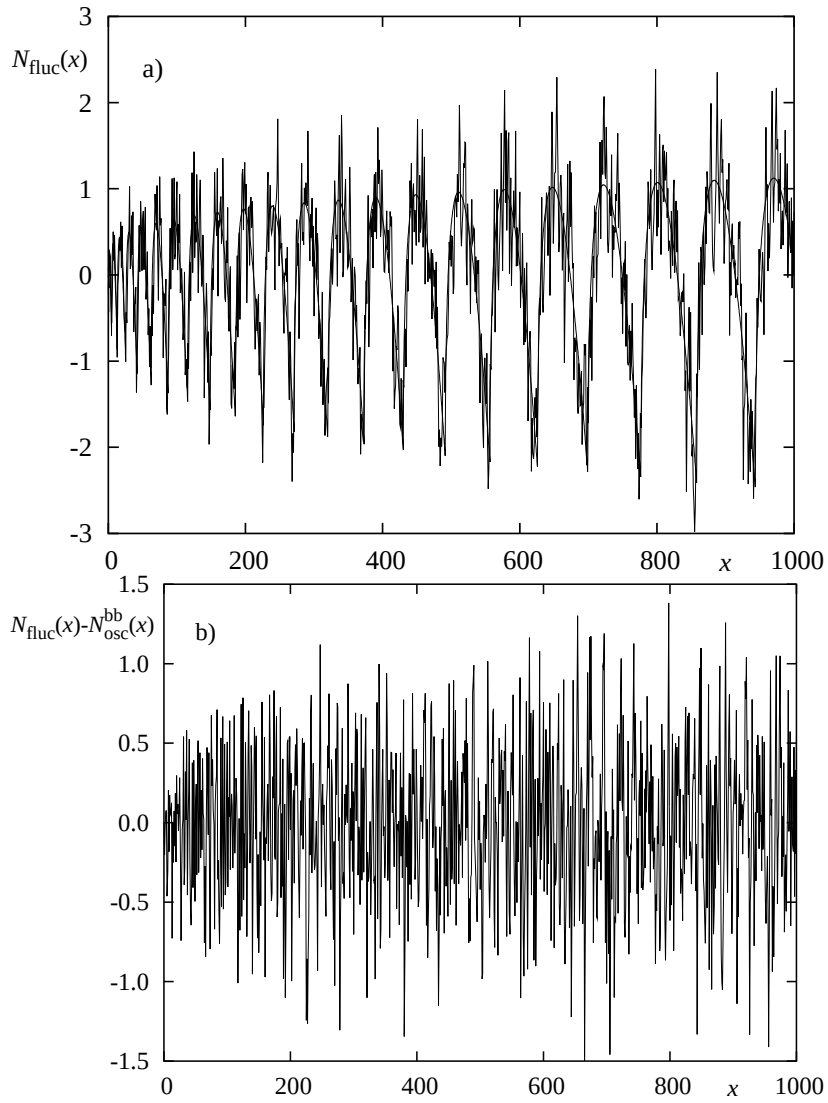

Fig. 13. Plot of $N_{\rm fluc}(x)$ for the stadium billiard ($a = 1.8$, odd-odd symmetry) together with the contribution from the bouncing ball orbits, dashed line, see (12). In b) the fluctuating part after subtraction of the contribution of the bouncing ball orbits is shown.

$N_{\rm fluc}(x)$ which is caused by the bouncing ball orbits. They form a one parameter family of periodic orbits having perpendicular reflections at the two parallel walls (of length a, see Fig. 15) of the stadium. The contribution of these orbits to the spectral staircase function reads [40]

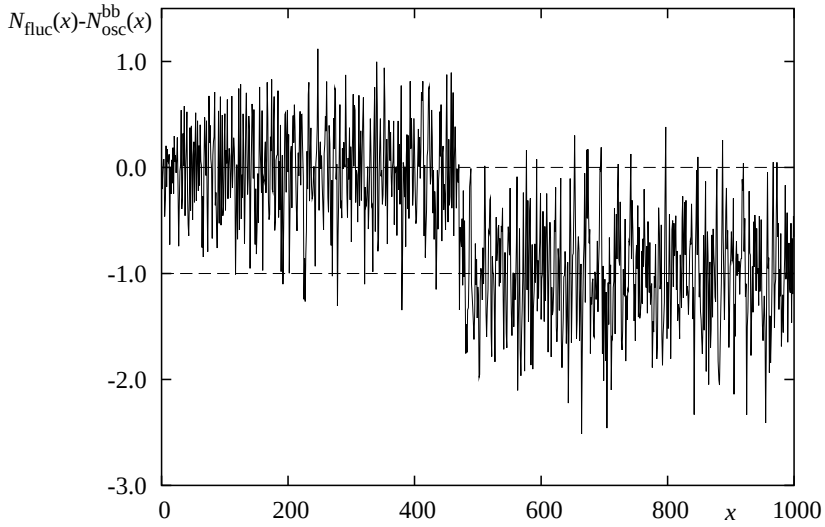

Fig. 14. Detection of missing levels using the δ_n-statistics.

$$N_{\rm fluc}^{\rm bb}(E) = \frac{a}{\pi}\sum_{n=1}^{\infty}\sqrt{E-E_n^{\rm bb}}\;\Theta\left(\sqrt{E}-\sqrt{E_n^{\rm bb}}\right)-\left(\frac{a}{4\pi}E-\frac{1}{2\pi}\sqrt{E}\right) \quad (12)$$

$$= \frac{a}{2\sqrt{\pi^3}}\,E^{\frac{1}{4}}\sum_{n=1}^{\infty}\frac{1}{n^{\frac{3}{2}}}\cos\left(2an\sqrt{E}-\frac{3\pi}{4}\right)\;, \quad (13)$$

where $E_n^{\rm bb}=\pi^2n^2$ are the eigenvalues of a particle in a one-dimensional box of length 1, and Θ is the Heaviside step function. Subtracting $N_{\rm osc}^{\rm bb}(x)$ from $N_{\rm fluc}(x)$ removes the additional oscillation, see Fig. 13b). If an eigenvalue is missing this is clearly visible by a 'jump' of δ_n in comparison to points fluctuating around 0, see Fig. 14 for an example where one eigenvalue has been removed 'by-hand'. Clearly, the energy interval in which a level is missing can be estimated from the plot.

In the same way as for quantum maps one can study the level spacing distribution and more complicated statistics, like the number variance, n-point correlation functions etc., see for example [41, 42] for some further examples for the cardioid billiard.

3.3 Computing Eigenvalues and Eigenfunctions for Quantum Billiards

There exist several numerical methods to solve the Helmholtz equation inside a domain $\Omega\subset\mathbb{R}^2$,

$$\Delta\psi(\boldsymbol{q})+k^2\psi(\boldsymbol{q})=0\;,\qquad \boldsymbol{q}\in\Omega\backslash\partial\Omega\;, \quad (14)$$

with Dirichlet boundary conditions

$$\psi(\boldsymbol{q}) = 0 \ , \qquad \boldsymbol{q} \in \partial\Omega. \tag{15}$$

For a good review on the determination of the eigenvalues of (14) see [43], which however does not cover finite element methods or boundary integral methods. Additionally, in the context of quantum chaos the plane wave decomposition [44] (see also [45] for a detailed description of the method), the scattering approach, see e.g. [46, 47, 48], and more recently the scaling method [49], are commonly used.

Here I will give a sketch of the derivation of the boundary integral method and discuss in more detail the numerical implementation. The boundary integral method reduces the problem of solving the two-dimensional Helmholtz equation (14) to a one-dimensional integral equation, see e.g. [50, 51, 52, 53, 54, 55, 56, 57, 58, 59, 60, 61, 62, 63, 64, 65] and references therein. Of course, the general approach also applies to higher dimensions but we will only discuss the two-dimensional case. For studies of three-dimensional systems by various methods see e.g. [66,67,68,69,70]. Boundary integral methods are also used in many other areas so that it is impossible to give a full account. For example they are also commonly used in acoustics, see e.g. [71] and the detailed list of references therein. Finally, the boundary integral method provides a starting point to derive the Gutzwiller trace formula, see e.g. [72, 73, 74, 75, 64].

Boundary Integral Equation

Let $G(\boldsymbol{q}, \boldsymbol{q}')$ be a Green function of the inhomogeneous equation, i.e.

$$(\Delta + k^2) G_k(\boldsymbol{q}, \boldsymbol{q}') = \delta(\boldsymbol{q} - \boldsymbol{q}') \ . \tag{16}$$

Considering the integral over Ω of the difference $\psi(\boldsymbol{q}')\cdot(16) - G_k(\boldsymbol{q}, \boldsymbol{q}')\cdot(14)$ one obtains

$$\begin{aligned} &\int\limits_{\Omega} \left[\psi(\boldsymbol{q}')\Delta' G_k(\boldsymbol{q}, \boldsymbol{q}') \ - \ G_k(\boldsymbol{q}, \boldsymbol{q}')\Delta'\psi(\boldsymbol{q}')\right] \, \mathrm{d}^2\boldsymbol{q}' \\ &= \int\limits_{\Omega} \psi(\boldsymbol{q}')\delta(\boldsymbol{q} - \boldsymbol{q}') \, \mathrm{d}^2\boldsymbol{q}' \ . \end{aligned} \tag{17}$$

Using the second Green theorem gives the Helmholtz representation

$$\begin{aligned} &\oint\limits_{\partial\Omega} \left[\psi(\boldsymbol{q}')\frac{\partial G_k}{\partial n'}(\boldsymbol{q}, \boldsymbol{q}') \ - G_k(\boldsymbol{q}, \boldsymbol{q}')\frac{\partial \psi}{\partial n'}(\boldsymbol{q}')\right] \, \mathrm{d}s' \\ &\qquad = \begin{cases} \psi(\boldsymbol{q}) \ ; & \boldsymbol{q} \in \Omega \setminus \partial\Omega \\ \frac{1}{2}\psi(\boldsymbol{q}) \ ; & \boldsymbol{q} \in \partial\Omega \\ 0 \ ; & \text{else} \end{cases} \ . \end{aligned} \tag{18}$$

Here $\boldsymbol{q}' \equiv \boldsymbol{q}(s')$ and $\frac{\partial}{\partial n'} = \boldsymbol{n}(s')\nabla$ with $\boldsymbol{n}(s) = (q_2'(s), -q_1'(s))$ denoting the outward pointing normal vector, where $(q_1(s), q_2(s))$ is a parametrization of the billiard boundary $\partial\Omega$ in terms of the arclength s, oriented counterclockwise. Special care has to be taken to obtain the result for $\boldsymbol{q} \in \partial\Omega$, see e.g. [51, 74]. (When $\boldsymbol{q}$ is in a corner of the billiard the factor $\frac{1}{2}$ has to be replaced by $\frac{\theta}{2\pi}$, where θ is the (inner) angle of the corner.) For Dirichlet boundary conditions one obtains

$$\oint\limits_{\partial\Omega} u(s') G_k(\boldsymbol{q}, \boldsymbol{q}') \, \mathrm{d}s' = 0 \ , \qquad \boldsymbol{q} \in \partial\Omega \ , \tag{19}$$

where

$$u(s) := \frac{\partial}{\partial n}\psi(\boldsymbol{q}(s)) := \boldsymbol{n}(s)\nabla\psi(\boldsymbol{q}(s)) := \boldsymbol{n}(s) \lim_{\substack{\boldsymbol{q}' \to \boldsymbol{q}(s) \\ \boldsymbol{q}' \in \Omega \setminus \partial\Omega}} \nabla\psi(\boldsymbol{q}') \tag{20}$$

is the normal derivative function of ψ.

In two dimensions a Green function for a free particle is given by the Hankel function of first kind

$$\begin{aligned} G_k(\boldsymbol{q}, \boldsymbol{q}') &= -\frac{\mathrm{i}}{4} \, H_0^{(1)}\left(k \left|\boldsymbol{q} - \boldsymbol{q}'\right|\right) \\ &= -\frac{\mathrm{i}}{4} \, \left[J_0\left(k \left|\boldsymbol{q} - \boldsymbol{q}'\right|\right) + \mathrm{i} \, Y_0\left(k \left|\boldsymbol{q} - \boldsymbol{q}'\right|\right)\right] \ . \end{aligned} \tag{21}$$

Since $H_0^{(1)}(z) \sim \frac{\mathrm{i}}{\pi} \ln z$ for $z \to 0$, the Green function $G_k(\boldsymbol{q}, \boldsymbol{q}')$ diverges logarithmically such that it is more convenient to derive an integral equation whose kernel is free of this singularity. To that end one (formally) applies the normal derivative $\frac{\partial}{\partial n}$ to (18). More carefully one has to consider a jump relation for the normal derivative function, see e.g. [51, 74]. The result is

$$u(s) = -2 \oint\limits_{\partial\Omega} \frac{\partial}{\partial n} G_k\left(\boldsymbol{q}(s), \boldsymbol{q}(s')\right) \, u(s') \, \mathrm{d}s' \ . \tag{22}$$

For the derivative of the Green function one obtains

$$\frac{\partial}{\partial n} G_k\left(\boldsymbol{q}(s), \boldsymbol{q}(s')\right) = \frac{\mathrm{i}k}{4} \cos(\phi(s, s')) \, H_1^{(1)}\left(k \, \tau(s, s')\right) \ , \tag{23}$$

where $\tau(s, s') = |\boldsymbol{q}(s) - \boldsymbol{q}(s')|$ is the Euclidean distance between the two points on the boundary and

$$\cos\phi(s, s') = \frac{\boldsymbol{n}(s)\left(\boldsymbol{q}(s) - \boldsymbol{q}(s')\right)}{\tau(s, s')} \ . \tag{24}$$

This gives the integral equation for the normal derivative $u(s)$

$$u(s) = \oint\limits_{\partial\Omega} Q_k(s,s')\, u(s')\, \mathrm{d}s' \quad , \tag{25}$$

with integral kernel

$$Q_k(s,s') = -\frac{\mathrm{i}k}{2} \cos\phi(s,s')\, H_1^{(1)}\left(k\,\tau(s,s')\right) \quad . \tag{26}$$

Equation (25) is a Fredholm equation of second kind which has non-trivial solutions if the determinant

$$D(k) := \det(\mathbf{1} - \widehat{Q}_k) \tag{27}$$

vanishes. Here $\widehat{Q}_k$ is the integral operator on $\partial\Omega$ defined by

$$\widehat{Q}_k(u(s)) = \oint\limits_{\partial\Omega} Q_k(s,s')\, u(s')\, \mathrm{d}s' \quad . \tag{28}$$

For eigenvalues E_n of the Helmholtz equation with Dirichlet boundary conditions one has $D(k) = 0$ for $k = \sqrt{E_n}$, see e.g. [74] for a detailed proof. However, for $\mathrm{Im}\, k < 0$ there can be further zeros of $D(k)$ which (for the interior Dirichlet problem) correspond to the outside scattering problem with Neumann boundary conditions [76, 77, 78] (see also [51]). Explicitly this can be seen from the factorization $D(k) = D(0)D_{\mathrm{int}}(k)D_{\mathrm{ext}}(k)$, where the factors can be written exclusively in terms of the interior and exterior problem. More aspects concerning the additional spurious solutions will be discussed in Sect. 3.3.

Before turning to the numerical implementation, let us discuss the behaviour of the integral kernel for small arguments. The Hankel function $H_1^{(1)}(x)$ reads for small arguments

$$H_1^{(1)}\left(k\,\tau(s,s')\right) \sim -\frac{2\mathrm{i}}{\pi k|s-s'|} \quad , \qquad \text{for } s - s' \to 0 \quad . \tag{29}$$

This singularity is compensated by the behaviour of

$$\cos\phi(s,s') \sim -\frac{1}{2}\kappa(s)\,|s-s'| \quad , \qquad \text{for } s' \to s \quad , \tag{30}$$

where $\kappa(s)$ is the curvature of the boundary in the point s. Here the curvature is defined by $\kappa(s) = q_1'(s)q_2''(s) - q_2'(s)q_1''(s)$ such that for example $\kappa(s) = 1$ for a circle of radius one. Thus for the integral kernel we obtain

$$Q_k(s,s') \to \frac{1}{2\pi}\kappa(s) \quad , \qquad \text{for } s - s' \to 0 \quad . \tag{31}$$

Desymmetrization

For systems with symmetries the numerical effort can be reduced by considering instead of the full system the symmetry reduced system with the corresponding Green function, see e.g. [56]. For a reflection symmetry with respect to the q_1-axis one has

$$G_k^{\pm}(\boldsymbol{q},\boldsymbol{q}') := G_k(|\boldsymbol{q}-\boldsymbol{q}'|) \pm G_k(|\boldsymbol{q}-(q_1',-q_2')|) \ , \tag{32}$$

where + applies to the case of even eigenfunctions (i.e. Neumann boundary conditions on the symmetry axis) and − to odd eigenfunctions (i.e. Dirichlet boundary conditions on the symmetry axis).

For a two-fold reflection symmetry (as in the case of the stadium billiard, see Fig. 15 for a sketch of the geometry and notations) one has altogether four different subspectra, corresponding to DD, DN, ND and DD boundary conditions on the symmetry axes q_1 and q_2, respectively. For example for Dirichlet-Dirichlet boundary conditions on the q_1- and q_2-axes the Green function reads

$$\begin{aligned} G_k^{\mathrm{DD}} =& G_k(|\boldsymbol{q}-\boldsymbol{q}'|) - G_k(|\boldsymbol{q}-(q_1',-q_2')|) \\ &+ G_k(|\boldsymbol{q}-(-q_1',-q_2')|) - G_k(|\boldsymbol{q}-(-q_1',q_2')|) \ . \end{aligned} \tag{33}$$

For Neuman boundary conditions on these two axes one gets

$$\begin{aligned} G_k^{\mathrm{NN}} =& G_k(|\boldsymbol{q}-\boldsymbol{q}'|) + G_k(|\boldsymbol{q}-(q_1',-q_2')|) \\ &+ G_k(|\boldsymbol{q}-(-q_1',-q_2')|) + G_k(|\boldsymbol{q}-(-q_1',q_2')|) \ . \end{aligned} \tag{34}$$

The advantage of exploiting the symmetries of the system is two-fold: firstly, we can separate the eigenvalues and eigenfunctions for the different symmetry

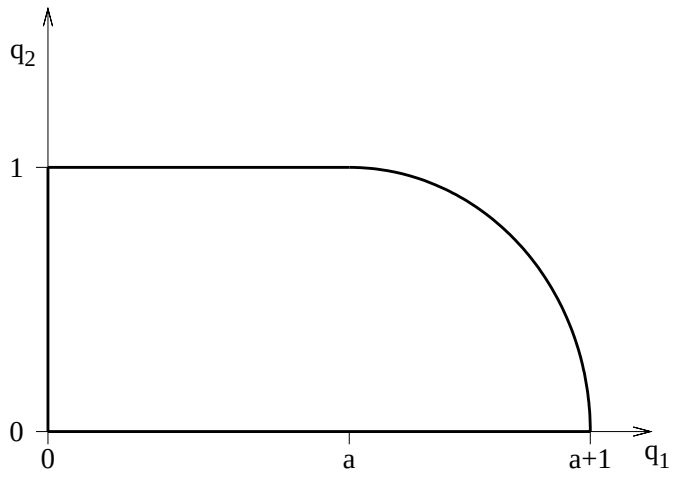

Fig. 15. Geometry of the desymmetrized stadium billiard.

classes, which is necessary for the investigation of the spectral statistics. Secondly, the numerical effort is reduced, since the integral over the whole boundary $\partial\Omega$ is reduced to an integral over a part of the boundary, which in the above examples is half or a quarter of the original boundary. The boundary along the symmetry axes need not be discretized as the boundary condition is already fulfilled by construction. Of course, for other geometries different choices for G can be more appropriate.

Finding the Eigenvalues

In the numerical computations the integral over the boundary is replaced by a Riemann sum. (There also exist more refined methods using polynomial approximations combined with Gauß-Legendre integration, see e.g. [60], which allow for a less fine discretization.) Let $\Delta s = \mathcal{L}/N$ be the discretization length of the boundary of length $\mathcal{L}$ into N pieces. Then we have

$$u(s_i) = \Delta s \sum_{j=0}^{N-1} Q_k(s_i, s_j)\, u(s_j) \ , \tag{35}$$

where $s_i = (i + 1/2)\Delta s$, $i = 0, \ldots, N-1$. Equation (35) can be written in matrix form as

$$A_k \boldsymbol{u} = 0 \ , \qquad \text{with} \quad A_{ij} = \delta_{ij} - \Delta s\, Q_k(s_i, s_j) \ . \tag{36}$$

Recall that for $s_i = s_j$ the kernel $Q_k(s_i, s_j)$ reduces to the result given in (31). The solutions of this linear equation provide approximations to the eigenvalues k_n^2 and eigenvectors u_n. This leads to the problem of finding the real zeroes of the determinant

$$\det(A_k) = 0 \tag{37}$$

as a function of $k = \sqrt{E}$, where A_k is a dense, complex non-Hermitean matrix. Due to the discretization of the integral the determinant $\det(A_k)$ will not become zero but only close to zero (actually, the discretization shifts the zeros slightly away from the real axis, see [58, 59]).

In the numerical computations it is very useful [60] to compute the singular values of the matrix A instead of its determinant. The singular value decomposition of a complex matrix is given by the product of an unitary matrix U, a diagonal matrix S and a second unitary matrix V

$$A = USV^\dagger \ . \tag{38}$$

The diagonal matrix S contains as entries SV_i the singular values of A and we have $|\det A| = |\prod \mathrm{SV}_i|$. Since the original integral equation has been discretized, the smallest singular value in general never gets zero, but just very small, see Fig. 16. Thus the minima of the smallest singular value provide

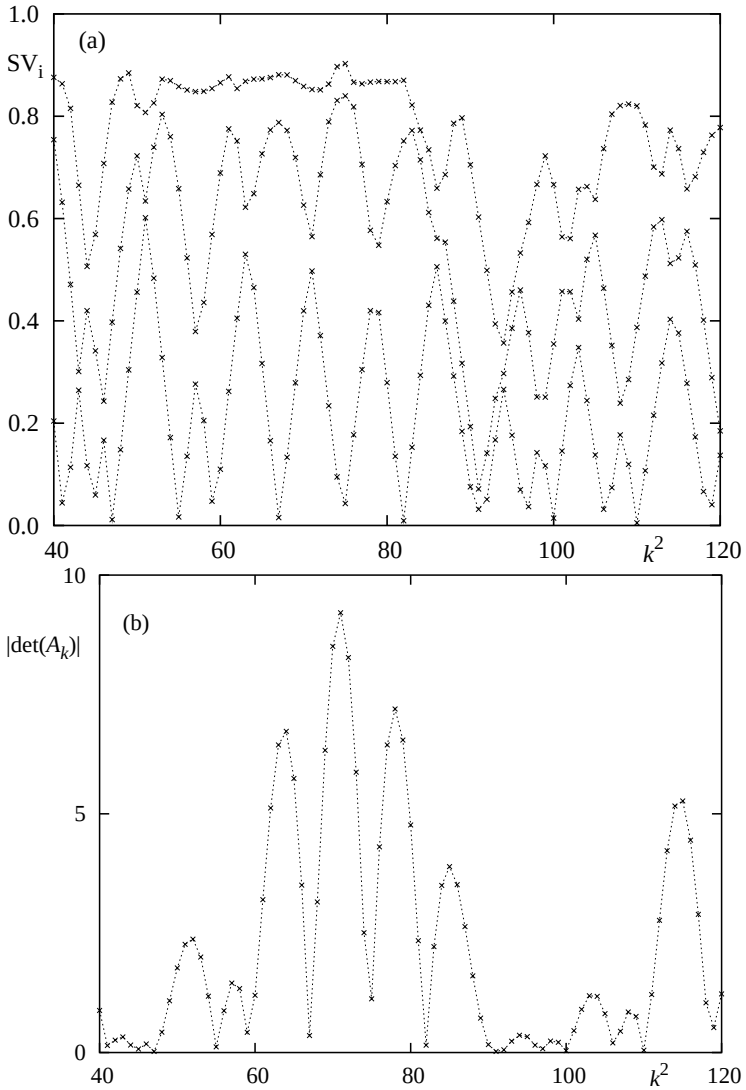

Fig. 16. In a) the three smallest singular values are shown as a function of the energy $E = k^2$ for the stadium billiard with $a = 1.8$ and odd-odd symmetry. The eigenvalues are located at the minima of the first singular value. The second and third singular values allow to locate places with near degeneracies as next to $k^2 = 90$, which can be resolved by magnification of the corresponding region, see Fig. 17. In b) $|\det(A_k)|$ is shown. The minima tend to be not as pronounced as those of the singular values.

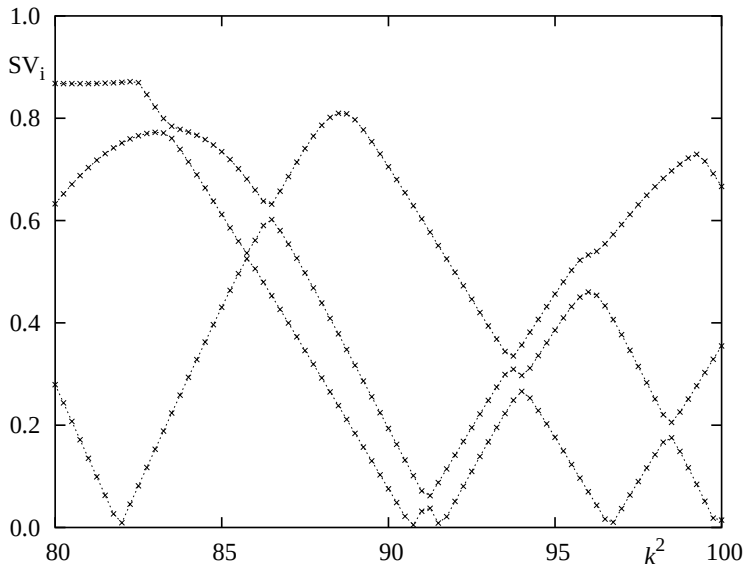

Fig. 17. A magnification of Fig. 16 shows that the singular value decomposition method easily allows to locate nearly degenerate energy levels.

approximations to the eigenvalues of the integral equation. For the numerical computation of the singular value decomposition one may for example use the NAG routine `F02XEF` or the LAPACK routines `ZGESVD` or `ZGESDD`. It turns out that the (more recent) routine `ZGESDD` is significantly faster (factor 3-5, at the expense of a higher memory consumption), in particular when also singular vectors are computed.

The advantage of the singular value decomposition in comparison to locating the zeros of the determinant is that degeneracies of eigenvalues can be detected by looking at the second singular value, which also gets small when there are two nearby eigenvalues (similarly higher degeneracies can be found by looking at the next singular values). In Fig. 16a) an example of the behaviour of the three smallest singular values is shown in the case of the stadium billiard ($a = 1.8$) with Dirichlet boundary conditions. For comparison a plot of $|\det(A_k)|$ is shown in Fig. 16b). One clearly sees that the singular value decomposition provides more information. For example, next to $k^2 = 90$ the minimum of $|\det(A_k)|$ looks slightly broader than the others, however, this does not give a clear indication that there might be more than one eigenvalue. In contrast, the singular value decomposition method allows to resolve such kind of near-degeneracies efficiently, see Fig. 17. Of course, this information is also available via $\det(A_k)$, see Fig. 18 where its real and imaginary part are plotted separately. Here (approximately) simultaneous zeros correspond to minima of $|\det(A_k)|$. However, notice that compared to

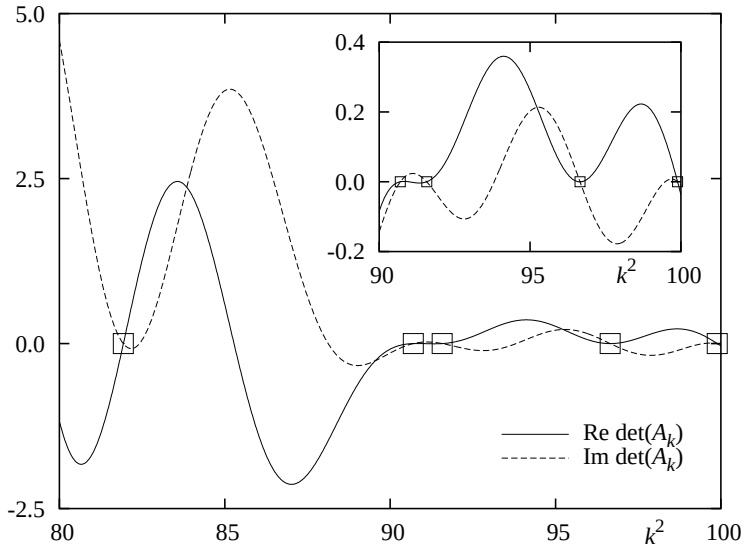

Fig. 18. Plot of real and imaginary part of $\det(A_k)$ as a function of k; the evaluation was done for 10 times as many points in k^2 than for Fig. 17. Approximately simultaneous zeros correspond to minima of $|\det(A_k)|$. The locations of the eigenvalues are marked by squares.

the singular value decomposition approach much more discretization points in $E = k^2$ are necessary.

To determine all energy levels in a given energy interval $[E_1, E_2]$ one proceeds in the following way: first one computes the singular values at equidistantly chosen points $k^2 \in [E_1, E_2]$; the energy is chosen as variable because for two-dimensional billiards the mean distance between two energy levels is approximately constant and according to the generalized Weyl formula (9) given by $\frac{4\pi}{\mathcal{A}}$. The finer the step size is chosen the easier the minima can be resolved, however, at the same time the computing time to cover a given energy range increases correspondingly. The actual step size is a compromise between these two aspects; good results have been achieved by using a step size of the order of $\frac{1}{5}\,\frac{4\pi}{\mathcal{A}}$ (for systems with many near level degeneracies, e.g. integrable or near-integrable systems, a smaller step size can be helpful).

The matrix size N is chosen according to $N = b\frac{\mathcal{L}}{\lambda} = b\frac{\mathcal{L}k}{2\pi}$, such that one obtains b discretization points per units of the inverse of the de Broglie wave length $\lambda = \frac{2\pi}{k}$ along the boundary $\mathcal{L}$. Typical choices for b are between 5 and 12 depending on the system and the wanted accuracy.

From the first scan one locates all minima of the smallest singular value. If also the second singular value has a minimum next to a minimum of the first one, one has to use a refined discretization in E around the minimum (the numerical implementation is a bit more sophisticated, in order to account for

several special situations, so that only a minimal number of additional points need to be computed). Once an isolated minimum is found, an approximation to the eigenvalue can be computed by different methods. Either one can perform a refined computation around the minimum, which can be quite time-consuming, or one can use a local approximation by a parabola [79]. A linear interpolation also gives good results: From the three points 1:$(k_1^2, SV_1(k_1^2))$, 2:$(k_2^2, SV_1(k_2^2))$, 3:$(k_3^2, SV_1(k_3^2))$, characterizing a minimum of the first singular value, one has two different lines $\overline{12}$ and $\overline{23}$ with different slopes, of which the line with the larger slope has to be chosen. The intersection of this line with the zero axis gives a good approximation to the eigenvalue, which one can refine if necessary. By repeatedly applying this for all minima, all energy levels in a given interval can be found. In fact, it is possible to develop a computer program which takes care of all this such that all levels can be found automatically.

A good check of the completeness is provided by considering the δ_n statistics, see the example in Sect. 3.2. The accuracy of the computed eigenvalues can be estimated from the bracket of the minimum given by the three points 1,2,3 if the matrix dimension N is large enough. For N too small (for a given resolution in E) one does not obtain a peaked, but a broad minimum. This is illustrated in Fig. 19 by magnifying Fig. 17 around the minimum with $k^2 \approx 96.5$ for different N. One clearly sees the parabolic structure around

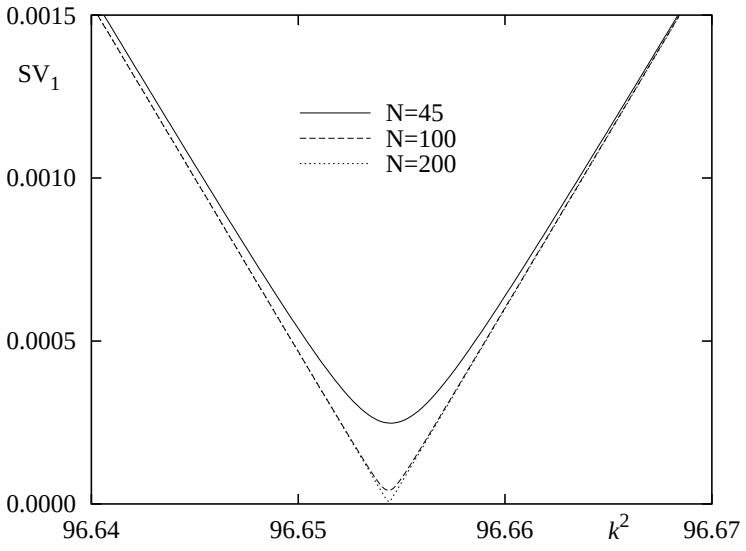

Fig. 19. Magnification of Fig. 17 around the minimum with $k^2 \approx 96.5$ for different matrix sizes N. One nicely sees the pronounced parabolic structure for $N = 45$ which gets smaller for larger N.

the minimum for smaller N and for larger N one recovers the essentially linear behaviour of the smallest singular value.

Tests of the accuracy of the method can be obtained by considering a system where the eigenvalues are known. For example for the circular billiard the eigenvalues can be computed with arbitrary accuracy. Also billiards where the eigenvalues can be computed by other methods (e.g. conformal mapping method [80, 81]) allow a determination of the accuracy of the method. For a study of the scaling of the error for various billiards see [63]. In addition computations of the normal derivative function $u_n(s)$ and the eigenfunction (both inside and outside of Ω) allow to check the quality of the numerical method and program.

Computing Eigenfunctions

From a minimum of the smallest singular value we obtain an approximation of the eigenvalue and at the same time the corresponding singular vector $\boldsymbol{u}$ gives an approximation to the normal derivative function $u(s)$. The NAG routine `F02XEF` scales the singular vector such that its first component is real. Thus for a correct solution also the other components should be essentially real, which provides another check for the implementation of the method and the accuracy of the eigenvalues.

The eigenfunction in the interior of the domain Ω can now be calculated from the normal derivative function,

$$\psi(\boldsymbol{q}) = -\frac{\mathrm{i}}{4} \oint\limits_{\partial\Omega} H_0^{(1)}\left(k\left|\boldsymbol{q}-\boldsymbol{q}(s)\right|\right)\, u(s)\, \mathrm{d}s \ , \qquad \text{for } \boldsymbol{q} \in \Omega \backslash \partial\Omega \ . \tag{39}$$

The computation of the eigenfunction can be simplified by taking into account that

$$\oint\limits_{\partial\Omega} J_0\left(k\left|\boldsymbol{q}-\boldsymbol{q}(s)\right|\right)\, u(s)\, \mathrm{d}s = 0 \ , \tag{40}$$

because the J_0-part of $G_k(\boldsymbol{q}, \boldsymbol{q}')$ is a solution of the homogeneous equation corresponding to (16). Thus (39) is equivalent to

$$\psi(\boldsymbol{q}) = \frac{1}{4} \oint\limits_{\partial\Omega} Y_0\left(k\left|\boldsymbol{q}-\boldsymbol{q}(s)\right|\right)\, u(s)\, \mathrm{d}s \ , \qquad \text{for } \boldsymbol{q} \in \Omega \backslash \partial\Omega \ . \tag{41}$$

If one uses a desymmetrization, such as (32), (33) or (34), the above formula (41) has to be modified accordingly.

In Fig. 20 we show some examples of normal derivatives $u_n(s)$ and the corresponding eigenfunctions of the billiard, computed via (41). The imaginary part of $u_n(s)$ is typically 5 or more orders of magnitude smaller than the real part. It is interesting to see that part of the structure of the eigenfunctions is also reflected in $u_n(s)$. For example for eigenstates with small probability in the region of the quarter circle also the normal derivative is small for $s < \pi/2$.

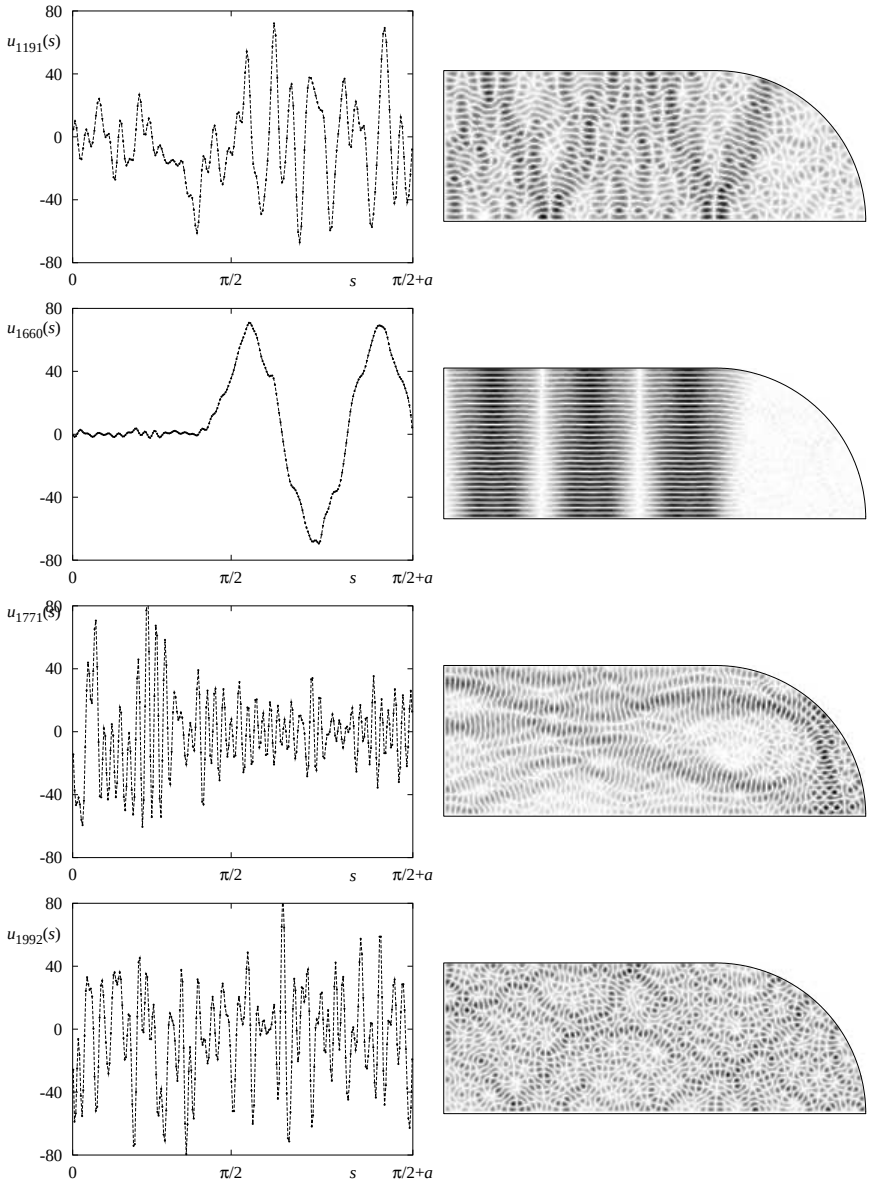

Fig. 20. Examples of normal derivative functions $u_n(s)$ and the corresponding eigenfunctions in the stadium billiard (odd-odd symmetry, $a = 1.8$). Here black corresponds to high intensity of $|\psi_n(\boldsymbol{q})|^2$.

Spurious Solutions I: Real Green Function Approach

In certain situations and for some numerical methods it may happen that one obtains in addition to the true solutions of the Helmholtz equation (14) further so-called *spurious solutions*. This question is discussed in some of the papers on the boundary integral method, in particular see [50, 52, 53] and [55, 58]. There are essentially two different situations in which they are encountered. The first is that one uses for the Green function instead of the Hankel function, see (21), just the real part, i.e.

$$G_k(\boldsymbol{q},\boldsymbol{q}') = \frac{1}{4} Y_0\left(k\left|\boldsymbol{q}-\boldsymbol{q}'\right|\right) \quad . \tag{42}$$

This seems reasonable as according to (40) the J_0-Bessel function does not contribute to the eigenfunction. Moreover then one can work with an entirely real matrix for which the singular value decomposition can be computed much faster. However, when using this approach, there appear additional zeros (for each correct one there is one additional one) and the singular values loose their nice linear structure, see Fig. 21. To overcome the problem of these additional zeros a parametrized Green function

$$G_k^{(\beta)}(\boldsymbol{q},\boldsymbol{q}') = \frac{1}{4}\ \left[\beta J_0\left(k\left|\boldsymbol{q}-\boldsymbol{q}'\right|\right) + Y_0\left(k\left|\boldsymbol{q}-\boldsymbol{q}'\right|\right)\right] \tag{43}$$

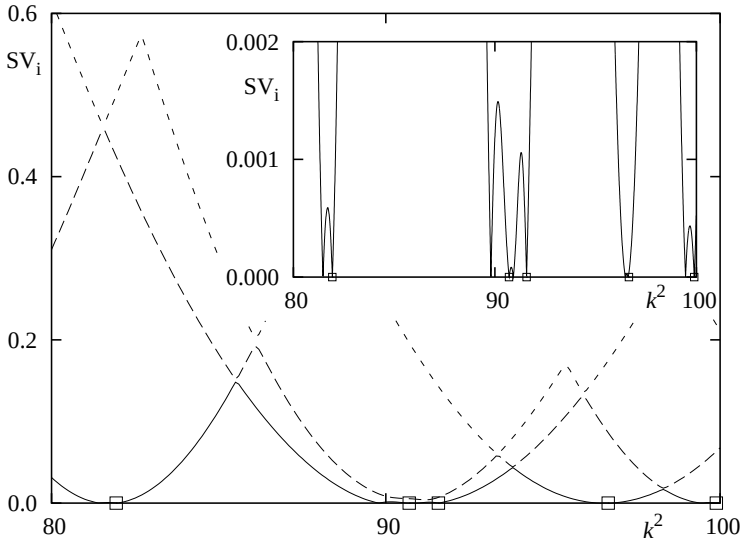

Fig. 21. Using the real Green function (42) leads to spurious solutions (see the inset) in addition to the correct eigenvalues marked by squares (compare with Fig. 17). For each true solution there is an additional spurious one (hardly visible at $k^2 \approx 91$ and $k^2 \approx 96$).

is used in [58]. Thus for $\beta = 0$ we obtain (42) and for $\beta = -\mathrm{i}$ we get (21). So using a purely real Green function means to vary $\beta \in \mathbb{R}$ which changes the location of the spurious solutions but not those of the true ones. This is illustrated in Fig. 22 around the eigenvalue $k^2 = 81.93\ldots$ with $\beta \in [0, 0.1]$. Clearly on this scale the true solution does not change under variation of β (apart from the region of the avoided crossing which is due to the finite matrix size and gets smaller for larger N) whereas the spurious solution strongly varies with β. For $\beta = -\gamma\mathrm{i}$ with increasing real γ the additional zeros move away from the real axis and it seems that for $\beta = -\mathrm{i}$ they do not have any significant influence on the real axis. Still there could be cases where also for $\beta = -\mathrm{i}$ such a solution becomes relevant, but for convex geometries we have not encountered this situation. For an example of a non-convex geometry see Sect. 3.3.

As an explicit example for the influence of parameterized Green function (43) let us consider the circular billiard with radius 1, where the Fredholm determinant reads (see e.g. [58, 74])

$$D(k) = \prod_{l=-\infty}^{\infty} \left[-\mathrm{i}\pi k H_l^{(1)'}(k) J_l(k)\right] \quad . \tag{44}$$

As this product converges absolutely in the whole complex k-plane (apart from a cut along the negative real axis) zeros of $D(k)$ occur when one of the

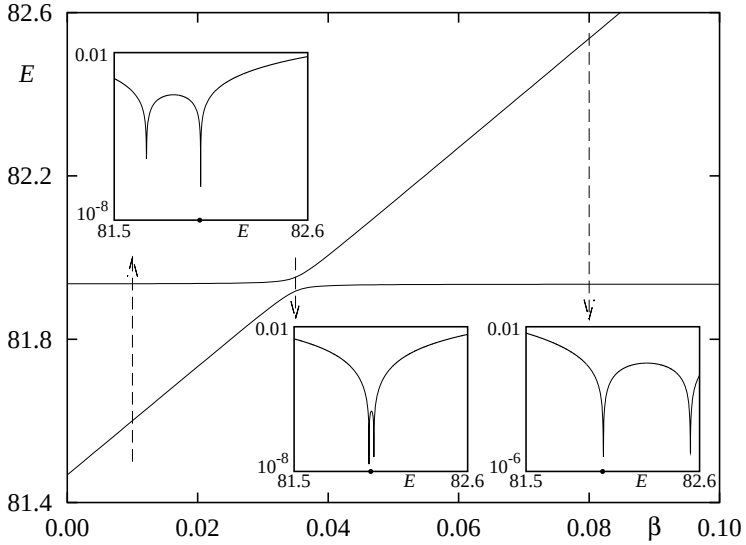

Fig. 22. Plot of the minima of the singular values around the eigenvalue $k^2 = 81.93\ldots$ with varying β using the parametrized Green function (43). The insets show the corresponding structure of the first singular value with a logarithmic vertical scale (matrix size for this computation: $N = 200$).

factors in the product vanishes [74]. Clearly, the real zeros of $D(k)$ correspond to the eigenvalues j_{ml} of the circular billiard with radius 1 and Dirichlet boundary conditions. The further zeros stem from the functions $H_l^{(1)'}(z)$ which have only zeros with $\mathrm{Im}\, z < 0$ [82], and do not correspond to physical solutions of the interior problem. However, they can be related to resonances of the exterior scattering problem, but with Neumann boundary conditions [76, 77]. Because of the radial symmetry the S-matrix is diagonal in angular momentum space

$$S_{l'l} = -\frac{H_l^{(2)'}(k)}{H_l^{(1)'}(k)} \delta_{l'l} \tag{45}$$

and therefore the resonances are at those complex k for which

$$H_l^{(1)'}(k) = 0 \ , \tag{46}$$

i.e. the same condition as implied by (44).

If one uses the parametrized Green function (43) one can show (analogous to the derivation of (44)) that for the circular billiard

$$D^{(\beta)}(k) = \prod_{l=-\infty}^{\infty} \left[\pi k \left(\beta J_l'(k) + Y_l'(k)\right) J_l(k)\right] \ . \tag{47}$$

For $\beta = 0$, which corresponds to the real Green function (42), we get additional zeros of $D^{(0)}(k)$ when $Y_l'(k) = 0$. Varying β from zero to $-\mathrm{i}$ these real zeros turn complex. At first sight one might think that these are connected to the places with $H_l^{(1)'}(k) = 0$, however numerical computations show that (for all studied cases) these move away from the real axis with a positive imaginary part and for $\beta = -\mathrm{i}$ one has $H_l^{(1)'}(k) = 0$ only for $\mathrm{Im}\, k < 0$. Thus the spurious solutions for the real Green function are not related to resonances of the scattering problem with Neumann boundary conditions.

These examples suggest to use the full complex Green function (21) instead of the real variant (42). Even though the numerical computation is more time-consuming for the complex case their advantages over choosing (42) are obvious as the variation of β is time-consuming as well (and non-trivial to implement in an automatic way).

Spurious Solutions II: Non-convex Geometries

Even when choosing the complex Green function (21) it is possible to encounter spurious solutions: For the circular the additional complex zeros of $D(k)$ are sufficiently far away from the real axis, i.e. $\mathrm{Im}\, k \ll 0$ so that they do not lead to problems with the application of the boundary integral method. However, when one considers different geometries the resonances of the corresponding scattering system could be closer to the real axis. This can be

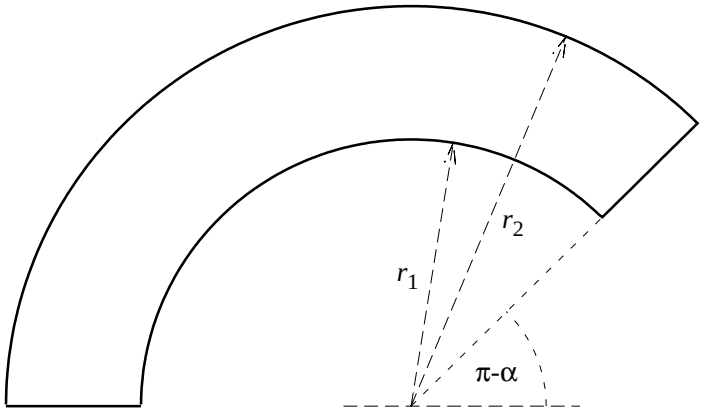

Fig. 23. Boundary of the annular sector billiard for $\alpha = \frac{7}{8}\pi$ and $r_1 = 0.4$ and $r_2 = 0.6$.

nicely studied for the annular sector billiard, see Fig. 23, as the eigenvalues and eigenfunctions can be determined numerically with arbitrary accuracy. Using the ansatz [83, §25]

$$\psi(r,\phi) = [J_\nu(kr) + cY_\nu(kr)]\sin(\nu\phi) \tag{48}$$

with $\nu = m\frac{\pi}{\alpha}$, $m = 0, 1, 2, ...$ and requiring $\psi(r_1, \phi) = 0$ and $\psi(r_2, \phi) = 0$ gives the (implicit) eigenvalue equation

$$J_\nu(kr_1)Y_\nu(kr_2) - Y_\nu(kr_1)J_\nu(kr_2) = 0 \ . \tag{49}$$

For each m one gets a sequence of zeros $k_{mn} = \sqrt{E_{mn}}$.

Figure 24 shows for the annular sector billiard with $\alpha = \frac{49}{50}\pi$ the first three singular values as a function of k^2. The solutions of (49) are marked by triangles. Clearly, there are additional minima, which can be associated with resonances of the dual scattering problem (for further details and examples of this association for the annular sector billiard see [84]). In the limit of $\alpha \to \pi$ these resonances are given by the eigenvalues of the circular billiard of radius r_1 with Neumann boundary conditions. For this billiard the ansatz $\psi(r,\phi) = J_m(kr)$ together with $\frac{\partial\psi(r,\phi)}{\partial r}\Big|_{r=r_1} = 0$ gives the eigenvalue equation

$$mJ_m(kr_1) - kr_1J_{m+1}(kr_1) = 0 \ . \tag{50}$$

The circles shown in Fig. 24 correspond to the solutions of (50) and provide a very good description of the additional minima.

Thus the question arises how to detect and distinguish these additional solutions. First, of course their existence and relevance strongly depends on the system one is studying. In many situations (for example convex geometries) there appear to be no complex solutions coming close enough to the

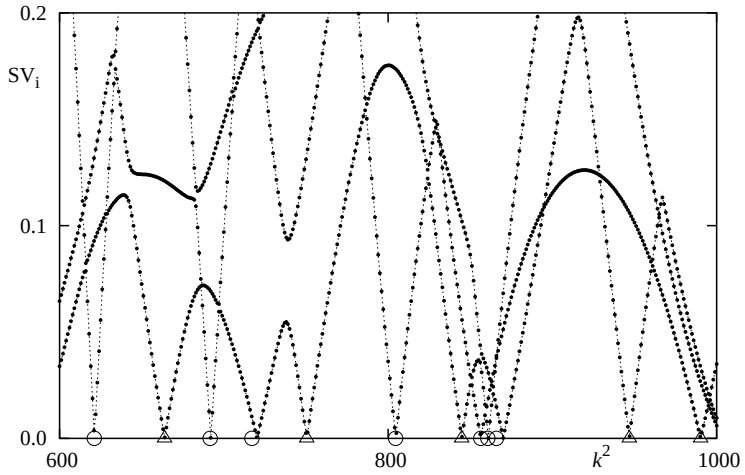

Fig. 24. First three singular values as a function of $E = k^2$ of the annular sector billiard for $\alpha = \frac{49}{50}\pi$ and $r_1 = 0.4$ and $r_2 = 0.6$. The triangles correspond to the exact eigenvalues for the annular sector billiard, computed from (49) and the circles correspond to the eigenvalues of the circular billiard with radius r_1 and Neumann boundary condition, determined via (50).

real axis. Intuitively this seems reasonable as long as there are no trapped orbits outside of the billiard as these should give rise to resonances with small imaginary part.

However, if such additional solutions exist they will show up in the δ_n statistics by an offset of $+1$ at each additional eigenvalue (unless one by chance misses the same number of 'correct' eigenvalues). If one has a system with such additional solutions one approach is to plot the corresponding normal derivative function $u(s)$ and the eigenfunction. Usually they will behave quite differently for a correct eigenvalue and for a spurious solution. For example for the case of the annular sector billiard the normal derivative function for a spurious solution is discontinuous along the boundary and the corresponding eigenfunction also has contributions outside of the billiard, see Fig. 26. Another test would be to use the normalization condition (51) for the normal derivative and compute the norm of the eigenfunction in the interior of the billiard. These two are the same for proper eigenfunctions whereas for spurious solutions they will disagree. Unfortunately, this is a highly inefficient method as the computation of the eigenfunction in Ω is quite time-consuming. Instead of computing the normalization for the full billiard one could restrict to smaller subregions, e.g. for the annular sector billiard one could integrate over the region of the circle with radius r_1 and check if it is different from zero indicating a spurious solution. For the annular sector billiard the additional zeros of the Fredholm determinant $D(k)$ are complex as long as $\alpha < \pi$. Thus for $N \to \infty$ these minima will stay bounded away from zero in contrast to

the minima corresponding to the eigenvalues. However, in practice it is not possible to check this as one has to make N too large to distinguish these from the correct eigenvalues.

More generally, spurious solutions can be understood by a second look at the boundary integral equations. Namely, for the interior Dirichlet problem we have the *single layer* equation, (19), and the *double layer* equation, (25). On the other hand, the single-layer equation for the outside scattering problem with Neumann boundary conditions at $\partial\Omega$ is also given by the double layer equation (25). (see e.g. [51, 50]). As a consequence, scattering solutions of the outside scattering problem with Neumann boundary conditions at $\partial\Omega$ may become relevant for real k. Namely, for resonances with small imaginary part they can lead to additional solutions for the double layer equation which are numerically indistinguishable from the correct solutions. However, these solutions do not correspond to solutions of the interior problem and they do not fulfill the single layer equation. So a possibility to distinguish spurious solutions for the interior Dirichlet problem is to check the validity of the single layer equation as well, which is only fulfilled simultaneously for correct solutions of the interior Dirichlet problem.

A common approach (see e.g. [50] and references therein) to incorporate this from the beginning is by combining the single layer and double layer equation using a linear superposition. By this the solutions of the outside problem with Neumann boundary conditions can be removed. Because of the singular kernel in the single layer equation special care has to be taken with

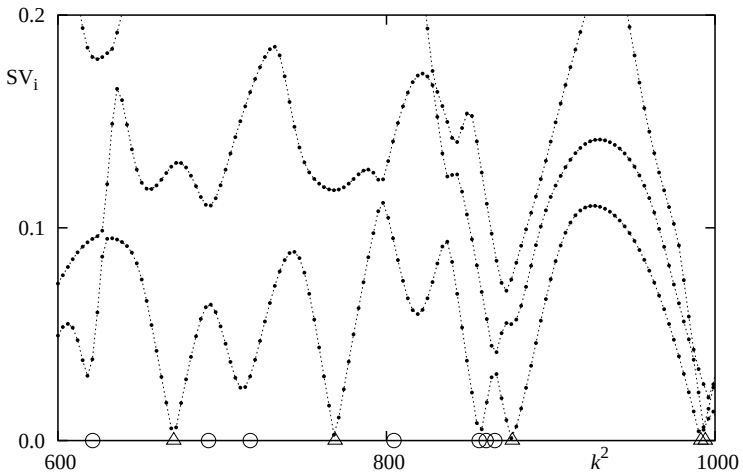

Fig. 25. First three singular values as a function of $E = k^2$ of the annular sector billiard for $\alpha = \frac{7}{8}\pi$ and $r_1 = 0.4$ and $r_2 = 0.6$. The triangles correspond to the exact eigenvalues for the annular sector billiard, computed from (49) and the circles correspond to the eigenvalues of the circular billiard with radius r_1 and Neumann boundary condition, determined via (50)

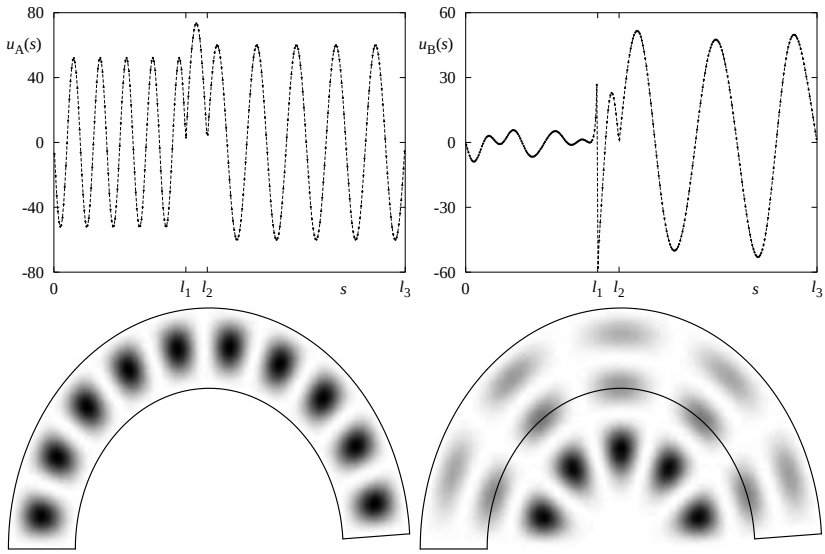

Fig. 26. Normal derivative functions $u_n(s)$ corresponding to the correct eigenvalue with $E = 663.88\ldots$ (left) and the spurious one with $E = 691.77\ldots$ (right). Here $l_1 = r_1\alpha$, $l_2 = r_1\alpha + r_2 - r_1$ and $l_3 = r_1\alpha + r_2 - r_1 + \alpha r_2$. One clearly sees the discontinuity in $u_n(s)$ for the spurious solution. This is also reflected in the structure of the eigenfunction which for the spurious solution has its main contribution outside of the billiard. Notice that in both cases the eigenfunction has been computed according to (40) inside and outside of Ω. The fact that for the correct eigenfunction $\psi_n(\boldsymbol{q}) = 0$ (within the numerical accuracy) for $\boldsymbol{q} \in \mathbb{R}^2 \backslash \Omega$ is another test of the accuracy of the eigenvalue computations and eigenfunctions.

the implementation. For the more difficult case of billiards with magnetic field see [65].

Derived Quantities in Terms of the Normal Derivative Function

As the normal derivative function contains all information to determine the eigenfunction, it is interesting to see if this approach can be used to compute other quantities of interest. For example, if one wants to calculate expectation values $\langle\psi|A|\psi\rangle$ of some operator A in the state ψ, one has to ensure that the eigenfunction ψ is normalized, $\langle\psi|\psi\rangle = \int_\Omega |\psi(\boldsymbol{q})|^2 \, \mathrm{d}^2 q = 1$. In principle this could be done by considering $\left(\langle\widetilde{\psi}|\widetilde{\psi}\rangle\right)^{-1} \widetilde{\psi}(\boldsymbol{q})$ of an unnormalized eigenfunction $\widetilde{\psi}$. However, an accurate computation of $\langle\widetilde{\psi}|\widetilde{\psi}\rangle$ using (41) is quite time consuming. Fortunately, there is a simpler way to achieve a normalized ψ: If ψ is a normalized eigenfunction with eigenvalue $E = k^2$ and $u(s)$ is the corresponding normal derivative then we have the following normalization condition for $u(s)$ [55, 59]

$$\frac{1}{2}\oint\limits_{\partial\Omega} \boldsymbol{n}(s)\boldsymbol{q}(s)\,|u(s)|^2\,\mathrm{d}s = k^2 \quad . \tag{51}$$

If $\widetilde{u}(s)$ is an unnormalized normal derivative, then one obtains by

$$u(s) = \frac{\sqrt{2}\,k}{\sqrt{\oint\limits_{\partial\Omega} \boldsymbol{n}(s)\boldsymbol{q}(s)\,|\widetilde{u}(s)|^2\,\mathrm{d}s}}\widetilde{u}(s) \tag{52}$$

a normalized one. Starting with a normal derivative normalized in this way, any other quantities (e.g. expectation values) determined in terms of $u(s)$ have the correct normalization.

This is just the first example out of many highlighting the importance of the normal derivative for numerical computations of quantities related to eigenfunctions. For example, there are explicit expressions in terms of $u_n(s)$ to compute the

– normalization of ψ, (51), [55, 59]
– eigenfunction ψ, (41)
– momentum distribution

$$\widehat{\psi}_n(\boldsymbol{p}) = \frac{1}{2\pi}\int\limits_{\Omega} \mathrm{e}^{-\mathrm{i}\boldsymbol{p}\boldsymbol{q}}\psi_n(\boldsymbol{q})\,\mathrm{d}^2q = -\frac{\mathrm{i}}{4\pi p_n^2}\int\limits_{\partial\Omega} \mathrm{e}^{-\mathrm{i}\boldsymbol{p}\boldsymbol{q}(s)}\boldsymbol{p}\boldsymbol{q}(s)u_n(s)\,\mathrm{d}s\,, \tag{53}$$

and radially integrated momentum distribution [85, 86]

$$I(\varphi) := \int\limits_0^\infty \left|\widehat{\psi}_n(r,\varphi)\right|^2 r\,\mathrm{d}r \quad , \tag{54}$$

see [86] for details.
– Husimi functions (see e.g. [87, 88])
– autocorrelation function of eigenstates [89].

In Figs. 27-29 we show for the cardioid billiard examples of eigenfunctions in position space, the corresponding momentum distributions, the angular momentum distributions (for further details and examples see [86]) and the corresponding Husimi functions $H_n(s,p)$. The first example in Fig. 27 shows an example of a scarred state, i.e. an eigenstate which shows localization round an unstable periodic orbit [90]. Below the three-dimensional plot of the state is the corresponding density plot (black corresponding to high intensity) in which the localization is clearly visible. Also the corresponding three-dimensional plot of the momentum distribution $\widehat{\psi}_{567}(\boldsymbol{p})$ reveals enhanced contributions in the directions $\varphi = \pi/2, 3\pi/2$. This is also seen in the plot of $I_{567}(\varphi)$ which shows that the probability to find the particle with momentum near $\pi/2$ is significantly enhanced compared to the mean of $1/(2\pi)$.

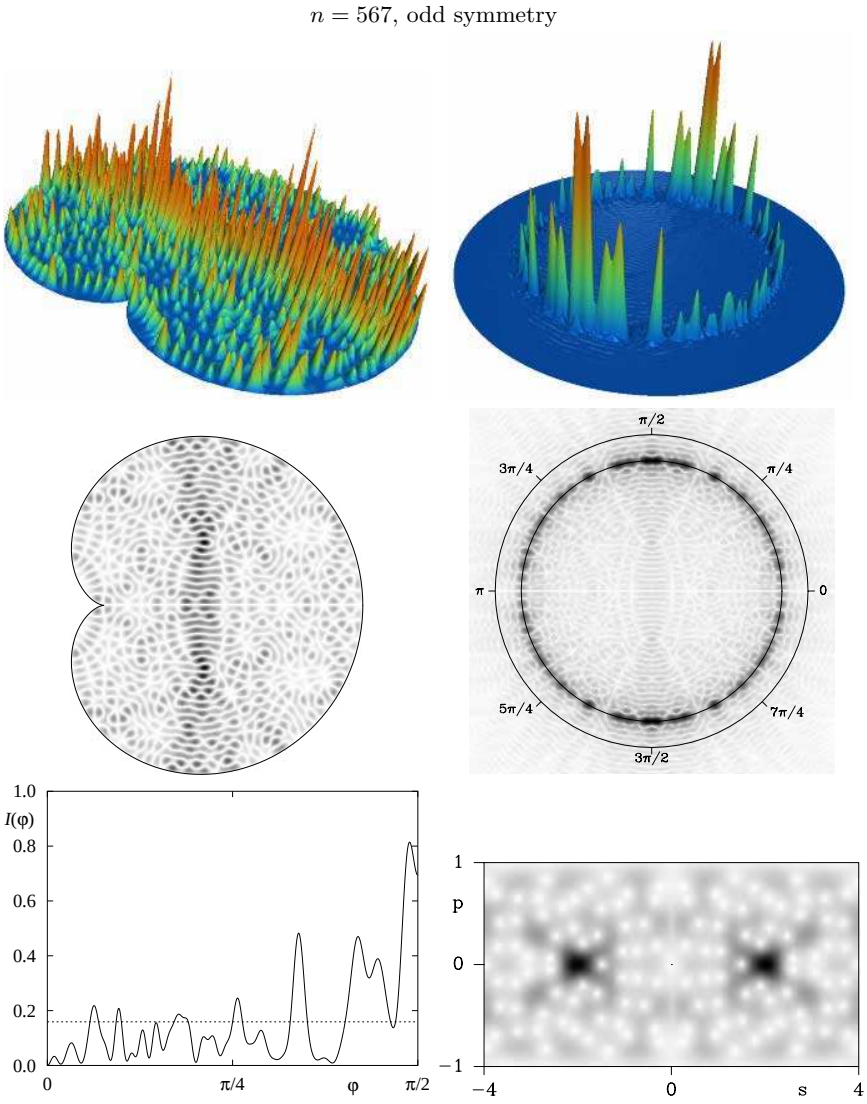

Fig. 27. Three-dimensional plots of $|\psi_{567}(\boldsymbol{q})|^2$, $|\widehat{\psi}_{567}(\boldsymbol{p})|^2$, their corresponding grey-scale pictures and the plot of the radially integrated momentum distribution $I_{567}(\varphi)$. The momentum distribution $|\widehat{\psi}_{567}(\boldsymbol{p})|^2$ is concentrated around the energy shell, which is indicated by the inner circle. This state is localized along the shortest unstable periodic orbit, leading to an enhancement of $|\widehat{\psi}_{567}(\boldsymbol{p})|^2$ near to $\varphi = \pi/2, 3\pi/2$, also seen in the plot of $I_{567}(\varphi)$ near to the momentum direction $\varphi = \pi/2$ (marked by a triangle). This localization is also clearly visible in the Husimi representation.

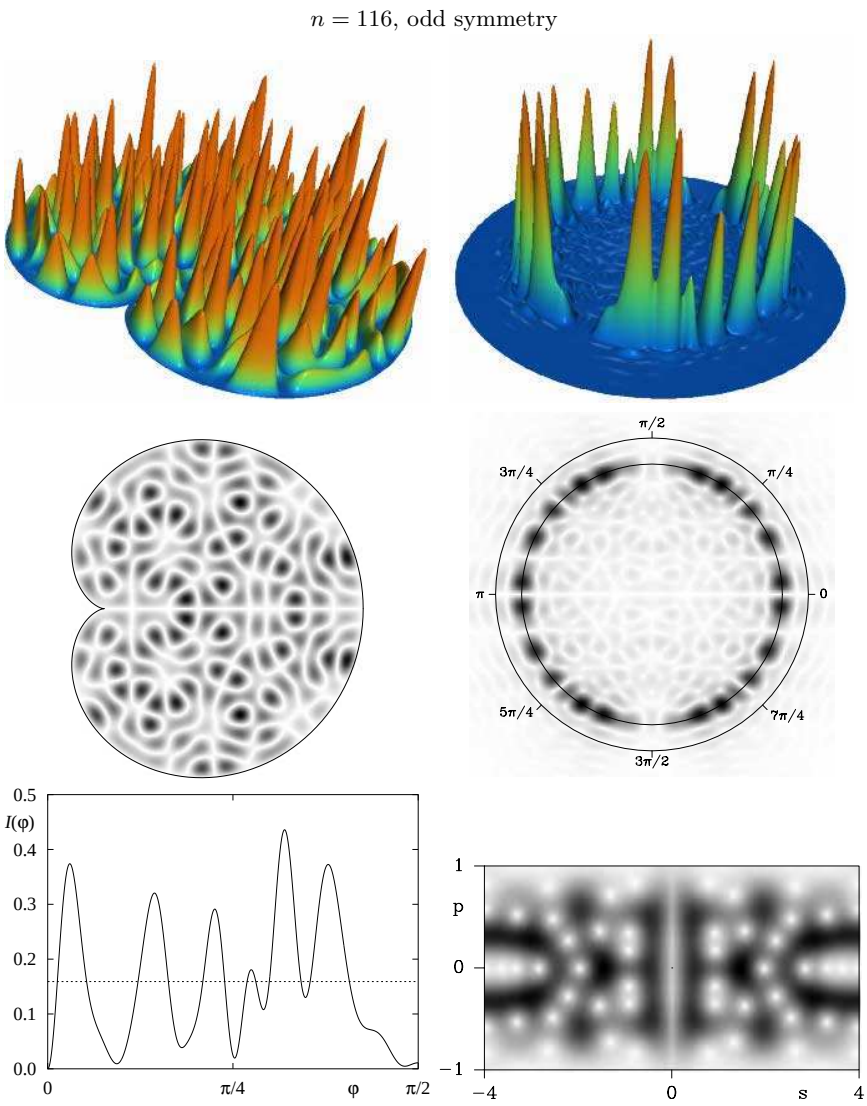

Fig. 28. Same as in the previous figure but for $n = 116$. In this case there is no prominent localization neither in position nor in momentum space.

Another representation is the Husimi-Poincaré representation $H_n(s, p)$ where s corresponds to the arclength coordinate along the billiard boundary and p corresponds to the projection of the unit velocity vector after the reflection on the tangent in the point s. In this picture the localization around the unstable orbit is maybe most clearly seen; the places of high intensity are on the

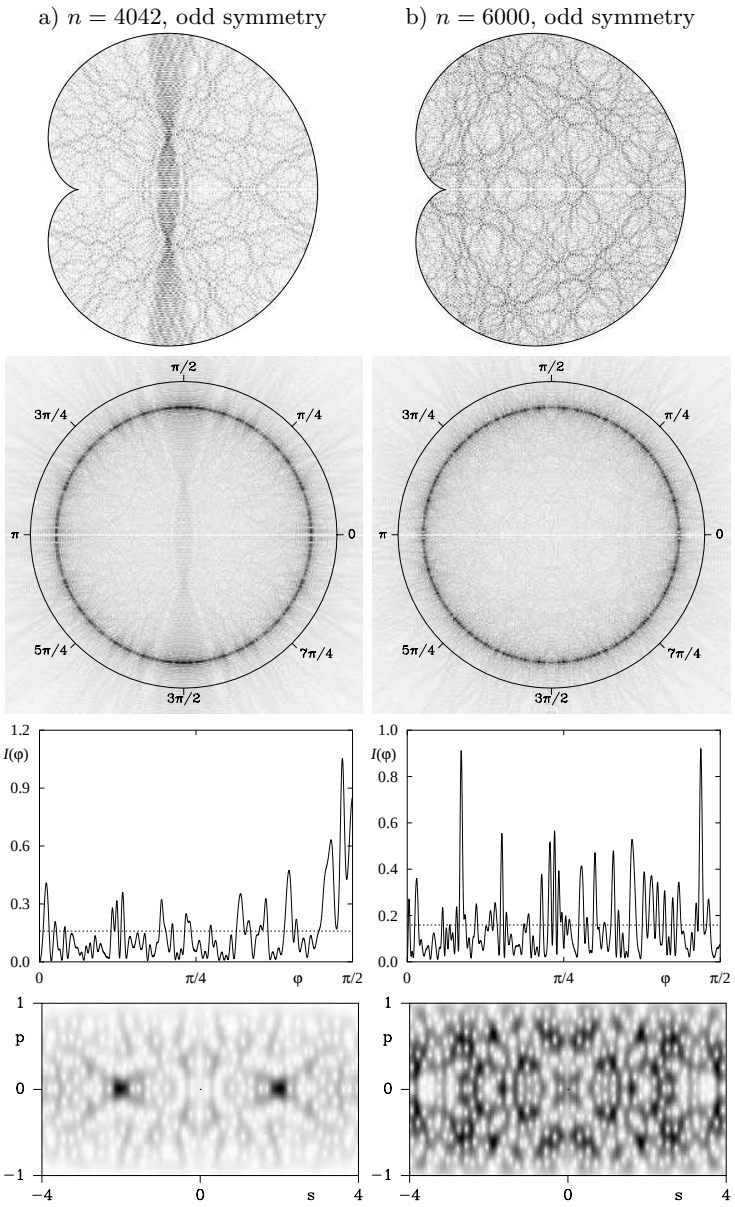

Fig. 29. The eigenfunction in a) shows localization along the shortest unstable orbit which is also reflected in the momentum distributions and in the Husimi function. The eigenfunction in b) is an example which appears to be quite delocalized both in position and in momentum space. The pictures look like those expected (according to the quantum ergodicity theorem) for a 'typical' eigenfunction.

line $p = 0$ (perpendicular reflection) and match perfectly with the position of the orbit.

The second example shown in Fig. 28 is an 'ergodic' state, i.e. a state which does not show any significant localization (as much as something like this is possible at low energies) neither in position nor in momentum space (apart from the localization on the energy shell). This is nicely reflected in the various representations. Two further examples are shown in Fig. 29 where a) is a higher lying scar and b) is another 'typical' state (in the sense of the quantum ergodicity theorem).

4 Concluding Remarks – Or What's Left ?

There are many more issues related to scientific computing in quantum chaos which I did not mention in these notes. They for example include visualization techniques, programming of parallel computers (e.g. using PVM or MPI), or using vector computers etc. Also the more implementation specific aspects, including the choice of a programming language have not been discussed. A good starting point to learn about computing in quantum chaos are quantum maps as their numerics is much easier (one can use a black-box routine to get all eigenvalues at once) than for billiard systems, where more complicated methods have to be used.

Acknowledgements

I would like to thank the organizers of the summer school *The Mathematical aspects of Quantum Chaos I* in Bologna, Mirko Degli Esposti and Sandro Graffi for all their effort, especially Mirko for dealing with everything (including food and wine ;-) in the 'Italian way'! Moreover, I am grateful to Grischa Haag for many discussions on quantum maps, and Ralf Aurich for discussions on the boundary element method. I would like to thank Professor Frank Steiner and Silke Fürstberger for useful comments on the manuscript and Professors Uzy Smilansky and Andreas Knauf for useful remarks on an earlier version of this text. I would like to thank Fernando Perez for pointing out some speed improvements of the `Python` implementation. Most parts of this work have been done during my stay at the School of Mathematics, University of Bristol, and the Basic Research Institute in the Mathematical Sciences, Hewlett-Packard Laboratories Bristol, UK. In particular I would to thank Professors Jonathan Keating and Sir Michael Berry for all their support. Moreover, I am particularly indebted to Professor Steiner and the University of Ulm for their support throughout the last months. I acknowledge partial support by the Deutsche Forschungsgemeinschaft under contract No. DFG-Ba 1973/1-1.

Appendix: Computing Eigenvalues of Quantum Maps

The first thing when thinking of solving a certain problem numerically is to decide on the programming language. There are numerous possibilities, ranging from Assembler, Fortran, Pascal, C, C++, Java, etc. to using packages like Octave, Matlab, Maple or Mathematica. Here I will use the quite recent scripting language `Python` [91]. Of course it is beyond the scope of this text to give an introduction to this language; several excellent introductions can be found on the Python homepage. In addition to the basic Python installation you will also need the `Numeric` package [92], which is also simple to install. The following programs together with further information can be obtained from [20]. If you have been wondering about the name - yes it originates from Monty Python's flying circus, and at several places the documentation refers to more or less famous Monty Python sketches.

So here is `pert_cat.py` (the full version can be obtained via [20]):

```
#!/usr/bin/env python

import cmath
from Numeric import zeros,Float,Complex
from math import sin,pi,sqrt
import LinearAlgebra

def quantum_cat(N,kappa):
 """For a given N and kappa this functions returns the
 corresponding unitary matrix U of the
 quantized perturbed cat map.
 """
 mat=zeros((N,N), Complex) # complex matrix with NxN elements
 I=1j # predefine sqrt(-1)
 # now fill each matrix element
 # (note: this can be done much faster, see the on-line version)
 for k in range(0,N):
 for l in range(0,N):
 mat[k,l]=cmath.exp(2.0*I*pi/N*(k*k-k*l+l*l)+ \
 I*kappa*N/2.0/pi*sin(2.0*pi/N*l))/sqrt(N)
 return(mat)

def compute_evals_pcat(N,kappa):
 """For a given N and kappa this functions returns
 the eigenvalues and eigenphase of the unitary matrix U
 filled via quantum_cat(N,kappa).
 """
 matU=quantum_cat(N,kappa) # fill matrix U_N
 # determine eigenvalues of U_N:
 evals=LinearAlgebra.eigenvalues(matU)

 # determine phase \in [0,2\pi] from the eigenvalues
 phases_N = arctan2(evals.imag,evals.real) + pi
```

```
 # useful to determine level-spacing
 phases = concatenate([phases_N,[phases_N[0]+2.0*pi]])
 return(evals,phases)

### Main (used if pert_cat.py is called as script)
if __name__ == '__main__':
 from string import atoi,atof
 import sys

 # Determine eigenvalues and eigenphases
 (evals,phases)=compute_evals_pcat(atoi(sys.argv[1]), \
 atof(sys.argv[2]))

 for k in range(0,N): # print eigenvalues
 print("% e % e % e ") % \
 (evals[k].real,evals[k].imag,phases[k],abs(evals[k]))
```

The only drawback of the above code is that the loop to fill the matrix is slower than a corresponding code in C or Fortran (notice that there are some very nice ways of overcoming this by inlining of code or on-the-fly compilation which are presently being developed for example in the context of SciPy [93]). However, as `diagonalize` uses the LAPACK library the most time-consuming part (at least for larger N) is done in an efficient way (not taking into account the possibility of using ATLAS [24] for further speed improvements).

As a first test do (for $N = 101$ and $\kappa = 0.3$)

```
python pert_cat.py 101 0.3
```

It will output the (complex) eigenvalues as a sequence x, y pairs. As a test, whether these all lie on the unit circle the third column is the absolute value of the eigenvectors. To plot the resulting data you may use

```
python pert_cat.py 101 0.3 > pcat_101_0.3.dat
```

which redirects the output of the program to the file `pcat_101_0.3.dat`. To plot the resulting file use your favourite plotting program, e.g. for `gnuplot` [94] just do

```
plot "pcat_101_0.3.dat" using 1:2 with points
```

Now we would like to compute the level spacing distribution. To do this let us use an interactive Python session in which we do

```
from Numeric import * # Numeric package
from pert_cat import compute_evals_pcat # above pert_cat routines
from AnalyseData import * # histogram (see below)

N=53
kappa=0.3
(evals,phases)=pert_cat.compute_evals_pcat(N,kappa);
# sort and unfold phases
```

```
s_phases=Numeric.sort(phases)*N/(2.0*pi)

# determine Level spacing
# (by computing the difference of the shifted eigenphases)
spacings=s_phases[1:]-s_phases[0:N]

(x_histogram,y_histogram)=histogram(spacings,0.0,10.0,100)
store_histogram(x_histogram,y_histogram,"histogram.dat")
```

Then use your favourite plotting program to plot the level spacing distribution. For gnuplot you could do

```
goe_approx(x)=pi/2.0*x*exp(-pi/4*x*x)
gue_approx(x)=32/pi/pi*x*x*exp(-4/pi*x*x)
plot "histogram.dat" w l,goe_approx(x),gue_approx(x),exp(-x)
```

Here the routines to compute and store the histogram are in `AnalyseData.py` whose core reads

```
 def histogram(data,min,max,nbins):
 from Numeric import *
 # first select only those which lie in the interval [min,max]
 hdat=compress( ((data<max)*(data>min)),data)
 bin_width=(max-min)/nbins
 # define the bins
 bins=min+bin_width*arange(nbins)
 # determine indices
 inds=searchsorted(sort(hdat),bins)
 inds=concatenate([inds,[len(hdat)]])
 # return bins and normalized histogram
 return(bins,(inds[1:]-inds[:-1])/(bin_width*len(hdat)))

def store_histogram(x_distrib,y_distrib,outdat):
 bin_width=x_distrib[1]-x_distrib[0]
 f=open(outdat,"w") # open file for writing
 for k in range(0,len(x_distrib)):
 f.write("% e % e \n" % (x_distrib[k],y_distrib[k]))
 f.write("% e % e \n" % (x_distrib[k]+bin_width, \
 y_distrib[k]))
 f.close()
```

Again, for further details and full routines see [20].

References

1. J. Meiss: *Symplectic maps, variational principles, and transport*, Rev. Mod. Phys. **64** (1992) 795-848.
2. J.-M. Strelcyn: *The "coexistence problem" for conservative dynamical systems: a review*, Colloquium mathematicum **62** (1991) 331–345.
3. P. Duarte: *Plenty of elliptic islands for the standard family of area preserving maps*, Ann. Inst. H. Poincaré Anal. Non Linéaire **11** (1994) 359–409.

4. A. Giorgilli and V. F. Lazutkin: *Some remarks on the problem of ergodicity of the standard map*, Phys. Lett. A **272** (2000) 359–367.
5. V. F. Lazutkin: *A remark on "Some remarks on the problem of ergodicity of the standard map"*, preprint, mp-arc 00-159 (2000).
6. M. Basilio de Matos and A. M. Ozorio de Almeida: *Quantization of Anosov maps*, Annals of Physics **237** (1993) 46–65.
7. P. A. Boasman and J. P. Keating: *Semiclassical asymptotics of perturbed cat maps*, Proc. R. Soc. London Ser. A **449** (1995) 629–653.
8. V. I. Arnold and A. Avez: *Ergodic Problems of Classical Mechanics*, Benjamin, NewYork, (1968).
9. M. V. Berry, N. L. Balazs, M. Tabor and A. Voros: *Quantum maps*, Annals of Physics **122** (1979) 26–63.
10. J. H. Hannay and M. V. Berry: *Quantization of linear maps on a torus — Fresnel diffraction by periodic grating*, Physica D **1** (1980) 267–290.
11. N. L. Balazs and A. Voros: *The quantized Baker's transformation*, Ann. Phys. **190** (1989) 1–31.
12. M. Saraceno: *Classical structures in the quantized baker transformation*, Ann. Phys. **199** (1990) 37–60.
13. M. Degli Esposti: *Quantization of the orientation preserving automorphisms of the torus*, Ann. Inst. H. Poincaré Phys. Théor. **58** (1993) 3 323–341.
14. M. Degli Esposti, S. Graffi and S. Isola: *Classical limit of the quantized hyperbolic toral automorphisms*, Commun. Math. Phys. **167** (1995) 471–507.
15. S. De Bièvre, M. Degli Esposti and R. Giachetti: *Quantization of a class of piecewise affine transformations on the torus.*, Commun. Math. Phys. **176** (1996) 73–94.
16. S. Zelditch: *Index and dynamics of quantized contact transformations.*, Ann. Inst. Fourier **47** (1997) 305–363.
17. G. Haag: *Quantisierte chaotische Abbildungen*, Diploma Thesis, Abteilung Theoretische Physik, Universität Ulm (1999).
18. S. De Bièvre: *Quantum chaos: a brief first visit* in: *Second Summer School in Analysis and Mathematical Physics: Topics in Analysis: Harmonic, Complex, Nonlinear and Quantization*, S. Perez-Esteva and C. Villegas-Blas (eds.), Contemporary Mathematics **289** (2001).
19. T. Prosen and M. Robnik: *Numerical demonstration of the Berry-Robnik level spacing distribution*, J. Phys. A **27** (1994) L459–L466, corrigendum: ibid. **27** (1994) 6633–6633.
20. See `http://www.physik.tu-dresden.de/ baecker/qmaps.html` for programs and further information.
21. The Numerical Algorithms Group (NAG), `http://www.nag.co.uk/`.
22. LAPACK – Linear Algebra PACKage, `http://www.netlib.org/lapack/`.
23. R. Ketzmerick, K. Kruse and T. Geisel: *Efficient diagonalization of kicked quantum systems*, Physica D **131** (1999) 247–253.
24. ATLAS, `http://math-atlas.sourceforge.net/` (Automatically Tuned Linear Algebra Software).
25. O. Bohigas, M.-J. Giannoni and C. Schmit: *Characterization of chaotic quantum spectra and universality of level fluctuation laws*, Phys. Rev. Lett. **52** (1984) 1–4.
26. M. V. Berry and M. Tabor: *Level clustering in the regular spectrum*, Proc. R. Soc. London Ser. A **356** (1977) 375–394.

27. J. P. Keating: *Asymptotic properties of the periodic orbits of the cat maps*, Nonlinearity **4** (1991) 277–307.
28. J. P. Keating: *The cat maps: Quantum mechanics and classical motion*, Nonlinearity **4** (1991) 309–341.
29. F. Mezzadri: *Boundary conditions for torus maps and spectral statistics*, Ph.D. thesis, School of Mathematics, University of Bristol, (1999).
30. J. P. Keating and F. Mezzadri: *Pseudo-symmetries of Anosov maps and spectral statistics*, Nonlinearity **13** (2000) 747–775.
31. T. A. Brody, J. Flores, J. B. French, P. A. Mello, A. Pandey and S. S. M. Wong: *Random-matrix physics: spectrum and strength fluctuations*, Rev. Mod. Phys. **53** (1981) 385–479.
32. F. Haake: *Quantum Signatures of Chaos*, Springer-Verlag, Berlin, 2nd edn., (2001).
33. C. E. Porter and R. G. Thomas: *Fluctuations of Nuclear Reaction Widths*, Phys. Rev. **104** (1956) 483–491.
34. P. Kurlberg and Z. Rudnick: *Value distribution for eigenfunctions of desymmetrized quantum maps*, Internat. Math. Res. Notices (2001) 995–1002.
35. B. Eckhardt: *Exact eigenfunctions for a quantised map*, J. Phys. A **19** (1986) 10 1823–1831.
36. A. Bouzouina and S. De Biévre: *Equipartition of the eigenfunctions of quantized ergodic maps on the torus*, Commun. Math. Phys. **178** (1996) 83–105.
37. S. De Bièvre and M. Degli Esposti: *Egorov theorems and equidistribution of eigenfunctions for the quantized sawtooth and baker maps*, Ann. Inst. Henri Poincaré, Physique Théorique **69** (1996) 1–30.
38. A. Bäcker and H. R. Dullin: *Symbolic dynamics and periodic orbits for the cardioid billiard*, J. Phys. A **30** (1997) 1991–2020.
39. H. P. Baltes and E. R. Hilf: *Spectra of Finite Systems*, Bibliographisches Institut, Mannheim, Wien, Zürich, (1976).
40. M. Sieber, U. Smilansky, S. C. Creagh and R. G. Littlejohn: *Non-generic spectral statistics in the quantized stadium billiard*, J. Phys. A **26** (1993) 6217–6230.
41. A. Bäcker, F. Steiner and P. Stifter: *Spectral statistics in the quantized cardioid billiard*, Phys. Rev. E **52** (1995) 2463–2472.
42. A. Bäcker and F. Steiner: *Quantum chaos and quantum ergodicity*, in *Ergodic Theory, Analysis and Efficient Simulation of Dynamical Systems*, B. Fiedler (ed.), 717- 752, Springer-Verlag Berlin/Heidelberg (2001).
43. J. R. Kuttler and V. G. Sigilito: *Eigenvalues of the Laplacian in two dimensions*, SIAM Review **26** (1984) 163–193.
44. E. J. Heller: *Wavepacket dynamics and quantum chaology*, in: *Proceedings of the 1989 Les Houches School on Chaos and Quantum Physics* (Eds. M.-J. Giannoni, A. Voros and J. Zinn Justin), North–Holland, Amsterdam, (1991).
45. B. Li and M. Robnik: *Statistical properties of high-lying chaotic eigenstates*, J. Phys. A **27** (1994) 5509–5523.
46. E. Doron and U. Smilansky: *Chaotic Spectroscopy*, Chaos **2** (1992) 117–124.
47. B. Dietz and U. Smilansky: *A scattering approach to the quantization of billiards – The inside-outside duality*, Chaos **3** (1993) 581–590.
48. H. Schanz and U. Smilansiky: *Quantization of Sinai's billiard – a scattering approach*, Chaos, Solitons and Fractals **5** (1995) 1289–1309.

49. E. Vergini and M. Saraceno: *Calculation of highly excited states of billiards*, Phys. Rev. E **52** (1995) 2204–2207.
50. A. J. Burton and G. F. Miller: *The application of integral equation methods to the numerical solution of some exterior boundary-value problems*, Proc. R. Soc. London Ser. A **323** (1971) 201–210.
51. R. E. Kleinman and G. F. Roach: *Boundary integral equations for the three dimensional Helmholtz equation*, SIAM Rev. **16** (1974) 214–236.
52. R. J. Riddel Jr.: *Boundary-distribution solution of the Helmholtz equation for a region with corners*, J. Comp. Phys. **31** (1979) 21–41.
53. R. J. Riddel Jr.: *Numerical solution of the Helmholtz equation for two-dimensional polygonal regions*, J. Comp. Phys. **31** (1979) 42–59.
54. P. A. Martin: *Acoustic scattering and radiation problems and the null-field method*, Wave Motion (1982) 391–408.
55. M. V. Berry and M. Wilkinson: *Diabolical points in the spectra of triangles*, Proc. R. Soc. London Ser. A **392** (1984) 15–43.
56. M. Sieber and F. Steiner: *Quantum chaos in the hyperbola billiard*, Phys. Lett. A **148** (1990) 415–419.
57. D. Biswas and S. Jain: *Quantum description of a pseudointegrable system: the $\pi/3$–rhombus billiard*, Phys. Rev. A **42** (1990) 3170–3185.
58. P. A. Boasmann: *Semiclassical Accuracy for Billiards*, Ph.D. thesis, H. H. Wills Physics Laboratory, Bristol, (1992).
59. P. A. Boasmann: *Semiclassical accuracy for billiards*, Nonlinearity **7** (1994) 485–537.
60. R. Aurich and F. Steiner: *Statistical properties of highly excited quantum eigenstates of a strongly chaotic system*, Physica D **64** (1993) 185–214.
61. C. Pisani: *Exploring periodic orbit expansions and renormalisation with the quantum triangular billiard*, Ann. Physics **251** (1996) 208–265.
62. I. Kosztin and K. Schulten: *Boundary integral method for stationary states of two-dimensional quantum systems*, Int. J. Mod. Phys. C **8** (1997) 293–325.
63. B. Li, M. Robnik and B. Hu: *Relevance of chaos in numerical solutions of quantum billiards*, Phys. Rev. E **57** (1998) 4095–4105.
64. M. Sieber: *Billiard systems in three dimensions: the boundary integral equation and the trace formula*, Nonlinearity **11** (1998) 6 1607–1623.
65. K. Hornberger and U. Smilansky: *The boundary integral method for magnetic billiards*, J. Phys. A **33** (1999) 2829–2855.
66. R. Aurich and J. Marklof: *Trace formulae for three-dimensional hyperbolic lattices and application to a strongly chaotic tetrahedral billiard*, Physica D **92** (1996) 101–129.
67. H. Primack and U. Smilansky: *Quantization of the 3-dimensional Sinai billiard*, Phys. Rev. Lett. **74** (1995) 4831–4834.
68. G. Steil: *Eigenvalues of the Laplacian for Bianchi groups*, in: *Emerging applications of number theory (Minneapolis, MN, 1996)*, 617–641, Springer, New York, (1999).
69. T. Prosen: *Quantization of generic chaotic 3D billiard with smooth boundary I: energy level statistic*, Phys. Lett. A **233** (1997) 323–331.
70. T. Prosen: *Quantization of generic chaotic 3D billiard with smooth boundary II: structure of high-lying eigenstates*, Phys. Lett. A **233** (1997) 332–342.
71. R. D. Ciskowski and C. Brebbia, eds.: *Boundary Element Methods in Acoustics*. Computational Mechanics Publications and Elsevier Applied Science, (1991).

72. E. B. Bogomolny: *Semiclassical quantization of multidimensional systems*, Nonlinearity **5** (1992) 805–866.
73. T. Harayama and A. Shudo: *Zeta function derived from the boundary element method*, Phys. Lett. A **165** (1992) 417–426.
74. B. Burmeister: *Korrekturen zur Gutzwillerschen Spurformel für Quantenbillards*, Diploma Thesis , II. Institut für Theoretische Physik, Universität Hamburg (1995).
75. M. Sieber, N. Pavloff and C. Schmit: *Uniform approximation for diffractive contributions to the trace formula in billiard systems*, Phys. Rev. E **55** (1997) 2279–2299.
76. B. Burmeister and F. Steiner: *Exact trace formula for quantum billiards*, unpublished (1995).
77. S. Tasaki, T. Harayama and A. Shudo: *Interior Dirichlet eigenvalue problem, exterior Neumann scattering problem, and boundary element method for quantum billiards*, Phys. Rev. E **56** (1997) R13–R16.
78. J.-P. Eckmann and C.-A. Pillet: *Zeta functions with Dirichlet and Neumann boundary conditions for exterior domains*, Helv. Phys. Acta **70** (1997) 44–65.
79. R. Aurich: private communication.
80. M. Robnik: *Quantising a generic family of billiards with analytic boundaries*, J. Phys. A **17** (1984) 1049–1074.
81. T. Prosen and M. Robnik: *Energy level statistics and localization in sparsed banded random matrix ensembles*, J. Phys. A **26** (1993) 1105–1114.
82. M. Abramowitz and I. A. Stegun (eds.): *Pocketbook of Mathematical Functions*, Verlag Harri Deutsch, Thun – Frankfurt/Main, abridged edn., (1984).
83. A. Sommerfeld: *Vorlesungen über Theoretische Physik, Band VI: Partielle Differentialgleichungen der Physik*, Harri Deutsch, Thun, (1984).
84. T. Hesse: *Semiklassische Untersuchung zwei– und dreidimensionaler Billardsysteme*, Ph.D. thesis, Abteilung Theoretische Physik, Universität Ulm, (1997).
85. K. Życzkowski: *Classical and quantum billiards, integrable, nonintegrable, and pseudo-integrable*, Acta Physica Polonica B **23** (1992) 245–270.
86. A. Bäcker and R. Schubert: *Chaotic eigenfunctions in momentum space*, J. Phys. A **32** (1999) 4795–4815.
87. J. M. Tualle and A. Voros: *Normal modes of billiards portrayed in the stellar (or nodal) representation*, Chaos, Solitons and Fractals **5** (1995) 1085–1102.
88. F. P. Simonotti, E. Vergini and M. Saraceno: *Quantitative study of scars in the boundary section of the stadium billiard*, Phys. Rev. E **56** (1997) 3859–3867.
89. A. Bäcker and R. Schubert: *Autocorrelation function of eigenstates in chaotic and mixed systems*, J. Phys. A **35** (2002) 539–564.
90. E. J. Heller: *Bound-state eigenfunctions of classically chaotic Hamiltonian systems: Scars of periodic orbits*, Phys. Rev. Lett. **53** (1984) 1515–1518.
91. Python, `http://www.python.org/`.
92. Numerical Python (NumPy), `http://sourceforge.net/projects/numpy/`.
93. SciPy, `http://www.scipy.org/`.
94. Gnuplot, `http://www.gnuplot.info/`.

[A5] Poincaré Husimi representation of eigenstates in quantum billiards

A. Bäcker, S. Fürstberger, R. Schubert

Phys. Rev. E **70** (2004) 036204 (10 pages)

For the representation of eigenstates on a Poincaré section at the boundary of a billiard different variants have been proposed. We compare these Poincaré Husimi functions, discuss their properties and based on this select one particularly suited definition. For the mean behaviour of these Poincaré Husimi functions an asymptotic expression is derived, including a uniform approximation. We establish the relation between the Poincaré Husimi functions and the Husimi function in phase space from which a direct physical interpretation follows. Using this, a quantum ergodicity theorem for the Poincaré Husimi functions in the case of ergodic systems is shown.

Poincaré Husimi representation of eigenstates in quantum billiards

A. Bäcker,[1,*] S. Fürstberger,[2,†] and R. Schubert[3,‡]
[1]*Institut für Theoretische Physik, TU Dresden, D-01062 Dresden, Germany*
[2]*Abteilung Theoretische Physik, Universität Ulm Albert-Einstein-Allee 11, D-89069 Ulm, Germany*
[3]*Department of Mathematics, University of Bristol, University Walk, Bristol BS8 1TW, United Kingdom*
(Received 25 July 2003; revised manuscript received 2 December 2003; published 14 September 2004)

For the representation of eigenstates on a Poincaré section at the boundary of a billiard different variants have been proposed. We compare these Poincaré Husimi functions, discuss their properties, and based on this select one particularly suited definition. For the mean behavior of these Poincaré Husimi functions an asymptotic expression is derived, including a uniform approximation. We establish the relation between the Poincaré Husimi functions and the Husimi function in phase space from which a direct physical interpretation follows. Using this, a quantum ergodicity theorem for the Poincaré Husimi functions in the case of ergodic systems is shown.

DOI: 10.1103/PhysRevE.70.036204 PACS number(s): 05.45.Mt, 03.65.Sq, 03.65.Ge

I. INTRODUCTION

The study of eigenfunctions of quantum systems, in particular, their dependence on the classical dynamics, has attracted a lot of attention. A prominent class of examples is provided by two-dimensional billiard systems, which are classically given by the free motion of a particle inside some domain with elastic reflections at the boundary. The corresponding quantum system is described by the Helmholtz equation inside a compact domain $\Omega \subset \mathbb{R}^2$ (in units $\hbar = 1 = 2m$),

$$\Delta \psi_n(\boldsymbol{x}) + k_n^2 \psi_n(\boldsymbol{x}) = 0, \quad \boldsymbol{x} \in \Omega, \tag{1}$$

with (for example) Dirichlet boundary conditions

$$\psi_n(\boldsymbol{x}) = 0, \quad \boldsymbol{x} \in \partial\Omega, \tag{2}$$

where the eigenfunctions $\psi_n(\boldsymbol{x})$ are in $L^2(\Omega)$. Assuming that the eigenvalues k_n^2 are ordered with increasing value, the semiclassical limit corresponds to $n \to \infty$. A detailed knowledge of the behavior of the eigenvalues k_n^2 and the structure of eigenstates is relevant for applications, for example, microwave cavities or mesoscopic systems (see, e.g., Ref. [1], and references therein).

For the description of the phase space structure of quantum systems usually the Wigner function [2] or Husimi function [3] is used. However, for a system with d degrees of freedom these are $2d$-dimensional functions, which are difficult to visualize for $d > 1$. Therefore, one usually considers the position representation, or the momentum representation [4], or sections through the Wigner or Husimi function, see, e.g., Ref. [5].

Another approach is the use of representations on the billiard boundary, acting as a global Poincaré section. In the literature one can find several variants for these representations, see, e.g., Refs. [6–8]. The reason is, as emphasized in Ref. [7], that there is no natural definition of a scalar product for functions on the billiard boundary. This raises the question whether one of these definitions has advantages over the others, which will be addressed in the following.

The representation of eigenstates on the Poincaré section plays an important role in several applications. For example, it is used to define scar measures [8,9], or to study conductance fluctuations, see Ref. [10], and references therein. Furthermore, these representations are used to determine the coupling of leads in open systems [11]. Another important application is the detection of regions where eigenstates localize, see, e.g., Refs. [12,13,11] (for an alternative approach based on the scattering approach see Refs. [14,15]). Representations of eigenstates on the Poincaré section have also been useful to understand the behavior of optical microresonators, see, e.g., Ref. [16], and references therein. More generally, the approach is not just applicable for billiard systems but it is also useful for Poincaré sections arising from Bogomolny's transfer operator approach [17].

In this paper we first compare two different definitions for the Poincaré Husimi representation, discuss their properties (Sec. II), and based on this we select one particular definition for the following. In Sec. III we derive the behavior of these Poincaré Husimi functions when averaged over several energies. In Sec. IV we establish a relation between the well-known Husimi function in phase space and the Poincaré Husimi function on the billiard boundary. This allows for a direct physical interpretation of the Poincaré Husimi functions. Moreover, for ergodic systems a quantum ergodicity theorem for the Poincaré Husimi functions is shown.

II. HUSIMI REPRESENTATION ON THE BOUNDARY

Let us first recall the definition and some properties of Husimi functions in phase space. For a solution ψ_n of the Helmholtz equation (1) with energy $E = k_n^2$ the Husimi function $H_n^B(\boldsymbol{p},\boldsymbol{q})$ is given by its projection onto a coherent state, i.e.,

$$H_n^B(\boldsymbol{p},\boldsymbol{q}) := \left(\frac{k_n}{2\pi}\right)^2 |\langle \psi^B_{(\boldsymbol{p},\boldsymbol{q}),k_n}, \psi_n \rangle_\Omega|^2. \tag{3}$$

Here

*Email address: baecker@physik.tu-dresden.de
†Email address: silke.fuerstberger@physik.uni-ulm.de
‡Email address: roman.schubert@bristol.ac.uk

$$\langle \psi_1, \psi_2 \rangle_\Omega := \int_\Omega \overline{\psi_1}(\boldsymbol{q}) \psi_2(\boldsymbol{q}) d^2q \tag{4}$$

is the scalar product in Ω, and $\overline{\psi_1}$ denotes the complex conjugate of ψ_1.

The coherent states are defined as

$$\psi^B_{(\boldsymbol{p},\boldsymbol{q}),k}(\boldsymbol{x}) := \left(\frac{k}{\pi}\right)^{1/2} (\det \operatorname{Im} B)^{1/4} e^{ik[\langle \boldsymbol{p}, \boldsymbol{x}-\boldsymbol{q}\rangle + (1/2)\langle \boldsymbol{x}-\boldsymbol{q}, B(\boldsymbol{x}-\boldsymbol{q})\rangle]}, \tag{5}$$

where $(\boldsymbol{p},\boldsymbol{q}) \in \mathbb{R}^2 \times \mathbb{R}^2$ denotes the point in phase space around which the coherent state is localized, and B is a symmetric complex 2×2 matrix which determines the shape of the coherent state. For the conventional coherent states one has $B = i\begin{pmatrix} 1 & 0 \\ 0 & 1 \end{pmatrix}$ and in general one has the condition $\operatorname{Im} B > 0$, i.e., $\langle v, \operatorname{Im} B\, v\rangle > 0$ for all $v \in \mathbb{R}^2 \setminus \{0\}$. Notice that because the variance of the coherent states is proportional to k, all Husimi functions are concentrated around the energy shell $|\boldsymbol{p}|^2 = 1$ (and not around $|\boldsymbol{p}|^2 = k^2$). By this it is possible to compare Husimi functions with different energies k_n^2, and, for example, consider their mean, see Eq. (7) below.

Such Husimi functions can be interpreted as probability distributions on phase space, because they satisfy the relation

$$\langle \psi_n, \boldsymbol{A}\psi_n \rangle_\Omega = \int_{\mathbb{R}^2} \int_{\mathbb{R}^2} a(\boldsymbol{p},\boldsymbol{q}) H^B_n(\boldsymbol{p},\boldsymbol{q}) d^2p d^2q + O(k_n^{-1}), \tag{6}$$

where $a(\boldsymbol{p},\boldsymbol{q})$ is a function on phase space and $\boldsymbol{A}$ its quantization. This relation also shows that the choice of the matrix B in the definition of the coherent states does not affect the leading order behavior of H^B_n as a probability density, since the left hand side of Eq. (6) does not depend on B.

The average of all Husimi functions $H^B_n(\boldsymbol{p},\boldsymbol{q})$ up to some energy $k^2 = E$ converges for $k \to \infty$ to the normalized invariant measure on the energy shell,

$$\lim_{k\to\infty} \frac{1}{N(k)} \sum_{k_n \leqslant k} H^B_n(\boldsymbol{p},\boldsymbol{q}) = \frac{1}{\pi A} \chi_\Omega(\boldsymbol{q}) \delta(1 - |\boldsymbol{p}|^2). \tag{7}$$

Here $N(k)$ denotes the spectral staircase function, $N(k) := \#\{k_n \leqslant k\}$, χ_Ω is the characteristic function on Ω, and A is the area of Ω. The mean behavior (7) is similar to the mean behavior of the spectral staircase function, which is given by the Weyl formula, i.e., for $k \to \infty$ one has $N(k) \sim (A/4\pi)k^2$. A similar asymptotic behavior can be derived for the mean of normal derivative functions, see Ref. [19] for a detailed discussion.

For billiards an extremely useful approach for describing the dynamics is the use of a Poincaré section $\mathcal{P}$ together with the corresponding Poincaré mapping P. Usually the section $\mathcal{P} := \{(q,p) \,|\, q \in [0,L], p \in [-1,1]\}$ is parametrized by the arclength coordinate q along the boundary $\partial\Omega$ of the billiard and the projection p of the (unit) momentum $\hat{\boldsymbol{p}}$ after the reflection on the tangent $\hat{\boldsymbol{t}}(q)$, i.e., $p = \langle \hat{\boldsymbol{p}}, \hat{\boldsymbol{t}}(q)\rangle$. By this the billiard flow induces an area-preserving map $P: \mathcal{P} \to \mathcal{P}$, where the invariant measure is given by $d\mu = dq\, dp$.

In order to have the advantages of such a reduced representation in quantum mechanics as well, one is interested in a Husimi representation $h_n(q,p)$ on the Poincaré section $\mathcal{P}$ which is associated with an eigenstate ψ_n. Such a *Poincaré Husimi function* should have similar properties as the ones expressed by relations (6) and (7) for the Husimi functions in phase space, and our aim is to study to what extent this is possible. More precisely, one would like that for the Husimi function on the billiard boundary a spectral average,

$$\mathcal{H}_k(q,p) := \frac{1}{N(k)} \sum_{k_n \leqslant k} h_n(q,p), \tag{8}$$

tends to the invariant measure on $\mathcal{P}$ as $k \to \infty$, in the same way as in Eq. (7).

The Husimi representation on the billiard boundary is usually defined using the normal derivative of the eigenfunction (hereafter called the boundary function),

$$u_n(s) := \langle \hat{\boldsymbol{n}}(s), \boldsymbol{\nabla} \psi_n(\boldsymbol{x}(s)) \rangle, \tag{9}$$

where $\boldsymbol{x}(s)$ is a point on the boundary $\partial\Omega$, parametrized by the arclength s, and $\hat{\boldsymbol{n}}(s)$ denotes the outer normal unit vector to $\partial\Omega$ at $\boldsymbol{x}(s)$. The boundary functions are a natural starting point for defining a Husimi representation because they determine the eigenfunctions uniquely, see Eq. (30). Thus the boundary functions form a reduced representation of the system. If an eigenfunction ψ_n is normalized, then the corresponding boundary function u_n fulfils the normalization condition [21]

$$\frac{1}{2} \int_{\partial\Omega} |u_n(s)|^2 \langle \hat{\boldsymbol{n}}(s), \boldsymbol{x}(s) \rangle ds = k_n^2. \tag{10}$$

For alternative derivations of Eq. (10) and more general boundary conditions see Refs. [22,23]. Notice that while the integrand depends on the chosen origin for the vector $\boldsymbol{x}(s)$, the integral is independent of this choice.

Starting from the boundary function a Husimi function on the Poincaré section can be defined by a projection onto a coherent state. There are different possibilities to define coherent states on the boundary of a billiard. A natural choice is the periodization of the usual one-dimensional coherent states,

$$c^b_{(q,p),k}(s) := \left(\frac{k}{\pi}\right)^{1/4} (\operatorname{Im} b)^{1/4} \sum_{m\in\mathbb{Z}} e^{ik[p(s-q+mL) + (b/2)(s-q+mL)^2]}, \tag{11}$$

where $(q,p) \in \partial\Omega \times \mathbb{R}$, and L denotes the length of the boundary. The parameter $b \in \mathbb{C}$, $\operatorname{Im} b > 0$, determines the shape of the coherent state. Then for an eigenstate ψ_n with boundary function u_n a Husimi function on the Poincaré

section $\mathcal{P}$ (or more precisely, on the cylindric phase space $\partial\Omega\times\mathbb{R}$) can be defined as [6,7]

$$h_n(q,p)=\frac{1}{2\pi k_n}\left|\int_{\partial\Omega}\overline{c}^{b}_{(q,p),k_n}(s)u_n(s)ds\right|^2. \tag{12}$$

The completeness relation for the coherent states gives

$$\int_{\partial\Omega}\int_{\mathbb{R}}h_n(q,p)dp\,dq=\frac{1}{k_n^2}\int_{\partial\Omega}|u_n(s)|^2ds, \tag{13}$$

so in view of relation (10) the Poincaré Husimi function $h_n(q,p)$ will in general not be normalized. This can be fixed by dividing $h_n(q,p)$ by the factor $(1/k_n^2)\int|u_n(s)|^2ds$, as was done, for instance, in Refs. [12,13]. But later on we will see that it is more natural to work with the non-normalized Husimi functions (12).

A different Poincaré representation has been proposed in Ref. [8],

$$\tilde{h}_n(q,p)=\frac{1}{2k_n^2}\frac{\left|\int_{\partial\Omega}\overline{c}^{b}_{(q,p),k_n}(s)u_n(s)\langle\hat{\boldsymbol{n}}(s),\boldsymbol{x}(s)\rangle ds\right|^2}{\int_{\partial\Omega}\overline{c}^{b}_{(q,p),k_n}(s)c^{b}_{(q,p),k_n}(s)\langle\hat{\boldsymbol{n}}(s),\boldsymbol{x}(s)\rangle ds}, \tag{14}$$

where the inclusion of the factor $\langle\hat{\boldsymbol{n}}(s),\boldsymbol{x}(s)\rangle$ is motivated by its appearance in the normalization condition (10). In order to compare the two definitions, we use the fact that for large k the coherent state becomes more and more concentrated around $s=q$ and so $\langle\hat{\boldsymbol{n}}(s),\boldsymbol{x}(s)\rangle\,\overline{c}^{b}_{(q,p),k_n}(s)\sim\langle\hat{\boldsymbol{n}}(q),\boldsymbol{x}(q)\rangle\overline{c}^{b}_{(q,p),k_n}(s)$. This leads to the relation

$$\tilde{h}_n(q,p)\sim\langle\hat{\boldsymbol{n}}(q),\boldsymbol{x}(q)\rangle h_n(q,p), \tag{15}$$

between the two definitions for Husimi functions.

Let us first illustrate the behavior of the Husimi representation given by Eq. (12). As a concrete example we consider a member of the family of limaçon billiards introduced by Robnik [24,25], whose boundary is given in polar coordinates by $\rho(\varphi)=1+\varepsilon\cos(\varphi)$, where $\varepsilon\in[0,1]$ is the family parameter. At $\varepsilon=0.3$ the billiard has a mixed phase space (see Fig. 1 in Ref. [12]) and at $\varepsilon=1$ it turns into the fully chaotic (i.e., ergodic, mixing, …) cardioid billiard. Because of the symmetry of the billiard we consider the half-limaçon billiard with Dirichlet boundary conditions everywhere. The eigenvalues have been computed using the conformal mapping technique [25,26] and then the boundary element method has been used to compute the eigenfunctions (see Ref. [27], and references therein). Figure 1 shows a comparison of eigenstates $\psi_n(\boldsymbol{q})$ with their Husimi representations $h_n(q,p)$ as gray-scale plots with black corresponding to large values. For the computations $b:=i\sigma^{-1}=i$ was chosen. In (a) an eigenstate which is localized around a stable periodic orbit with period three is shown which is clearly reflected in its Poincaré Husimi function to the right. The symmetry $h_n(q,p)=h_n(q,-p)$ is due to the time-reversal symmetry of the system and the symmetry $h_n(q,p)=h_n(L-q,p)$ stems from the reflection symmetry of the system. The plots in Figs. 1(b) and 1(c) are at $\varepsilon=1.0$, i.e., for the cardioid billiard. The eigenstate shown in (b) is localized around an unstable periodic orbit of period two which is also nicely seen in the prominent peaks for the corresponding Poincaré Husimi function. In (c) an irregular state in the cardioid billiard is displayed which is spread out over the full billiard and also $h_n(q,p)$ does not show any prominent localization.

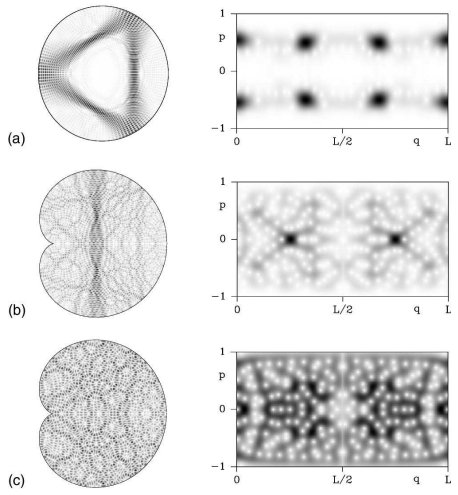

FIG. 1. Examples of eigenstates $\psi_n(\boldsymbol{q})$, shown to the left, and to the right their Poincaré Husimi functions $h_n(q,p)$. In (a) an eigenstate ($n=1952$) localizing around a regular orbit for the limaçon billiard at $\varepsilon=0.3$ is shown. In (b) and (c) two eigenstates for the cardioid billiard are shown ($n=1817$ and $n=1277$).

Now we turn to a comparison of the two Poincaré Husimi representations given by Eqs. (12) and (14). In Fig. 2 a plot of $\mathcal{H}_k(q,p)$ is shown where $k=125.27\ldots$ is chosen such that the first 2000 states are taken into account. Both definitions, Eqs. (12) and (14), lead to a similar nonuniform behavior of $\mathcal{H}_k(q,p)$ in p direction. We will discuss this behavior in more detail in the following section. In addition we observe that $\mathcal{H}_k(q,p)$ has a minimum at $(q,p)=(0,0)$ and $(q,p)=(\pm\mathcal{L}/2,0)$, which is due to the desymmetrization. Figure 2(b) shows a plot of $\tilde{H}_k(q,p)$ which is defined as $\mathcal{H}_k(q,p)$, but instead of $h_n(q,p)$ the functions $\tilde{h}_n(q,p)$ are used, see definition (14). In this case we observe in addition a clear variation in q. The reason for this is the factor $\langle\hat{\boldsymbol{n}}(q),\boldsymbol{x}(q)\rangle$ as explained by relation (15). Another important point is that the definition (14) depends on the chosen origin as the factor $\langle\hat{\boldsymbol{n}}(q),\boldsymbol{x}(q)\rangle$ does, and therefore the integrals in Eq. (14) are not invariant under a shift of the origin. Because of the variation of $\tilde{h}_n(q,p)$ in q and the dependence on the origin we prefer the definition (12) and will use this exclusively in the following.

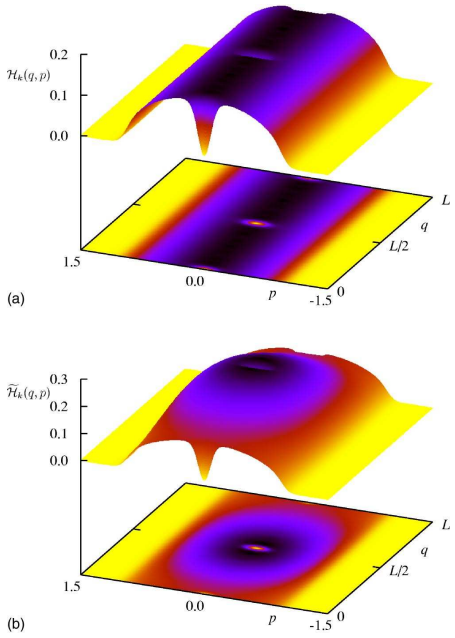

FIG. 2. Plot of $\mathcal{H}_k(q,p)$ for $k=125$ using the first 2000 eigenstates in the limaçon billiard of odd symmetry at $\varepsilon=0.3$. In (a) the result for $\mathcal{H}_k(q,p)$ using definition (12) for $h_n(q,p)$ is shown and in (b) a corresponding $\widetilde{\mathcal{H}}_k(q,p)$ using definition (14) is displayed. In addition to the symmetry related dips at $(q,p)=(0,0)$ and $(L/2,0)$ one clearly sees the variation in p direction in both cases and in (b) we, moreover, observe a variation in q.

III. MEAN BEHAVIOR OF BOUNDARY HUSIMI FUNCTIONS

In this section we determine the asymptotic behavior of the mean $\mathcal{H}_k(q,p)$ of the boundary Husimi functions for large energies. To this end we will use the methods from our previous work [19]. Let us introduce

$$g^\rho(k,s,s') := \sum_{n\in\mathbb{N}} \frac{u_n(s)\overline{u_n}(s')}{k_n^2}\rho(k-k_n), \tag{16}$$

where ρ is a smooth function whose Fourier transform $\hat{\rho}$ is supported in a neighborhood $[-\eta,\eta]$, with η smaller than the length of the shortest periodic orbit of the billiard flow, and satisfies in addition $\hat{\rho}(0)=1$. The function $g^\rho(k,s,s')$ was studied in Ref. [19] and an asymptotic expansion was derived. Its leading term reads

$$g^\rho(k,s,s') = \frac{k}{2\pi^2}\int_0^{2\pi} \langle \hat{\boldsymbol{n}}(s),\hat{\boldsymbol{e}}(\varphi)\rangle \times\langle \hat{\boldsymbol{n}}(s'),\hat{\boldsymbol{e}}(\varphi)\rangle e^{ik\langle \boldsymbol{x}(s)-\boldsymbol{x}(s'),\hat{\boldsymbol{e}}(\varphi)\rangle} d\varphi[1+O(k^{-1})], \tag{17}$$

where $\boldsymbol{x}(s)$ denotes the position vector on the boundary at point s, $\hat{\boldsymbol{n}}(s)$ denotes the outer unit normal vector to the boundary at s, and $\hat{\boldsymbol{e}}(\varphi)=(\cos\varphi,\sin\varphi)$ is the unit vector in direction φ. In general the right hand side of Eq. (17) is a sum of oscillating terms corresponding to reflected orbits, the condition on the support of the Fourier transform of ρ is necessary in order that only one term contributes.

Multiplying Eq. (17) with $\overline{c^b_{(q,p),k}}(s)$ and $c^b_{(q,p),k}(s')$ and integrating over s and s' leads to

$$\sum_{n\in\mathbb{N}} \rho(k-k_n)h_n(q,p) = \frac{k^2}{4\pi^3}\int_0^{2\pi}\left|\int_{\partial\Omega}\langle \hat{\boldsymbol{n}}(s),\hat{\boldsymbol{e}}(\varphi)\rangle\, e^{ik\langle \boldsymbol{x}(s),\hat{\boldsymbol{e}}(\varphi)\rangle}\overline{c^b_{(q,p),k}}(s)ds\right|^2 d\varphi \times[1+O(k^{-1})], \tag{18}$$

where we have used $\|c^b_{(q,p),k}-c^b_{(q,p),k_n}\|^2 \leqslant C(k-k_n)^2/(k+k_n)^2$ in order to obtain the left hand side. The s integral can be computed by the method of stationary phase,

$$\begin{aligned}\int_{\partial\Omega}&\langle \hat{\boldsymbol{n}}(s),\hat{\boldsymbol{e}}(\varphi)\rangle e^{ik\langle \boldsymbol{x}(s),\hat{\boldsymbol{e}}(\varphi)\rangle}\overline{c^b_{(q,p),k}}(s)ds \\ &= \left(\frac{k}{\pi}\right)^{1/4}(\mathrm{Im}\, b)^{1/4}\int_{-\infty}^{\infty}\langle \hat{\boldsymbol{n}}(s),\hat{\boldsymbol{e}}(\varphi)\rangle \times e^{ik[\langle \boldsymbol{x}(s),\hat{\boldsymbol{e}}(\varphi)\rangle - p(s-q)-\overline{(b/2)}(s-q)^2]}ds \\ &= \left(\frac{4\pi}{k}\right)^{1/4}\frac{(\mathrm{Im}\, b)^{1/4}}{[i\widetilde{b}]^{1/2}}\langle \hat{\boldsymbol{n}}(q),\hat{\boldsymbol{e}}(\varphi)\rangle \times e^{ik[\langle \boldsymbol{x}(q),\hat{\boldsymbol{e}}(\varphi)\rangle+(1/2\widetilde{b})\{p-\langle \hat{\boldsymbol{t}}(q),\hat{\boldsymbol{e}}(\varphi)\rangle\}^2]}[1+O(k^{-1/2})],\end{aligned} \tag{19}$$

with

$$\widetilde{b} = \overline{b} + \kappa(q)\langle \hat{\boldsymbol{n}}(q),\hat{\boldsymbol{e}}(\varphi)\rangle, \tag{20}$$

where $\kappa(q)$ is the curvature of the boundary at q. Inserting this result we obtain

$$\sum_{n\in\mathbb{N}} \rho(k-k_n)h_n(q,p) = \frac{2k^2}{(2\pi)^3}\left(\frac{4\pi}{k}\right)^{1/2}\int_0^{2\pi}\frac{(\mathrm{Im}\, b)^{1/2}}{|\widetilde{b}|}|\langle \hat{\boldsymbol{n}}(q),\hat{\boldsymbol{e}}(\varphi)\rangle|^2 \times e^{-k(\mathrm{Im}\, b/|\widetilde{b}|^2)[p-\langle \hat{\boldsymbol{t}}(q),\hat{\boldsymbol{e}}(\varphi)\rangle]^2} d\varphi[1+O(k^{-1/2})], \tag{21}$$

and for $|p|<1$ the φ integral can again be solved by the method of stationary phase (notice that there are two stationary points) which yields

$$\sum_{n\in\mathbb{N}} \rho(k-k_n)h_n(q,p) = \frac{k}{\pi^2}\sqrt{1-p^2}[1+O(k^{-1/2})]. \quad (22)$$

By integrating this equation, and using a Tauberian Lemma as in proofs of the Weyl formula (see, e.g., Ref. [28], Lemma 17.5.6), we finally obtain

$$\mathcal{H}_k(q,p) \equiv \frac{1}{N(k)}\sum_{k_n\leqslant k} h_n(q,p) = \frac{2}{A\pi}\sqrt{1-p^2} + O(k^{-1/2}). \quad (23)$$

In the derivation of Eq. (22) from Eq. (21) we have assumed that $|p|<1$ because then the stationary points are nondegenerate. For $|p|>1$ the stationary points become complex and the integral is exponentially decreasing for $k\to\infty$.

Previously, such a $\sqrt{1-p^2}$ behavior appeared in the context of Fredholm methods for Poincaré Husimi functions [30] and was also obtained in connection with the inverse participation ratio [9].

Next we want to derive a uniform approximation which describes the mean behavior of the Husimi functions near $|p|=1$ and the crossover from the regime $|p|<1$ to the exponential decrease for $|p|>1$. We will study the case $p\approx 1$, the case $p\approx -1$ is completely analogous. Let φ_0 be the angle corresponding to the direction of $\hat{\boldsymbol{t}}(q)$ and expanding the amplitude and phase function in Eq. (21) around φ_0 leads to

$$\begin{aligned}
\sum_{n\in\mathbb{N}} \rho(k-k_n)h_n(q,p) &= \frac{4k^2}{(2\pi)^3}\left(\frac{4\pi}{k}\right)^{1/2}\int_0^\infty \frac{(\mathrm{Im}\ b)^{1/2}}{|\tilde{b}|}\varphi^2 e^{-k(\mathrm{Im}\ b/|\tilde{b}|^2)(p-1+\varphi^2)^2}d\varphi\,[1+O(k^{-1/2})]\\
&= \frac{4k^2}{(2\pi)^3}\left(\frac{4\pi}{k}\right)^{1/2}\int_0^\infty \frac{(\mathrm{Im}\ b)^{1/2}}{|\tilde{b}|}x^{1/2}e^{-k(\mathrm{Im}\ b/|\tilde{b}|^2)(p-1+x)^2}dx[1+O(k^{-1/2})]\\
&= e^{-k(\mathrm{Im}\ b/|\tilde{b}|^2)(p-1)^2}\frac{(2k)^{3/4}}{2\pi^{5/2}}\left(\frac{|\tilde{b}|^2}{\mathrm{Im}\ b}\right)^{1/4}\int_0^\infty x^{1/2}e^{-[(2k\ \mathrm{Im}\ b)^{1/2}/|\tilde{b}|](p-1)x-x^2/2}dx[1+O(k^{-1/2})]\\
&= \frac{(2k)^{3/4}}{(2\pi)^2}e^{-k(\mathrm{Im}\ b/2|\tilde{b}|^2)(1-p)^2}\left(\frac{|\tilde{b}|^2}{\mathrm{Im}\ b}\right)^{1/4}D_{-3/2}\left(\frac{(2k\ \mathrm{Im}\ b)^{1/2}}{|\tilde{b}|}(p-1)\right)[1+O(k^{-1/2})], \quad (24)
\end{aligned}$$

where $D_{-3/2}(x)$ denotes the parabolic cylinder function and we have used one of the standard integral representations, see, e.g., Ref. [31].

This result was derived under the assumption $p\approx 1$ such that $(p^2-1)\approx 2(p-1)$. Substituting $(p-1)$ by $(p^2-1)/2$ allows us to combine the results for the different p regions in one formula,

$$\sum_{n\in\mathbb{N}} \rho(k-k_n)h_n(q,p) = \frac{k}{\pi^2}F_k(p)[1+O(k^{-1/2})], \quad (25)$$

where

$$F_k(p) = \frac{1}{2(2k)^{1/4}}e^{-k(\mathrm{Im}\ b/8|\tilde{b}|^2)(1-p^2)^2}\left(\frac{|\tilde{b}|^2}{\mathrm{Im}\ b}\right)^{1/4} \times D_{-3/2}\left(\frac{(k\ \mathrm{Im}\ b)^{1/2}}{2^{1/2}|\tilde{b}|}(p^2-1)\right). \quad (26)$$

For $|p|<1$ one has $F_k(p)=\sqrt{1-p^2}+O(k^{-1})$, since $D_{-3/2}(x) \sim 2^{3/2}|x|^{1/2}e^{x^2/4}$ for $x\to-\infty$. Recall that $\tilde{b}$ is defined in Eq. (20). In Fig. 3 we compare the expression (26) with $|\tilde{b}|^2/\mathrm{Im}\ b=1$ for different values of k. It is clearly visible that the asymptotic result is reached slowly with increasing k.

Integrating Eq. (26), analogous to the transition from Eq. (22) to Eq. (23), one can compare the uniformized mean behavior with the numerical result. In Fig. 4 a section of $\mathcal{H}_k(q,p)$ at $q=3.0$ is shown for $k=125$, compare with Fig. 2(a). The remaining differences are due to higher order corrections.

In the derivation of the results (22) and (25) we have implicitly assumed that the boundary of Ω is sufficiently smooth, because only then we can use the stationary phase formula. But it is easy to extend the results to the case that the boundary is only piecewise smooth. Since we multiply in Eq. (18) by a coherent state centered in q, all the following computations remain valid if q is in the smooth part of the boundary, since the contributions from the singular points are exponentially suppressed then. So it could only happen that some additional mass sits at the singular points of the boundary, i.e., we have

$$\lim_{k\to\infty}\frac{1}{N(k)}\sum_{k_n\leqslant k} h_n(q,p) = \frac{2}{A\pi}\sqrt{1-p^2} + \mu_S(p,q), \quad (27)$$

where $\mu_S(p,q)dp\,dq$ is a measure supported on the singular part of the boundary (i.e., if $(p,q)\in \mathrm{supp}\ \mu_S$ then q is in the singular part of the boundary). We want to show that $\mu_S=0$ if the billiard is star shaped. We first show that $\mu_S\geqslant 0$, let $\mu_S=\mu_S^+ + \mu_S^-$ be the decomposition into its positive and negative parts, and let $S^\pm$ be the support of $\mu_S^\pm$. We define for any $\varepsilon>0$ $S_\varepsilon^-:=\{z;\inf_{s\in S^-}|z-s|\}$, and with $\lim_{\varepsilon\to 0}\int_{S_\varepsilon^-}\mu^+ dpdq=0$ and $\lim_{\varepsilon\to 0}\int_{S_\varepsilon^-}\sqrt{1-p^2}dpdq=0$ we get

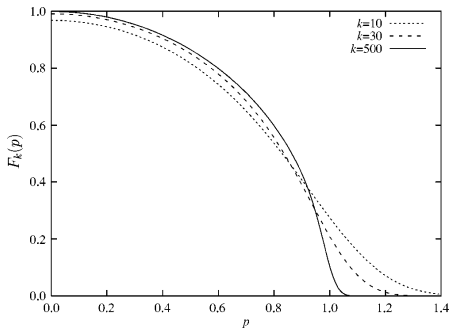

FIG. 3. Comparison of the uniformized asymptotic behavior $F_k(p)$, see Eq. (26), with $|\tilde{b}|^2/\mathrm{Im}\, b=1$ and for $k=10,30,500$. The asymptotic semicircle behavior is reached slowly.

$$\lim_{\varepsilon\to 0}\lim_{k\to\infty}\frac{1}{N(k)}\sum_{k_n\leqslant k}\int_{S_\varepsilon^-} h_n(q,p)dpdq=\int_{S^-}\mu_S^-. \tag{28}$$

But the right hand side is negative, whereas the left hand side is positive, and therefore $\mu_S^-=0$ and $\mu_S\geqslant 0$. Now the completeness relation for the coherent states and the normalization (10) gives $\lim_{k_n\to\infty}\frac{1}{2}\int\int\langle\hat{\boldsymbol{n}}(q),\boldsymbol{x}(q)\rangle h_n(q,p)dpdq=1$, and together with the relation $1/2\int\int\langle\hat{\boldsymbol{n}}(q),\boldsymbol{x}(q)\rangle\times(2/A\pi)\sqrt{1-p^2}dpdq=1$ this yields

$$\int_{-1}^{1}\int_{\partial\Omega}\langle\hat{\boldsymbol{n}}(q),\boldsymbol{x}(q)\rangle\mu_S(p,q)dq\ dp=0. \tag{29}$$

But for a star-shaped billiard one can choose the origin of the coordinate system such that $\langle\hat{\boldsymbol{n}}(q),\boldsymbol{x}(q)\rangle>0$ for all $q\in\partial\Omega$, and so $\mu_S=0$. Therefore Eqs. (22) and (25) remain true for star-shaped billiards with piecewise smooth boundary with the only possible modification that the error term might decay more slowly at the singular points of the boundary.

IV. FROM HUSIMI FUNCTIONS IN PHASE SPACE TO HUSIMI FUNCTIONS ON THE BOUNDARY

In this section we derive a direct relation between the Husimi function in phase space and the one on the Poincaré section, as given by Eq. (12). By this we obtain a physical interpretation of the Poincaré Husimi representation. For the calculations in this section we have to assume that the billiard domain Ω is convex. Let ψ be a solution of the Helmholtz equation (1) in Ω which satisfies Dirichlet boundary condition on $\partial\Omega$. Any such function can be represented as

$$\psi(\boldsymbol{x})=-\int_{\partial\Omega}G_k(\boldsymbol{x}-\boldsymbol{x}(s))u(s)ds, \tag{30}$$

where $G_k(\boldsymbol{x}-\boldsymbol{y})$ is a free Greens function and $u(s)$ is the normal derivative of ψ on the boundary. Notice that the right hand side of Eq. (30) gives an extension of $\psi(\boldsymbol{x})$ to $\mathbb{R}^2$ with $\psi(\boldsymbol{x})=0$ for $\boldsymbol{x}\in\mathbb{R}\backslash\overline{\Omega}$ (this follows from Green's formula).

Let $\psi_{\boldsymbol{z}}$ be a coherent state (5) centered at $\boldsymbol{z}=(\boldsymbol{p},\boldsymbol{q})\in T^*\mathbb{R}^2$, for reasons of simplicity we restrict ourselves to the case of a nonsqueezed symmetrical state, i.e., $B=i\begin{pmatrix}1&0\\0&1\end{pmatrix}$, and omit the index B in the following. We want to compute the overlap $\langle\psi,\psi_{\boldsymbol{z}}\rangle$ given by

$$\langle\psi,\psi_{\boldsymbol{z}}\rangle_\Omega=\langle\psi,\psi_{\boldsymbol{z}}\rangle_{\mathbb{R}^2}=-\int_{\partial\Omega}\langle G_k(\cdot-\boldsymbol{x}(s)),\psi_{\boldsymbol{z}}\rangle_{\mathbb{R}^2}\overline{u(s)}ds, \tag{31}$$

where we have used the aforementioned extension of $\psi(\boldsymbol{x})$ to $\mathbb{R}^2$ given by Eq. (30). We now observe that

$$\langle G_k(\cdot-\boldsymbol{x}(s)),\psi_{\boldsymbol{z}}\rangle_{\mathbb{R}^2}=\mathbf{G}_k^\dagger\psi_{\boldsymbol{z}}(\boldsymbol{x}(s)), \tag{32}$$

where

$$\mathbf{G}_k=\lim_{\varepsilon\to 0}\frac{-1}{\Delta+k^2+i\varepsilon} \tag{33}$$

is the resolvent operator, whose kernel is the Greens function. From Eq. (32) we see that the function $\mathbf{G}_k^\dagger\psi_{\boldsymbol{z}}$ is restricted to the billiard boundary. For the resolvent operator we use the integral representation

$$\mathbf{G}_k^\dagger=\frac{i}{k}\int_{-\infty}^{0}e^{ikt}\,\mathbf{U}(t)dt, \tag{34}$$

where $\mathbf{U}(t)=e^{(i/k)t\Delta}$ is the free time evolution operator with $1/k$ playing the role of $\hbar$, and inserting Eq. (34) into Eq. (32) we obtain

$$\langle G_k(\cdot-\boldsymbol{x}(s)),\psi_{\boldsymbol{z}}\rangle_{\mathbb{R}^2}=\frac{i}{k}\int_{-\infty}^{0}e^{ikt}\,\mathbf{U}(t)\psi_{\boldsymbol{z}}(\boldsymbol{x}(s))dt. \tag{35}$$

But the free time evolution of a coherent state centered in $\boldsymbol{z}$ is well known (see, e.g., Refs. [32,33]) to give again a coherent state, centered around the image of $\boldsymbol{z}$ under the classical flow and with transformed variance,

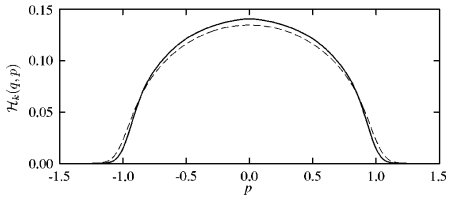

FIG. 4. The full curve shows a section of $\mathcal{H}_k(q,p)$ at $q=3.0$ with $k=125$ for the desymmetrized limaçon billiard, see Fig. 2(a), and the second line is the uniformized mean behavior. The remaining deviations are caused by higher order corrections.

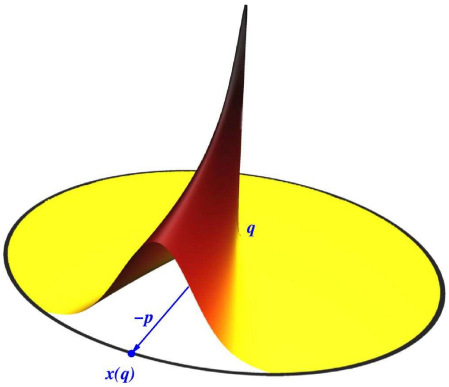

FIG. 5. Illustration of a Gaussian beam as given by Eq. (38) inside the limaçon billiard at $\varepsilon=0.3$.

$$\mathbf{U}(t)\psi_{\mathbf{z}}(\mathbf{x}) = e^{ik|\mathbf{p}|^2 t}\left(\frac{k}{\pi}\right)^{1/2}\frac{1}{1+2it}e^{ik[\langle \mathbf{p},\mathbf{x}-\mathbf{q}(t)\rangle+[i/\{2(1+2it)\}](\mathbf{x}-\mathbf{q}(t))^2]}, \tag{36}$$

with $\mathbf{q}(t)=\mathbf{q}+2t\mathbf{p}$. Therefore, $\mathbf{G}_k^\dagger\psi_{\mathbf{z}}(\mathbf{x})$ has the structure of a Gaussian beam emanating from the point $\mathbf{q}$ in direction $\mathbf{p}$ backwards in time. If we introduce a new coordinate system $\mathbf{x}=(x_\parallel,x_\perp)$ centered at $\mathbf{q}$ with $x_\parallel$ parallel to $\mathbf{p}$ and $x_\perp$ perpendicular to $\mathbf{p}$, we obtain by a stationary phase approximation that for $x_\perp$ and $1-|\mathbf{p}|$ small (i.e., near the energy shell)

$$\mathbf{G}_k^\dagger\psi_{\mathbf{z}}(\mathbf{x}) = \frac{i}{\sqrt{2}k(1+ix_\parallel)^{1/2}}e^{ik[x_\parallel+\{i/(2(1+ix_\parallel))\}x_\perp^2+(i/2)(1-|\mathbf{p}|)^2]} \times[1+O(k^{-1/2})] \tag{37}$$

holds, where we have assumed that $x_\parallel<0$. For $x_\parallel\approx 0$ and $x_\parallel>0$ the integral leads to an error function which describes the transition from the exponentially decaying regime with $x_\parallel>0$ to the regime $x_\parallel<0$ in Eq. (37). For $|\mathbf{p}|=1$ the result reads

$$\mathbf{G}_k^\dagger\psi_{\mathbf{z}}(\mathbf{x})|_{|\mathbf{p}|=1} = \frac{i}{\sqrt{2}k(1+ix_\parallel)^{1/2}}e^{ik[x_\parallel+\{i/(2(1+ix_\parallel))\}x_\perp^2]} \times\frac{1}{2}\mathrm{erfc}\left(\sqrt{\frac{k}{2}}\frac{x_\parallel}{(1+ix_\parallel)^{1/2}}\right)[1+O(k^{-1/2})], \tag{38}$$

where $\mathrm{erfc}(z)$ denotes the complementary error function, and the absolute value of this expression is shown in Fig. 5.

Next we want to evaluate this expression on the boundary. To this end, let $\mathbf{x}(q)$ be the point of intersection between the boundary and the line from $\mathbf{q}$ in direction $-\mathbf{p}$. (Here we need the assumption that the billiard domain Ω is convex, in order that there is only one such point.) Then we obtain with $\mathbf{x}(s)=\mathbf{x}(q)+\hat{\mathbf{t}}(q)(s-q)-\kappa(q)/2\hat{\mathbf{n}}(q)(s-q)^2+O((s-q)^3)$ that

$$x_\parallel = |\mathbf{q}-\mathbf{x}(q)| + p(s-q) - \frac{\kappa(q)}{2}(1-p^2)^{1/2}(s-q)^2 + O((s-q)^3), \tag{39}$$

$$x_\perp = (1-p^2)^{1/2}(s-q)+O((s-q)^2), \tag{40}$$

where $p:=\langle\hat{\mathbf{p}},\hat{\mathbf{t}}\rangle\in[-1,1]$. Inserting these expressions in Eq. (37) gives

$$\langle G_k(\cdot-\mathbf{x}(s)),\psi_{\mathbf{z}}\rangle_{\mathbb{R}^2} = \frac{i\pi^{1/4}}{\sqrt{2}k^{5/4}}\frac{1}{(1-p^2)^{1/4}}e^{ik|\mathbf{q}-\mathbf{x}(q)|+i\theta}e^{-(k/2)(1-|\mathbf{p}|)^2}c^b_{(q,p),k}(s) \times[1+O(k^{-1/2})], \tag{41}$$

where $c^b_{(q,p),k}(s)$ is a coherent state on the boundary, as defined in Eq. (11), with variance $b=i(1-p^2)/[1+i|\mathbf{q}-\mathbf{x}(q)|]-\kappa(q)(1-p^2)^{1/2}$ and $e^{i\theta}=[|\mathbf{q}-\mathbf{x}(q)|+i]^{1/2}/[|\mathbf{q}-\mathbf{x}(q)|^2+1]^{1/4}$. Notice that although we started with a symmetric coherent state in the interior, the projected coherent state on the boundary is no longer symmetric and has a nontrivial squeezing parameter b which depends on the position of the original state, the angle of intersection of the ray in direction $-\mathbf{p}$ with the boundary, and the curvature of the boundary.

If we insert the expression (41) into Eq. (31) we obtain a semiclassical relation between the projection of an eigenstate onto a coherent state in the interior and the projection of the normal derivative on the boundary onto a coherent state on the boundary,

$$\langle\psi_n,\psi_{\mathbf{z}}\rangle_\Omega = -\frac{i\pi^{1/4}}{\sqrt{2}\,k_n^{5/4}}\frac{1}{(1-p^2)^{1/4}} \times e^{ik_n|\mathbf{q}-\mathbf{x}(q)|+i\theta}e^{-(k_n/2)(1-|\mathbf{p}|)^2} \times\langle u_n,c^b_{(q,p),k_n}\rangle_{\partial\Omega}[1+O(k_n^{-1/2})]. \tag{42}$$

In turn from this we obtain the central result of this section, a direct relation between the corresponding Husimi functions

$$H_n(\mathbf{p},\mathbf{q}) = \delta_{k_n}(1-|\mathbf{p}|)\frac{1}{4}\frac{h_n(q,p)}{\sqrt{1-p^2}}[1+O(k_n^{-1/2})], \tag{43}$$

with

$$\delta_{k_n}(1-|\mathbf{p}|) := \left(\frac{k_n}{\pi}\right)^{1/2}e^{-k_n(1-|\mathbf{p}|)^2}. \tag{44}$$

Let us first discuss the meaning of the individual terms on the right hand side of Eq. (43). The function $\delta_{k_n}(1-|\mathbf{p}|)$ is a delta sequence for $k_n\to\infty$, and describes the localization of $H_n(\mathbf{p},\mathbf{q})$ around the energy shell. The factor $1/\sqrt{1-p^2}$ comes from the projection of the Gaussian beam to the plane tangent to the boundary, see Fig. 5. The right hand side of Eq.(43) has still a dependence on the phase space point $(\mathbf{p},\mathbf{q})$ on the left hand side through the parameter b in the coherent state in Eq. (41). But as we will discuss after Eq. (45) below (and in more detail in the Appendix), when integrating the

Husimi function against an observable the result does not depend on b in leading order.

As in the preceding section we have assumed that the boundary is smooth. But by the localization of the coherent states the results can be again extended to the case that the boundary is piecewise smooth, then Eq. (43) remains valid if q is not a singular point of the boundary.

The direct connection between the Husimi function in the interior and the one on the boundary, given by Eq. (43), allows us to derive interesting relations between the two Husimi functions and can be used to give a direct physical interpretation of the Husimi function on the boundary. From Eq. (6) together with relation (43) we obtain

$$\langle \psi_n, \boldsymbol{A}\psi_n\rangle_\Omega = \int_{-1}^{1}\int_{\partial\Omega} \frac{h_n(q,p)}{4\sqrt{1-p^2}}\langle a\rangle(q,p) l(q,p) dq\, dp + O(k_n^{-1/2}), \tag{45}$$

where $l(q,p)$ denotes the length of a ray emanating from $\boldsymbol{q}(q)\in\partial\Omega$ in the direction determined by p until it hits the boundary again. Furthermore,

$$\langle a\rangle(q,p) := \frac{1}{l(q,p)}\int_0^{l(q,p)} a(\boldsymbol{q}(q)+t\hat{\boldsymbol{e}}(q,p),\hat{\boldsymbol{e}}(q,p))dt \tag{46}$$

is the mean value of the classical observable between two bounces, where $\hat{\boldsymbol{e}}(q,p)$ denotes the unit vector at $\boldsymbol{q}(q)$ in direction p. A relation of the same type as Eq. (45) has been obtained recently by different methods in Ref. [34] for certain localized functions on the boundary. Equation (45) now shows that the dependence on the parameter b in the coherent states used to define h_n can be discarded in leading order, see the Appendix for a detailed discussion. This means that if we move from the pointwise relation (43) to the integral relation (45), we gain the freedom to define the Husimi functions on the boundary with an arbitrary parameter b.

We conclude from relation (45) that

$$\mathfrak{h}_n(q,p) := \frac{1}{4}\frac{h_n(q,p)}{\sqrt{1-p^2}} \tag{47}$$

is a reduction of the probability density defined by the Husimi function on the whole phase space to the boundary. So if one wants a proper representation of eigenfunctions on the Poincaré section which is an approximate probability density, and whose general properties are independent of the billiard shape, then Eq. (47) seems to be the best choice. Of course a drawback of the function (47) is the singularity of $1/\sqrt{1-p^2}$ at $p=\pm 1$ which is relevant at any finite energy. So for numerical computations the definition (12) is more suitable and the importance of Eq. (47) lies in the physical interpretation.

In particular, relation (45) implies an asymptotic normalization condition on $\mathfrak{h}_n(q,p)$,

$$\int_{-1}^{1}\int_{\partial\Omega} \mathfrak{h}_n(q,p) l(q,p) dq\, dp = 1 + O(k_n^{-1/2}). \tag{48}$$

Since $l(q,p)dq\,dp$ is the phase space volume in the energy shell corresponding to the volume element $dq\,dp$ of the Poincaré section, the factor $l(q,p)$ can be viewed as a normalization which makes $\mathfrak{h}_n(q,p)$ independent of the billiard shape, i.e., for any $\mathcal{D}\subset\partial\Omega\times[-1,1]$, we get that $\int_{\mathcal{D}}\mathfrak{h}_n(q,p)l(q,p)dq\,dp$ is the probability for the particle in the state ψ_n to be found in the region $\hat{D}:=\Pi^{-1}\mathcal{D}$ on the energy shell, where the map Π describes the projection of the domain $\hat{D}$ to the boundary.

We would like to close this section with some remarks on the implications of quantum ergodicity to the behavior of the Poincaré Husimi functions. If the classical billiard flow in Ω is ergodic, then the quantum ergodicity theorem [35,36] (see Ref. [20] for an introduction) tells us that almost all Husimi functions $H_n(\boldsymbol{p},\boldsymbol{q})$ tend weakly to $1/2\pi A$. Our result (43) then immediately implies that in the semiclassical limit almost all Poincaré Husimi functions $h_n(q,p)$ tend to $[2/\pi A]\sqrt{1-p^2}$ in the weak sense. So this proves a quantum ergodicity theorem for the boundary Husimi functions. Recently related results have been obtained establishing quantum ergodicity for observables on the Poincaré section [35,37,38]. Notice that the $\sqrt{1-p^2}$ behavior is also visible in the plot of $h_n(q,p)$ for the irregular state shown in Fig. 1(c) for the ergodic cardioid billiard.

V. SUMMARY

Poincaré representations of eigenstates play an important role in several areas. However, *a priori* there is no unique way for their definition. In this paper we single out the definition given by Eq. (12) and show that the asymptotic mean behavior of these Husimi functions is proportional to $\sqrt{1-p^2}$. For this asymptotic semicircle behavior we in addition derive a uniform asymptotic formula. Furthermore we establish a direct relation between the Husimi function in phase space and the Poincaré Husimi function (12) on the billiard boundary. By this a physically meaningful interpretation, see Eq. (43), of the previously *ad hoc* chosen definition for the Poincaré Husimi function is obtained. Namely, the Poincaré Husimi function $\mathfrak{h}_n(q,p)$ can be viewed as a probability density on the Poincaré section. For ergodic systems our result implies a quantum ergodicity theorem for the Poincaré Husimi functions, i.e., almost all Poincaré Husimi functions become equidistributed with respect to the appropriate measure.

ACKNOWLEDGMENTS

A.B. and R.S. would like to thank the Mathematical Sciences Research Institute, Berkeley, USA, for financial support and hospitality where part of this work was done. R.S. was supported by the European Commission under the Research Training Network (Mathematical Aspects of Quantum Chaos) Grant No. HPRN-CT-2000-00103 of the IHP Programme.

APPENDIX: HUSIMI FUNCTIONS AND EXPECTATION VALUES

In this appendix we recall some facts about Husimi functions, see, e.g., Ref. [18] and the contribution by Helffer in

the same volume. With this information we discuss the dependence of the Husimi functions on the parameter b, as given in the definition (11) of the coherent states. In the following we will use the notation $z=(p,q)$. A Husimi function is a smoothed version of the Wigner function,

$$\frac{k}{2\pi}|\langle c^b_{z,k},u\rangle|^2=\int W[c^b_{z,k}](z')W[u](z')dz', \qquad \text{(A1)}$$

where $W[u](z')$ denotes the Wigner function of u. The Wigner function of the coherent state $c^b_{z,k}$ is given by $W[c^b_{z,k}](z')=(k/\pi)e^{-k\langle z'-z,g(z-z')\rangle}+O(e^{-c/k})$, where

$$g=\begin{pmatrix} 1/\mathrm{Im}\ b & -\mathrm{Re}\ b/\mathrm{Im}\ b \\ -\mathrm{Re}\ b/\mathrm{Im}\ b & \mathrm{Im}\ b+(\mathrm{Re}\ b)^2/\mathrm{Im}\ b \end{pmatrix}. \qquad \text{(A2)}$$

Relation (A1) holds as well if b depends on z.

We will now use the fact that if $\boldsymbol{A}$ is the Weyl quantization of a function $a(z)$, see, e.g., Ref. [29], then $\langle u,\boldsymbol{A}u\rangle=\int a(z)W[u](z)dz$. Using this and Eq. (A1) one obtains

$$\int a(z)\frac{k}{2\pi}|\langle c^b_{z,k},u\rangle|^2dz=\int\int a(z)W[c^b_{z,k}](z')W[u](z')dzdz'$$
$$=\langle u,\tilde{\boldsymbol{A}}u\rangle, \qquad \text{(A3)}$$

where $\tilde{\boldsymbol{A}}$ is the Weyl quantization of the function

$$\tilde{a}(z)=\int a(z')W[c^b_{z',k}](z)dz'. \qquad \text{(A4)}$$

If we assume that the matrix g is either constant, or satisfies $||\partial_z^\alpha g(z)||\leqslant C_\alpha$ for all $\alpha\in\mathbb{N}^2$ and $z\in\mathrm{supp}\ a$, which is equivalent to the requirement that $b(z)$ is smooth and $\mathrm{Im}\ b(z)>0$ for $z\in\mathrm{supp}\ a$, then the method of stationary phase gives

$$\tilde{a}(z)=a(z)+\frac{1}{k}R(k,z), \qquad \text{(A5)}$$

where $R(k,z)$ is a smooth bounded functions with bounded derivatives. Hence the Weyl quantization of $R(k,z)$ is bounded by the Calderon-Vallaincourt theorem (see Ref. [29]), so $||\boldsymbol{A}-\tilde{\boldsymbol{A}}||\leqslant C/k$ and therefore

$$\left|\int a(z)\frac{k}{2\pi}|\langle c^b_{z,k},u\rangle|^2\,dz-\langle u,\boldsymbol{A}u\rangle\right|\leqslant C/k. \qquad \text{(A6)}$$

Since $\langle u,\boldsymbol{A}u\rangle$ is independent of b we have for any smooth $b(z),\tilde{b}(z)$ with $\mathrm{Im}\ b(z)>0$, $\mathrm{Im}\tilde{b}(z)>0$ for $z\in\mathrm{supp}\ a$ the estimate

$$\left|\int a(z)\frac{k}{2\pi}|\langle c^b_{z,k},u\rangle|^2\,dz-\int a(z)\frac{k}{2\pi}|\langle c^{\tilde{b}}_{z,k},u\rangle|^2dz\right|\leqslant C/k. \qquad \text{(A7)}$$

This shows that in the definition of the family of coherent states we can choose any nondegenerate, possibly z-dependent, parameter b and still get in leading order the same probability distribution defined by the corresponding Husimi densities. In this sense the dependence of the Husimi functions on b is weak.

Let us now look at relations (43) and (45) from the perspective of the preceding discussion. In the Husimi function appearing on the right hand side of Eq. (43) the parameter b is given by $b=i(1-p^2)/[1+i|\boldsymbol{q}-\boldsymbol{x}(q)|]-\kappa(q)(1-p^2)^{1/2}$, so it depends on $z=(p,q)$ and additionally on $\boldsymbol{q}$, and it degenerates for $p\to\pm1$. If the classical observable a in relation (45) has support in the interior of Ω, then $\langle a\rangle$ is supported away from $p=\pm1$ and we can replace b by any nondegenerate $\tilde{b}$. If the support of a includes the boundary $\partial\Omega$, then $\langle a\rangle$ is not necessarily zero at $p=\pm1$ and we can only replace b by one which has the same type of behavior for $p\to\pm1$, such as, e.g., $b^{(0)}(p,q)=i(1-p^2)-\kappa(q)(1-p^2)^{1/2}$.

[1] H.-J. Stöckmann, *Quantum Chaos* (Cambridge University Press, Cambridge, 1999).
[2] E. P. Wigner, Phys. Rev. **40**, 749 (1932).
[3] K. Husimi, Proc. Phys. Math. Soc. Jpn. **22**, 264 (1940).
[4] A. Bäcker and R. Schubert, J. Phys. A **32**, 4795 (1999).
[5] G. Veble, M. Robnik, and J. Liu, J. Phys. A **32**, 6423 (1999).
[6] B. Crespi, G. Perez, and S.-J. Chang, Phys. Rev. E **47**, 986 (1993).
[7] J. M. Tualle and A. Voros, Chaos, Solitons Fractals **5**, 1085 (1995).
[8] F. P. Simonotti, E. Vergini, and M. Saraceno, Phys. Rev. E **56**, 3859 (1997).
[9] W. E. Bies, L. Kaplan, M. R. Haggerty, and E. J. Heller, Phys. Rev. E **63**, 066214 (2001).
[10] L. Kaplan, Phys. Rev. E **62**, 3476 (2000).
[11] A. Bäcker, A. Manze, B. Huckestein, and R. Ketzmerick, Phys. Rev. E **66**, 016211 (2002).
[12] A. Bäcker and R. Schubert, J. Phys. A **35**, 527 (2002).
[13] A. Bäcker and R. Schubert, J. Phys. A **35**, 539 (2002).
[14] D. Klakow and U. Smilansky, J. Phys. A **29**, 3213 (1996).
[15] S. D. Frischat and E. Doron, J. Phys. A **30**, 3613 (1997).
[16] M. Hentschel, H. Schomerus, and R. Schubert, Europhys. Lett. **62**, 636 (2003).
[17] E. B. Bogomolny, Nonlinearity **5**, 805 (1992).
[18] T. Paul, in *Quasiclassical Methods*, The IMA Volumes in Mathematics and Applications, Vol. 95 (Springer, New York, 1997), pp. 51–88.
[19] A. Bäcker, S. Fürstberger, R. Schubert, and F. Steiner, J. Phys. A **35**, 10 293 (2002).
[20] A. Bäcker, R. Schubert, and P. Stifter, Phys. Rev. E **57**, 5425 (1998); **58**, 5192 (1998).
[21] F. Rellich, Math. Z. **46**, 635 (1940).
[22] M. V. Berry and M. Wilkinson, Proc. R. Soc. London, Ser. A **392**, 15 (1984).
[23] P. A. Boasman, Nonlinearity **7**, 485 (1994).
[24] M. Robnik, J. Phys. A **16**, 3971 (1983).

[25] M. Robnik, J. Phys. A **17**, 1049 (1984).
[26] T. Prosen and M. Robnik, J. Phys. A **26**, 2371 (1993).
[27] A. Bäcker, in *The Mathematical Aspects of Quantum Chaos I*, edited by I M. Degli Esposti and S. Graffi, Springer Lecture Notes in Physics 618 (Springer, Berlin, 2003), pp. 91–144.
[28] L. Hörmander, *Grundlehren der Mathematischen Wissenschaften* (Springer-Verlag, Berlin, 1985), Vol. 274.
[29] M. Dimassi and J. Sjöstrand (Cambridge University Press, Cambridge, 1999).
[30] F. P. Simonotti and M. Saraceno, Phys. Rev. E **61**, 6527 (2000).
[31] *Pocketbook of Mathematical Functions*, edited by M. Abramowitz and I. A. Stegun (Harri Deutsch, Frankfurt, 1984).
[32] G. A. Hagedorn, Commun. Math. Phys. **71**, 1 (1980); **71**, 77 (1980).
[33] R. G. Littlejohn, Phys. Rep. **138**, 4 (1986). **138**, 193 (1986).
[34] S.-Y. Lee and S. C. Creagh, Ann. Phys. (N.Y.) **302**, 392 (2003).
[35] P. Gérard and E. Leichtnam, Duke Math. J. **71**, 559 (1993).
[36] S. Zelditch and M. Zworski, Commun. Math. Phys. **175**, 673 (1996).
[37] A. Hassell and S. Zelditch, Commun. Math. Phys. **248**, 119 (2004).
[38] N. Burq, e-print math.AP/0301349.

[A6] Flooding of regular islands by chaotic states

A. Bäcker, R. Ketzmerick, and A. Monastra
Phys. Rev. Lett. **94** (2005) 054102 (4 pages)

We introduce a criterion for the existence of regular states in systems with a mixed phase space. If this condition is not fulfilled chaotic eigenstates substantially extend into a regular island. Wave packets started in the chaotic sea progressively flood the island. The extent of flooding by eigenstates and wave packets increases logarithmically with the size of the chaotic sea and the time, respectively. This new effect can be observed for island chains with just 10 islands.

Flooding of Chaotic Eigenstates into Regular Phase Space Islands

Arnd Bäcker, Roland Ketzmerick, and Alejandro G. Monastra
Institut für Theoretische Physik, Technische Universität Dresden, 01062 Dresden, Germany
(Received 13 September 2004; published 7 February 2005)

We introduce a criterion for the existence of regular states in systems with a mixed phase space. If this condition is not fulfilled chaotic eigenstates substantially extend into a regular island. Wave packets started in the chaotic sea progressively flood the island. The extent of flooding by eigenstates and wave packets increases logarithmically with the size of the chaotic sea and the time, respectively. This new effect is observed for the example of island chains with just ten islands.

DOI: 10.1103/PhysRevLett.94.054102 PACS numbers: 05.45.Mt, 03.65.Sq

One of the cornerstones in the understanding of the structure of eigenstates in quantum systems is the semiclassical eigenfunction hypothesis [1]: in the semiclassical limit the eigenstates concentrate on those regions in phase space which a typical orbit explores in the long-time limit. For integrable systems these are the invariant tori. For ergodic dynamics the eigenstates become equidistributed on the energy shell [2]. Typical systems have a mixed phase space, where regular islands and chaotic regions coexist. In this case the semiclassical eigenfunction hypothesis implies that the eigenstates can be classified as being either regular or chaotic according to the phase-space region on which they concentrate. Note that this may fail for an infinite phase space [3].

In this Letter we study mixed systems with a compact phase space, but away from the semiclassical limit. Here the properties of eigenstates depend on the size of phase-space structures compared to Planck's constant h. In the case of 2D maps this can be very simply stated [4]: a regular state with quantum number $m = 0, 1, \ldots$ will concentrate on a torus enclosing an area $(m + 1/2)h$, as can be seen in Fig. 1(c).

We show that this WKB-type quantization rule is not a sufficient condition. We find a second criterion for the existence of a regular state on the mth quantized torus,

$$\gamma_m < \frac{1}{\tau_{\mathrm{H}}}. \tag{1}$$

Here $\tau_{\mathrm{H}} = h/\Delta_{\mathrm{ch}}$ is the Heisenberg time of the chaotic sea with mean level spacing Δ_{ch}, and γ_m is the decay rate of the regular state m if the chaotic sea were infinite. Quantized tori violating this condition do not support regular states. Instead, chaotic states *flood* these regions; see Fig. 1(a). In terms of dynamics we find that wave packets started in the chaotic sea progressively flood the island as time evolves. Partial and even complete flooding is possible, depending on system properties. These findings are relevant for islands surrounded by a large chaotic sea.

We numerically demonstrate the flooding and the disappearance of regular states for the important case of island chains. In typical Hamiltonian systems they appear around any regular island. On larger scales they are relevant for Hamiltonian ratchets [5], the kicked rotor with accelerator modes [6], and the experimentally [7–9] and theoretically [10] studied kicked atom systems. The flooding of regular islands by chaotic states is a new quantum signature of a classically mixed phase space. This phenomenon shows that not only local phase-space structures, but also global properties of the phase space, determine the characteristics of quantum states.

Before we explain the origin of Eq. (1), we numerically study its consequences. We choose a system, where we can change τ_{H} by increasing the system size without affecting the rates γ_m. A one dimensional kicked system

$$H(p, x, t) = T(p) + V(x)\sum_n \delta(t - n), \tag{2}$$

has a stroboscopic time evolution given by the mapping, $x_{t+1} = x_t + T'(p_t)$, $p_{t+1} = p_t - V'(x_{t+1})$. The phase space is compact with periodic boundary conditions for $x_t \in [0, M]$ and $p_t \in [-1/2, 1/2]$. Choosing the functions $V'(x)$ and $T'(p)$ appropriately [11] we get a chain of M islands, one per unit cell (see Fig. 1). The islands cover a

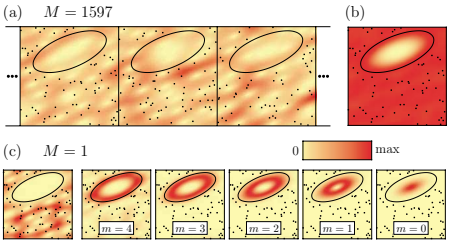

FIG. 1 (color online). (a) Husimi representation of a chaotic state flooding the regular islands. Shown are three phase-space cells out of $M = 1597$. The full curves are classical tori close to the border of the regular islands and the black dots are iterates of a chaotic orbit. This eigenstate extends well into the islands, while having no weight in their central region. (b) Average of the eigenstate over all M cells. (c) For $M = 1$ eigenstates concentrate either on the chaotic component (left) or over the mth quantized regular torus. For all plots $h_{\mathrm{eff}} \approx 1/30$ is used.

relative area $A_{\mathrm{reg}} = 0.215$ and have fine structure close to their boundary that is negligible for the quantum properties studied here. Points inside an island are mapped one unit cell to the right; i.e., the island chain is transporting.

The eigenstates $|\psi\rangle$ of the quantum system are determined by the eigenvalue equation, $\hat{U}|\psi\rangle = e^{i\varphi}|\psi\rangle$, where $\hat{U}$ is the unitary time-evolution operator over one time period, $\hat{U} = \exp[-2\pi i T(\hat{p})/h_{\mathrm{eff}}]\exp[-2\pi i V(\hat{x})/h_{\mathrm{eff}}]$. The spatial periodicity after M cells requires an effective Planck's constant $h_{\mathrm{eff}} = M/N$, with incommensurate integers M and N. We choose for M/N the rational approximants of $h_{\mathrm{eff}} = 1/(d+\sigma)$ with $\sigma = (\sqrt{5}-1)/2$ the golden mean and, e.g., $d = 29$ in Fig. 1. This ensures that there are no undesired periodicities and that h_{eff} is approximately constant when varying M. Moreover, the operator $\hat{U}$ reduces to an $N \times N$ periodic band matrix. Using the symmetrized version of the map and making a unitary transformation to a band matrix we are able to calculate the eigenstates $|\psi\rangle$ of $\hat{U}$ up to $N \approx 10^5$.

For $M = 1$, Fig. 1(c) shows a typical chaotic eigenstate and five regular states. The chaotic state extends over the chaotic phase-space component and the regular states concentrate on quantized tori. The eigenstates are represented on the classical phase space by the Husimi distribution, where for visualization we use tilted coherent states adapted to the shape of the island. For larger system sizes we find that chaotic states flood the islands of classically regular motion. Figure 1(a) shows such a state for $M = 1597$ that clearly ignores the outer tori of the island, which for $M = 1$ act as barriers for chaotic states [Fig. 1(c), left]. In the central part of the island, however, this state has essentially no weight. This partial flooding of the island is observed even better in Fig. 1(b), where an average of the Husimi function of this state is taken over all M unit cells. The almost constant value in the chaotic component extends well into the island. Inside the island, clearly away from its outer boundary, the Husimi function sharply drops to zero.

For a quantitative description of this flooding we now analyze the weight W of each eigenstate inside the islands. We determine this weight by integrating the normalized Husimi function (calculated on a 30×30 grid per unit cell) over the islands. In the semiclassical limit, $h_{\mathrm{eff}} \to 0$, regular states have $W = 1$, while chaotic states have $W = 0$. The distribution $P(W)$ of these weights for all eigenstates is shown in Fig. 2 for various system sizes and $h_{\mathrm{eff}} \approx 1/10$ [12]. For $M = 1$ we observe, as expected, a main peak near $W = 0$ coming from the chaotic eigenstates and two distinct peaks at larger W from the two regular states; see

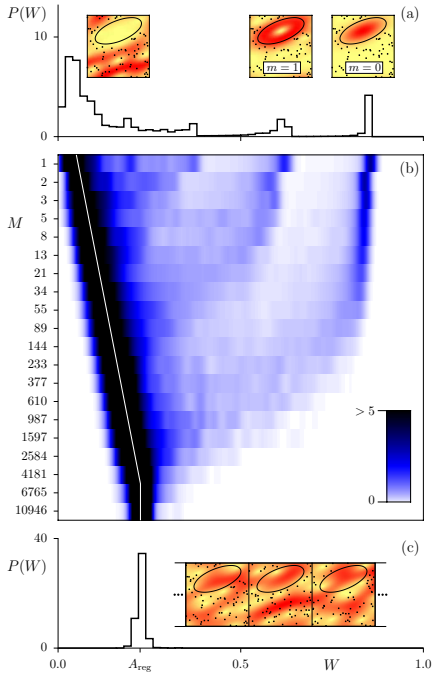

FIG. 2 (color online). Distribution $P(W)$ of the weights W of the eigenstates in the regular islands for $h_{\mathrm{eff}} \approx 1/10$. (a) $M = 1$: the main peak near $W = 0$ is due to chaotic states and two further peaks are due to regular states $m = 0, 1$ (see the insets). (b) For increasing M the main peak shifts to larger values of W (white line) and the two peaks from the regular states disappear sequentially. (c) $M = 10\,946$: a narrow peak remains around $W = A_{\mathrm{reg}}$. Three phase-space cells of an eigenstate show a complete flooding of the islands.

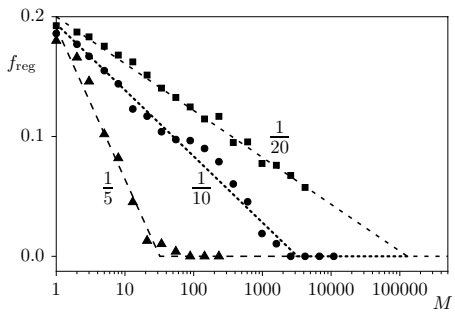

FIG. 3. Fraction f_{reg} of regular states vs system size M for $h_{\mathrm{eff}} \approx 1/5$ (triangles), $1/10$ (circles), and $1/20$ (squares). An approximately linear decrease with $\ln M$ to $f_{\mathrm{reg}} = 0$ can be seen (lines are a guide to the eye). Already for small system sizes $M \approx 10$ and small h_{eff} a significant reduction of regular states is observed.

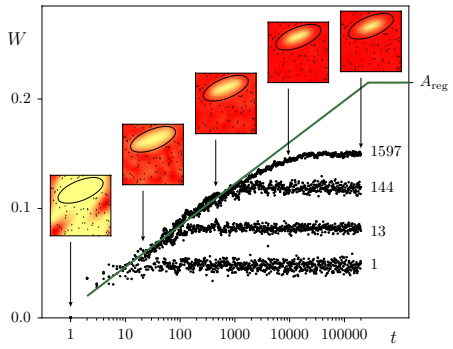

FIG. 4 (color online). Weight W in the island vs time t for a wave packet initially started as a coherent state in the chaotic sea at $(x, p) = (0.4, -0.2)$ for system sizes $M = 1, 13, 144, 1597$ and $h_{\text{eff}} \approx 1/30$. The thick (green) line guides the eye to the linear increase with $\ln t$ until $W = A_{\text{reg}}$. The insets show the time-evolved wave packet averaged over all cells for the case $M = 1597$, demonstrating the progressive flooding of the island.

Fig. 2(a). A remarkable shift of the main peak of $P(W)$ to larger values of W can be observed in Fig. 2(b). This shows that by enlarging the system size M all chaotic states continuously increase their weight inside the regular islands. This increase stops when the center of the main peak reaches $W = 0.22$, which corresponds to the area A_{reg} of the island. For these system sizes all states completely flood the island [Fig. 2(c), inset], as observed in Ref. [3].

What happens to the regular states as M is increased? Figure 2(b) shows that the corresponding peaks in the distribution $P(W)$ disappear. Notably, the peak for $m = 0$ is much longer visible than the peak for $m = 1$. The nemesis of the regular states can be quantified by determining their fraction f_{reg} as a function of M. To this end we define a state to be regular when its weight W inside the islands exceeds 50%, where the exact criterion does not affect our analysis. Figure 3 shows that the fraction f_{reg} decreases from approximately A_{reg} all the way to zero. The decay is slower for smaller h_{eff}.

Remarkably, in Fig. 3 we see strong signatures of the decrease of f_{reg} already for small system sizes $M \approx 10$. This holds even for small values of h_{eff}, where the complete flooding of the island is numerically not accessible. Similarly, a shift of the main peak in Fig. 2(b) is clearly detectable for such small systems. We thus find that partial flooding of regular islands is easily observable.

Why do chaotic states flood the islands of regular motion, and why do regular states disappear as the system size is increased? Let us consider a single regular island coupled by tunneling to a chaotic sea. If the chaotic sea is infinite, its states form a continuum. A regular state on the mth quantized torus has a decay rate γ_m to the continuum [13]. Thus, it is not an eigenstate, but it is dissolved into chaotic states. As a consequence, the chaotic states occupy the mth quantized torus of the island. If the chaotic sea is finite, but large enough, this decay of the mth regular state may still take place. The condition for the decay is that during the time $1/\gamma_m$ the discrete chaotic spectrum is not resolved, leading to $1/\gamma_m \ll h/\Delta_{\text{ch}} = \tau_{\text{H}}$ [15]. On the other hand, if the chaotic sea is so small that during the time $1/\gamma_m$ the chaotic spectrum is well resolved, then the regular state m does not decay, yielding Eq. (1). Note that γ_m increases monotonically with m; as for larger m, the mth torus is closer to the boundary of the island.

The quantized tori of an island can thus be grouped into two classes: (i) the inner tori, $m = 0, \ldots, m^* - 1$, where condition (1) is fulfilled and regular states exist and (ii) the outer tori, $m = m^*, \ldots, m_{\text{max}} - 1$, where Eq. (1) is violated and which is flooded by chaotic states. Here m_{max} is the number of quantized tori at a given h_{eff}. We find for the fraction f_{reg} of regular states and the weight W_{ch} of chaotic states inside the island

$$f_{\text{reg}} = A_{\text{reg}} \frac{m^*}{m_{\text{max}}}, \qquad W_{\text{ch}} = A_{\text{reg}}\left(1 - \frac{m^*}{m_{\text{max}}}\right). \tag{3}$$

Variation of the system size M in our example allows us to change the Heisenberg time $\tau_{\text{H}} \sim M$, while keeping the rates γ_m fixed. Enlarging M leads via Eq. (1) to a decrease of m^*, starting from $m^* = m_{\text{max}} - 1$ all the way to $m^* = 0$. Together with Eq. (3) this explains Fig. 2(b), where the regular state with $m = 1$ disappears before the $m = 0$ state and the weight W_{ch} grows until $W_{\text{ch}} = A_{\text{reg}}$, where the island is completely flooded; see Fig. 2(c). This also explains the decrease of f_{reg} from A_{reg} to 0, as observed in Fig. 3. This decrease occurs over an exponentially large range in M, due to the roughly exponential dependence of γ_m on m. A quantitative understanding requires a theory for the decay rates γ_m, which is the subject of current research on dynamical tunneling [16,17]. Note that in the case of chaos-assisted tunneling the splitting of symmetry related regular states fluctuates strongly, depending on individual chaotic states. In contrast, the decay rate γ_m describes an average tunneling to a continuum of chaotic states.

Variation of h_{eff} affects both γ_m and τ_{H} in Eq. (1). While $\tau_{\text{H}} \sim M/h_{\text{eff}}$, one expects in analogy to WKB theory that $\gamma_m \sim \exp[-g(m/m_{\text{max}})/h_{\text{eff}}]$, where the system specific function g decreases monotonically to $g(1) = 0$. From the definition of m^* follows $m^*/m_{\text{max}} = g^{-1}[h_{\text{eff}} \ln(M/h_{\text{eff}})]$, where g^{-1} decreases monotonically. Decreasing h_{eff} reduces the argument of g^{-1} such that m^*/m_{max} increases. Equation (3) implies that f_{reg} grows and W_{ch} decreases. Note that in the semiclassical limit, $h_{\text{eff}} \to 0$, we obtain $m^*/m_{\text{max}} \to 1$. This is in agreement with the semiclassical eigenfunction hypothesis, namely, $f_{\text{reg}} = A_{\text{reg}}$ and there is no flooding. In contrast, if the system size is infinite, we have an infinite τ_{H} and our argument leads to $m^* = 0$, i.e., complete flooding, for any h_{eff}. This coincides with the

considerations of [3] implying a failure of the semiclassical eigenfunction hypothesis.

Our explanation is complete for systems without localization. For example, this is the case if the average classical drift of a unit cell is nonzero, as in atom optic experiments in the presence of gravity [9,10]. Localization, however, sets a lower bound to the effective mean level spacing, $\Delta_{\mathrm{ch}} \sim 1/\lambda$, where λ is the localization length. For $M > \lambda$, this leads to $\tau_{\mathrm{H}} \sim \lambda$ and m^* stays at its value for $M = \lambda$. According to Eq. (3) the same holds for f_{reg} and W_{ch}. This applies, e.g., to dynamical localization in the kicked rotor. For transporting islands, as in the model studied here, $\lambda \sim 1/\gamma_0$ is unusually large [3,14,18], such that already for $M = \lambda$ one has $m^* = 0$, $f_{\mathrm{reg}} = 0$, and $W_{\mathrm{ch}} = A_{\mathrm{reg}}$. In this case, localization has no consequences [19].

We generalize our analysis to the dynamics of wave packets, which is experimentally of great relevance [9]. A wave packet started on the mth torus is restricted to that region if condition (1) is fulfilled; i.e., $m < m^*$. If $m > m^*$, however, the wave packet decays into the chaotic sea. Particularly interesting is the case of a wave packet started inside the chaotic sea. The island is progressively flooded; i.e., the mth torus at time $t_m \sim 1/\gamma_m$ for $m > m^*$. For $t > \tau_{\mathrm{H}}$ the weight $W(t)$ saturates at W_{ch} [Eq. (3)]. This is confirmed in Fig. 4, for increasing values of M.

Our results have consequences for spectral statistics in mixed systems which go well beyond the previously studied effects of dynamical tunneling (see, e.g., [16,20]). The effective size of the regular region, f_{reg}, in Eq. (3), entering the Berry-Robnik formula [21] is drastically reduced.

Our analysis applies as well to hierarchical states [22], which are confined by partial transport barriers with turnstile areas smaller than h. We predict the additional condition $\gamma < 1/\tau_{\mathrm{H}}$ for their existence, where γ describes the decay through these partial barriers. For regular states on island chains within that hierarchical region, condition (1) applies, with τ_{H} given by the mean level spacing of the surrounding hierarchical states.

Finally, we emphasize that the time periodicity of the system (2) and the restriction of our discussion to maps is not crucial and that we expect flooding of islands for any Hamiltonian with a mixed phase space. We stress that this new quantum signature of chaos for eigenstates and wave packet dynamics already appears for small system sizes, e.g., island chains of length 10. This makes numerical explorations very feasible and should lead to experimental observations, for example, using optical lattices [7–9].

We thank Holger Schanz for discussions and the DFG for support under Contract No. KE 537/3-2.

[1] I. C. Percival, J. Phys. B **6**, L229 (1973); M. V. Berry, J. Phys. A **10**, 2083 (1977); A. Voros, in *Stochastic Behavior in Classical and Quantum Hamiltonian Systems* (Springer, Berlin, 1979), p. 326.

[2] See, e.g., A. Bäcker, R. Schubert, and P. Stifter, Phys. Rev. E **57**, 5425 (1998), and references therein.

[3] L. Hufnagel, R. Ketzmerick, M.-F. Otto, and H. Schanz, Phys. Rev. Lett. **89**, 154101 (2002).

[4] M. V. Berry, N. L. Balazs, M. Tabor, and A. Voros, Ann. Phys. (N.Y.) **122**, 26 (1979).

[5] H. Schanz, M.-F. Otto, R. Ketzmerick, and T. Dittrich, Phys. Rev. Lett. **87**, 070601 (2001).

[6] F. M. Izrailev, Phys. Rep. **196**, 299 (1990).

[7] D. A. Steck, W. H. Oskay, and M. G. Raizen, Science **293**, 274 (2001).

[8] W. K. Hensinger *et al.*, Nature (London) **412**, 52 (2001).

[9] M. K. Oberthaler *et al.*, Phys. Rev. Lett. **83**, 4447 (1999); S. Schlunk, M. B. d'Arcy, S. A. Gardiner, and G. S. Summy, Phys. Rev. Lett. **90**, 124102 (2003).

[10] S. Fishman, I. Guarneri, and L. Rebuzzini, Phys. Rev. Lett. **89**, 084101 (2002); J. Stat. Phys. **110**, 911 (2003); M. B. d'Arcy *et al.*, Phys. Rev. E **69**, 027201 (2004).

[11] We start with linear functions $t'(p) = 1/2 \pm (1 - 2p)$ for $0 < \pm p < 1/2$ (periodically extended) and $v'(x) = -k - r(x - k)$ for $k - 1/2 < x < k + 1/2$, where $k \in \mathbb{Z}$. Smoothing with a Gaussian, $G(z) = \exp(-z^2/2\varepsilon^2)/\sqrt{2\pi\varepsilon^2}$, gives analytic functions $T'(p) = \int dz t'(p + z)G(z)$ and $V'(x) = \int dz v'(x + z)G(z)$. We use $r = 0.65$, and $\varepsilon = 0.015$, as for Fig. 1(a) in Ref. [3].

[12] We improve the statistics for small M by varying the phase of the boundary condition in the x direction, which does not affect the underlying classical dynamics. For large M we use 2000 eigenstates.

[13] This is in analogy to a discrete state coupled to a continuum discussed in U. Fano, Nuovo Cimento, N. s. **12**, 154 (1935). In practice one can determine the rates γ_m by starting suitable wave packets as in [14].

[14] J. D. Hanson, E. Ott, and T. M. Antonsen, Phys. Rev. A **29**, 819 (1984).

[15] A barrier tunneling analogy is given in E. J. Heller and M. J. Davies, J. Phys. Chem. **85**, 307 (1981). For a discussion of time scales in quantum chaos, see, e.g., F. Borgonovi and G. Casati, in *Frontiers in Quantum Physics* (Springer, Singapore, 1998), p. 127. By Fermi's golden rule one can show that the reasoning using time scales is equivalent to the comparison of the coupling matrix element v_m to the mean spacing Δ_{ch}.

[16] V. A. Podolskiy and E. E. Narimanov, Phys. Rev. Lett. **91**, 263601 (2003).

[17] M. J. Davis and E. J. Heller, J. Chem. Phys. **75**, 246 (1981); O. Bohigas, S. Tomsovic, and D. Ullmo, Phys. Rep. **223**, 43 (1993); O. Brodier, P. Schlagheck, and D. Ullmo, Ann. Phys. (N.Y.) **300**, 88 (2002); C. Eltschka and P. Schlagheck, Phys. Rev. Lett. **94**, 014101 (2005).

[18] A. Iomin, S. Fishman, and G. M. Zaslavsky, Phys. Rev. E **65**, 036215 (2002), and references therein.

[19] Depending on the factor between λ and $1/\gamma_0$, the $m = 0$ state might couple to very few chaotic states only. The emerging eigenstates may look more like hybrid states that are regular in some unit cells and chaotic in others, explaining such an observation in Fig. 4 of Ref. [3].

[20] T. Prosen and M. Robnik, J. Phys. A **27**, 8059 (1994).

[21] M. V. Berry and M. Robnik, J. Phys. A **17**, 2413 (1984).

[22] R. Ketzmerick, L. Hufnagel, F. Steinbach, and M. Weiss, Phys. Rev. Lett. **85**, 1214 (2000).

[A7] Nano-wires with surface disorder: Giant localization lengths and quantum-to-classical crossover

J. Feist, A. Bäcker, R. Ketzmerick, S. Rotter, B. Huckestein, and J. Burgdörfer
Phys. Rev. Lett. **97** (2006) 116804 (4 pages)

We investigate electronic quantum transport through nano–wires with one–sided surface roughness. A magnetic field perpendicular to the scattering region is shown to lead to exponentially diverging localization lengths in the quantum–to–classical crossover regime. This effect can be quantitatively accounted for by tunneling between the regular and the chaotic components of the underlying mixed classical phase space.

Nanowires with Surface Disorder: Giant Localization Lengths and Quantum-to-Classical Crossover

J. Feist,[1,*] A. Bäcker,[2] R. Ketzmerick,[2] S. Rotter,[1,3] B. Huckestein,[4] and J. Burgdörfer[1]

[1]*Institute for Theoretical Physics, Vienna University of Technology, 1040 Vienna, Austria*
[2]*Institut für Theoretische Physik, Technische Universität Dresden, 01062 Dresden, Germany*
[3]*Department of Applied Physics, Yale University, New Haven, Connecticut, 06520, USA*
[4]*Institut für Theoretische Physik III, Ruhr-Universität Bochum, 44780 Bochum, Germany*

(Received 20 June 2006; published 13 September 2006)

We investigate electronic quantum transport through nanowires with one-sided surface roughness. A magnetic field perpendicular to the scattering region is shown to lead to exponentially diverging localization lengths in the quantum-to-classical crossover regime. This effect can be quantitatively accounted for by tunneling between the regular and the chaotic components of the underlying mixed classical phase space.

DOI: 10.1103/PhysRevLett.97.116804 PACS numbers: 73.63.Nm, 05.45.Mt, 72.20.Dp, 73.23.Ad

Transport through a disordered medium is a key issue in solid state physics which comprises countless applications in (micro-) electronics and optics [1]. The ubiquitous presence of disorder plays a prominent role for the behavior of transport coefficients governing, e.g., the metal-insulator transition [2]. The interest in disordered media has recently witnessed a revival due to new experimental possibilities to study the "mesoscopic" regime of transport where a quantum-to-classical crossover gives rise to a host of interesting phenomena [3].

In most investigations a static disorder is assumed to be present in the *bulk* of a material. The strength and distribution of the disorder potential determine whether transport will be ballistic, diffusive, or suppressed in the localization regime [1,3]. In nanodevices the reduction of system sizes leads, however, to an increased surface-to-volume ratio, for which *surface roughness* can represent the dominant source of disorder scattering. While random matrix theory (RMT) is successful in describing bulk disordered systems [4], its application to wires with surface disorder is not straightforward [5].

In the present Letter we study electronic quantum transport through a nanowire in the presence of one-sided surface disorder and a magnetic field. We show both numerically and analytically that by increasing the number of open channels N in the wire, or equivalently, by increasing the wave number k_F, the localization length ξ increases exponentially. Using a numerical approach that allows to study extremely long wires we show an increase by a factor 10^7 (Fig. 1). Such a giant localization length falls outside the scope of RMT predictions, $\xi \propto N$, previously studied for this system [6]. Instead it can be understood in terms of the underlying mixed regular-chaotic classical motion in the wire. We find that the conductance through the wire is controlled by tunneling from the regular to the chaotic part of phase space. This process, often referred to as "dynamical tunneling" [7], has been actively studied in quantum chaos and plays an important role in the context of classically transporting phase-space structures [8–12]. Here we establish a direct quantitative link between the exponential increase of the localization length in mesoscopic systems and the suppression of tunneling from the regular to the chaotic part of phase space in the semiclassical limit.

We consider a 2D wire with surface disorder to which two leads of width W are attached (Fig. 1, inset), with a homogeneous magnetic field B perpendicular to the wire present throughout the system. We simulate the disorder by a random sequence of vertical steps. The wire can thus be assembled from rectangular elements, referred to in the following as modules, with equal width l, but random

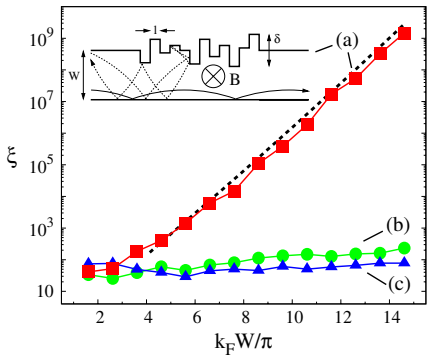

FIG. 1 (color online). Localization length ξ for a wire with surface roughness vs $k_F W/\pi = 1/h_{\text{eff}}$. Results are compared for wires with (a) one-sided disorder (OSD) with $B \neq 0$ (red ■), (b) OSD with $B = 0$ (green ●), and (c) two-sided disorder with $B \neq 0$ (blue ▲). In (a) an exponential increase of ξ is observed in excellent agreement with Eq. (8) which has no adjustable parameters (dashed line).

heights h, uniformly distributed in the interval $[W - \delta/2, W + \delta/2]$. This particular representation of disorder allows for an efficient numerical computation of quantum transport for remarkably long wires $L \to \infty$ by employing the modular recursive Green's function method [13]. We first calculate the Green's functions for $M = 20$ rectangular modules with different heights. A random sequence of these modules is connected by means of a matrix Dyson equation. Extremely long wires can be reached by implementing an "exponentiation" algorithm [14]: Instead of connecting the modules individually, we iteratively construct different generations of "supermodules", each consisting of a randomly permuted sequence of M modules of the previous generation. Repeating this process leads to the construction of wires whose length increases exponentially with the number of generations [15].

The transmission (t_{mn}) and reflection amplitudes (r_{mn}) for an electron injected from the left are evaluated by projecting the Green's function at the Fermi energy E_F onto all lead modes $m, n \in \{1, \ldots, N\}$ in the entrance and exit lead, respectively. Here $N = \lfloor k_F W/\pi \rfloor$ is the number of open lead modes and k_F the Fermi wave number. We obtain the localization length ξ in a wire composed of L modules (i.e., length Ll) by analyzing the dimensionless conductance $g = \mathrm{Tr}(t^\dagger t)$ in the regime $g \ll 1$, extracting ξ from $\langle \ln g \rangle \sim -L/\xi$. The brackets $\langle \cdots \rangle$ indicate the ensemble average over 20 different realizations of disorder and 3 neighboring values of wave numbers k_F.

For increasing k_F, we adjust the magnetic field B such that the cyclotron radius $r_c = \hbar k_F/(eB)$ remains constant. This leaves the classical dynamics invariant and allows for probing the quantum-to-classical crossover as $k_F \to \infty$. We choose $r_c = 3W$ and a disorder amplitude $\delta = (2/3)W$ such that we obtain a large regular region in phase space (see below) and use a module width $l = W/5$. We find for one-sided disorder an exponential increase of the localization length ξ (Fig. 1), while ξ remains almost constant when either (i) the magnetic field is switched off or (ii) a two-sided disorder is considered. The latter clearly rules out that the observed giant localization length is due to edge states of the quantum Hall effect [3].

Before giving an analytic determination of the exponentially increasing localization length, we provide an explanation invoking the mixed classical phase-space structure which captures the essential features of this increase.

The classical dynamics inside the disordered wire is displayed by a Poincaré section in Fig. 2(b), for a vertical cut at the wire entrance ($x = 0$) with periodic boundary conditions in the x direction. The resulting section (y, p_y) for $p_x > 0$ shows a large regular region with invariant curves corresponding to skipping motion along the lower straight boundary of the wire. Close to the upper disordered boundary ($y > W - \delta/2$) the motion appears to be chaotic for all p_y. A corresponding Poincaré section for $p_x < 0$ (not shown) is globally chaotic. The lowest transverse

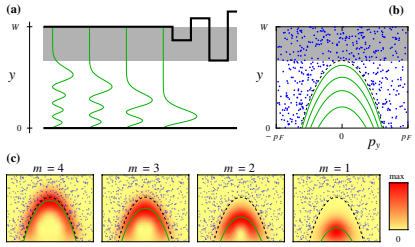

FIG. 2 (color online). (a) Nanowire with the regular transverse modes (green) $m = 4, 3, 2, 1$ for $k_F W/\pi = 14.6$. The gray shaded part indicates the y range affected by disorder. (b) Poincaré section showing a large regular island with outermost torus (dashed), a chaotic sea (blue dots), and quantized tori corresponding to the regular modes (green). (c) Poincaré-Husimi functions of these modes and their quantizing tori.

modes [Fig. 2(a)] of the incoming scattering wave functions overlap primarily with the regular island [Fig. 2(b)]. Only their exponential tunneling tail through the diamagnetic potential barrier (in Landau gauge)

$$V(y) = \tfrac{1}{2} m_e \omega_c^2 (y - y^0)^2 - E_F \qquad (1)$$

touches the upper disordered surface at $y > W - \delta/2$. In Eq. (1), m_e is the electron mass, ω_c the cyclotron frequency, and y^0 the guiding center coordinate. These regular modes can be semiclassically quantized as [16,17]

$$\frac{A}{h} = \frac{B\mathcal{A}}{h/e} = (m - 1/4) \quad \text{with} \quad m = 1, 2, \ldots, \qquad (2)$$

where A is the area in the Poincaré section enclosed by a quantized torus and $\mathcal{A} = r_c A/p_F$ is the area in position space enclosed by a segment of a skipping orbit. One finds $A = p_F r_c[\arccos(1-\nu) - (1-\nu)\sqrt{1-(1-\nu)^2}]$ for $0 \le \nu \le \nu_{\max} \le 1$, where νr_c is the y position at the top of the cyclotron orbit. The size A_{reg} of the regular island is found for $\nu = \nu_{\max} = (W - \delta/2)/r_c$. The Poincaré-Husimi projections (i.e., projections onto coherent states of the transverse eigenfunctions) show, indeed, a density concentration near the quantized tori residing in the regular region of phase space [Fig. 2(c)].

The lowest mode $m = 1$ in the center of the island has the smallest tunneling rate [8,18,19]

$$\gamma_1 \sim \exp\left(-C\frac{A_{\mathrm{reg}}}{h}\right) \qquad (3)$$

to the chaotic sea with some constant C (see below). Its temporal decay $\exp(-\gamma_1 t)$ together with its velocity $v_1 = \hbar k_x/m_e$ lead to an exponential decay as a function of propagation length x, $\exp(-\gamma_1 x/v_1)$. This gives a localization length $\xi \sim \gamma_1^{-1}$ [10]. When increasing k_F, while keeping the cyclotron radius r_c fixed, the classical dynam-

ics remains invariant while the island area scales as $A_{\rm reg} = a_{\rm reg} A_{\rm PS}$. Here $A_{\rm PS} = 2p_F W$ is the area of the Poincaré section and $a_{\rm reg}$ is the relative size of the island. This semiclassical limit is thus equivalent to decreasing the effective Planck's constant $h_{\rm eff} := h/A_{\rm PS} = (k_F W/\pi)^{-1}$ and results in an exponential increase of the localization length

$$\xi \sim \exp\left(C \frac{a_{\rm reg}}{h_{\rm eff}}\right), \tag{4}$$

for $h_{\rm eff} \to 0$, qualitatively explaining Fig. 1(a). Moreover, this exponential increase should set in when the first mode fits into the island, i.e., for $A_{\rm reg}/h \approx 1$. For the parameters of Fig. 1(a) we have $\nu_{\rm max} = 2/9$, resulting in the critical value $k_F W/\pi \approx 3.5$, which is in very good agreement with the numerical result. By contrast, for two-sided disorder or for $B = 0$ no regular island with skipping orbits exists and ξ shows no exponential increase; see Fig. 1.

We now turn to an analytical derivation of the localization length using the specifics of the scattering geometry (Fig. 1 inset). To this end we first calculate the transmission amplitude t_{11} of the transverse regular mode $m = 1$ by considering its consecutive projections from one module to the next

$$t_{11} \approx \prod_{j=1}^{L-1} \int_0^{W+\delta/2} \chi_{h(j)}(y) \chi_{h(j+1)}(y) dy, \tag{5}$$

where $\chi_{h(j)}(y)$ is the mode wave function in module j with height $h(j)$. Equation (5) amounts to a sequence of *sudden approximations* for the transition amplitude between adjacent surface steps. As the wave function is exponentially suppressed at the upper boundary, the scale lk_F introduced by the corners drops out of the calculation. For simplicity, a few technical approximations have been invoked, whose accuracy can be checked numerically: (i) terms in the transmission from one module to the next that involve reflection coefficients and are typically smaller by a factor of 5 are neglected, (ii) contributions from direct coupling between different island modes are neglected, and (iii) the factor $(2y - y^0_{h(j)} - y^0_{h(j+1)})$ from the orthonormality relation for the χ functions [13] is omitted in the above integral as its contribution is negligible.

The modes pertaining to different heights h can be written as $\chi_h(y) = [\chi_\infty(y) - \varepsilon_h(y)]/N_h$, where $\chi_\infty(y)$ is the mode wave function if there was no upper boundary, $\varepsilon_h(y)$ is the correction that is largest at the upper boundary [where $\chi_h(h) = 0$], and N_h is a normalization factor. Keeping only terms of order $O(\varepsilon_h)$ and using a WKB approximation for $\varepsilon_h(y)$ around $y = h_{\rm min} = W - \delta/2$ leads to

$$t_{11} \approx (1 - \sigma)^{2L/M} \quad \text{with} \quad \sigma = \frac{\chi^2_\infty(h_{\rm min})}{k_F \sqrt{V(h_{\rm min})/E_F}}. \tag{6}$$

According to Eq. (6) the coupling strength is quantitatively determined by the tunneling electron density at $y = h_{\rm min}$ in the classically forbidden region of the 1D diamagnetic potential, Eq. (1). The conductance in the regime $g \ll 1$ is now given by

$$g = |t_{11}|^2 \approx \exp(-4\sigma L/M), \tag{7}$$

resulting in a localization length $\xi = M/(4\sigma)$. Using a WKB approximation for $\chi_\infty(y)$ we find

$$\xi(h_{\rm eff}) \approx (a h_{\rm eff}^{-2/3} - b) \exp[c h_{\rm eff}^{-1} (1 - d h_{\rm eff}^{2/3})^{3/2}], \tag{8}$$

with coefficients $a = (16\pi^5)^{1/3} \zeta M \eta \rho^{-1/3}$, $b = -2\pi z_0 \zeta M$, $c = \pi (32/9)^{1/2} \eta^{3/2} \rho^{-1/2} [1 + (3/20)\eta\rho^{-1}]$, $d = -z_0 \rho^{1/3}/(2^{1/3}\pi^{2/3}\eta)$. Here $z_0 \approx -2.338$ is the first zero of the Airy function $\mathrm{Ai}(z)$, $\zeta = \int_{z_0}^\infty \mathrm{Ai}(z)^2 dz$, $\eta = h_{\rm min}/W$, and $\rho = r_c/W$ are dimensionless parameters [20]. Equation (8) is in very good quantitative agreement with the numerically determined localization length [Fig. 1(a)]. We conclude that tunneling from the regular phase-space island is primarily due to interaction of each regular mode with the rough surface rather than via successive transitions from inner to outer island modes.

We note that the constant C in Eqs. (3) and (4) is found to be $C = 2\pi[1 + (289/960)\eta\rho^{-1}]$, which differs from $C = 2\pi$ [19] and $C = 3 - \ln 4$ [18] derived for other examples of dynamical tunneling from a resonance-free regular island to a chaotic sea. We also note that the scaling behavior of ξ in Eq. (8) is reminiscent of previously obtained results for diffusive 2D systems (see [1]).

For the case of a constant magnetic field B, increasing k_F increases the cyclotron radius, $r_c \propto k_F$, and the classical dynamics is no longer invariant. In particular, the area of the regular island $A_{\rm reg} \sim \sqrt{k_F}$ shrinks compared to $A_{\rm PS} \sim k_F$ as skipping motion is increasingly suppressed. Nevertheless, the arguments leading to Eqs. (4) and (8) remain applicable and yield a localization length that increases dramatically as $\xi \sim \exp(\mathrm{const}\sqrt{k_F})$ in agreement with numerical observations (not shown).

Now we turn to the behavior of the conductance for wires of lengths smaller than the localization length. Modes with larger m have larger amplitudes near the rough surface and thus couple more strongly to the chaotic part of phase space. They have, consequently, larger tunneling rates γ_m and smaller localization lengths $\xi_m \sim \gamma_m^{-1}$. The successive elimination of modes as a function of the length L of the wire results in a sequence of plateaus [Fig. 3(a)]. For $L > \xi_m$ the mode m no longer contributes to transport, as can be seen by its individual contribution to the transmission in Fig. 3(b). This disappearance of regular modes is reflected in the averaged Poincaré-Husimi distributions calculated from incoherent superpositions of all modes entering from the left and scattering to the right. Also shown are the complementary distributions obtained for backscattering from right to right. For small L these Poincaré-Husimi functions are outside the regular island, while with increasing L they begin to "flood" it [11]. This

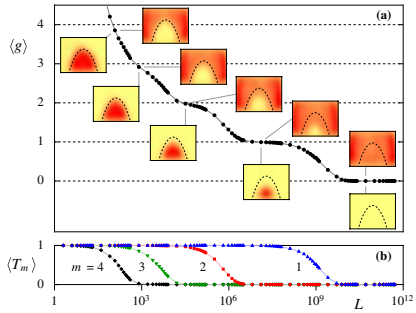

FIG. 3 (color online). (a) Averaged conductance $\langle g \rangle$ vs length L of the wire. The stepwise decrease is accompanied by the disappearance of the regular modes and the flooding of the island region by chaotic states. The Poincaré-Husimi distributions to the left (right) of the curve correspond to scattering from left to right (backscattering from right to right). (b) Transmission $\langle T_m \rangle$ of the incoming mode m vs L.

process is complete for lengths $L \gg \xi$. The complementarity of the Husimi distributions illustrates that tunneling between the regular island and the chaotic sea proceeds symmetrically in both directions, as required by the unitarity of the scattering matrix.

Summarizing, we have presented a numerical computation and an analytical derivation for the exponential increase of the localization length in a two-dimensional system of a quantum wire with one-sided surface disorder. Our approach, based on a mixed phase-space analysis, also explains the increase of ξ over 1 order of magnitude under increase of the magnetic field observed in Ref. [6]. It sets in for a magnetic field for which the regular island is large enough to accommodate at least one quantum mechanical mode. Clearly, the RMT result, $\xi \propto N$, which ignores the mixed phase-space structure, no longer applies. Instead, we find that the giant localization length (Fig. 1) in this disordered mesoscopic device is determined by the tunneling from the regular to the chaotic region, the rate of which is exponentially suppressed in the semiclassical regime.

A. B. and R. K. acknowledge support by the DFG under Contract No. KE 537/3-2, J. F., S. R., and J. B. acknowledge support by the FWF-Austria (Grant No. P17354) and the Max-Kade foundation, New York.

*Electronic address: johannes.feist@tuwien.ac.at

[1] P. Sheng, *Introduction to Wave Scattering, Localization and Mesoscopic Phenomena* (Academic, New York, 1995); P. A. Lee and T. V. Ramakrishnan, Rev. Mod. Phys. **57**, 287 (1985); *Mesoscopic Phenomena in Solids*, edited by B. L. Altshuler, P. A. Lee, and R. A. Webb (North-Holland, Amsterdam, 1991).
[2] P. W. Anderson, Phys. Rev. **109**, 1492 (1958).
[3] S. Datta, *Electronic Transport in Mesoscopic Systems* (Cambridge University Press, Cambridge, United Kingdom, 1995); D. K. Ferry and S. M. Goodnick, *Transport in Nanostructures* (Cambridge University Press, Cambridge, United Kingdom, 1997).
[4] C. W. J. Beenakker, Rev. Mod. Phys. **69**, 731 (1997).
[5] M. Leadbeater, V. I. Falko, and C. J. Lambert, Phys. Rev. Lett. **81**, 1274 (1998); J. A. Sánchez-Gil, V. Freilikher, I. Yurkevich, and A. A. Maradudin, Phys. Rev. Lett. **80**, 948 (1998); A. García-Martín and J. J. Saenz, Phys. Rev. Lett. **87**, 116603 (2001); F. M. Izrailev, J. A. Mendez-Bermudez, and G. A. Luna-Acosta, Phys. Rev. E **68**, 066201 (2003); E. I. Chaikina, S. Stepanov, A. G. Navarrete, E. R. Mendez, and T. A. Leskova, Phys. Rev. B **71**, 085419 (2005).
[6] A. García-Martín, M. Governale, and P. Wölfle, Phys. Rev. B **66**, 233307 (2002).
[7] M. J. Davis and E. J. Heller, J. Chem. Phys. **75**, 246 (1981).
[8] J. D. Hanson, E. Ott, and T. M. Antonsen, Phys. Rev. A **29**, 819 (1984).
[9] S. Fishman, I. Guarneri, and L. Rebuzzini, Phys. Rev. Lett. **89**, 084101 (2002); H. Schanz, T. Dittrich, and R. Ketzmerick, Phys. Rev. E **71**, 026228 (2005).
[10] L. Hufnagel, R. Ketzmerick, M.-F. Otto, and H. Schanz, Phys. Rev. Lett. **89**, 154101 (2002); A. Iomin, S. Fishman, and G. M. Zaslavsky, Phys. Rev. E **65**, 036215 (2002).
[11] A. Bäcker, R. Ketzmerick, and A. G. Monastra, Phys. Rev. Lett. **94**, 054102 (2005).
[12] M. Prusty and H. Schanz, Phys. Rev. Lett. **96**, 130601 (2006).
[13] S. Rotter *et al.*, Phys. Rev. B **62**, 1950 (2000); , **68**, 165302 (2003).
[14] J. Skjånes, E. H. Hauge, and G. Schön, Phys. Rev. B **50**, 8636 (1994).
[15] With this approach we can study wires with up to $\sim 10^{12}$ modules, beyond which numerical unitarity deficiencies set in. For wires with up to 10^5 modules we can compare this supermodule technique containing pseudorandom sequences with truly random sequences of modules. For configuration-averaged transport quantities the results are indistinguishable from each other.
[16] A. M. Kosevich and I. M. Lifshitz, Zh. Eksp. Teor. Fiz. **29**, 743 (1955) [Sov. Phys. JETP **2**, 646 (1956)].
[17] C. W. J. Beenakker and H. van Houten, Phys. Rev. Lett. **60**, 2406 (1988).
[18] V. A. Podolskiy and E. E. Narimanov, Phys. Rev. Lett. **91**, 263601 (2003); P. Schlagheck, C. Eltschka, and D. Ullmo, nlin.CD/0508024; M. Sheinman, Masters thesis, Technion, 2005.
[19] M. Sheinman, S. Fishman, I. Guarneri, and L. Rebuzzini, Phys. Rev. A **73**, 052110 (2006).
[20] Setting $d = 0$ corresponds to a quantization at the minimum of the diamagnetic potential $V(y)$ in Eq. (1). This produces the correct leading order, but for our largest $1/h_{\text{eff}} = 14.6$ the result would be wrong by a factor 10^5.

[A8] Universality in the flooding of regular islands by chaotic states

A. Bäcker, R. Ketzmerick, and A. Monastra

Phys. Rev. E, in press (2007), ArXiv, nlin.CD/0701032

We investigate the structure of eigenstates in systems with a mixed phase space in terms of their projection onto individual regular tori. Depending on dynamical tunneling rates and the Heisenberg time, regular states disappear and chaotic states flood the regular tori. For a quantitative understanding we introduce a random matrix model. The resulting statistical properties of eigenstates as a function of an effective coupling strength are in very good agreement with numerical results for a kicked system. We discuss the implications of these results for the applicability of the semiclassical eigenfunction hypothesis.

Universality in the flooding of regular islands by chaotic states

Arnd Bäcker[1], Roland Ketzmerick[1], and Alejandro G. Monastra[1,2]
[1] *Institut für Theoretische Physik, Technische Universität Dresden, 01062 Dresden, Germany*
[2] *Departamento de Física, Comisión Nacional de Energía Atómica, Av. del Libertador 8250, 1429 Buenos Aires, Argentina*

(Dated: 05.01.2007)

We investigate the structure of eigenstates in systems with a mixed phase space in terms of their projection onto individual regular tori. Depending on dynamical tunneling rates and the Heisenberg time, regular states disappear and chaotic states flood the regular tori. For a quantitative understanding we introduce a random matrix model. The resulting statistical properties of eigenstates as a function of an effective coupling strength are in very good agreement with numerical results for a kicked system. We discuss the implications of these results for the applicability of the semiclassical eigenfunction hypothesis.

PACS numbers: 05.45.Mt, 03.65.Sq

I. INTRODUCTION

The classical dynamics in Hamiltonian systems shows a rich behaviour ranging from integrable to fully chaotic motion. In chaotic systems nearby trajectories separate exponentially in time and ergodicity implies that a typical trajectory fills out the energy-surface in a uniform way. However, integrable and fully chaotic dynamics are exceptional [1] as typical Hamiltonian systems show a mixed phase space in which regions of regular motion, the so-called regular islands around stable periodic orbits, and chaotic dynamics, the so-called chaotic sea, coexist.

For quantized Hamiltonian systems the fundamental questions concern the behaviour of the eigenvalues and the properties of eigenfunctions, especially in the semiclassical regime. From the semiclassical eigenfunction hypothesis [2, 3, 4, 5, 6] one expects that in the semiclassical limit the eigenstates concentrate on those regions in phase space which a typical orbit explores in the long-time limit. For integrable systems these are the invariant tori. In contrast, for ergodic systems almost all orbits fill the energy shell in a uniform way. For this situation the semiclassical eigenfunction hypothesis is proven by the quantum ergodicity theorem which shows that almost all eigenstates become equidistributed on the energy shell [7].

For systems with a mixed phase space, in the semiclassical limit ($h \to 0$), the semiclassical eigenfunction hypothesis implies that the eigenstates can be classified as being either regular or chaotic according to the phase-space region on which they concentrate. This is supported by several studies, see e.g. [8, 9, 10, 11, 12, 13]. It is also possible, that the influence of a regular island quantum mechanically extends beyond the outermost invariant curve due to partial barriers like cantori and that quantization conditions remain approximately applicable even outside of the island [8]. However, it was recently shown that the classification into regular and chaotic states does not hold when the phase space has an infinite volume [14]. In this case eigenstates may completely ignore the classical phase space boundaries between regular and chaotic regions.

In order to understand the behaviour of eigenstates away from the semiclassical limit, i.e. at finite values of the Planck constant h, one has to compare the size of phase-space structures with h. Let us consider for simplicity the case of two-dimensional area preserving maps and their quantizations. Regular states of an island concentrate on tori which fulfill the EBK-type quantization condition

$$\oint p\,\mathrm{d}q = (m+1/2)h \qquad m = 0, 1, \ldots \tag{1}$$

for the enclosed area [15]. This quantization rule explicitly shows that regular eigenstates only appear if $h/2$ is smaller than the area A_{reg} of that island.

Another consequence of finite h in systems with a mixed phase space is dynamical tunneling [16], i.e. tunneling through dynamically generated barriers in phase space, in contrast to the usual tunneling under a potential barrier. Dynamical tunneling couples the subspace spanned by the regular basis states, corresponding to the quantization condition (1), with the complementary subspace [17] composed of chaotic basis states. This raises the question whether the *eigenstates* of such a quantum system can still be called *regular* or *chaotic*.

In Ref. [18] it was shown that (1) is not a sufficient condition for the existence of a regular eigenstate on the m-th quantized torus. In addition one has to fulfill

$$\gamma_m < \frac{1}{\tau_{\mathrm{H,ch}}}, \tag{2}$$

where $\tau_{\mathrm{H,ch}} = h/\Delta_{\mathrm{ch}}$ is the Heisenberg time of the surrounding chaotic sea with mean level spacing Δ_{ch} and γ_m is the decay rate of the m-th regular state, if the chaotic sea were infinite. When condition (2) is violated one observes eigenstates which extend over the chaotic region and flood the m-th torus [18]. To distinguish them from the chaotic eigenstates that do not flood the torus, they are referred to as *flooding eigenstates*. For the limiting case of complete flooding of all tori, the corresponding eigenstates were called amphibious [14]. Recently, the

consequences of flooding for the transport properties in rough nano-wires were studied [19].

The process of flooding was explained and demonstrated for a kicked system in Ref. [18]. Condition (2) was obtained by scaling arguments, which cannot provide a prefactor. Moreover, for an ensemble of systems, one would like to know the probability for the existence of a regular eigenstate. In particular, when varying the Heisenberg time, how broad is the transition regime during which this probability goes from 1 to 0? Another question is, how do the chaotic eigenstates turn into flooding eigenstates for a given torus?

In this paper we give quantitative answers to these questions. We study the flooding of regular tori in terms of the weight of eigenstates inside the regular region and devise a random matrix model which allows for describing the statistics of these weights in detail. Random matrix models have been very successful for obtaining quantitative predictions on eigenstates in both fully chaotic systems and systems with a mixed phase space, see e.g. [8, 20, 21, 22, 23, 24]. For the present situation we propose a random matrix model which takes regular basis states and their coupling to the chaotic basis states into account. The only free parameters are the strength of the coupling and the ratio of the number of regular to the number of chaotic basis states. From this model the weight distribution for eigenstates is determined.

For a kicked system we define the weight by the projection of the eigenstates onto regular basis states localized on a given torus m. The distribution of the weights allows for studying the flooding of each torus separately. The resulting distributions are compared with the prediction of the random matrix model and, after an appropriate rescaling, very good agreement is observed. This agreement shows explicitly the universal features underlying the process of flooding, giving a precise criterion for the existence or non–existence of regular, chaotic, and flooding eigenstates in mixed systems.

The text is organized as follows. In section II we introduce the kicked system used for the numerical illustrations, both classically (part A) and quantum mechanically (part B). In section II C we define the weight of an eigenstate by its projection onto regular basis states and investigate the distribution of the weights for the kicked system. In section III we introduce the random matrix model and determine the corresponding weight distribution as a function of the coupling strength. In section IV the relation between parameters of the kicked system and the random matrix model is derived. This allows for a direct comparison of the distributions. In section V we consider the fraction of regular eigenstates, both for an individual torus and for the entire island. In section VI we briefly discuss the consequences of the random matrix model on the number of flooding eigenstates. A summary and discussion of the eigenfunction structure in generic systems with a mixed phase space is given in section VII.

II. THE KICKED SYSTEM

A. Classical dynamics

For a general one-dimensional kicked Hamiltonian

$$H(p,q,t) = T(p) + V(q) \sum_{n=-\infty}^{\infty} \delta(t-n) \ , \qquad (3)$$

the dynamics is fully determined by the mapping of position and momentum (q_n, p_n) at times $t = n + 0^+$ just after the kicks

$$q_{n+1} = q_n + T'(p_n) \ , \qquad (4)$$
$$p_{n+1} = p_n - V'(q_{n+1}) \ . \qquad (5)$$

Choosing the functions $T'(p)$ and $V'(q)$ appropriately, one can obtain a system with a large regular island and a homogeneous chaotic sea. For the system considered in [18], first introduced in [14], one starts with the piecewise linear functions (see Fig. 1b)

$$t'(p) = \frac{1}{2} + \left(\frac{1}{2} - sp\right) \mathrm{sign}\left(p - \lfloor p + 1/2 \rfloor\right) \ , \qquad (6)$$
$$v'(q) = -rq - (1-r)\lfloor q + 1/2 \rfloor \ , \qquad (7)$$

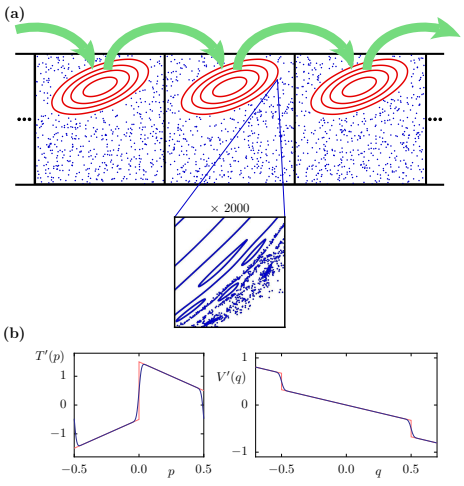

FIG. 1: (color online) (a) Classical dynamics of the kicked system given by Eqs. (4) and (5). Invariant tori of the regular island are shown (red curves) and the transport to the right is indicated by the arrows. The blue dots correspond to one chaotic orbit. The magnification shows that the boundary of the island to the chaotic sea is rather sharp with only very small secondary islands. (b) Smoothed functions $T'(p)$ and $V'(q)$ (blue lines) and discontinuous functions $t'(p)$ and $v'(q)$ (red lines) according to Eqs. (6-9).

where $\lfloor x \rfloor$ is the floor function, and s and r are two parameters determining the properties of the regular island and the chaotic sea. Using a Gaussian smoothing with $G_\varepsilon(z) = \exp(-z^2/2\varepsilon^2)/\sqrt{2\pi\varepsilon^2}$, one obtains analytic functions

$$T'(p) = \int_{-\infty}^{\infty} \mathrm{d}z\, t'(p+z)\, G_\varepsilon(z) \;, \tag{8}$$

$$V'(q) = \int_{-\infty}^{\infty} \mathrm{d}z\, v'(q+z)\, G_\varepsilon(z) \;. \tag{9}$$

By construction, these functions have the periodicity properties

$$T'(p+k) = T'(p) \;, \tag{10}$$

$$V'(q+k) = V'(q) - k \;, \tag{11}$$

for any integer k. We consider $p \in [-1/2, 1/2[$ and $q \in [-1/2, -1/2+M[$ with periodic boundary conditions. The phase space is composed of a chain of transporting islands centered at $(\bar{q}, \bar{p}) = (k, 1/4)$ with $0 \le k \le M-1$ that are mapped one unit cell to the right (see Fig. 1a). The surrounding chaotic sea has an average drift to the left as the overall transport is zero [25, 26]. The fine scale structure at the boundary of the island to the chaotic sea has a very small area (see the magnification in Fig. 1a). Resonances in this layer are irrelevant in the h regime studied here. For $s = 2$, $r = 0.65$ and $\varepsilon = 0.015$ the regular island has a relative area $A_{\mathrm{reg}} \approx 0.215$.

B. Quantization

In kicked systems, the quantum evolution of a state after one period of time

$$|\psi(t+1)\rangle = \hat{U}|\psi(t)\rangle \;, \tag{12}$$

is fully determined by the unitary operator, see e.g. [15, 27, 28, 29, 30],

$$\hat{U} = \exp\left(-\frac{2\pi\mathrm{i}}{h_{\mathrm{eff}}} V(\hat{q})\right) \exp\left(-\frac{2\pi\mathrm{i}}{h_{\mathrm{eff}}} T(\hat{p})\right) \;. \tag{13}$$

Here the effective Planck's constant h_{eff} is Planck's constant h divided by the size of one unit cell. The eigenstates of this operator are defined by

$$\hat{U}|\psi_j\rangle = \mathrm{e}^{2\pi\mathrm{i}\varphi_j}|\psi_j\rangle \;, \tag{14}$$

where the eigenphase φ_j is the quasienergy divided by $\hbar\omega$. In order to fulfill the periodicity of the classical dynamics in p direction, the quantum states have to obey the quasi-periodicity condition

$$\langle p+1|\psi\rangle = \mathrm{e}^{-2\pi\mathrm{i}\chi_p}\langle p|\psi\rangle \;. \tag{15}$$

One can show that this leads to quantum states that are a linear combination of the discretized position states $|q_j\rangle$, with $q_j = h_{\mathrm{eff}}(j+\chi_p)$. Additionally, imposing periodicity

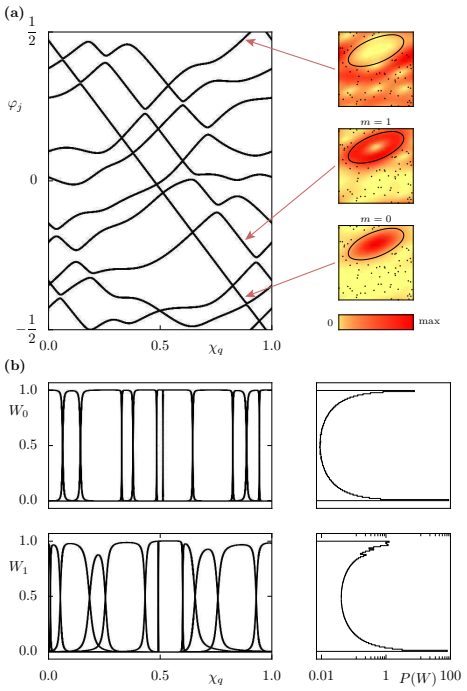

FIG. 2: (color online) (a) Eigenphases of the kicked system vs χ_q for $h_{\mathrm{eff}} = 1/10$. The pattern of straight lines (interrupted by avoided crossings) with negative slope corresponds to regular eigenstates with $m = 0$ and $m = 1$ whose Husimi functions are shown to the right. The other eigenstates are chaotic and live outside of the regular region, as can be seen from the Husimi representation. (b) Weights W_0 and W_1 of all eigenstates vs χ_q (left). Distribution $P(W)$ of these weights in a log-linear representation (right).

after M unit cells in q direction, quantum states have to fulfill the property

$$\langle q+M|\psi\rangle = \mathrm{e}^{2\pi\mathrm{i}\,\chi_q}\langle q|\psi\rangle \;. \tag{16}$$

Because of the required periodicity the phase space is compact and the effective Planck's constant can only be a rational number

$$h_{\mathrm{eff}} = \frac{M}{N} \;. \tag{17}$$

We consider the case of incommensurate M and N, so that the quantum system is not effectively reduced to less than M cells.

The properties (10), (11) of $T'(p)$ and $V'(q)$ imply for their integrals

$$T(p+k) = T(p) , \tag{18}$$

$$V(q+k) = V(q) - kq - \frac{k^2}{2} . \tag{19}$$

From this one finds that the propagator $\hat{U}$ is consistent with the periodicity conditions (15) and (16) if and only if

$$M\left(\chi_p + \frac{N}{2}\right) \in \mathbb{Z} . \tag{20}$$

For given M and N, this condition limits the possible values of the phase χ_p, while χ_q remains arbitrary. Thus, in the basis given by the position states $|q_j\rangle$, with $0 \le j \le N-1$, where N is the dimension of the Hilbert space, the propagator $\hat{U}$ is represented by the finite $N \times N$ unitary matrix

$$U_{kl} = \frac{1}{N} \sum_{j=0}^{N-1} \mathrm{e}^{-\frac{\mathrm{i}}{h_{\mathrm{eff}}}[V(q_k)+T(p_j)+p_j(q_l-q_k)]} , \tag{21}$$

where $0 \le k, l \le N-1$ and $p_j = (j+\chi_q)/N$. Finding the solution of (14), i.e. the eigenphases and eigenstates of the system, therefore reduces to the numerical diagonalization of the matrix (21). The result is illustrated in Fig. 2(a) for $h_{\mathrm{eff}} = 1/10$, where the eigenphases are plotted as a function of χ_q. The straight lines with negative slope correspond to the regular eigenstates [25, 26], whose Husimi distributions are shown to the right in Fig. 2(a). Lines with an average positive slope correspond to chaotic eigenstates.

When the system consists of M unit cells one has M regular basis states localized on the m-th torus. Their EBK eigenphases are equispaced with a distance $1/M$ [31].

C. Projection onto regular basis states

In order to investigate the amount of flooding we use the projection of the eigenstates onto regular basis states of the island region. For the considered kicked system regular basis states can be constructed from harmonic oscillator eigenstates, as the invariant tori are accurately approximated by ellipses [31]. The expression for the m-th harmonic oscillator state, centered in a phase space point $(\bar{q}, \bar{p})$, is

$$\langle q|\varphi^m_{\bar{q},\bar{p}}\rangle = \frac{1}{\sqrt{2^m m!}} \left(\frac{\mathrm{Re}\,\sigma}{\pi h_{\mathrm{eff}}}\right)^{1/4} H_m\left(\sqrt{\frac{\mathrm{Re}\,\sigma}{h_{\mathrm{eff}}}}(q-\bar{q})\right) \times \exp\left(-\frac{\sigma}{2h_{\mathrm{eff}}}(q-\bar{q})^2 + \frac{\mathrm{i}}{h_{\mathrm{eff}}}\bar{p}(q-\bar{q}/2)\right) \tag{22}$$

where H_m is the Hermite polynomial of degree m. The complex constant σ takes into account the squeezing and rotation of the state. From the linearized map at the stable fixed point of the island one finds $\sigma = (\sqrt{351} - 13\,\mathrm{i})/40$.

For a chain with M identical cells, a regular basis state is a linear combination of the harmonic oscillator states $|\varphi^m_{k,1/4}\rangle$, centered in the k-th island for $0 \le k \le M-1$ and properly normalized and periodized in the q and p directions [31]. The subspace spanned by these M regular basis states is the same as the one spanned by the M harmonic oscillator states $|\varphi^m_{k,1/4}\rangle$. Therefore, we define the weight W_m of a normalized state $|\Psi\rangle$ by its projection onto this subspace corresponding to the m-th quantized torus

$$W_m = \sum_{k=0}^{M-1} |\langle\Psi|\varphi^m_{k,1/4}\rangle|^2 . \tag{23}$$

By means of the weight W_m for all eigenstates of Eq. (21) we can study the process of flooding for each torus separately. This allows for a detailed analysis and a quantitative comparison with a random matrix model. Therefore this is a considerable improvement compared to our previous analysis [18], where the weight was defined as the integral of the Husimi distribution of an eigenstate over the whole region of the island, which means that the information on individual tori is not accessible.

In Fig. 2(b) we show the weights W_0 and W_1 of all the eigenstates as a function of χ_q. For W_0 we observe that for almost all χ_q the weights are essentially zero or one. Only at avoided crossings of regular and chaotic eigenstates their weights have intermediate values. For $m = 1$

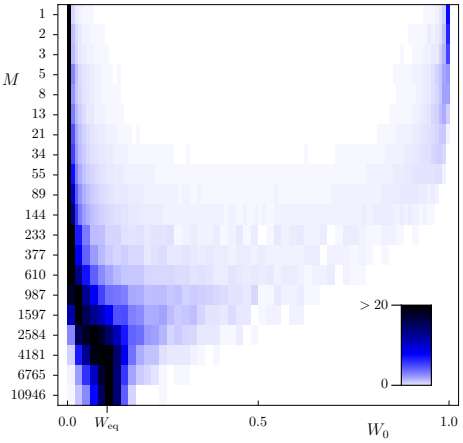

FIG. 3: (color online) Distribution of W_0 (Eq. (23)) vs system size M for effective Planck's constant $h_{\mathrm{eff}} \approx 1/10$.

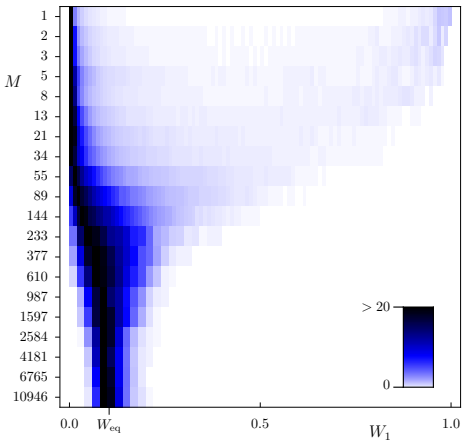

FIG. 4: (color online) Distribution of W_1 (Eq. (23)) vs system size M for effective Planck's constant $h_{\rm eff} \approx 1/10$.

the avoided crossings are much broader due to the larger coupling and the value $W = 1$ is not reached between several avoided crossings. This is also seen in the weight distributions shown to the right in Fig. 2(b), where the two peaks from the chaotic eigenstates (at $W = 1$) and from the regular eigenstates (at $W = 0$) are broader for $m = 1$ in comparison with $m = 0$. Note, that in the situation of isolated avoided crossings the involved eigenstates are often referred to as hybrid states.

The distribution of the weights W_m allows for studying the process of flooding in a quantitative way. To violate condition (2) we need to increase the Heisenberg time, while keeping the tunneling rates γ_m constant. We can achieve this by choosing a sequence of rational approximants M/N of $h_{\rm eff} = 1/(d+g)$, with $d \in \mathbb{N}$ and the golden mean $g = (\sqrt{5}-1)/2 \approx 0.618$. This ensures that, while the system size M is increased, $h_{\rm eff}$ is essentially kept at a fixed value, and therefore the tunneling rates γ_m are independent of M. Simultaneously, the dimensionless Heisenberg time $\tau_{\rm H,ch} = 1/\Delta_{\rm ch}$ increases linearly with M,

$$\tau_{\rm H,ch} = N_{\rm ch} = \left(\frac{1}{h_{\rm eff}} - m_{\rm max}\right) M \ , \qquad (24)$$

where we used $\Delta_{\rm ch} = 1/N_{\rm ch}$ and $N_{\rm ch} = N - m_{\rm max} M$ is the number of chaotic states. Here $m_{\rm max}$ is the maximal number of regular states in a single island according to the EBK quantization condition (1), $m_{\rm max} = \lfloor A_{\rm reg}/h_{\rm eff} + 1/2 \rfloor$. As discussed in Ref. [18], $\tau_{\rm H,ch}$ may be bounded, due to localization effects: For M larger than the localization length λ the effective mean level spacing $\Delta_{\rm ch} \sim (\lambda N_{\rm ch}/M)^{-1}$ leads to $\tau_{\rm H,ch} \sim \lambda N_{\rm ch}/M \approx \lambda h_{\rm eff}$, where λ is measured in multiples of a unit cell and $N_{\rm ch}/M$ is the number of chaotic states per unit cell. For transporting islands, like in the model studied here, $\lambda \sim 1/\gamma_0$ is unusually large [14, 32, 33], leading to a maximal value $\tau_{\rm H,ch} \sim h_{\rm eff}/\gamma_0$.

In Figs. 3 and 4 we show the distribution of W_0 and W_1 for $d = 9$ (giving approximants $h_{\rm eff} = 1/10$, $2/19$, $3/29$, $5/48$, ...) for increasing system size M. For small system sizes we increased the statistics by varying the phase χ_q in the quantization, as it was shown in Fig. 2(b). To present the results in a compact form each histogram is shown using a color scale. The horizontal strips for $M = 1$ in Fig. 3 and Fig. 4 correspond to the histograms previously shown in Fig. 2(b).

In Fig. 3 one clearly observes for small M two separate peaks corresponding to chaotic eigenstates at $W = 0$ [34] and regular eigenstates with $m = 0$ at $W = 1$. With increasing system size these regular eigenstates disappear while the weight W_0 of the chaotic eigenstates starts to increase and they turn into flooding eigenstates.

Comparing Fig. 4 for W_1 with Fig. 3 for W_0 one observes a qualitatively similar behavior. The difference is that the regular eigenstates with $m = 1$ disappear for much smaller system size $M \approx 100$ than the eigenstates with $m = 0$, as expected from Eq. (2) and their ratio of tunneling rates, $\gamma_0/\gamma_1 \ll 1$.

For the largest values of M only flooding eigenstates are left which fully extend over the chaotic sea and the regular island. The flooding is complete and the N eigenstates are equally distributed in the Hilbert space. Projecting them onto the M regular basis states leads to the average value $W_{\rm eq} = M/N = h_{\rm eff} \approx 1/10$, in agreement with the observed position of the peaks in Figs. 3 and 4 and the findings in Ref. [14].

III. RANDOM MATRIX MODEL

In order to find universality in the process of flooding we consider a random matrix model. Such models for the case of mixed systems have successfully been used for the description of the level splitting in the context of chaos assisted tunneling, see e.g. [8, 22, 35, 36]. In contrast, we have to describe the statistics of eigenvectors for the situation of a chain of $N_{\rm reg}$ regular islands. In this case one has equispaced regular levels corresponding to the m-th quantized torus and GOE distributed chaotic levels coupled by dynamical tunneling, see Fig. 5. For this situation we propose a random matrix model with the following block structure

$$H = \left(\begin{array}{c|c} H_{\rm reg} & V \\ \hline V^T & H_{\rm ch} \end{array}\right) \ . \qquad (25)$$

This matrix is real symmetric because the kicked system under consideration obeys time reversal symmetry.

The first block $H_{\rm reg}$ models the regular basis states associated with one specific torus, while for simplicity we neglect the regular basis states quantized on other tori. As discussed at the end of Sec. II B, in the considered kicked system, the EBK eigenphases of the $N_{\rm reg}$ regular basis states are equispaced. To mimic this behavior we consider for $H_{\rm reg}$ a diagonal matrix with elements $(k+\chi)/N_{\rm reg}$, $k=0,1,\ldots,N_{\rm reg}-1$. The parameter χ can be chosen from a uniform distribution between zero and one. The energies lie in the interval [0,1] with fixed spacing $\Delta_{\rm reg}=1/N_{\rm reg}$.

The block $H_{\rm ch}$ models the $N_{\rm ch}$ chaotic basis states, where we assume $N_{\rm ch}>N_{\rm reg}$. It is also a diagonal matrix whose elements $\{E_l\}$ are the eigenphases of an $N_{\rm ch}\times N_{\rm ch}$ matrix of the Circular Orthogonal Ensemble (COE). These energies $\{E_l\}$ lie in the interval [0,1] with a uniform average density and show the typical level repulsion of chaotic systems. The mean level spacing of these basis states is $\Delta_{\rm ch}=1/N_{\rm ch}$. Note, that a GOE matrix for this block would have been less convenient as it leads to a non-uniform density of levels according to Wigner's semicircle law.

The off-diagonal block V accounts for the coupling between the regular and chaotic basis states. It is a $N_{\rm reg}\times N_{\rm ch}$ rectangular matrix, where each element is a random Gaussian variable with zero mean and variance $(v\Delta_{\rm ch})^2$. The positive parameter v is the coupling strength in units of the chaotic mean level spacing $\Delta_{\rm ch}$. Thereby the results become asymptotically independent of the dimension $N_{\rm tot}=N_{\rm reg}+N_{\rm ch}$ of the matrix for fixed v and $N_{\rm reg}/N_{\rm ch}$.

We identify the regular region with the subspace spanned by the first $N_{\rm reg}$ components. Therefore, for any normalized vector $(\Psi_0,\ldots,\Psi_{N_{\rm reg}-1},\Psi_{N_{\rm reg}},\ldots,\Psi_{N_{\rm tot}-1})$ we define the weight W inside the regular region as

$$W=\sum_{j=0}^{N_{\rm reg}-1}|\Psi_j|^2\ . \tag{26}$$

For a particular realization of the ensemble through the numbers $\{E_l\}$, χ, and the block V, we compute the weights W of the eigenvectors. We take for the statistics only those eigenvectors whose eigenenergies are in the interval [0.1, 0.9] to avoid possible border effects. We determine the distribution of W by averaging over many different realizations. Increasing the matrix size $N_{\rm tot}$ for a fixed ratio $N_{\rm reg}/N_{\rm ch}$ we find that the distribution converges. Considering a ratio $N_{\rm reg}/N_{\rm ch}=1/(8+g)$ and a small coupling strength $v\approx 0.1$ the distribution converges around $N_{\rm tot}=200$. For $v\approx 1$ bigger matrices of $N_{\rm tot}\approx 1000$ are necessary. For $v\approx 10$, we used $N_{\rm tot}\approx 10000$. The limiting distributions depend sensitively on the coupling strength v.

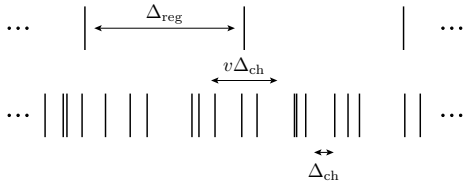

FIG. 5: Schematical plot of the regular levels with spacing $\Delta_{\rm reg}$ coupled with strength $v\Delta_{\rm ch}$ to the GOE distributed chaotic levels with mean spacing $\Delta_{\rm ch}$.

In Fig. 6 we plot the distribution of W for different values of v. We have to distinguish between the uncoupled regular and chaotic basis states of our model and the resulting eigenstates in the presence of the coupling. The eigenstates fall into three classes: a) *Regular eigenstates* ($W>0.5$), which predominantly live in the regular subspace. The remaining states, which predominantly live in the chaotic subspace, are divided into two classes, depending on the strength of their projection onto the regular subspace compared to the equilibrium value $W_{\rm eq}=N_{\rm reg}/N_{\rm tot}$. This leads to b) *flooding eigenstates* ($0.5W_{\rm eq}<W<0.5$), and c) *chaotic eigenstates* ($W<0.5W_{\rm eq}$). Note, that the constants 0.5 in these definitions are arbitrary.

From the energy scales in the random matrix model, see Fig. 5, we expect three qualitatively different situations for the distribution of W:

i) $v\ll 1$, regular and chaotic eigenstates: In this regime the regular and chaotic blocks are practically decoupled as the coupling $v\Delta_{\rm ch}$ is much smaller than the

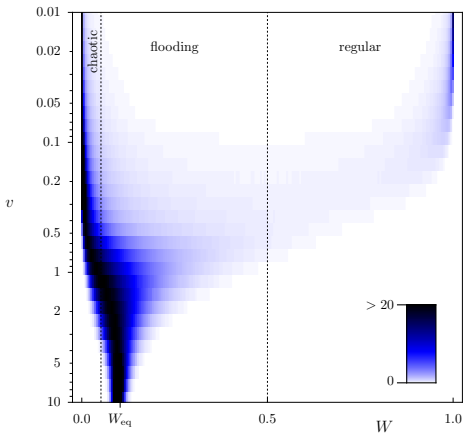

FIG. 6: (color online) Distribution of weights in the random matrix model vs coupling strength v. The ratio $N_{\rm reg}/N_{\rm ch}$ approximates the value $1/(8+g)$. The dashed lines at $W=0.5$ and $W=0.5W_{\rm eq}\approx 0.052$ separate chaotic, flooding, and regular eigenstates.

mean spacing of the chaotic basis states, $v\Delta_{\rm ch} \ll \Delta_{\rm ch}$. Two sharp peaks are observable, one at $W \approx 0$ due to the chaotic eigenstates, and the other at $W \approx 1$ due to the regular eigenstates. The latter peak has a smaller weight as the density of regular basis states is smaller.

ii) $v \approx 1$, chaotic and flooding eigenstates: Here the coupling $v\Delta_{\rm ch}$ is approximately of the same order as the mean chaotic spacing $\Delta_{\rm ch}$. All regular basis states are strongly coupled to several chaotic basis states and none of the eigenstates is predominantly regular. On the other hand one has different types of eigenstates as $v\Delta_{\rm ch} < \Delta_{\rm reg}$: Chaotic basis states, which are close in energy to a regular basis state, strongly couple and thus turn into flooding eigenstates. In contrast, there are many chaotic basis states which are far away from any regular basis state and only couple weakly. These lead to chaotic eigenstates which show essentially no flooding ($W < 0.5W_{\rm eq}$).

iii) $v \gg N_{\rm ch}/N_{\rm reg}$, flooding eigenstates: All chaotic basis states are strongly coupled to the regular basis states, $v\Delta_{\rm ch} \gg \Delta_{\rm reg}$. The resulting eigenstates equally flood the regular subspace. The distribution of W gets a Gaussian shape with mean value $W_{\rm eq} = N_{\rm reg}/N_{\rm tot}$ and a decreasing width.

In the transition from situation i) to ii) the two peaks of $P(W)$ near $W = 0$ and $W = 1$ broaden and move to the center. The regular peak broadens faster, and at $v \approx 0.25$ its maximum disappears. At $v \approx 1$ practically no eigenstates are localized in the regular subspace. When moving from situation ii) to iii) the different types of chaotic and flooding eigenstates transform into a single type of flooding eigenstates with a similar weight $W = W_{\rm eq}$ in the regular subspace.

How do the resulting distributions depend on the ratio $N_{\rm reg}/N_{\rm ch}$? First, the average of $P(W)$ is given by $W_{\rm eq} = N_{\rm reg}/N_{\rm tot} = 1/(1 + N_{\rm ch}/N_{\rm reg})$. Secondly, the regular peak in situation i) is independent of $N_{\rm reg}/N_{\rm ch}$ apart from a trivial scaling of the normalization with $N_{\rm reg}/N_{\rm ch}$. Numerically we checked that this is even true up to $v \approx 1$ for the distribution with $W > 0.5$ and $N_{\rm reg}/N_{\rm ch} \leq 1/(8+g)$. Decreasing $N_{\rm reg}/N_{\rm ch}$ enlarges the size of the transition regime between ii) and iii). In particular, the peak near $W = 0$ should stay there up to larger values of v.

IV. COMPARISON

The distribution of weights for the random matrix model, Fig. 6, shows a clear similarity to the results obtained for the kicked system, Figs. 3 and 4. In order to obtain a quantitative comparison one has to determine the relation between the coupling strength v of the random matrix model and the system size M of the kicked system. This can be deduced from Fermi's golden rule in dimensionless form

$$\gamma = (2\pi)^2 \frac{\langle V^2 \rangle}{\Delta} \ , \tag{27}$$

where the decay rate γ of a regular state to a continuum of states with mean level spacing Δ is given by the variance of the coupling matrix elements V. In the random matrix model we have $\langle V^2 \rangle = (v\Delta_{\rm ch})^2$, $\Delta = \Delta_{\rm ch} = 1/N_{\rm ch}$, and therefore (27) implies

$$v = \frac{\sqrt{\gamma N_{\rm ch}}}{2\pi} \ . \tag{28}$$

Applying this relation to the kicked system, we first note that the tunnelling rate γ_m for each torus can be determined numerically [31] (for recent theoretical results see [37, 38, 39, 40, 41, 42]). The determination of the correct value $N_{\rm ch}$ for the kicked system requires a detailed discussion: A regular basis state on the m-th torus, in the case where the tori $m^*, m^*+1, ..., m_{\rm max}-1$ are already flooded, will couple effectively to $N - m^*M$ states for $h_{\rm eff} = M/N$. A change of m^* affects $N_{\rm ch}$ and therefore v. This dependence, however, can be neglected for the numerical comparison in our case: The ratio of the maximal and minimal possible values of v is approximately $\sqrt{(1-h_{\rm eff})/(1-A_{\rm reg})}$. For $h_{\rm eff} \approx 1/10$ and $A_{\rm reg} = 0.215$ this gives a difference of less than 7%. Therefore we simply use the maximal value $N_{\rm ch} = N - M$ in the following.

For these values of γ and $N_{\rm ch}$ in Eq. (28) the m-th torus of the kicked system has a coupling strength

$$v = \frac{\sqrt{\gamma_m (1/h_{\rm eff} - 1)}}{2\pi} \sqrt{M} \ . \tag{29}$$

This allows for rescaling the results of the kicked system shown in Figs. 3 and 4 from M to v using the values $\gamma_0 = 0.0015$ and $\gamma_1 = 0.030$ [31]. The comparison with the results from the random matrix model is shown in Fig. 7. The agreement is very good for both tori over a wide range of coupling strengths v showing the universality of the flooding process. For $v > 5$, however, the distribution reaches a constant width in Fig. 7(b), while the variance decreases for the random matrix model, Fig. 7(c). We attribute this discrepancy to the localization of eigenstates in the kicked system for $M > 1000$ [14]. As a consequence, the effective number of chaotic basis states near an island saturates (see the discussion after Eq. (24)), leading to an effective saturation of v.

In Figs. 8 and 9 we compare individual histograms for the weights W_0 for $m = 0$. To visualize the low values of the distributions we choose a logarithmic-linear representation in Figs. 8(a) and 9(a). For $M = 144$ one can distinguish the peak near $W = 0$, due to chaotic eigenstates, from the second peak caused by regular eigenstates. For $M = 1597$ these two peaks have merged and only a very small fraction of regular eigenstates is left. In both cases the distributions agree very well with the prediction of the random matrix model using v according to Eq. (29). To resolve the peak near $W = 0$ we show in Figs. 8(b) and 9(b) the distributions of $\ln W_0$. Again very good agreement with the predictions of the random matrix model is observed.

Fig. 10 shows the distribution of $\ln W_1$ for $m = 1$ of all eigenstates for $h_{\rm eff} = 13/125$. We observe discrepan-

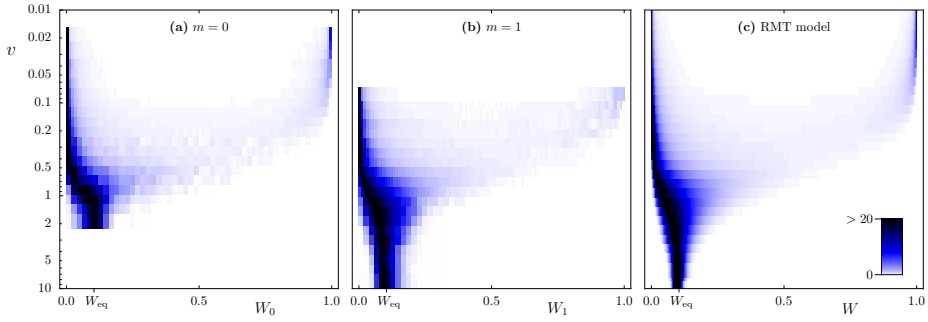

FIG. 7: (color online) Distributions of the weights (a) W_0 and (b) W_1, taken from Figs. 3 and 4, with M rescaled to v according to (29). (c) Result for the random matrix model from Fig. 6 on the same scale for a better comparison.

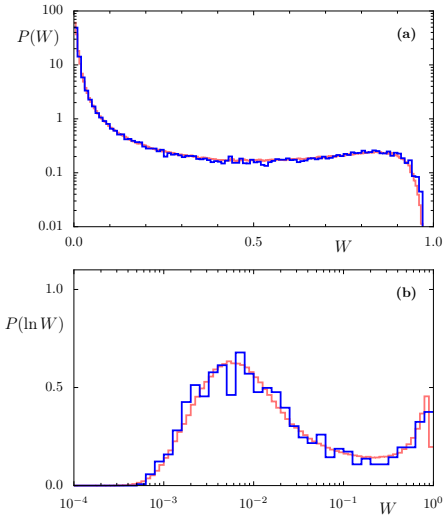

FIG. 8: (color online) Distribution of (a) W_0 and (b) $\ln W_0$ for $h_{\rm eff} = 144/1385$ (dark lines). Results of random matrix model for $v = 0.218$ and $N_{\rm reg}/N_{\rm ch} = 1/8.618$ (light lines).

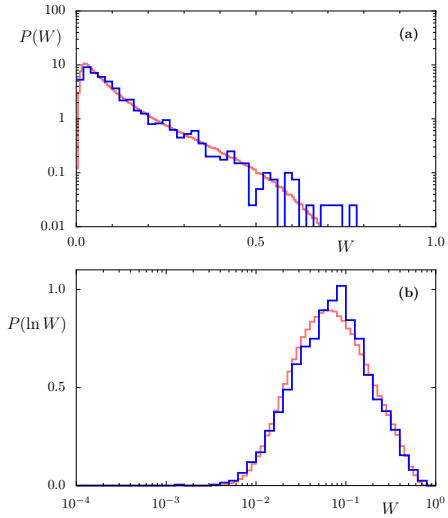

FIG. 9: (color online) Distribution of (a) W_0 and (b) $\ln W_0$ for $h_{\rm eff} = 1597/15360$ (dark lines). Results of random matrix model for $v = 0.726$ and $N_{\rm reg}/N_{\rm ch} = 1/8.618$ (light lines).

cies at weights smaller than 10^{-3} in comparison to the random matrix model. This difference can be explained as follows: Among all the eigenstates of the kicked system there are regular eigenstates localized on the torus $m = 0$ which are not considered in the random matrix model for $m = 1$. These eigenstates have a negligible overlap with the regular basis states with $m = 1$ because they are practically decoupled and only influence the histogram at very small weights. This is confirmed by computing the distribution, under exclusion of all eigenstates with $W_0 > 0.5$. The resulting distribution matches remarkably well with the prediction of our random matrix model.

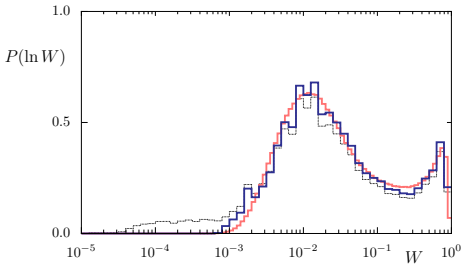

FIG. 10: (color online) Distribution of $\ln W_1$ of all eigenstates (thin line) for $h_{\rm eff} = 13/125$. After excluding states with $W_0 > 0.5$ (thick dark line) much better agreement with the random matrix model (light line) is found.

V. FRACTION OF REGULAR EIGENSTATES

A more global quantity than the individual distributions $P(W)$ is the fraction of regular eigenstates. This has been studied in Ref. [18] for the total number of regular eigenstates as a function of the system size. With the projection onto individual regular basis states we are now able to study this fraction for each torus m separately. For the kicked system with M cells there are at most M regular eigenstates localized on the m-th torus. However, during the process of flooding, some of these eigenstates disappear. Thus, we define the fraction $f_{\rm reg}$ of regular eigenstates on the m-th torus as the number of eigenstates with weight $W_m > 0.5$ divided by M. For small system sizes this fraction is averaged over several different phases χ_q. To compare the resulting dependence on M for different values of m and $h_{\rm eff}$ we determine the coupling strength v using Eq. (29). These results are shown in Fig. 11.

For the random matrix model we compute $f_{\rm reg}$ as the number of eigenstates with $W > 0.5$ divided by the number of regular basis states $N_{\rm reg}$, averaged over many realizations of the ensemble. As discussed at the end of section III, the distribution $P(W)$ for $W > 0.5$ is independent of $N_{\rm reg}/N_{\rm ch}$, apart from a trivial rescaling. Therefore the resulting curve $f_{\rm reg}(v)$ is independent of the ratio $N_{\rm reg}/N_{\rm ch}$ in contrast to the individual distributions. The agreement of the fractions determined for the kicked system with the random matrix curve in Fig. 11 is very good. This shows that $f_{\rm reg}(v)$ is a universal curve describing the disappearance of regular eigenstates. For $v \leq 0.1$ the fraction of regular eigenstates is larger than 98%. For $v \geq 1$ the fraction of regular eigenstates is less than 1% and the corresponding regular torus is completely flooded.

The criterion (2) for the existence of a regular eigenstate, expressed in terms of tunneling rate and Heisenberg time, can be transformed using Eqs. (28) and (24), into the condition

$$v < \frac{1}{2\pi} \ . \tag{30}$$

The position of $v = 1/(2\pi)$ is indicated in Fig. 11 and roughly corresponds to 93% of regular eigenstates still existing (by the $W > 0.5$ criterion). While in Ref. [18] condition (2) for the existence of regular eigenstates was obtained from a scaling argument which does not provide a prefactor, our random matrix model analysis shows that it is quite close to 1.

For the transition regime $1/2\pi < v < 1$ this model shows a decreasing probability for the existence of a regular eigenstate. For $v > 1$, which implies

$$\gamma_m > (2\pi)^2 \frac{1}{\tau_{\rm H,ch}}, \tag{31}$$

we find that almost no regular eigenstate exists on the m-th torus. Thus $v = 1$ defines a critical system size M_m associated with each quantized torus

$$M_m = \frac{4\pi^2 h_{\rm eff}}{\gamma_m (1 - h_{\rm eff})} \ . \tag{32}$$

With the knowledge about the flooding of individual tori we can now consider the total fraction of regular eigenstates. The regular tori with larger m have typically a larger tunneling rate, $\gamma_0 \ll \gamma_1 \ll \ldots \ll \gamma_{m_{\rm max}-1}$. Therefore the flooding of the regular tori happens sequentially from the outside of the island as the system size increases, as found in [18]. The total fraction of regular eigenstates $\mathcal{F}_{\rm reg}$ is defined as the number of eigenstates with weights $W_m > 0.5$ for any m, divided by the total number of eigenstates N. With Eq. (32) we get the

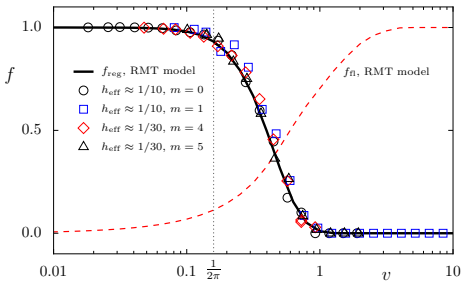

FIG. 11: (color online) Fraction of regular states $f_{\rm reg}$ vs coupling strength v for random matrix model (full line) and kicked system for various $h_{\rm eff}$ and m (symbols), where the system size M is rescaled to v according to Eq. (29). Fraction of flooding eigenstates $f_{\rm fl}(v)$ for the random matrix model (dashed line) for $N_{\rm reg}/N_{\rm ch} = 1/(8+g)$ showing a broader transition.

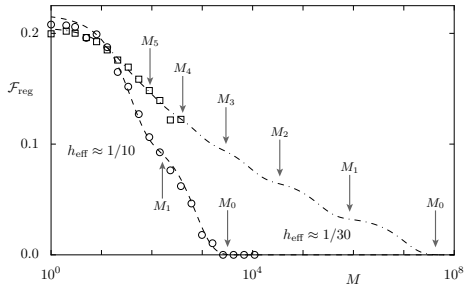

FIG. 12: Total fraction of regular states $\mathcal{F}_{\rm reg}$ vs system size M according to the prediction Eq. (33), (lines) in agreement with the data for the kicked system for $h_{\rm eff} \approx 1/10$ (circles) and $h_{\rm eff} \approx 1/30$ (squares). The arrows indicate the critical system sizes M_m according to Eq. (32).

prediction

$$\mathcal{F}_{\rm reg}(M) \;=\; \frac{M}{N} \sum_{m=0}^{m_{\rm max}-1} f_{\rm reg}\left(\sqrt{\frac{M}{M_m}}\right) \;, \qquad (33)$$

where $f_{\rm reg}(v)$ is the universal curve from the random matrix model. For small system sizes $M < M_m$ for all m the total fraction of regular eigenstates is $\mathcal{F}_{\rm reg}(M) = Mm_{\rm max}/N \approx A_{\rm reg}$, as expected from the semiclassical eigenfunction hypothesis. Fig. 12 shows $\mathcal{F}_{\rm reg}(M)$ with a succession of plateaus and drops before each critical size M_m. Considering that the ratio of successive M_m only varies moderately, the overall behavior of $\mathcal{F}_{\rm reg}$ is an approximately linear decrease on a logarithmic scale in M, explaining the observations of Ref. [18]. The agreement of Eq. (33) with the fraction of regular eigenstates for the kicked system for different $h_{\rm eff}$ as seen in Fig. 12 is remarkably good.

We conclude this section with the remark that due to the independence of $f_{\rm reg}(v)$ on the ratio $N_{\rm reg}/N_{\rm ch}$ one can obtain this universal curve by considering a simpler random matrix model, where only one regular basis state is coupled to an infinite number of chaotic basis states [35]. For this simpler model it might be possible to obtain analytical expressions for $f_{\rm reg}(v)$.

VI. FRACTION OF FLOODING EIGENSTATES

The random matrix model also allows for investigating the fraction of flooding eigenstates. While the regular eigenstates disappear with increasing coupling strength v, more eigenstates turn into flooding eigenstates with $0.5W_{\rm eq} < W < 0.5$. Fig. 11 shows the increasing fraction of these states for the random matrix model with $N_{\rm reg}/N_{\rm ch} = 1/(8+g)$. Note, that this fraction is defined as the number of flooding eigenstates divided by the number $N_{\rm tot}$ of all eigenstates. At $v = 1$ all regular eigenstates have disappeared, however, the fraction of flooding eigenstates is just 70%. The remaining eigenstates are chaotic, which have no substantial weight in the regular subspace. For larger values of v they turn into flooding eigenstates. This roughly happens when each chaotic basis state is coupled to at least one regular basis state, i.e. when $v\Delta_{\rm ch} = \Delta_{\rm reg}/2$, see Fig. 5. This gives $v = N_{\rm ch}/(2N_{\rm reg}) \approx 4.8$ which is in good agreement with the saturation observed in Fig. 11. This shows that the fraction of flooding eigenstates explicitly depends on the parameter $N_{\rm reg}/N_{\rm ch}$ in contrast to the fraction of regular states $f_{\rm reg}(v)$.

Applying this result of the random matrix model to the kicked system where $v = N_{\rm ch}/(2N_{\rm reg}) \approx N/(2M)$, we find using Eqs. (28) and (24), that the fraction of flooding eigenstates is saturated at $f_{\rm fl} = 1$ for

$$\gamma_m > \left(\frac{\pi}{h_{\rm eff}}\right)^2 \frac{1}{\tau_{\rm H,ch}} \qquad (34)$$

Note, that this prefactor increases in the semiclassial limit leading to a broader transition to flooding eigenstates.

VII. SUMMARY AND DISCUSSION

We provide a detailed quantitative description of the flooding of regular islands. By using the projection of eigenstates onto regular basis states, which defines the weights W_m, the process of flooding can be described separately for each torus. The distribution of these weights in the kicked system agrees accurately with the distribution obtained by the proposed random matrix model. This model depends on two parameters only: the coupling strength v between regular and chaotic basis states and the ratio of the number of those states $N_{\rm reg}/N_{\rm ch}$. The connection of this coupling strength with the parameters of the kicked system is given by Eq. (29).

From the random matrix model we gain the following general insights into the flooding of the m-th torus in terms of its tunneling rate γ_m and the Heisenberg time $\tau_{\rm H,ch}$:

i) $\gamma_m < \frac{1}{\tau_{\rm H,ch}}$: All regular eigenstates on the m-th torus exist. None of the eigenstates predominantly extending over the chaotic region has substantially flooded the m-th torus.

ii) $\gamma_m = (2\pi)^2 \frac{1}{\tau_{\rm H,ch}}$: No regular eigenstates on the m-th torus exist. Some of the eigenstates predominantly extending over the chaotic region have substantially flooded the m-th torus.

iii) $\gamma_m > \left(\frac{\pi}{h_{\rm eff}}\right)^2 \frac{1}{\tau_{\rm H,ch}}$: All of the eigenstates predominantly extending over the chaotic region have substantially flooded the m-th torus.

What do these results imply for the applicability of the semiclassical eigenfunction hypothesis? For a fixed

system size in the semiclassical limit $h_{\rm eff} \to 0$, which implies a roughly exponential decrease of γ_m, one ends up in regime i), in agreement with the semiclassical eigenfunction hypothesis. In contrast, for small $h_{\rm eff} \neq 0$ fixed and systems with M cells and $M \to \infty$, one obtains a large value for $\tau_{\rm H,ch} \propto M$, limited by dynamical localization only. Depending on the localization length one ends up in regime iii) for some or all tori m. As in our case one has $\tau_{\rm H,ch} \sim h_{\rm eff}/\gamma_0$, regime iii) is realized for all tori, i.e. complete flooding of the island [14].

The universality in the transition from i) to ii) can be seen for the fraction of regular states $f_{\rm reg}(v)$ localized on a given torus. For the random matrix model this fraction does not depend on the ratio $N_{\rm reg}/N_{\rm ch}$ and the agreement with the results for the kicked system is remarkably good for different quantized tori and values of $h_{\rm eff}$. In contrast to the disappearance of regular eigenstates on the m-th torus, the transition to flooding eigenstates on this torus is much broader and extends to regime iii).

It is also important to discuss, what these results imply for the case of a single island in a chaotic sea ($M = 1$). Most commonly one is in regime i), i.e. regular and chaotic eigenstates exist and only mix at accidental avoided crossings. For a sufficiently small island, compared to the size of the chaotic region, regime ii) can be reached. Here $h_{\rm eff}$ is small enough to quantum mechanically resolve the small regular island, but a corresponding regular state does not exist. It is not possible, however, to get into regime iii) where all eigenstates would be flooding eigenstates: In Eq. (34) we have $h_{\rm eff} = 1/N$ and $\tau_{\rm H,ch} = N_{\rm ch} \approx N$ such that the right hand side is approximately $\pi^2 N$, which is always larger than the tunneling rates $\gamma_m < 1$.

In the case of an island chain of period p embedded in a chaotic sea it might be possible to get into regime iii): In the derivation of Eq. (34) we now have to use $v = N_{\rm ch}/(2N_{\rm reg}) \approx N/(2p) = 1/(2ph_{\rm eff})$, leading with Eqs. (28) and $N_{\rm ch} \approx N = 1/h_{\rm eff}$ to $\gamma > \pi^2/(p^2 h_{\rm eff})$. The right hand side can be smaller than 1 if p is sufficiently large while $h_{\rm eff}$ is small enough to resolve the individual islands of the chain. Whether this is indeed possible in typical systems requires further investigations.

This discussion shows that the semiclassical limit in generic systems with a mixed phase space, where islands of arbitrarily small size exist, is rather complicated. For example one can ask how small does $h_{\rm eff}$ have to be such that at least one regular state exists on a small island of size $A_{\rm reg}$? Let us define the ratio $r = h_{\rm eff}/A_{\rm reg}$ The quantization condition Eq. (1) implies that $r < 2$ is necessary to quantum mechanically resolve the island. However, we find that the necessary ratio r becomes arbitrarily small for small islands: Regime i) for $m = 0$ requires $\gamma_0 < 1/\tau_{\rm H,ch} \approx h_{\rm eff}$. The tunneling rate γ_0 is an approximately exponentially decreasing function $\gamma_0 \sim \exp(-C/r)$ with C of the order of 1 [19, 32]. Thus we have to fulfill $\exp(-C/r)/r < A_{\rm reg}$, which for decreasing $A_{\rm reg}$ is only possible if r is sufficiently small.

We conclude by emphasizing that the universality given by the random matrix model not only holds for the kicked system studied here, but is applicable to any system with a mixed phase space. The consequences for the semiclassical limit in the hierarchical phase–space structure of generic systems needs much further investigation.

Acknowledgements

We thank S. Tomsovic, D. Ullmo and H. Weidenmüller for useful discussions, Lars Schilling for providing us with the data for the tunneling rates, and the Deutsche Forschungsgemeinschaft for support under contract KE 537/3-2.

[1] L. Markus and K. Meyer, *Generic Hamiltonian Dynamical Systems are neither Integrable nor Chaotic*, no. 114 in Mem. Amer. Math. Soc. (American Mathematical Society, Providence, Rhode Island, 1974).
[2] I. C. Percival, J. Phys. B **6**, L229 (1973).
[3] A. Voros, Annales de l'Institut Henri Poincaré A **24**, 31 (1976).
[4] M. V. Berry, J. Phys. A **10**, 2083 (1977).
[5] A. Voros, in *Stochastic Behavior in Classical and Quantum Hamiltonian Systems*, no. 93 in Lecture Notes in Physics, pages 326–333 (Springer-Verlag, Berlin, 1979).
[6] M. V. Berry, in G. Iooss, R. H. G. Hellemann and R. Stora (eds.), *Comportement Chaotique des Systèmes Déterministes — Chaotic Behaviour of Deterministic Systems*, pages 171–271 (North-Holland, Amsterdam, 1983).
[7] See e.g. A. Bäcker, R. Schubert and P. Stifter, Phys. Rev. E **57** (1998) 5425, and references therein.
[8] O. Bohigas, S. Tomsovic and D. Ullmo, Phys. Rep. **223**, 43 (1993).
[9] T. Prosen and M. Robnik, J. Phys. A **26**, 5365 (1993).
[10] B. Li and M. Robnik, J. Phys. A **28**, 4843 (1995).
[11] G. Carlo, E. Vergini and A. J. Fendrik, Phys. Rev. E **57**, 5397 (1998).
[12] G. Veble, M. Robnik and J. Liu, J. Phys. A **32**, 6423 (1999).
[13] J. Marklof and S. O'Keefe, Nonlinearity **18**, 277 (2005).
[14] L. Hufnagel, R. Ketzmerick, M.-F. Otto and H. Schanz, Phys. Rev. Lett. **89**, 154101 (2002).
[15] M. V. Berry, N. L. Balazs, M. Tabor and A. Voros, Ann. Phys. **122**, 26 (1979).
[16] M. J. Davis and E. J. Heller, J. Chem. Phys. **75**, 246 (1981).
[17] Whether these subspaces are orthogonal or only approximately orthogonal has no consequences for the present work and for simplicity we assume orthogonality, as e.g. in Ref. [8].
[18] A. Bäcker, R. Ketzmerick and A. G. Monastra, Phys. Rev. Lett. **94**, 054102 (2005).
[19] J. Feist, A. Bäcker, R. Ketzmerick, S. Rotter, B. Huck-

estein and J. Burgdörfer, Phys. Rev. Lett. **97**, 116804 (2006).
[20] M. Kuś, J. Mostowski and F. Haake, J. Phys. A **21**, L1073 (1988).
[21] F. Haake and K. Życzkowski, Phys. Rev. A **42**, 1013 (1990).
[22] S. Tomsovic and D. Ullmo, Phys. Rev. E **50**, 145 (1994).
[23] A. Bäcker, in: *The Mathematical Aspects of Quantum Maps*, M. Degli Esposti and S. Graffi (Eds.), Springer Lecture Notes in Physics **618**, 91 (2003).
[24] J. P. Keating, F. Mezzadri and A. G. Monastra, J. Phys. A **36**, L53 (2003).
[25] H. Schanz, M. F. Otto, R. Ketzmerick and T. Dittrich, Phys. Rev. Lett. **87**, 070601 (2001).
[26] H. Schanz, T. Dittrich and R. Ketzmerick, Phys. Rev. E **71**, 026228 (2005).
[27] J. H. Hannay and M. V. Berry, Physica D **1**, 267 (1980).
[28] S.-J. Chang and K.-J. Shi, Phys. Rev. A **34**, 7 (1986).
[29] M. Degli Esposti, Ann. Inst. H. Poincaré Phys. Théor. **58**, 323 (1993).
[30] M. Degli Esposti and S. Graffi, in: *The Mathematical Aspects of Quantum Maps*, M. Degli Esposti and S. Graffi (Eds.), Springer Lecture Notes in Physics **618**, 49 (2003).
[31] L. Schilling, PhD thesis, TU Dresden (2006); A. Bäcker, R. Ketzmerick, A. G. Monastra and L. Schilling, in preparation.
[32] J. D. Hanson, E. Ott and T. M. Antonsen, Phys. Rev. A **29**, 819 (1984).
[33] A. Iomin, S. Fishman, and G. M. Zaslavsky, Phys. Rev. E **65**, 036215 (2002) and references therein.
[34] Note, that also regular states on the $m = 1$ torus contribute to this peak, see Fig. 10.
[35] F. Leyvraz and D. Ullmo, J. Phys. A **29**, 2529 (1996).
[36] J. Zakrzewski, D. Delande and A. Buchleitner, Phys. Rev. E **57**, 1458 (1998).
[37] T. Onishi, A. Shudo, K. S. Ikeda and K. Takahashi, Phys. Rev. E **64**, 025201 (2001).
[38] O. Brodier, P. Schlagheck and D. Ullmo, Ann. Phys. **300**, 88 (2002).
[39] V. A. Podolskiy and E. E. Narimanov, Phys. Rev. Lett. **91**, 263601 (2003).
[40] C. Eltschka and P. Schlagheck, Phys. Rev. Lett. **94**, 014101 (2005).
[41] P. Schlagheck, C. Eltschka and D. Ullmo, arXiv.org:nlin/0508024 (2005).
[42] M. Sheinman, S. Fishman, I. Guarneri and L. Rebuzzini, Phys. Rev. A **73**, 052110 (2006).

Erklärung

Hiermit erkläre ich, dass die vorliegende Habilitationsschrift von mir selbst und ohne andere als die darin angegebenen Hilfsmittel angefertigt sowie wörtlich oder inhaltlich übernommene Stellen als solche gekennzeichnet wurden. Ein früheres Habilitationsgesuch an einer anderen Hochschule ist nicht erfolgt.

Arnd Bäcker